

Modelling interfacial tribochemistry in the mixed lubrication regime

Abdullah Azam

Submitted in accordance with the requirements for the degree of
Doctorate of Philosophy

The University of Leeds
Institute of Functional Surfaces
School of Mechanical Engineering

February, 2018

The candidate confirms that the work submitted is his own and that appropriate credit has been given where reference has been made to the work of others.

This copy has been supplied on the understanding that it is copyright material and that no quotation from the thesis may be published without proper acknowledgement.

Assertion of moral rights:

The right of **Abdullah Azam** to be identified as Author of this work has been asserted by him in accordance with the Copyright, Designs and Patents Act 1988.

Acknowledgements

I would like to thank my supervisors Dr **Mark Wilson**, Professor **Ardian Morina** and Professor **Anne Neville** for their help and support throughout my PhD. They have always been there to guide me whenever I was lost. I would like to express my sincere appreciation for my sponsors, FP7 programme for funding my PhD through the Marie Curie Initial Training Network (MC-ITN) entitled “FUTURE-BET – Formulating an Understanding of Tribocorrosion in ArdUous Real Environments – Bearing Emerging Technologies. Without this financial support, I would not have been able to pursue my study and present the outcomes. And special thanks to my supervisor and mentor Anne Neville for the financial help that she provided through the final year when my funding ended.

Special thanks to the High Performance Computing team at the University of Leeds. They have always helped me in enabling the infrastructure and resources and software installation and related complex issues. Their support was remarkable. All my colleagues in the FUTURE-BET project have been outstanding and we have shared some memorable moments together that kept us moving. The friends at the Institute of Functional Surfaces here at Leeds university have all been wonderful. I would not say names as it creates a division but having a wonderful team around was a blessing. I really wish I could spend some more time in the company of Professor Duncan Dowson. This would have made my PhD degree a bit easier.

Special thanks to my wife, Rabia who shared this tough time with me. My daughters Menaal and Zainab have been the blessings throughout this time. I would never have completed my PhD without the prayers of my father and mother and my siblings.

Abdullah Azam

Abstract

The need to reduce the cost of components is driving more and more machine elements to operate under mixed lubrication conditions. With higher operating pressures, the lubricant film is becoming thinner and eventually reaches nanometre scales, comparable to the surface roughness. Thus, understanding the mixed lubrication phenomenon is becoming increasingly important. However, the mixed lubrication phenomenon is difficult to capture experimentally and the lubricant additive ZDDP (Zinc Dialkyl Dithio Phosphate) shows its full antiwear character in the mixed lubrication conditions. This research stems from the need for models that can simulate contact mechanics, lubrication and tribochemistry in a single framework. This is the key to understanding and optimizing the lubrication systems to meet future needs.

To this end, a numerically efficient procedure based upon the tridiagonal solution of the Reynolds equation is developed and is implemented, in Fortran to solve the equations line by line to incorporate more information from the current iteration step. The asperity contacts are handled by the unified solution algorithm. A new strategy to simulate plastic deformation in a lubricated contact is developed.

Under practical loading conditions, the pressures inside the contact can reach values far above the material yielding limit. Thus, an efficient numerical scheme is devised to include the elastic perfectly plastic behaviour in the EHL solution procedure to simulate realistic contact conditions with minimal increase in computational cost.

The Boussinesq deformation integrals result in a convolution of pressure and the deformation which is solved using Fast Fourier Transforms (FFTs) by modifying the solution domain to create a cyclic convolution. Code is developed to allow exploration

of the highly optimized C-based library (www.fftw.org). The use of FFTs speeds up the solution process many times and makes the use of denser grids and larger time scales accessible.

A mesh size of 129 x 129 is found to give reasonable results. The simulation results from the current study agree very well with the previously published results. The evolution of contact area ratio and the central film thickness exhibit a Stribeck type behaviour and the transition speeds at which the contact transits from EHL to mixed and from mixed to complete boundary lubrication can be precisely identified.

Existing tribofilm growth models developed for boundary lubrication are reviewed and a model based on the interface thermodynamics is adapted and integrated with the mixed lubrication model to simulate tribochemistry. The problems with existing EHL concepts such as λ ratio and central film thickness are identified and new definitions are proposed to allow understanding of the mixed lubrication mechanics. The mutual interaction between the tribofilm growth and lubricant film formation is studied. Finally the wear of the tribological system is studied and the wear track profiles are predicted.

The new model is then applied to study a ball-on-disc system to explore wear, tribochemistry and roughness evolution. The ZDDP tribofilm growth is studied and it is found that the final ZDDP tribofilm thickness is very weakly affected by increasing SRR but the rate of formation and removal are strongly affected by the SRR value. The tribofilm growth results are validated against published numerical and experimental results. It is found that the antiwear action of the ZDDP tribofilm is not only due to its chemical action but the ZDDP tribofilm helps to entrain more lubricant and improves contact performance. The presence of tribofilm roughens the contact and the contact area and load ratio both increase due to tribofilm growth. It

was also found that the use of conventional EHL parameters to analyse the behaviour of tribosystem is misleading. The flattening of the roughness inside the contact and the proper identification of the central film thickness are crucial to the interpretation of the mixed lubrication results. The roughness of the ball generally decreases due to wear but the presence of tribofilm limits this reduction. Contrary to this, the surface roughness of the ball generally increases due to wear but the presence of tribofilm results in increased roughness of the ball.

Table of Contents

Acknowledgements	iii	
Abstract	iv	
Table of Contents	vii	
List of Figures	xii	
Chapter 1	Introduction and Outline	2
1.1	Introduction	2
1.2	Motivation	8
1.3	Impact.....	12
1.4	Objectives.....	14
1.5	Thesis Structure.....	15
Chapter 2	Theory and Background.....	18
2.1	Elastohydrodynamic lubrication	18
2.2	Transient EHL equation set.....	20
2.2.1	Reynolds equation	21
2.2.2	Film thickness equation	22
2.2.3	Load balance equation.....	22
2.2.4	Pressure-viscosity equation	23
2.2.5	The density pressure equation	24
2.3	Mixed Lubrication Modelling.....	26
2.3.1	Elastohydrodynamic lubrication with roughness	27
2.3.2	Mixed Lubrication: EHL with asperity-asperity contacts ..	30
2.4	The antiwear additive ZDDP	32
2.4.1	The antiwear action of ZDDP	36
2.4.2	Mechanical behaviour of ZDDP tribofilms.....	37
2.4.3	Composition and structural properties of ZDDP tribofilms	37
2.4.4	Tribofilm growth and growth kinetics.....	38

2.4.5	Tribochemistry of ZDDP antiwear film formation	40
2.5	Friction with ZDDP	42
2.6	Summary	43
Chapter 3	Mixed Lubrication Model: Numerical, Algorithmic and Computational Details.....	46
3.1	Governing Equations for mixed lubrication problem	48
3.2	Non-dimensionalization	51
3.3	Discretization	52
3.3.1	Discrete Reynolds Equation	53
3.3.2	Discretized deformation integral	55
3.3.3	Discretized Load balance equation.....	55
3.4	Numerical procedure for solving the Reynolds Equation	56
3.5	Constructing coefficient matrix for the Reynolds Equation	57
3.5.1	Conventional solution procedure.....	58
3.6	Design and development of a robust solver for the mixed lubrication problem	60
3.6.1	Iterative approaches in EHL / ML solutions	61
3.6.2	A survey of numerical approaches	61
3.6.3	The Semisystem approach: insights into numerical stability	65
3.6.4	The unified solution algorithm	68
3.6.5	The line by line TDMA solver	69
3.7	Implications of reduced Reynolds equation: weak coupling	71
3.7.1	Implementation of the unified solution algorithm.....	74
3.7.2	Implementation of boundary conditions.....	75
3.7.3	Relaxation scheme and convergence criteria	76
3.8	Deformation convolution using Fast Fourier Transforms (FFTs) .	78
3.9	Implementation of fftw library in FORTRAN.....	82

3.10	Validation of the Mixed lubrication model.....	85
3.10.1	Criteria.....	85
3.11	Summary	96
Chapter 4	Elastic-Perfectly plastic deformation modelling in lubrication ...	100
4.1	Model and Algorithm.....	100
4.1.1	Sahlin et al. s' Approach (existing).....	101
4.1.2	The new algorithm: developed in current study.....	103
4.2	Implementation Details	108
4.3	Results.....	109
4.3.1	Smooth surface elastic-plastic contact.....	109
4.3.2	Rough surface elasto-plastic contact	110
4.3.3	Model validation and the effect of load on the elastoplastic contact performance	114
4.3.4	A note on the hardness value.....	120
4.4	Effect of geometry update on plastic deformation.....	122
4.5	Summary	126
Chapter 5	Modelling tribochemistry in mixed lubrication	129
5.1	Introduction and background	129
5.2	Factors driving the tribofilm growth.....	130
5.3	Numerical simulation of tribofilm growth in boundary lubrication	132
5.4	Mixed lubrication models with tribochemistry.....	133
5.5	Selection of the tribofilm growth model: A short survey	134
5.5.1	The calculation of flash temperatures	144
5.5.2	Mechanical properties of tribofilm.....	146
5.6	Illustrative simulation of tribofilm growth.....	148
5.6.1	System and model configuration.....	149
5.6.2	Tribofilm growth results and analysis	152

5.6.3	The patchy growth of tribofilm (3-D evolution of tribofilm)	154
5.6.4	Tribofilm growth on smooth counterpart surface (Ball, $R_a = 10$ nm, $R_q = 12$ nm).....	156
5.6.5	Tribofilm growth on Rougher counterpart surface (Disc, $R_a = 100$ nm, $R_q = 127$ nm).....	157
5.7	Effect of slide to roll ratio on the tribofilm growth.....	158
5.8	Model validation and discussion.....	161
5.9	Summary	167
Chapter 6	Interfacial Mechanics: The interaction between tribochemistry and lubrication science.....	170
6.1	Background to problem.....	171
6.2	Terminology update for describing mixed lubrication.....	175
6.2.1	Minimum film thickness (h_m).....	175
6.2.2	Central film thickness (h_c).....	176
6.2.3	Film thickness ratio (λ ratio / λ ratio).....	177
6.2.4	Conventional Film thickness ratio λ_{OLD}	178
6.2.5	Contact area ratio A_c	178
6.2.6	Contact load ratio, W_c	179
6.3	Illustrative tribochemical simulation of mixed lubrication.....	179
6.3.1	Numerical details.....	180
6.3.2	Input parameters for simulations to study the comparative effect of tribofilm growth and wear	180
6.3.3	Input parameters to study the effect presence and absence of tribofilm	181
6.3.4	Results	181
6.3.5	Discussion: The presence of tribofilm and its effects	185
6.4	Summary	199
Chapter 7	Predicting wear and wear track profiles.....	202

7.1	Introduction	202
7.2	Wear prediction and its significance	205
	7.2.1 Inclusion of tribochemistry.....	207
7.3	Attempts at modelling and predicting wear tracks.....	209
7.4	Operating and numerical parameters	210
7.5	Results and discussion	210
	7.5.1 Mean wear depth	211
	7.5.2 Wear track and worn surface profiles (2-D).....	214
	7.5.3 Wear track profiles (3-D)	218
7.6	Summary	219
Chapter 8	Conclusion and Future Outlook	223
8.1	Summary of key developments and advances achieved	223
8.2	General conclusion and discussion	225
8.3	Future work	228
	Bibliography.....	231

List of Figures

Figure 1-1: A schematic representation of conformal and non-conformal contact cases. (a) conformal contact. (b) non-conformal / counter-conformal contact. . 4	4
Figure 1-2: A schematic representation of various lubrication regimes. The curve shows friction behaviour with change in specific film thickness. Symbol definitions: μ = friction coefficient, η = lubricant viscosity, U = mean speed of lubricant and P is the pressure inside the contact..... 5	5
Figure 1-3: A simplified illustration of the components of a typical ball bearing. All modes of lubrication are active during its operation [9]. 7	7
Figure 1-4: Reduction in lubricant film thickness in bearings [13]. 9	9
Figure 1-5: Example of a retrieved total hip implant showing signs of mechanically assisted corrosion [27]. 13	13
Figure 1-6: Enhanced damage at the rubbing interfaces of a ship anchor chain. These regions undergo maximum wear and limit the life of these components. 14	14
Figure 2-1: (a) A schematic representation of tribological contact between a flat disc and ball. (b) Enlarged view of contact zone. If this is scaled onto an A4 paper then the thickness of the paper gives an estimate of the lubricant film thickness 19	19
Figure 2-2: EHL contact configuration outlining the key parameters in the mathematical model. 21	21
Figure 2-3: A comparison of the two laws for the pressure dependence of fluid viscosity. The Roelands equation gives more accurate representation of the EHL phenomenon [29]. 24	24
Figure 2-4: The increase in density with pressure. The density increase is limited to a value of $1.34\rho_0$ [29]..... 25	25
Figure 2-5: Pioneering results from Petrusевич et al. [32]. The momentary increase in pressure (spike) and decrease in film thickness (constriction) can be observed clearly towards the exit of contact. 26	26
Figure 2-6: The lubrication regimes explained [50]. 28	28
Figure 2-7: An illustration of the limitations of stochastic models [17] 30	30

Figure 2-8: The structure and mechanical properties of the ZDDP antiwear tribofilm. The scale on the y-axis gives the representative thickness of each layer within the complete film [84]. (a) shows the complete anti-wear tribofilm formed by the action of a simple ZDTP molecule. (b) the same film after washing with a solvent.	33
Figure 2-9 Schematic of the structure of ZDDP molecule [88].....	35
Figure 2-10 An illustration of the gradient in structure and composition of ZDDP tribofilm [85].....	36
Figure 2-11: Schematic representation of the basic principle of tribofilm thickness measurement using SLIM [113].	39
Figure 3-1: Contact simplification and definition of key parameters	48
Figure 3-2: The distinction between the stencil of pressure differences and the stencil for discretizing the Reynolds coefficients. The open points and red indices refer to the stencil for Reynolds coefficients.....	53
Figure 3-3: Flow chart to illustrate the numerical algorithm for solving the unified mixed lubrication problem.	57
Figure 3-4: Various approaches for solving the EHL / mixed lubrication problem.	63
Figure 3-5: Illustration of the tridiagonal matrix formation. This matrix forms for a single line in the solution domain.	72
Figure 3-6: The line by line TDMA algorithm explained. The numerical flow of information is shown by arrows. Note: the information flow direction can be along other directions as well but the line by line solution should be performed.	73
Figure 3-7: The superior performance achieved by the line by line TDMA algorithm explained for solution on a single node. For comparison, the nodal Gauss-Seidel and Jacobi stencils are also given.	74
Figure 3-8: The application of boundary conditions for the TDMA algorithm. The boundary condition of zero pressure diffuses inwards to define the cavitation boundary.	76

Figure 3-9: Modifications required to change the linear convolution to the cyclic convolution. These modifications are necessary for applying the FFT procedure to solve convolution.	80
Figure 3-10: The influence matrix plotted over the entire domain. (a) shows the original influence matrix (b) shows the influence matrix after pre-treatment, modified to account for cyclic convolution as explained.	81
Figure 3-11: The application of the fftw library to numerically solve the convolution of pressure and deformation matrix using FFTs. The actual lines from the Fortran code used are given.	84
Figure 3-12: The discontinuities at the entrainment of contact leading to the grid dependence of the mixed lubrication / EHL solutions [159].	86
Figure 3-13: Grid justification for high to medium speed simulations in a mixed lubricated contact. The increase in film thickness with grid refinement is noticeable.	87
Figure 3-14: Grid justification for medium speed simulations in a mixed lubricated contact. The dependence of film thickness results on the grid density is more pronounced.	89
Figure 3-15: Grid justification for ultra-low speed simulations in a mixed lubricated contact. The choice of grid density strongly affects the results at such low speeds.	90
Figure 3-16: The pressure and film thickness profiles at the middle cross-section of contact from current study. (a) speed 15000 mm/s (b) speed 0.001 mm/s. Current study.	92
Figure 3-17: The pressure and film thickness profiles at the middle cross-section of contact. (a) speed 15000 mm/s (b) speed 0.001 mm/s. These plots are from ref. [76].	93
Figure 3-18: The mixed lubrication parameters contact area ratio (normalized) and the central film thickness plotted against the rolling speed. The entire transition of lubrication from full film down to boundary lubrication can be seen. The speeds corresponding to transition from full film to mixed and from mixed to boundary have been marked by the vertical lines.	95

Figure 4-1: A schematic representation of the penetration of plane of plastically deforming points. 105

Figure 4-2: Flow chart and algorithm to extend the unified mixed lubrication solver to handle elastoplastic contacts as developed in the current study. 107

Figure 4-3: Smooth surface PEHL results. (a) The contact plane convergence. This plane converges by itself through the solution. (b) The undeformed and deformed geometry of the ball at the centre cross-section of the contact..... 111

Figure 4-4: Rough surface PEHL results. The original smooth surface profile is also shown along with the undeformed rough surface and the corresponding deformed rough surface geometry. 112

Figure 4-5: PEHL pressure profiles. The pressure profile for the original starting smooth surface solution is also given for comparison. The actual rough surface pressures without plastic deformation and with deformation show increase in area of contact. The starting pressure profile shows strong EHL by the presence of the pressure spike..... 113

Figure 4-6: PEHL film thickness profiles. The presence of roughness effectively improves lubricant entrainment. The presence of plastic deformation flattens the film thickness profile. 113

Figure 4-7: The results for PEHL from the current model. (a) pressure profile. (b) non-dimensionalized plastic deformation (cross-section at $Y=0$). 116

Figure 4-8: The lubricant film thickness results in nanometres for PEHL from the current model. (a) grid of 129 x 129 (b) grid of 65 x 65..... 117

Figure 4-9: The effect of geometry update on the PEHL film thickness results. (a) non-dimensionalized film thickness profiles without geometry update. The plastic deformation is allowed to accumulate in every iteration. (b) The geometry is updated every iteration until no more plastic deformation takes place. 118

Figure 4-10: PEHL results. (Left hand side) solutions for different loads from Ren et al. [162]. (Right hand side) solutions for different loads from current study. Results are normalized by the half width of Hertzian contact radius at initial yield..... 119

Figure 4-11: The effect of Hardness value used in the current model. (a) pressure profiles for varying hardness valeus. (b) film thickness profiles for varying hardness values.	121
Figure 4-12: The effect of considering geometry update due to material removal. Various curves correspond to the iteration number at which the material was removed and if it was removed in a single step. (a) pressure profiles. (b) film thickness profiles	124
Figure 4-13: The effect of considering geometry update due to material removal. Various curves correspond to the iteration number at which the material was removed and if it was removed in a single step. (a) Plastic deformation profiles. (b) Central film thickness evolution with iteration number.....	125
Figure 5-1: Tribofilm growth model from Fujita and Spikes [92]. (a) Results for different temperatures. (b) Results for different concentrations.	135
Figure 5-2: Mean tribofilm thickness results from the tribofilm growth model of Andersson et al. [22].	137
Figure 5-3: Tribofilm growth model results. The plots show the experimental results of tribofilm growth and the corresponding model fitted tribofilm profiles for different temperatures [175].....	140
Figure 5-4: Variable hardness model for numerical simulation of mechanical behaviour of tribofilm. Case 1. Corresponds to the case where the tribofilm on one of the surfaces deforms. Case 2. Corresponds to the situation where the tribofilm deforms on both the contacting bodies. Case 3. Corresponds to complete tribofilm deformed on both the contacting surfaces. The plastic deformation has reached the substrate. Figure reproduced from [183].	148
Figure 5-5: Flow chart to explain the numerical simulation of tribofilm growth / removal and wear of substrate in mixed lubrication conditions.	151
Figure 5-6: The growth of tribofilm on rough surface. (a) the original rough surface. (b) tribofilm formed on rubbing track. The rubbing track is aligned with the X-direction. The direction of flow is indicated by the arrow.....	153
Figure 5-7: ZDDP tribofilm formation in the rubbing track. Coverage and thickness of tribofilm increases with time as well as the mean tribofilm thickness. Arrows point to the direction of flow. An area of 0.5 mm x 0.5 mm is shown.	155

Figure 5-8: Mean tribofilm thickness on the smoother counterpart. (Ball surface roughness, $R_a = 10$ nm, $R_q = 12$ nm.....	157
Figure 5-9: Mean tribofilm thickness on the rougher counterpart. (Disc surface roughness, $R_a = 100$ nm, $R_q = 127$ nm.....	158
Figure 5-10: Tribofilm growth and mean tribofilm thickness as a function of time for different slide to roll ratios on the ball. (a) negative SRR values. (b) positive SRR values.....	159
Figure 5-11: Comparison of tribofilm growth from current model against the work of Ghanbarzadeh et al. [120]	161
Figure 5-12: Tribofilm thickness values as a function of time for different values of positive SRR.	164
Figure 5-13: Tribofilm thickness results from Andersson et al. [22].....	164
Figure 5-14: Experimental validation of tribofilm growth results. Experimental results are digitized from the work of Parsaeian et al. [185].....	166
Figure 6-1: The state of the art in unified mixed lubrication models being able to predict the contact parameters through all the lubrication regimes [20, 76, 82].	173
Figure 6-2: A glimpse of complex phenomena happening at the interface [20].....	174
Figure 6-3: The illustration of the wear track and associated parameters.....	181
Figure 6-4: Central film thickness evolution in a 2 hour simulation. The relative importance of tribofilm growth and wear can be identified. The hump in the beginning is where the tribofilm is dominating the contact characteristics. The latter part refers to the region where wear dominates the contact performance.	182
Figure 6-5: Film thickness ratio / λ ratio evolution in a 2 hour simulation. The relative importance of tribofilm growth and wear can be identified.....	183
Figure 6-6: The changes in the contact area ratio and contact load ratio in a 2 hour simulation test. The relative importance of tribofilm growth and wear can be easily identified in the contact area ratio while the contact load ratio seems unaffected by the growth of tribofilm.	185

Figure 6-7: Assessment of the effect of tribofilm growth on roughness evolution. These plots correspond to the ball surface.	186
Figure 6-8: The effect of tribofilm growth on the conventional lambda ratio. The central film thickness value in this plot is a constant value based upon Dowson and Higginson formulation (equation (2-6)).	188
Figure 6-9: The effect of tribofilm growth on the R_q and R_a roughness values over time. The presence of tribofilm roughens the contact.	189
Figure 6-10: The effect of tribofilm growth on the central film thickness. The central film thickness value is the average of the instantaneous film thickness values within the contact region.	191
Figure 6-11: The effect of tribofilm growth on the film thickness ratio. The results are plotted over time and the presence of tribofilm improves contact performance.	192
Figure 6-12: The effect of polar additives on the contact area ratio. Maximum Hertzian pressure is 0.292 GPa. (a) The effect of adding polar additive nonylic acid to Hexadecane. (b) The effect of adding polar additive nonylic acid to mineral oil [197].	194
Figure 6-13: A comparison of the effect of tribofilm growth on the roughness evolution of the ball and disc.	196
Figure 6-14: The effect of tribofilm growth on the maximum instantaneous value of pressure. The pressures are non-dimensionalized with the Hertzian pressure and the results are plotted over time.	197
Figure 6-15: The effect of tribofilm growth on the contact area ratio (A_c) and contact load ratio (W_c). The results are plotted over time and the magnitude of both A_c and W_c increase due to the tribofilm.	198
Figure 7-1: Various forms in which abrasive wear manifests itself [8].	204
Figure 7-2: Modes of abrasion. (Top) Two body abrasion. (Bottom) Three body abrasion [8].	204
Figure 7-3: Mean wear depth on the ball surface calculated from the current model over time. The legends are the SRR values. (a) positive SRR. (b) negative SRR	212

Figure 7-4: Mean wear depth on the disc surface calculated from the current model over time. The legends are the SRR values. (a) positive SRR. (b) negative SRR 213

Figure 7-5: The profile of wear on the surface of ball for different SRR values. The plots present values for the worn geometry at the cross-section in the middle of contact at $Y=0$ 215

Figure 7-6: The profile of actual worn geometry of the surface of ball for different SRR values. The plots present values for the worn geometry at the cross-section in the middle of contact at $Y=0$ 216

Figure 7-7: The profile of wear on the surface of disc for different SRR values. The plots present values for the worn geometry at the cross-section in the middle of contact at $Y=0$ 217

Figure 7-8: 3-D wear track profiles on the ball. Arrows indicate increase in wear. 221

Figure 7-9: 3-D wear track profiles on the Disc. Arrows indicate increase in wear. 222

Part-I

Introduction and Background

Chapter 1

Introduction and Outline

This chapter starts with a general introduction about tribology and tribochemistry in view of the scope of the thesis. Then a brief account of motivation for this research and the potential impact of this work are given. This is followed by an outline of the objectives and structure of the thesis.

1.1 Introduction

The science of interacting surfaces is called tribology, meaning science of rubbing. The most general divisions of tribology are wear, friction and lubrication. **Wear** is the damage that occurs to either one or both of the interacting surfaces due to the tribological loads. This damage ultimately leads to component failure and all tribological designs require this damage to be minimum. **Friction** is omnipresent in contacting surfaces in relative motion, and can be constructive or destructive depending upon the application. Design of components requires control over friction. **Lubrication** helps to control both friction and wear; the process of lubrication greatly reduces friction and wear and prolongs the life of components. Common lubricants consist of a base oil and certain additives that interact with the surface under extreme conditions to control / reduce friction, wear and seizure. The presence of these additives makes the system much more complex and the effect of rubbing on these chemical interactions requires detailed information at the interface. **The subject of this thesis is the modelling of these interactions for the lubricated contact.**

The use of lubrication dates back to the age of the Pyramids where lubricant was applied to transport heavy blocks but it took quite long for understanding of the physics of lubrication and film build-up to be established. The hydrodynamic pressure

generation was explained first by Osborne Reynolds in the late 19th century [1]. He simplified the Navier-Stokes equations by using a thin film approximation and came up with the famous Reynolds equation that is widely used in lubrication analysis today.

The lubrication behaviour in a tribosystem can be categorized as one of five types: hydrodynamic lubrication (HL), hydrostatic lubrication (HS), elastohydrodynamic lubrication (EHL), mixed lubrication (ML), or boundary lubrication (BL). Hydrodynamic lubrication is the main mode of lubrication in conformal contacts (greater geometrical conformity and larger load carrying area) e.g. thrust bearings, journal bearings etc. Here the lubricant supplies the pressure to hold the load by forming a viscous film due to relative movement of the tribopair with no elastic deformation of the surfaces. These are low load applications where the lubricant film thickness stays above 1 μm generally while operating pressures remain below 10 Mpa [2]. In contrast, hydrostatic lubrication is characterized by active generation of pressure by an external source rather than relying on the relative movement of surfaces.

If the contact is non-conformal (less geometrical conformity – small load carrying area), very small areas are supporting very high loads. The corresponding mode of lubrication changes from hydrodynamic to EHL. Figure 1-1: A schematic representation of conformal and non-conformal contact cases. (a) conformal contact. (b) non-conformal / counter-conformal contact. This regime of lubrication is characterized by significant elastic deformation (and possible plastic deformation) of the contacting solids. The load carrying capacity increases several orders of magnitude, on the order of giga Pascal and typical lubricant film thickness is less than a micrometre. Rolling element bearings, cams and gears all operate in the EHL

regime. Figure 1-1 gives a schematic representation to identify conformal and non-conformal contacts.

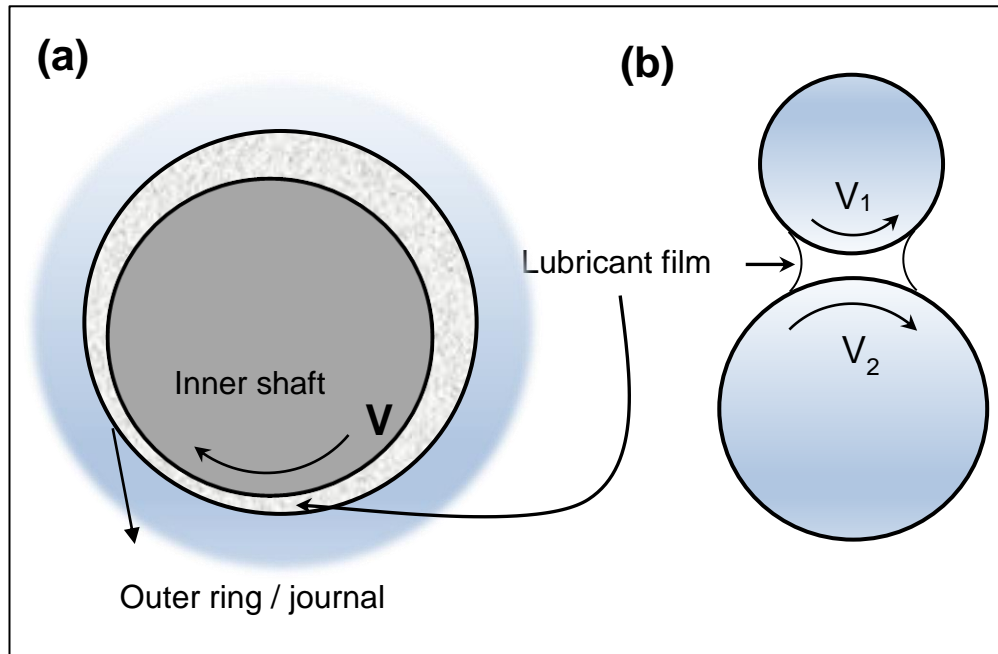


Figure 1-1: A schematic representation of conformal and non-conformal contact cases. (a) conformal contact. (b) non-conformal / counter-conformal contact.

With further increase in applied load and/or reduction of speed, the lubricant film becomes significantly thinner than the roughness of the corresponding surfaces. The result is the formation of distinct solid contact patches which start carrying a portion of the load while the rest is still carried by the lubricant. If the load sharing between these solid contact spots and the lubricant is roughly less than 85 % and greater than 0 % (no asperity contact), the regime of lubrication is termed as ML. **Modelling the mixed lubrication regime is a challenging task.**

If the load sharing is increased further by a reduction in speed or the increase in load etc. to greater than 85 %, the lubrication regime transits into boundary lubrication

where the load is mainly carried by the asperity contact spots and this governs the contact behaviour. Various lubrication regimes have been identified on a typical Stribeck curve shown in Figure 1-2.

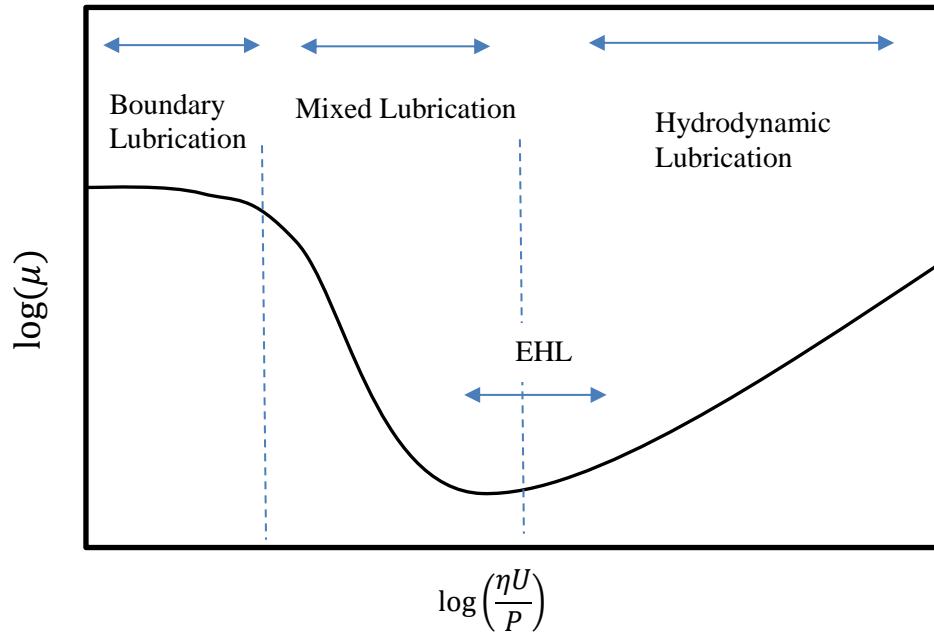


Figure 1-2: A schematic representation of various lubrication regimes. The curve shows friction behaviour with change in specific film thickness. Symbol definitions: μ = friction coefficient, η = lubricant viscosity, U = mean speed of lubricant and P is the pressure inside the contact.

Tribology is a highly interdisciplinary science, including but not limited to, mechanical engineering, chemistry, biomedical, physics etc. The tribo-contact involves complex phenomena such as high contact stresses accompanied with thermal effects. The situation is worsened by the chemical interactions taking place at the interface. The complex geometrical interfaces are shown in Figure 1-3 for a typical ball bearing. Environmental effects i.e. the lubricant itself, humidity and ambient air further complicate the process [3].

A lubricant performs different functions during different operating conditions. At higher speeds, it reduces friction and wear by forming a continuous layer of lubricant to keep the surfaces apart. At lower speeds, it forms a chemically adsorbed / reacted layer on the solid surfaces to protect against excessive wear and control friction and seizure. To do this, the lubricant contains an additive package in addition to the base oil. The contents of the package are mainly active under extreme pressure conditions. Its most important constituents are extreme pressure (EP) additives, antioxidants, antiwear (AW) additives to mitigate wear, and friction modifiers (FM), viscosity index (VI) improvers to maintain viscosity over the operating temperature range.

Tribochemistry deals with chemical and physiochemical changes of matter caused by mechanical action [4]. Tribocorrosion is considered to be caused by water contaminated oil systems and/or, under harsh environments (high temperatures, high pH etc.), due to the degradation of oil [5]. Tribocorrosion is a subgroup of tribochemical processes. Hence, the operation and functionality of the lubricant additives is a tribochemical process. Various reactions occur at the contact interface and mechanical action affects these reactions. The simplest mechano-chemical action alters only the rate of chemical reaction. In the more complex cases, the path of reaction is affected as well. Tribochemistry involves both the tribochemical changes in the lubricant and the tribochemical reactions transforming the sliding surfaces.

ZDDP (Zinc dialkyldithiophosphate) is the most extensively used AW additive, mainly due to its low cost and versatile functionality. Historically, ZDDP was introduced as an antioxidant [6, 7]. But it was soon discovered that it is also a very good AW agent. There are several proposals about the decomposition and action of ZDDP but these are beyond the scope of this thesis and readers are referred to detailed

reviews [8]. Some details of these mechanisms will follow in chapter 2 where the literature on ZDDP is reviewed.

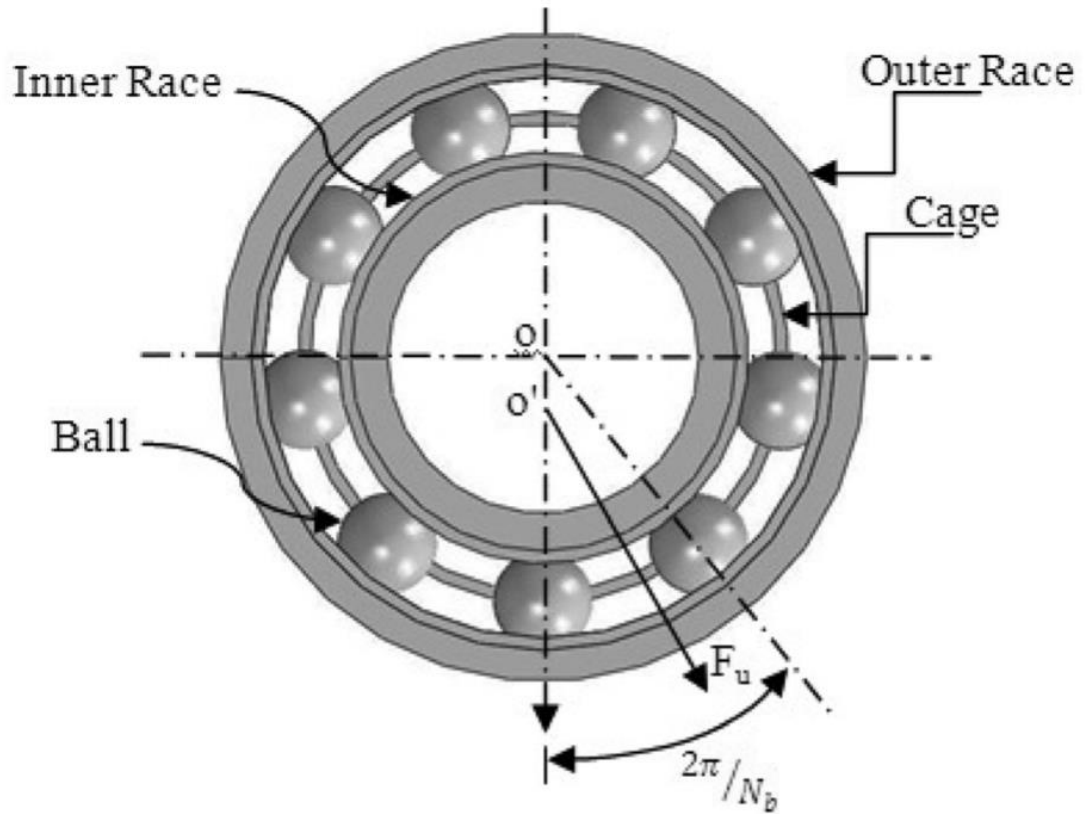


Figure 1-3: A simplified illustration of the components of a typical ball bearing. All modes of lubrication are active during its operation [9].

In summary, the topic of this study is to model the tribochemical aspects of lubrication. It is achieved in two steps: first, developing a mixed lubrication model that is robust enough to simulate the entire speed range (very high to almost zero), second, the development and implementation of a tribofilm growth model to simulate real time chemical changes occurring due to mechanical stimuli and simulate its effect on the macroscopic properties: friction and wear. This is the first mixed lubrication model that incorporates tribochemistry. The challenge undertaken in this study is to capture not all but some key aspects of the problem that are still poorly understood.

1.2 Motivation

Industrial applications of lubricated components are posing more severe conditions of operation resulting in lesser quantity of lubricant to use, severe temperature operation, and thinner lubricant films. The trends in machine downsizing, increased loading and better sealing performance are ultimately leading towards thinner lubricant films and components are prone to direct solid-solid interaction resulting in loss of energy inefficiency [10, 11]. Lubrication analysis is incomplete without proper consideration of topography as it is the topography that defines how and when surface contacts will occur. As mentioned before, most technologically important components operate in the near EHL or mixed lubrication regime and the load is generally shared between the solid and lubricated regions [12]. Such contacts are counterformal in nature and the lubricant film thickness is usually of the same order as the surface roughness, sometimes of molecular dimensions. To illustrate this reduction in film thickness, Figure 1-4 presents this progressive shrinking of the lubricant film thickness in bearings [13]. Analysing component performance and lives under such conditions requires a mixed lubrication model that is robust enough to handle such small films and can smoothly transit between different lubrication regimes. Moreover, handling the very small thicknesses of the order of nanometers means that the mixed lubrication model should also consider the tribochemical changes occurring at the interface.

The mixed lubrication regime is a rather difficult phenomenon to understand, observe and model. ML is experimentally challenging to quantify. The presence of surface roughness and the dynamic movement of surfaces result in momentary changes in the contact zone which are difficult to capture. Moreover, it is not possible to accurately measure the variables that quantify the ML regime.

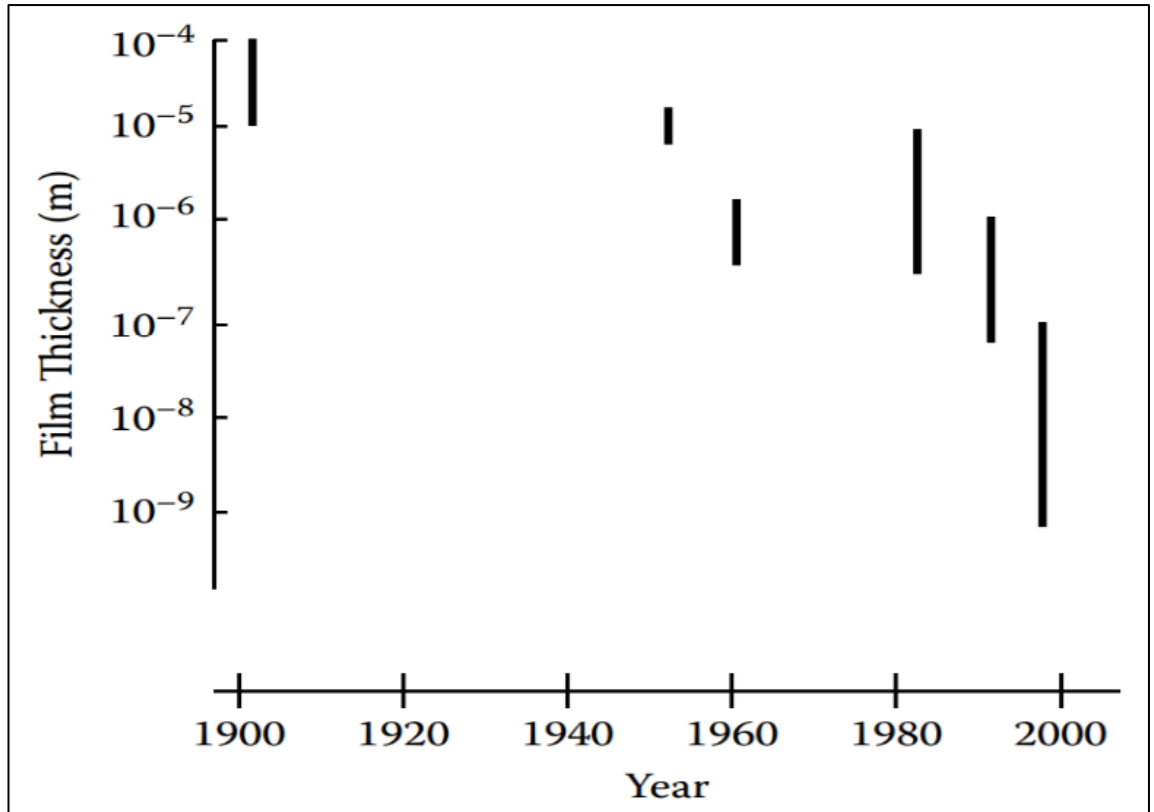


Figure 1-4: Reduction in lubricant film thickness in bearings [13].

Most of the experimental techniques that work efficiently for the hydrodynamic lubrication regime; like capacitance [14], electrical methods [15], X-rays [16] etc., do not give satisfactory results when put to test under the mixed lubrication. The main reason is that the ability of these techniques to handle asperity-asperity contact due to roughness is still a question. Optical interferometry methods also fail due to the same reason, since samples should be super smooth and have ample light reflection. The resolution for the optical methods for measuring very small thicknesses is also a big challenge when dealing with rough surfaces [17]. The new techniques like the ultrasonic measurements [18] and acoustic emission [19] measurements are still in the phase of development, although significant success has been achieved in film thickness measurement with these techniques.

Modelling the mixed lubrication phenomenon is by itself a big challenge. This can be attributed to various difficulties; the elastic deformations of surfaces and the high pressure rheology of the fluid result in strong non-linear effects, the simultaneous modelling of the fluid and asperity contacts etc. From the computational point of view, the refined grid sizes limit the deterministic mixed lubrication models to only counterformal contacts [17, 20]. The coexistence of fluid and solid contact parts in the same contact makes the algorithm complex as the boundaries between these complimentary regions are time dependent and uneven.

The physics underlying the mixed lubrication phenomenon is complex and multidisciplinary. It has full film lubrication on one extreme, which has been quite well established and characterized, while boundary lubrication on the other extreme. So, in principle, a good understanding of the mixed lubrication requires a good understanding of both these extreme cases. This is where the mixed lubrication models have to overcome another challenge as the boundary lubrication phenomenon is still evolving and in the early stages of understanding. The processes occurring in the mixed lubrication are expected to be happening at the nano-scale where the boundaries between typical engineering subjects are vague.

Tribology is a complex science considering friction, lubrication and wear in a single formalism. Even after a century of understanding of the wear phenomenon, and myriad of wear laws available, we cannot have a consensus on a single generalized wear law. Thus, wear is a complex phenomenon on its own [21]. With increasing temperatures and harsh environments, the wear process is further complicated by the surface chemical interactions. These interactions are caused by the tribological action and thus are called tribochemical interactions and should be considered in tribological models.

The lubricant is formulated with the intention to keep friction and wear in control under extreme pressure conditions by adding AW, FM and EP additives. These additives become active under extreme pressure and deposit protective and functional layers. The friction energy can increase the rate of chemical reactions. This change in the rate can manifest itself in terms of wear. Either the wear rate (might increase or decrease) or the wear mechanism or both can change during this tribochemical action. The mechanisms behind this change are fairly unclear due to the complex nature of the phenomenon.

ZDDP is one of the most studied lubricant additives. It possesses multifunctional properties. It is not only a good AW additive but also possesses good antioxidation ability and can also give EP performance to some extent. Although it is used in several industries, its main use is in engine oils. Engine oils constitute half of the lubricants used in the world. Due to its environmental hazards, an alternative to ZDDP with similar or better antiwear properties is required. But it is not easy to find this alternative due to the lower cost and effectiveness of ZDDP. But due to environmental legislations becoming stricter, it will eventually be fully or partially replaced. The performance mechanisms of ZDDP are still quite unclear and it is due to this reason that a lot of research is still in ongoing.

There have been very few attempts to model tribochemical effects in lubrication. The approaches adopted are either not on the realistic scale or do not include the effect of lubricant and lubrication in the tribosystem. There are only very few works on modelling tribochemistry and all are for boundary lubrication conditions with no effect of lubrication [22, 23]. A mixed lubrication model with tribochemistry was given very recently by Brizmer et. Al. [24] with a focus on modelling the micropitting performance. Their model does not update the geometry with tribofilm growth and is

based upon a Semi-Analytical mixed lubrication model. This study aims to formulate such a framework for lubricated contacts. It is expected to add to and complement the existing knowledge and understanding of the functionality of ZDDP. More importantly, the framework developed will give a starting point for further research and will be generally applicable to the design and analysis of other lubricant additives as well.

In summary, all mixed lubrication models currently available only model the mechanical aspects while the available models that consider interfacial chemistry are all for boundary lubrication. There is a strong need to develop mixed lubrication models that consider interfacial chemistry [20] as this is the regime where ZDDP actually shows its AW character [25]. Thus, this study sets out to develop a mixed lubrication framework that can simulate tribological parameters (contact pressure, temperature and film thickness etc.) as well as tribochemical parameters (tribofilm growth and tribochemical wear) and their mutual interaction. A model that can simulate the interfacial chemistry through all lubrication regimes (full film EHL to mixed to boundary) is definitely the need of the time in tribological research.

1.3 Impact

The mixed lubrication regime is critically important due to three main reasons. *First* of all, there is growing need in industry to downsize the components and to operate components at ever higher loads. This leads to mixed lubricated systems where the lubricant only carries partial load. *Second*, during the start-up and slow down of components, this condition occurs almost inevitably and unavoidably. *Third*, from the biomedical industry, the wear of Total Hip Replacements (THR) is expected to occur mainly in this regime [26]. From the contact mechanics point of view, the mixed lubrication regime is critical in bridging the full film and boundary lubrication regimes

by defining the mode of transition [17] and in determining the surface failure modes. So, in-depth understanding of the process of mixed lubrication will have crucial impact in developing better understanding and predicting the performance of engineering components like gears, bearings, seals and biomedical implants etc.



Figure 1-5: Example of a retrieved total hip implant showing signs of mechanically assisted corrosion [27].

Tribochemistry is not only important in the field of lubrication for design and formulation of lubricant additives but it is equally important during the fretting wear of bolted connections, mild wear of metals, mechanoactivation of reactions in industrial processing, and performance of seals in rotating components etc. [28]. Figure 1-5 shows an example of mechanically enhanced damage at the contacting interfaces on various parts of a retrieved hip implant. Failures in such cases are highly undesirable as re-surgery brings along many complications, the intergrowth of bone in the metal being one of these. Therefore, there is a constant need to improve the design of hip implants so that they last longer and without complications.

The impetus for the development of tribochemistry research comes mainly from biomedical implant, power generation, marine diesel engines and offshore industries and the green energy systems like tidal, wind and wave energy conversion systems.



Figure 1-6: Enhanced damage at the rubbing interfaces of a ship anchor chain. These regions undergo maximum wear and limit the life of these components.

The offshore metallic installations are the most susceptible to these mechano-chemical processes as shown in Figure 1-6. This is because the humid and corrosive environment cannot be avoided and it is due to this reason that these systems undergo frequent failures sometimes without warning. Understanding the effect of friction on these chemical changes will improve our design practices and increase reliability of these systems by predicting failure mechanisms and lifetimes.

So this research has big implications towards both industry and healthcare.

1.4 Objectives

The current shift in interest from purely mechanical aspects of contact to gaining an in depth understanding of the processes at the interface is obvious from the above discussion. The field is highly interdisciplinary and evolving. This complexity and the gap in literature to fill this paradigm shift from mechanical to interfacial aspects is huge. The main objectives set out in this study are:

1. Development of a mixed lubrication framework to simulate the entire transition from full film to boundary lubrication
2. Development of a framework to simulate tribochemical interactions under mixed lubrication conditions
3. Development of a framework to simulate wear for the chemically active ML system.
4. Model the effects of tribochemical layer on the mixed lubrication phenomenon.

1.5 Thesis Structure

The thesis is divided into three parts. The first part is named *introduction and background* and gives the general literature review to the mixed lubrication and tribochemistry modelling as two chapters. The second part gives first set of results. This part is named as *model development and numerical algorithm improvements*. It has been divided into two chapters. First the mixed lubrication model development is presented then the plastoelastohydrodynamic lubrication analysis is given. All key numerical details about the mixed lubrication model development and the integration of plastic behaviour are given. The third part is named the *model application* section and contains three chapters. In this part, the tribofilm growth model integration into the mixed lubrication model is presented first along with the tribofilm growth results. Then the interfacial mechanics in a tribochemically activated mixed lubrication model is analysed by comparing the evolution of key lubrication parameters with time. The model is tested to produce roughness evolution and wear measurements. The *last chapter*, Chapter 8 presents thesis conclusion and future directions.

Following a general introduction and background to the problem in Chapter 1, the Chapter 2 gives detailed background and literature review to the problem. The first

half of Chapter 2 reviews the literature on mixed lubrication after presenting the EHL equations. The second half of the chapter reviews the literature on tribochemistry. Special emphasis is given to review the modelling of tribochemistry of the antiwear additive ZDDP in the contact mechanics and lubrication models.

The mixed lubrication model with all the numerical details is presented in Chapter 3. This chapter also contains a section on the implementation of fftw library¹ in Fortran programming to compute the convolution by implementing the FFT² method for solving the deformation integrals. The plastic deformation model is developed and implemented into the mixed lubrication model to get a PlastoElastoHydrodynamic Lubrication (PEHL) mode and the details of this model are presented in Chapter 4. The PEHL model can handle plastic deformation induced by either lubricant or asperity interaction pressures. These two chapters together constitute part-II of the thesis on model development and numerical algorithm improvement.

The last part, part-III consists of three chapters. In Chapter 5, the framework for modelling the growth of tribochemical reaction layers is developed and implementation details given. The driving factors for ZDDP tribofilm growth are discussed and the modelling efforts analysed. This chapter presents results for the tribofilm growth in lubricated contacts. In Chapter 6 the mutual interaction between the lubrication film formation and the tribofilm growth is studied and the results for the effect of tribofilm growth on the mixed lubrication performance are given by studying the evolution of lubrication parameters under tribochemically active

¹ <http://www.fftw.org/>

² Fast Fourier Transforms

lubrication conditions. The last chapter in part-II is Chapter 7 in which the general behaviour of the contact is studied by applying the developed model to reproduce experimental observations on wear. The ability of the present model to capture the wear track profile (width, depth and topography) is assessed.

Chapter 8 marks the end of this thesis by giving the conclusion and some future improvements that can be implemented to enhance the capabilities of the model are given.

Chapter 2

Theory and Background

This chapter presents the theory of mixed lubrication (ML). Due to the very nature of mixed lubrication, it cannot be separated from EHL. The theory of rough surface elastohydrodynamic lubrication (EHL) is actually applicable and discussed first in section 2.3.1. Then the historical account of how roughness started to appear as a critical parameter controlling the EHL characteristics to actually having a mixed contact (individual fluid and solid contact spots) is presented and discussed in section 2.3.2.

Then in section 2.4 the current literature about the importance and effect of tribochemistry in lubrication analysis is reviewed with emphasis on the antiwear additive ZDDP. An account of the modelling attempts in tribochemistry is given. The literature suggests a huge gap in modelling tribochemical / tribocorrosive interactions in mixed lubrication as only very few modelling studies have been done and these are limited to boundary lubrication and have only appeared very recently.

2.1 Elastohydrodynamic lubrication

The lubricated contact between two rough surfaces is characterized as EHL if the roughness has only the effect in modifying the pressure profile and film thickness as a result of increased fluid density and viscosity and the bulk deformation of solids but there is no direct solid to solid contact. The Elastohydrodynamic lubrication occurs, generally, in lubricated non-conformal contacts. Such contacts occur in rolling element bearings, cams, gears, tappets, etc. To illustrate the scales of parameters involved, Figure 2-1 shows the contact area drawn on an A4 paper to give an estimate of comparative magnitude of lubricant film thicknesses involved. The lubricant film

thickness is of the In such small contact area, the lubricant pressures can be high enough to easily cause elastic deformation of the contacting solids. In fact, the lubricant viscosity increase with pressure is so severe that the lubricant under very high pressure, theoretically behaves like a solid.

The EHL problem is defined by the Reynolds equation (a differential equation), the elasticity equation (an integral equation) and the load balance equation, and two equations of state relating the fluid viscosity and density to pressure. The solution to this problem gives the pressure profile and the film thickness distribution inside the contact [29].

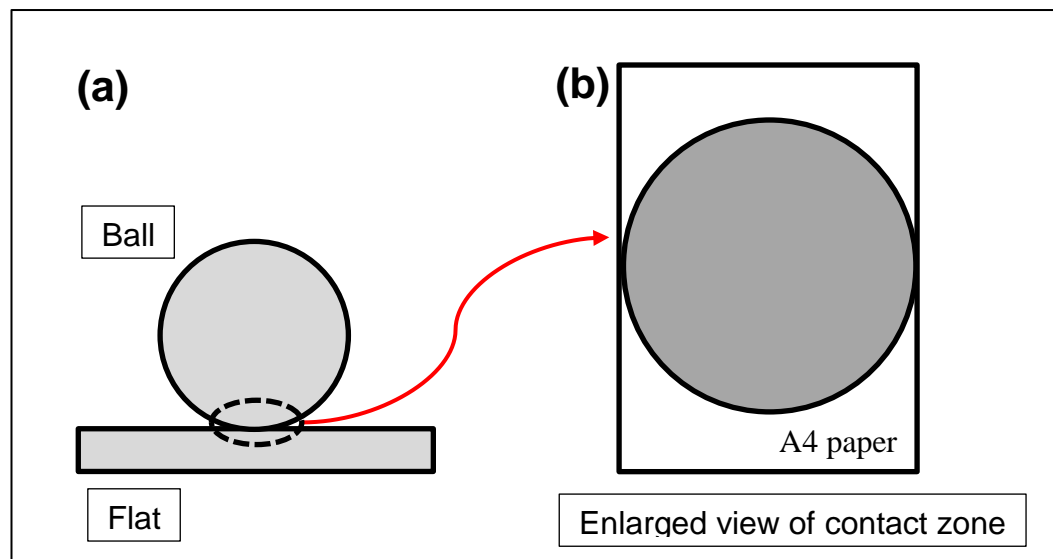


Figure 2-1: (a) A schematic representation of tribological contact between a flat disc and ball. (b) Enlarged view of contact zone. If this is scaled onto an A4 paper then the thickness of the paper gives an estimate of the lubricant film thickness

The EHL equation set has a strong non-linear behaviour which makes it unstable during numerical solution. There are two causes to this non-linearity: the Reynolds coefficients are functions of pressure due to density and viscosity being functions of pressure and the cavitation condition is imposed on the solution. The instability is

mainly linked to the Reynolds coefficients becoming too small at high pressures due to highly increased viscosity and very small film thicknesses and the loss of coupling in the transverse direction. The convergence of the Reynolds equation with a simple forward iteration procedure is very slow and various methods have been proposed to improve its solution convergence [20]. This makes the numerical solution of EHL equation system very complicated.

The mixed lubrication regime lies in-between the Elastohydrodynamic (EHL) lubrication and the boundary lubrication (BL) regime. In this thesis mixed lubrication is considered as rough surface EHL with actual asperity-asperity contacts. It is not possible to separate mixed lubrication from EHL. The following section outlines the Elastohydrodynamic lubrication problem. The same equation set is applicable to ML solution but the solver needs to be robust enough to handle asperity-asperity contacts. A mixed lubrication solver should in essence converge to EHL on one extreme and boundary lubrication / dry contact on the other extreme.

2.2 Transient EHL equation set

The transient EHL equations have a time derivative of film thickness in the Reynolds equation. The EHL problem in principle is defined by the Reynolds equation, the film thickness equation and the load balance equation. The Reynolds equation contains viscosity and density which are functions of pressure. So the addition of two equations of state ($\eta = \eta(p)$ and $\rho = \rho(p)$) makes the system complete. The complete EHL solution set is described now. The various parameters involved in defining these equations can be identified in Figure 2-2.

2.2.1 Reynolds equation

The application of thin film approximation to the actual Navier-Stokes equations gives Reynolds equation [1].

$$\frac{\partial}{\partial x} \left(\frac{\rho h^3}{12\eta} \frac{\partial P}{\partial x} \right) + \frac{\partial}{\partial y} \left(\frac{\rho h^3}{12\eta} \frac{\partial P}{\partial y} \right) - U_r \frac{\partial(\rho h)}{\partial x} - \frac{\partial(\rho h)}{\partial t} = 0 \quad (2-1)$$

In this equation, x and y are the coordinate axes directions. The x -axis is normally aligned with the flow direction to simplify calculations. The term $\rho = \rho(p)$ gives the density of fluid, h is the film thickness, $\eta = \eta(p)$ is the viscosity of the fluid, P gives the fluid pressure and U_r is the entrainment velocity (average speed of the contact pair) of the fluid.

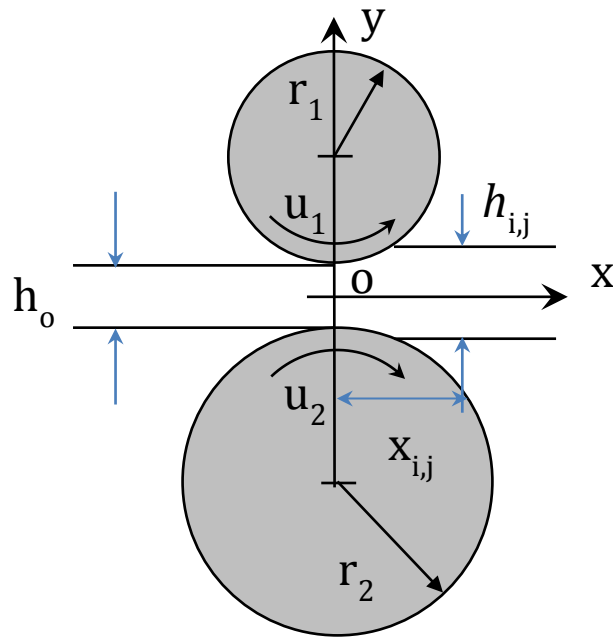


Figure 2-2: EHL contact configuration outlining the key parameters in the mathematical model.

The Reynolds equation (2-1) has three main terms and it is important to know the meaning of each term. The first two terms define the pressure flow and are called the *Poiseuille flow* terms. The third term in the Reynolds equation is the wedge flow / shear flow term. These are called *Couette flow* terms. The fourth term gives the transient flow of the fluid and is called *squeeze flow* term. The shear flow and the transient together define the entrainment flow. Thus, the Reynolds equation is essentially based upon two types of flows: the ***pressure flow*** and the ***entrainment flow***.

2.2.2 Film thickness equation

The film thickness equation (2-2) is solved to update the film thickness values every time the Reynolds equation is used to update pressures. All the parameters defining the gap between the surfaces are included in the film thickness equation to define the problem (see Figure 2-2). The film thickness equation is given below.

$$h(x, y) = h_o + \frac{x^2}{2R_x} + \frac{y^2}{2R_y} + \frac{2}{\pi E'} \int_{-\infty}^{+\infty} \int_{-\infty}^{+\infty} \frac{p(x', y')}{\sqrt{(x-x')^2 + (y-y')^2}} dx' dy' - R(x, y) \quad (2-2)$$

In this equation, h_o gives the undeformed gap, R_x and R_y define the radius of curvature in the x and y direction ($R_x = R_y$ in a circular contact), p is the pressure, the term $R(x, y)$ is the roughness (microgeometry) of the surface and the term E' is the combined elastic modulus defined as $\frac{2}{E'} = \left(\frac{1-\nu_1^2}{E_1} + \frac{1-\nu_2^2}{E_2} \right)$.

2.2.3 Load balance equation

The load balance equation (2-3) ensures that the iterating pressures converge to realistic values that are in equilibrium with the applied load. This equation states that the sum of all the pressures should be equal to the applied load and is given below.

$$W = \int_{-\infty}^{+\infty} \int_{-\infty}^{+\infty} p(x', y') dx' dy' \quad (2-3)$$

In this equation, W is the applied load and $p(x', y')$ is the pressure within the contact. The pressure is summed over the complete solution domain and compared against the applied load to ensure that the calculated pressures are the true pressures.

2.2.4 Pressure-viscosity equation

The viscosity is a function of pressure and temperature. In this thesis, temperature dependence has been excluded. The pressure-viscosity dependence can be described by equation (2-4) and equation (2-5).

The Barus equation

$$\eta(p) = \eta_o e^{\alpha p} \quad (2-4)$$

The Roelands equation

$$\eta(p) = \eta_o e^{\left((\ln(\eta_o) + 9.67) \left(-1 + \left(1 + \frac{p}{p_o} \right)^z \right) \right)} \quad (2-5)$$

In the above equations, η is the viscosity, η_o is the reference viscosity and is a fixed value and p_o is the reference pressure. Roelands [30] has given their values $\eta_o = 6.315 \times 10^{-5}$ Pa.s and $p_o = 1.98 \times 10^8$ Pa.

The Roelands equation is more accurate as it captures the true physics by limiting the viscosity increase as shown in Figure 2-3. Barus law on the other hand is not suitable to use at very high pressures.

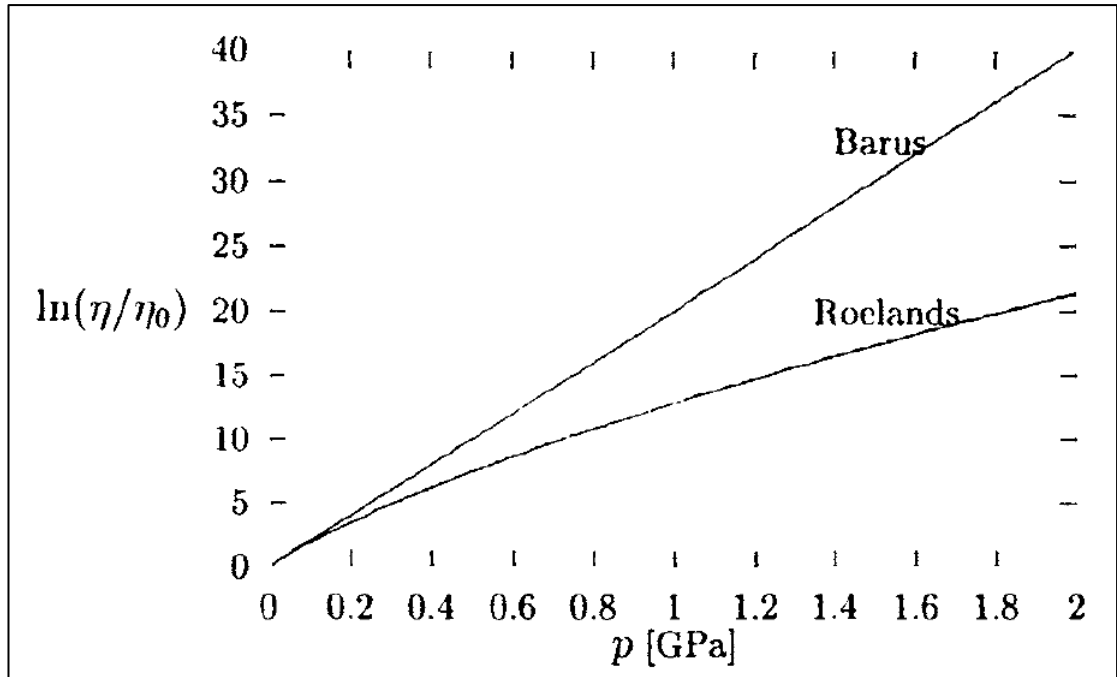


Figure 2-3: A comparison of the two laws for the pressure dependence of fluid viscosity. The Roelands equation gives more accurate representation of the EHL phenomenon [29].

2.2.5 The density pressure equation

The density-pressure relationship is given by an empirical relationship given by Dowson and Higginson [31] (see equation (2-6)). The increase in density is not similar to the changes in viscosity with pressure. The density increase has been observed to be limited to an asymptotic value with increase in pressure as seen in Figure 2-4.

$$\rho(p) = \rho_o \frac{5.9 \times 10^8 + 1.34p}{5.9 \times 10^8 + p} \quad (2-6)$$

In this equation, ρ is the density of fluid and ρ_o is the atmospheric density of the fluid and the number 5.9×10^8 is the reference pressure in Pascal. This equation is very important to describe the EHL pressure spike and affects the central film thickness.

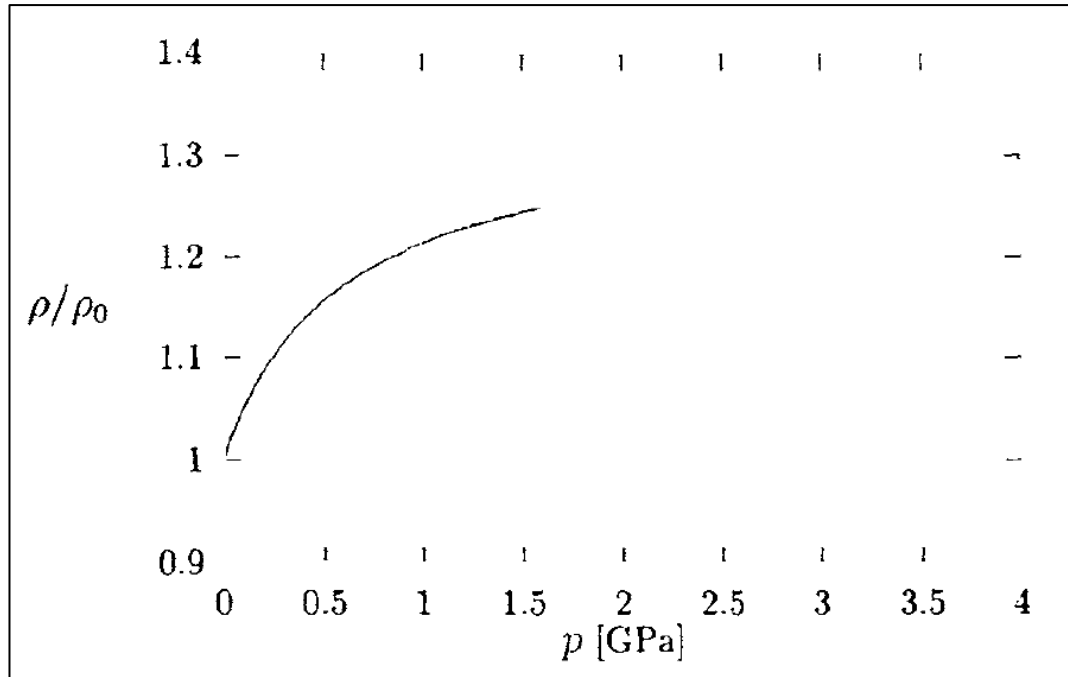


Figure 2-4: The increase in density with pressure. The density increase is limited to a value of $1.34\rho_0$ [29].

The EHL pressure spike and downstream flow constriction (towards the exit) are the key characteristics identifying an EHL pressure and film thickness profile, respectively. In non-conformal contacts, due to very high pressures inside the contact and ambient pressures outside the contact zone, the fluid undergoes rapid expansion. This expansion may lead to flow *cavitation* as well. Thus, the area of flow decreases towards the exit region of contact to ensure flow continuity.

Petrusevich was the first to observe this phenomenon correctly by simulating EHL equations, hence, the pressure spike is also termed as *Petrusevich spike*. The groundbreaking results for the EHL pressure spike produced by Petrusevich are shown in Figure 2-5.

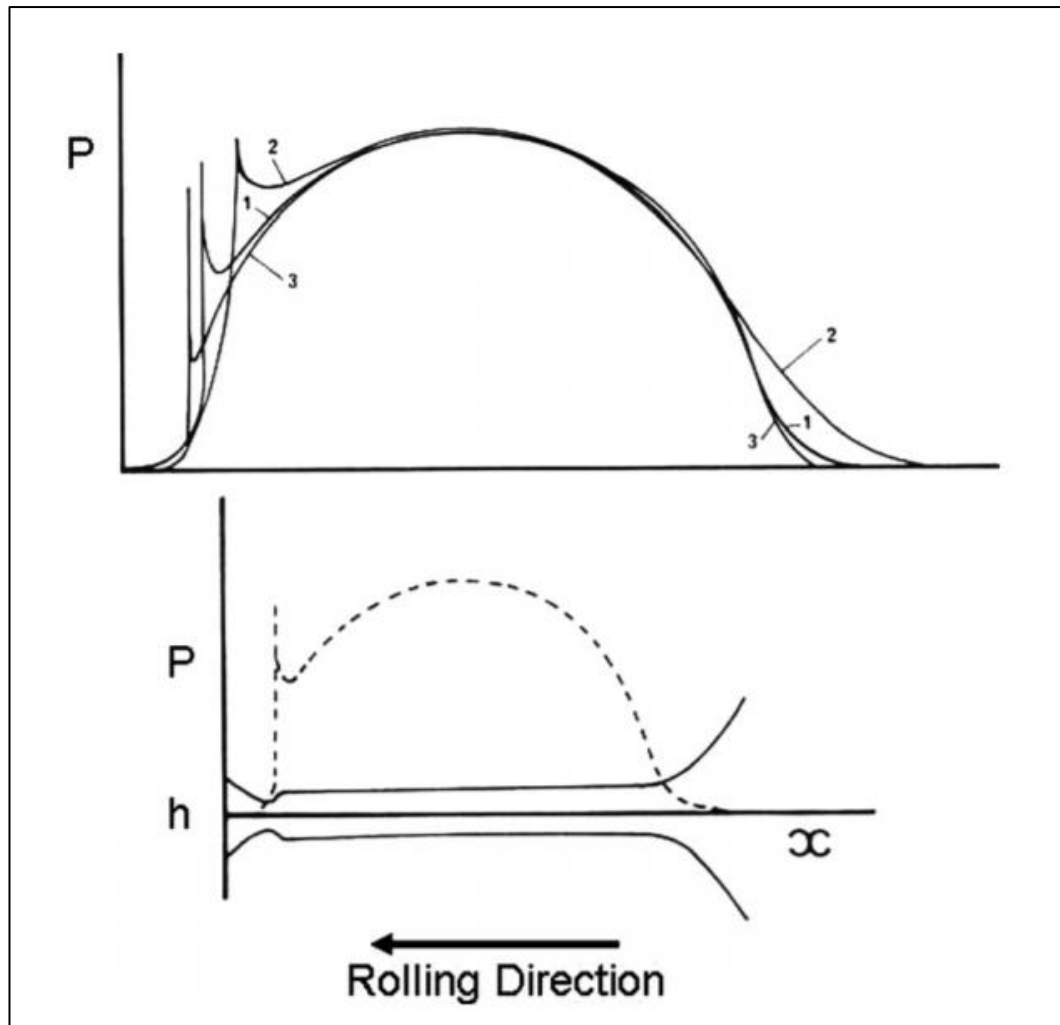


Figure 2-5: Pioneering results from Petrusевич et al. [32]. The momentary increase in pressure (spike) and decrease in film thickness (constriction) can be observed clearly towards the exit of contact.

2.3 Mixed Lubrication Modelling

In this section the goal is to review the state of the art in mixed lubrication modelling. The mixed lubrication models were developed as an extension to the micro-EHL models. Initial efforts were mainly to simulate the effect of roughness in EHL. This is better called micro-EHL / rough surface EHL. The models reviewed here are the EHL models with actual asperity contacts, mixed lubrication models. Figure 2-6 explains these lubrication models. The presence of lubricant filled and actual asperity- asperity

contact regions can be seen in the mixed lubrication regime. Thus, first the literature on micro-EHL is reviewed and then the mixed lubrication models are deeply reviewed.

2.3.1 Elastohydrodynamic lubrication with roughness

The pioneering work from Patir and Cheng [33, 34] is considered to be the first attempt to simulate elastohydrodynamic lubrication with rough surfaces although the efforts started earlier with the work of Christensen and Tonder [35, 36] by developing three variations of Reynolds equation to represent different roughness patterns and orientations. Patir and Cheng simplified these three equations to a single equation with generalized flow factors to consider the effect of roughness in the Reynolds equation. Johnson et al [37] actually extended the ideas from Christensen and Tonder to develop analytical formulae for central film thickness and they were able to see qualitative effects of roughness in modifying lubrication which was coupled with stochastic dry contact theory to get one of the first mixed lubrication models by Greenwood and Williamson [38]. In the meantime several researchers actively worked, especially Tallian and coworkers [39-44]. The efforts by Elrod et al [45-47] to study artificial roughness patterns followed by the work from Berthe and Godet [48] all contributed towards improving the understanding of roughness effects. Elrod actually gave a brief account [49] of the existing understanding about rough EHL and mixed lubrication. But the key study in this era was the work of Patir and Cheng's as it enabled the numerical study of the effect of roughness in mixed EHL. All this above mentioned work had one very big assumption that the *roughness was considered non-deformable*.

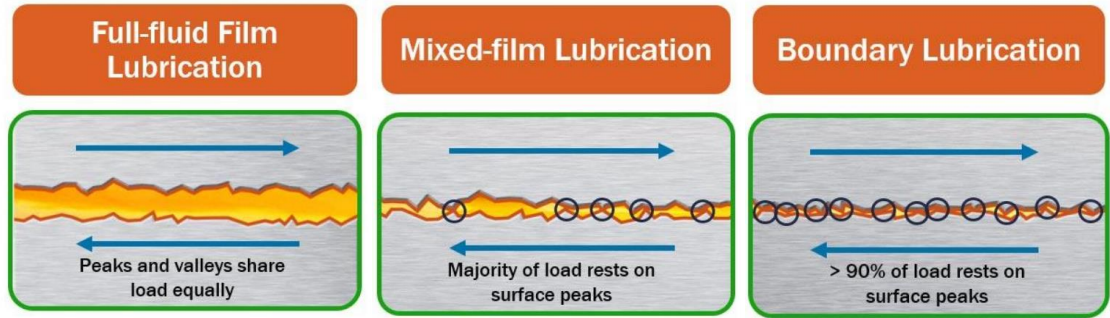


Figure 2-6: The lubrication regimes explained [50].

The work from Lee and Cheng [51] was one of the earliest approaches to consider elastic deformable roughness. They proved by performing simulations on a single asperity passing through an EHL conjunction that roughness actually undergoes significant elastic deformation. The problem now was the lack of computational resources to solve the full EHL problem. A breakthrough came with the development and application of multigrid techniques in EHL by Venner et al. [52] and Kweh et al. [53] and improved by Chang et al. [54, 55]. Solutions involving more realistic roughness started to appear [56, 57].

For a modelling study, the above literature makes more sense if put in the following perspective. Roughness in EHL can be treated either stochastically or deterministically. Stochastic modelling uses some key statistical quantities to describe the surface and relate these to lubrication. The Patir and Cheng [58] model is a classic example of stochastic models of rough surface EHL for line contacts. It employed the average flow Reynolds equations derived by Patir and Cheng [33] to simulate the hydrodynamic action and the load compliance relation developed by Greenwood and Tripp [59] to model rough surface EHL. The model was extended to point contact cases in 1988 by Zhu and Cheng [60, 61].

Stochastic models cannot give localized details [20]. With availability and improvement of computational resources the trend shifted towards deterministic inclusion of roughness in EHL modelling. Early attempts employed simplified artificial roughness (sinusoidal, simple geometrical irregularities, etc.) [53, 54, 62, 63]. Then more realistic 2-D machined or random roughness was used by Venner [56] and Kweh et al. [57]. Finally complete solutions employing 3-D machined roughness in point contact EHL was given by Xu and Sadhegi [64] and Zhu and Ai [65]. None of these deterministic models could handle *asperity-asperity* contacts.

Stochastic modelling is not used in this study. Stochastic models do not actually simulate the mixed lubrication process [66, 67] as the average effect of roughness is employed through flow factors in Reynolds equations. These flow factors are numerically using a limited number of statistical parameters and without asperity deformation. This leads to over approximations and system specific solutions. The generalization of these results is questionable as for a particular average film thickness, there can be various possibilities of having a rough surface contact. There may be no asperity contact or severe asperity contact depending upon the real time situation at the contact [17]. An illustration of these limitations is given in Figure 2-7. The figure is not drawn to scale and is solely meant to explain the limitations described above.

Some of these limitations can be handled with proper asperity interference inclusion in stochastic models. The lambda ratio / film thickness ratio (ratio of central film thickness to composite roughness) is no more a simple fixed value due to instantaneous movement of roughness causing film thickness changes. In a single contact, there can be asperities that are under elastic deformation, some under plastic deformation while others in an intermediate state of elasto-plastic situation.

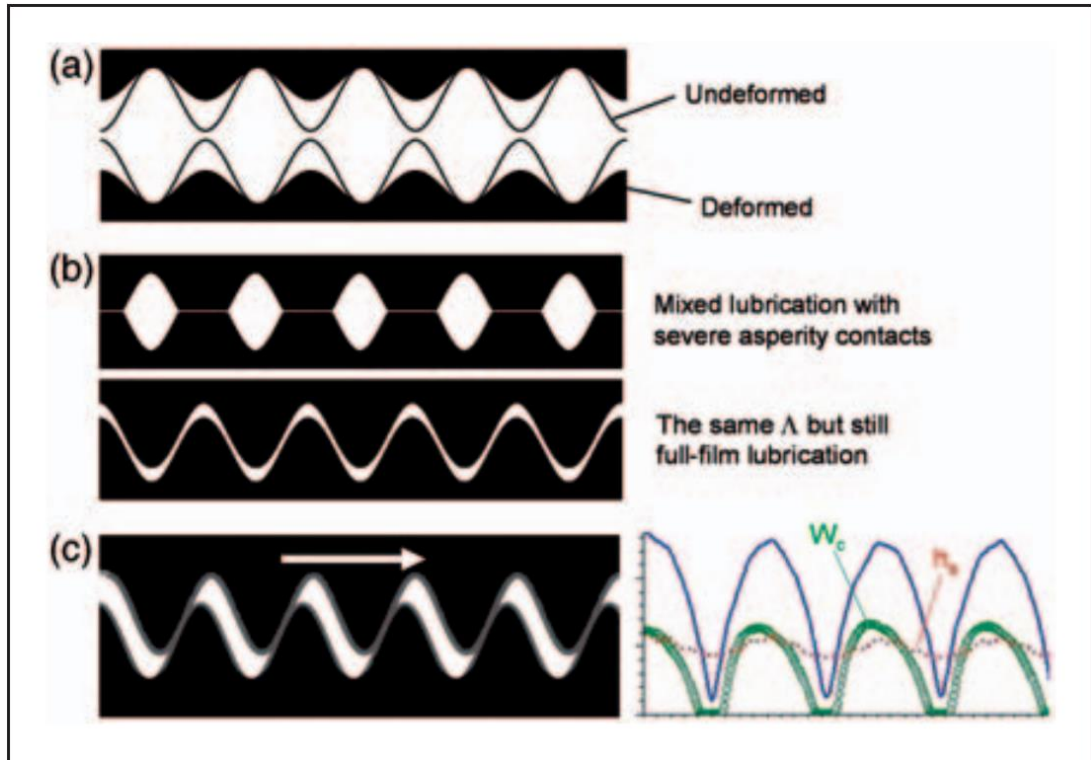


Figure 2-7: An illustration of the limitations of stochastic models [17]

The variation of deformation should be included into the models if realistic experimental conditions are to be achieved but when the roughness is averaged in Reynolds equation this key aspect is missing. Some recent efforts to overcome these limitations have started to appear in the literature recently [68, 69]. The stochastic models cannot give reliable information for film thickness when the film thickness ratio is less than 1 [66].

2.3.2 Mixed Lubrication: EHL with asperity-asperity contacts

The mixed lubrication regime is characterized by discrete asperity-asperity contacts occurring due to surface roughness being of the same order as the lubricant film thickness. There are two distinct regions that are to be handled in mixed lubrication analysis: the lubricated regions and the asperity-asperity contact regions and as such there are two distinct ways of handling them while numerically solving the ML

problem [20]. The first approach, the *separate* approach, handles the asperity contact regions and the lubricated regions as two distinct regions and solves the EHL pressures and the solid contact pressures with different physical models. The second approach, the *unified* approach, handles the lubricated regions and asperity contact regions in a single framework, solving the EHL and solid contact pressures at once through the same equation system (The Reynolds equation).

The first study using the separate approach was presented by Chang [70] for line contacts with sinusoidal roughness. The first model for point contacts was presented by Jiang et al. [11] in 1999. They used digitized machined roughness and used the separate approach. The separate approach was further used by Zhao et al. [71] in 2001 and Holmes et al [72] in 2003 to analyse ML during start up, Zhao and Sadeghi [73] in 2003 to ML during contact shut down and Popovichi et al. [74] in 2004 again to study contact start up. All these examples have clearly defined patches of lubricant and asperity contacts and the boundary conditions are easy to handle [20]. The unified solution algorithm was also presented and applied to point contact with machined roughness in 1999 by Zhu and Hu [75] and then by Hu and Zhu [76] in 2000. They applied and improved the semi-system approach developed by Ai [77] to formulate the model. Some later studies utilizing unified solutions algorithm were also presented by Holmes et al [78], and then by Li and Kahraman [79]. The unified solution algorithm has been extended and improved since then. Liu et al. [80, 81] improved the approach by investigating the effect of mesh density, differential scheme and viscosity model on the unified solution algorithm. Zhu [82] compared the numerical accuracy in thin film and mixed lubrication cases. Wang et al. [83] validated the model for very low speeds.

The separate approach is not employed in this study. The main reason being that a complete model to simulate the entire transition from full film through EHL down to mixed and boundary lubrication is required and for separate approaches, dynamic boundaries formed between lubricated and contact regions are very difficult to handle [17]. The target in this work is to simulate interface mechanics and chemistry in a single framework. The unified model of ML successfully bridges the field of contact mechanics and lubrication science by utilizing a solution algorithm where the Reynolds equation gives the dry contact pressures as well. The dry contact is the state when there is no hydrodynamic lubricant film present between the contacting bodies. But the hydrodynamic film is still a continuum which imposes a limitation that the atomic and molecular level events cannot be captured [20].

This challenge has been undertaken in this study and a framework is developed to extend the unified mixed lubrication model to incorporate the tribochemistry of ZDDP. In the following section, the tribochemistry is reviewed in general. Specific emphasis is given to the tribochemistry of ZDDP and the modelling studies to include tribochemical information in the lubrication models.

2.4 The antiwear additive ZDDP

In this section the current state of knowledge regarding the understanding of the functionality of ZDDP is assessed. The ZDDP additive can act as a corrosion and oxidation inhibitor as well but here only the antiwear character is considered and reviewed. The limitations and gaps in literature are emphasised.

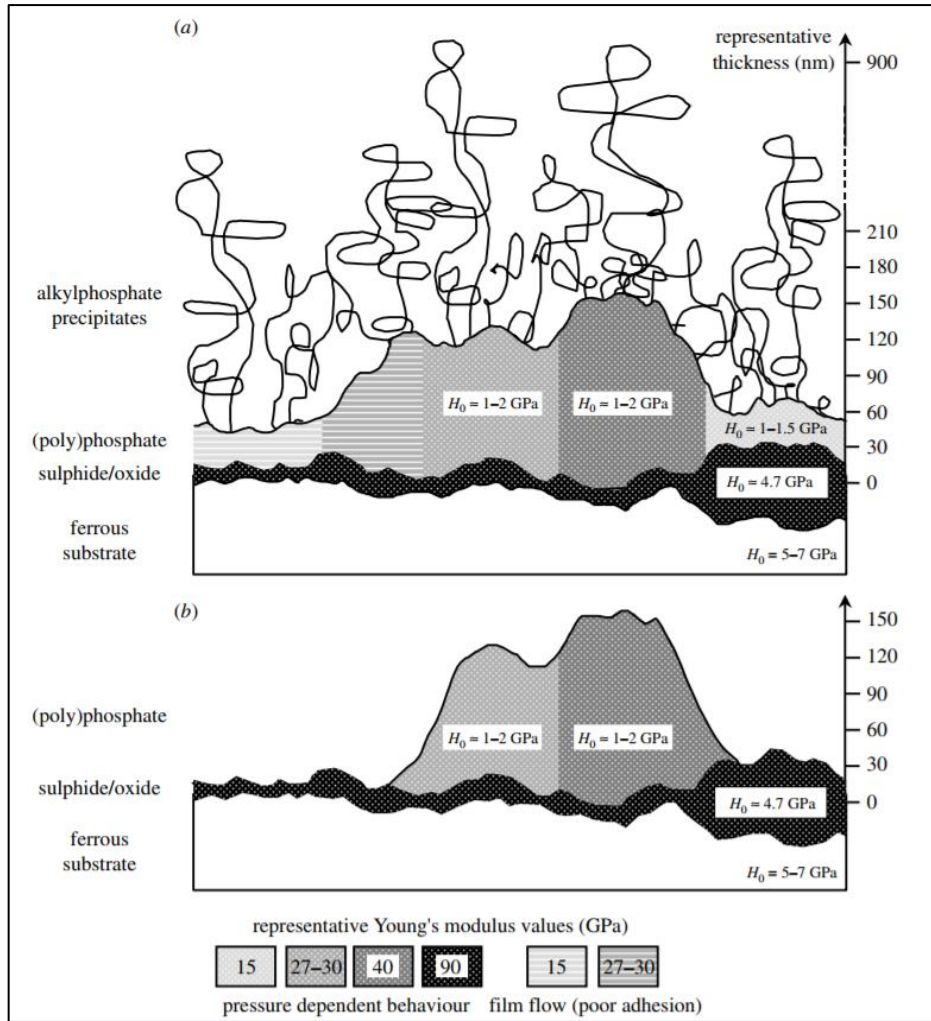


Figure 2-8: The structure and mechanical properties of the ZDDP antiwear tribofilm. The scale on the y-axis gives the representative thickness of each layer within the complete film [84]. (a) shows the complete anti-wear tribofilm formed by the action of a simple ZDTP molecule. (b) the same film after washing with a solvent.

Even after 70 years since its introduction into the lubrication industry, the antiwear additive zinc dithiophosphate (ZDDP) is still the most successful lubricant additive devised [85]. It is an essential element in engine oils. The structure of the tribofilm formed by ZDDP is shown in Figure 2-8 where the comparative scale of the key constituents is suggested to be the source of its antiwear performance. There has been extensive research going on to discover the remarkable functionality of this additive. On the other hand, the use of ZDDP has been restricted due to the presence of

phosphorous which harms the modern exhaust emission control technologies. The use of ZDDP is thus restricted and it is expected that one day it will be replaced by the phosphorous free compounds. There is still no alternative to the use of ZDDP as antiwear additive. Even after extensive research, no complete alternative is found that gives the same performance, as ZDDP at similar cost [86].

The versatile environments in which ZDDP operates is also remarkable. The functionality of ZDDP has been very actively explored since its discovery [87, 88]. The reasons behind this versatility of operation and ability to function in most environments are still unanswered [86] and requires further research. ZDDP was initially introduced as an antioxidant and corrosion inhibitor but its antiwear character was soon realized. The antiwear performance of ZDDP is attributed to its ability to form tenacious tribofilms at the sliding interface.

The adsorption of the ZDDP molecule is considered a precursor to the formation of any surface film and any reaction to occur [89]. The van der Waals forces between the additive ZDDP or its decomposition products and the solid surface provide the driving force for the movement of these species from bulk to the surface. When there is a full lubricant film separating the surfaces, this will result in a layered stacking of species based upon their relative polarity. Higher polarity species tend to be closer to the surface [90]. As the load or temperature or both are increased, many of these species undergo thermal desorption. Mechanical action might remove some strongly attached molecules as well. Thus with increasing load, the preferential movement of species (towards the surface) changes from more easily removed particles to strongly adhering particles and the antiwear action becomes active. As the loading is further increased, it is expected that the extreme pressure action is activated. Thus, the

applications in this thesis are restricted to the loading conditions where the ZDDP shows its antiwear character rather than its extreme pressure capabilities.

In the engine oil, ZDDP exists as a monomer or oligomer based upon its surrounding environment. The ZDDP in Engine oil formulations is generally a mixture of 85% secondary alkyl and 15% secondary alkyl ZDDP [91]. The chemical structure of the ZDDP molecule is given by several authors [85, 88] (see Figure 2-9).

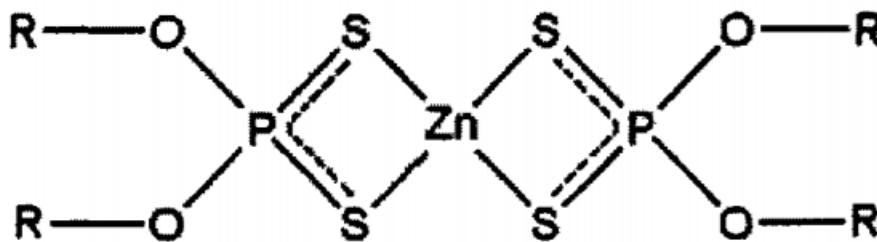


Figure 2-9 Schematic of the structure of ZDDP molecule [88]

Once either the ZDDP molecule or its decomposition products have reached the surface, a chemical reaction or more appropriately, a series of chemical reactions takes place resulting in thick, tenacious structural layers. It is proposed that an oxidation reaction takes place between the substrate surface and the ZDDP molecule and a final step of condensation polymerization converts the reaction products into glassy phosphates [88].

The tribofilm formation initially starts with a pad like structure with inhomogeneous film growth and eventually the whole surface is covered with a thick tribofilm. The thickness of these tribofilms can reach up to 150 nm and are generally in the range of 50 to 150 nm [92, 93]. There are oxides / sulphides of iron and zinc near the surface underneath a thick glassy phosphate layer. The outermost parts of the tribofilm contain polyphosphates [94].

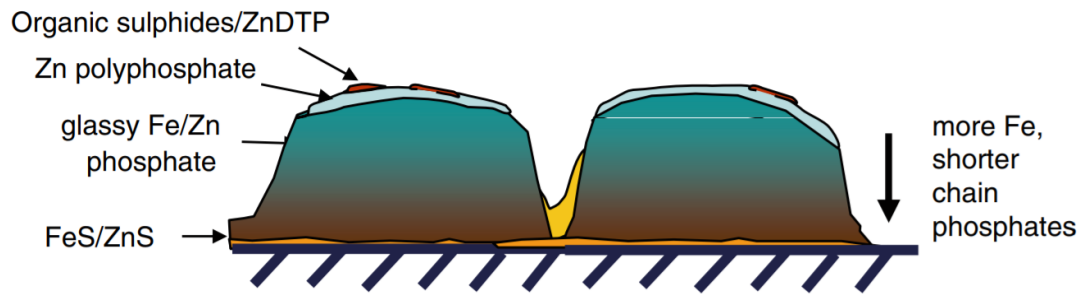


Figure 2-10 An illustration of the gradient in structure and composition of ZDDP tribofilm [85]

The tribofilm of ZDDP has been confirmed to grow on aluminium-silicon alloys, diamond like carbon (DLC) coatings [95], silicon[96], tungsten carbide [97], and ceramics [98]. The composition and structural properties are not much different on either ferrous or non-ferrous steels. Its main constituents are iron, zinc, phosphate, sulphide and oxygen. These substances are not distributed evenly. The composition of iron increases towards the bulk substrate while more phosphorous is present when moving towards the outer edge of tribofilm [85, 99]. The structure of the glassy tribofilm varies from highly amorphous at the outer edge to ortho- and pyro-phosphate glasses to base of tribofilm [100]. Figure 2-10 shows the gradient structure and composition of ZDDP tribofilm.

2.4.1 The antiwear action of ZDDP

The antiwear additive ZDDP performs its antiwear action in one of the following ways [85]. Three theories have been given to explain the antiwear character of ZDDP.

- I. Formation of a soft / compliant layer on top of the substrate, preventing direct solid to solid contact by providing a barrier [101].

- II. Hard third body abrasive iron oxide particles are believed to be absorbed by the antiwear action of ZDDP.
- III. The glassy phosphate layer formed on the contacting asperities is viscous in nature and act to provide a sliding interface with lower stresses [102].

2.4.2 Mechanical behaviour of ZDDP tribofilms

The mechanical nature of the tribofilms has been characterized quite well using AFM and nano-indentation experiments [84, 88, 103-107]. All these studies conclude that ZDDP tribofilms possess smart behaviour. The tribofilm responds to loads and environments. The hardness and stiffness vary through the film depth. There is no clear answer to this smart behaviour of the tribofilms and research is still ongoing. The hardness of the tribofilm varies between 1.5 and 3.5 GPa [85] and the elastic modulus is a function of hardness as well.

To explain the superior functionality of ZDDP, Mosey et al. [108] used molecular dynamics simulations to relate the theory of pressure induced crosslinking to the formation and behaviour of the ZDDP tribofilms. Their study aimed at development of new antiwear additives by improving the understanding of ZDDP tribofilms. Although they relate their results to a wide range of experimental data, their simulation parameters are unrealistic. The properties of ZDDP tribofilm as a function of temperature were quantified using nano-indentation and AFM set up [109]. A simple model was used to extract the elastic modulus of the film.

2.4.3 Composition and structural properties of ZDDP tribofilms

It is widely accepted that the antiwear tribofilms possess a gradient in structure as well as composition. The tribofilm forms layer by layer but the layers closer to the substrate contain shorter chain length structures while the outer layers have longer chain phosphates [110, 111]. These studies report the presence of a viscous layer of

physically adsorbed additive above the actual tribofilm. This layer can be easily removed by solvents. The layer of antiwear tribofilm just below this viscous layer contains long chain amorphous zinc and iron polyphosphates chemically adsorbed to the layers underneath. The chemically reacted layer very next to the substrate and above contains short chain polyphosphates. There is no sharp interfacial separation but a gradual variation of chain lengths graded from top to bottom. The composition of the tribofilm also changes from top to bottom with higher concentration of zinc in the top part of the tribofilm and a higher concentration of iron towards the part of the tribofilm near the substrate. This gradient in structure and composition is related to the variation in mechanical properties of the tribofilm with depth. The hard layers near the substrate bear the load while the middle and top layers in the tribofilm provide an interface that can be easily sheared and prevents wear [112].

2.4.4 Tribofilm growth and growth kinetics

The growth rate and the steady state film thickness value achieved by the tribofilm are the key parameters to consider. The apparatus used to study the thickness of the tribofilm is the Spacer Layer Interferometry Method (SLIM). A steel ball is rubbed against a steel disc and lubricant is supplied inside the contact. Depending upon the type of additive present, the tribofilm will form. The tribofilm on the ball surface is monitored through time. The experiment is stopped and the ball is pressed against a glass disc coated with spacer layer. An interference image is obtained which can be interpreted as thickness of tribofilm.

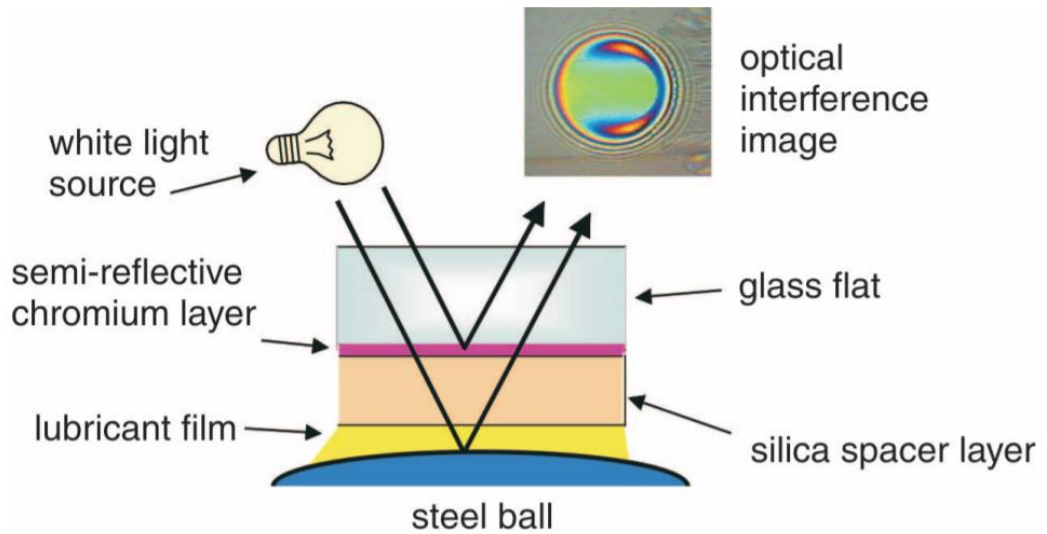


Figure 2-11: Schematic representation of the basic principle of tribofilm thickness measurement using SLIM [113].

The SLIM is integrated with a ball on disc set up in a mini traction machine [113] and its schematic principle of tribofilm thickness measurement is shown in Figure 2-11. The tribofilm thickness over the whole interference image is averaged and a mean value is given as an output.

The growth behaviour of ZDDP has been studied extensively [103, 107, 114-117]. The first successful attempt to capture the growth kinetics was made by Fujita et al [92].

They used a Mini Traction Machine equipped with SLIM to quantify the growth of tribofilm. An empirical model to capture the kinetics of the tribofilm growth was also developed and fitted to experimental data. The importance of having a complete approach for simulating the growth and removal of the tribofilm was emphasized. The concept of removal of tribofilm can be related to the characteristics of the tribo surface. A time delay in the formation and removal kinetics was suggested as well.

The work from Fujita et al [92] considered primary and secondary ZDDPs. The tribofilms were found to grow with different rates and reach a final steady state value. The study of tribofilm growth using single asperity contacts using Atomic Force Microscope (AFM) was done by Gosvami et al. [96]. The growth of tribofilm was studied in situ. Thermal energy and stress were identified as key parameters controlling the growth kinetics. They also presented an Arrhenius based model to capture the growth behaviour of tribofilms.

Andersson et al. [22] presented the first complete approach to calculate the tribofilm growth in a deterministic boundary lubrication framework. Their growth model was purely Arrhenius based with no effect of shear stress. A theoretical model to predict the growth of tribofilm based upon the thermodynamics of interfaces [118, 119] was developed by Ghanbarzadeh et al. [120]. They considered the simultaneous growth and removal of the tribofilm with deterministic definitions of roughness, wear and tribofilm growth. Their model included the effect of both temperature and shear stress. In a recent study by Zhang and Spikes [97], the tribofilm formation under solely EHL conditions with no solid to solid contacts has been observed, suggesting that the growth of tribofilm is a stress-activated chemical reaction phenomenon [121-124]. They used high friction lubricants to grow tribofilms on tungsten carbide balls. The ball and disc were super finished with roughness (R_q) values of 10 nm and 7 nm, respectively.

2.4.5 Tribochemistry of ZDDP antiwear film formation

The antiwear action of ZDDP starts with the presence of ZDDP in the solution phase. The ZDDP from its solution phase should reach the surface of the substrate where further chemical reactions occur to form the antiwear tribofilm.

In the solution / bulk phase, the type and size of the radical group controls the properties of the ZDDP molecule. Alkyl groups are generally found on the ZDDPs employed in engine oils. A distribution of several alkyl chain lengths is used to get required solubility and thermal stability [90]. This solution phase ZDDP then reaches the surface. Whether it reaches as ZDDP molecule or its decomposition products is still not clear. At the surface of substrate, the ZDDP reacts to form the antiwear film. It is proposed that ZDDP undergoes an oxidation reaction on the surface followed by a condensation polymerization step to form a glassy phosphate film [125].

The decomposition of ZDDP is a complex process and several possible pathways have been suggested. The dithiophosphate ligands are weak so the zinc cation can be easily replaced by iron or copper forming less stable metal-dialkyldithiophosphates [126]. The ligand exchange behaviour of ZDDP becomes critically important when other additives especially friction modifiers are blended together [127, 128]. The ability of ZDDP to decompose hydroperoxides [129] and peroxy [130, 131] radicals also results in the decomposition of ZDDP. This route of decomposition of ZDDP defunct the antiwear action of ZDDP [7, 132] and the main reaction products are no longer the glassy phosphates. In the absence of hydroperoxides and peroxy radicals, the ZDDP undergoes a different route to decomposition at temperatures of around 130°C to 230°C [85]. The oxygen and sulphur exchange takes place within the ZDDP molecule [133].

The next step is the adsorption of ZDDP on the substrate surface. The ZDDP adsorbs on iron via the Sulphur atom on the P=S bond [134]. Once the temperature reaches around 60°C an irreversible reaction occurs and the ZDDP loses its Zn atoms. It has also been proposed that the O/S isomer actually adsorbs on steel surface [135].

Whether ZDDP directly adsorbs on the surface or this exchange isomer reacts with the substrate is still a debate.

ZDDP can form either thermal or tribo- films depending upon the route of formation (heat or friction). Although chemically the same, the tribofilms are considered to be more durable [135-137] than the thermal films and require the asperity-asperity contacts and sliding to grow on the substrate [23]. The tribofilms mainly form on the sliding tracks [85, 113, 138] and can form even at ambient temperatures. The rate of formation of these tribofilms is increased with increasing temperature [92].

2.5 Friction with ZDDP

Some ZDDPs are considered to increase friction compared to non-additive lubricant situations. This characteristic has recently been highlighted due to the fuel economy considerations in engine oils [85]. Initially it was thought that ZDDP tribofilms produce a higher magnitude of boundary friction but further experiments revealed that the friction increase was mainly in mixed lubrication conditions [139]. Later studies confirmed that the higher friction due to ZDDP had nothing to do with boundary friction but the experiments showed that the complete Stribeck curve was shifted to the right. This was linked to the roughening of the surface due to tribofilm which grows in a patchy manner [84, 109]. Further research on this led to the conclusion that even smooth tribofilms have higher friction in mixed lubrication [139, 140]. The presence of the tribofilm is believed to hinder fluid entrainment and delay lubricant film development. These high friction properties of ZDDP are generally harmful but might prove blessing in some applications like continuously variable transmissions.

2.6 Summary

Mixed lubrication and elastohydrodynamic lubrication are described by the same equation set. The solution to these equations is very difficult especially under extreme conditions. Developing a mixed lubrication solver essentially involves developing a robust solver that can handle asperity contacts efficiently. The currently available solvers are classified as either stochastic or deterministic depending upon whether the roughness is treated stochastically or deterministically. In the current study stochastic models are not being used due to their inability give localized contact details.

A mixed lubrication solver that can simulate lubrication transition from full film down to mixed lubrication is required. Depending upon how the contact pressures are solved, the deterministic solvers can be separate models or unified models. For lubrication transition studies, a unified solver is required. Thus, a mixed lubrication solver based upon the unified solution approach is required and this challenge is undertaken in this study.

ZDDP is the preferred choice as an antiwear additive in engine oils due to its superior functionality and low cost. It performs its antiwear action by forming a smart layer on top of the substrate to protect it. The digestion of the hard abrasive iron oxide particles is also one of the proposed modes of its operation. It grows in a patchy manner and is inhomogeneous. The chemical and structural inhomogeneity through its thickness results in gradually varying mechanical properties. This makes the tribofilm a smart material and it responds to the loading conditions to provide superior protection against wear. The tribochemistry is quite unclear and complex. Various reaction pathways have been proposed but there is no definitive answer yet. The growth of ZDDP tribofilm is not restricted to steels or metals. Tribofilm growth on ceramics, diamond like carbon coatings (DLCs) and non-ferrous substrates has been observed

and experimentally verified. The strength and durability of the tribofilms is considered to be crucial in controlling wear. The current consensus on the growth kinetics of the ZDDP tribofilm is that it undergoes a stress-activated chemical reaction where the shear stress reduces the activation barrier facilitating the chemical interaction.

The literature on the understanding of the ZDDP tribofilm growth in a lubricated contact is limited. The studies dealing with this problem only consider boundary lubrication. The models considering the effect of lubrication are very rare. Thus, a mixed lubrication model that is capable of simulating the entire transition from full lubricant film thickness to dry contact conditions is required. The model should also consider the tribochemistry. Thus, enabling the study of tribofilm growth in all the lubrication regimes and the dynamic changes of lubrication regimes to be analysed.

The unified mixed lubrication model successfully bridges the gap between lubrication and contact mechanics. The inclusion of tribochemistry will allow the study of problems involving multiphysics phenomenon of lubrication, contact mechanics and tribochemistry in a single framework.

It is to be noted that the literature review in this chapter is more generalized and specific review relevant to each topic is provided in Chapter 3, Chapter 4, Chapter 5, Chapter 6 and Chapter 7.

PART II

Model Development and Numerical Algorithm Improvements

Chapter 3

Mixed Lubrication Model: Numerical, Algorithmic and Computational Details

In this chapter the complete mathematical, numerical and computational details of the mixed lubrication model are developed and the details presented. The mixed lubrication model was developed and complete computer code was developed from scratch using the FORTRAN programming language resulting in a highly useful tool to access problems at the engineering scale.

The mathematical model for the mixed lubrication problem is outlined in section 3.1. The equations defining the EHL / mixed lubrication problem are outlined. These equations are then non-dimensionalized in section 3.2. Solvers for the Reynolds equation are prone to slow convergence at high pressures and it is very difficult to get converged solutions when actual asperity-asperity contact takes place. The conventional solvers fail under such mixed physics situations. Thus, the problem of developing a mixed lubrication solver essentially means developing a robust solver that can handle discrete fluid and solid contact spots.

The numerical solvers developed for the EHL / mixed lubrication problem are reviewed with specific emphasis on the ability of solvers to handle extreme conditions in section 3.6.2. The key reasons causing this loss of convergence are explored and among various solvers, the semi-system method is chosen and implemented. This method requires the entrainment flow terms to be included in the development of coefficient matrix to ensure diagonal dominance in both low and high load conditions. The unified mixed lubrication algorithm is introduced and the details of the implementation specific to this study are given. The discretized Reynolds equation

results in a system of equations that needs to be solved numerically. The TriDiagonal Matrix Algorithm (TDMA) algorithm is introduced in section 3.6.5. To address the issue of a loss of coupling in the direction transverse to flow at higher pressures, the TDMA algorithm is implemented in a line by line manner; details of implementation and a discussion of the superiority of this algorithm are given in section 3.6.5. The application of boundary conditions is then addressed in section 3.7.2. For a TDMA algorithm, it is slightly tricky to handle the boundary conditions.

The calculation of deformation by the Boussinesq integral is very time consuming and its calculation scales as $O(N^2)$ due to the double integral. The calculation of deformation requires multiplication of the influence coefficient matrix with pressure. This multiplication with the summation results in a linear convolution. If this convolution is converted into a cyclic convolution, fast Fourier transforms (FFT) can be used to solve this convolution in the frequency domain. This reduces the computation time significantly and the method scales as $O(N \log(N))$. Thus allowing simulations with larger number of iterations and much finer meshes can be used. The details of the complete procedure of transforming the linear convolution into a cyclic convolution by pre-treating the influence coefficient matrix and the pressure matrix are given. The Fourier transforms are computed with the highly optimized FFTW library (www.fftw.org) that is freely available. Therefore, section 3.9 details the implementation of the FFT algorithm and the implementation of the specific interface to link the FFTW library with FORTRAN programming language. The use of FFT method reduces the computation time by several orders.

The validation of the mixed lubrication model is presented in section 3.10. The EHL calculations based upon finite differences are prone to grid dependence and the grid justification is performed by calculating the central and the minimum film thickness

values for increasing values of mesh density. The calculations are performed for speeds ranging from very high to ultra-low values. Then the model output in the form of pressure and film thickness profiles for a smooth contact and at specific speeds is compared against published results. Excellent agreement is found both qualitatively and quantitatively. Finally, the ability of the model to capture lubrication transitions is explored.

3.1 Governing Equations for mixed lubrication problem

The governing equations have been presented already in chapter 2 but here these are repeated for the sake of convenience and completeness. The lubrication problem is simplified by using equivalent values for the radius and modulus as shown in Figure 3-1. This enables the change of contact configuration from having two cylinders in contact to the contact between a ball and flat. This simplified configuration is used throughout this study and is presented in Figure 3-1.

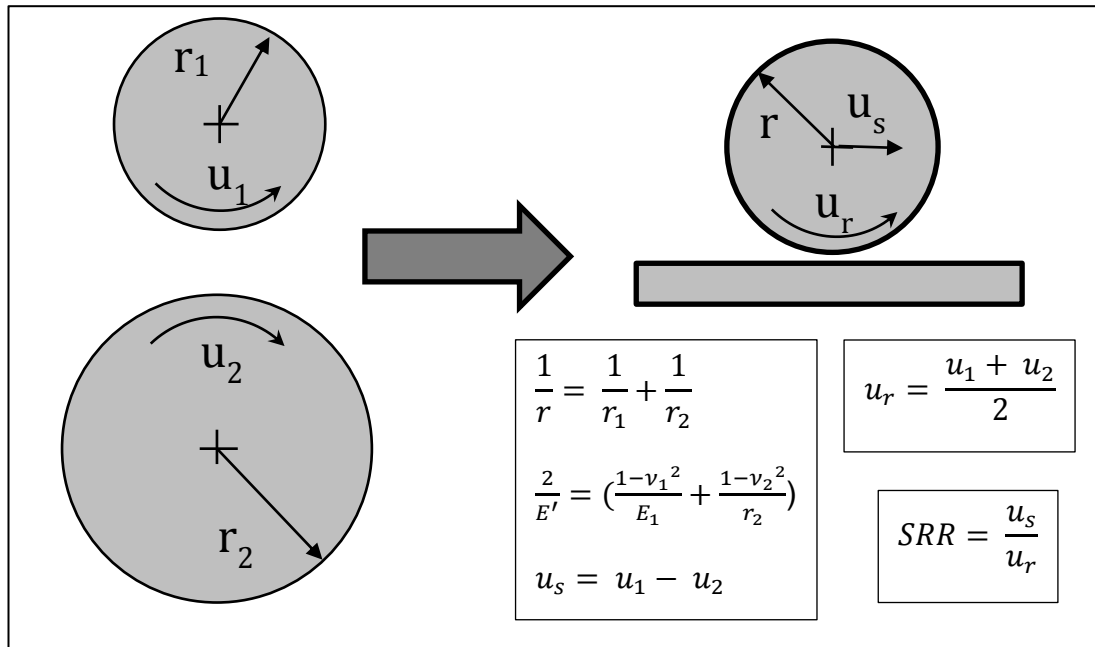


Figure 3-1: Contact simplification and definition of key parameters

The mixed lubrication problem is mathematically defined by three basic equations: the fluid flow equation, the elasticity equation (film thickness) and the load balance equation. This system is inconsistent and requires two additional equations relating density and viscosity as a function of pressure. Thus the complete system is solved by these five equations which are outlined below.

Reynolds equation

$$\frac{\partial}{\partial x} \left(\frac{\rho h^3}{12\eta} \frac{\partial P}{\partial x} \right) + \frac{\partial}{\partial y} \left(\frac{\rho h^3}{12\eta} \frac{\partial P}{\partial y} \right) - U_r \frac{\partial(\rho h)}{\partial x} - \frac{\partial(\rho h)}{\partial t} = 0 \quad (3-1)$$

Film thickness equation

$$h(x, y, t) = h_o(t) + \frac{x^2}{2R_x} + \frac{y^2}{2R_y} + V(x, y, t) - R(x, y, t) \quad (3-2)$$

where the last two terms represent elastic deformation of the contacting half spaces and the roughness function, respectively. The elastic deformation is calculated by the Boussinesq integral.

$$V(x, y, t) = \frac{2}{\pi E'} \int_{-\infty}^{+\infty} \int_{-\infty}^{+\infty} \frac{p(x', y')}{\sqrt{(x-x')^2 + (y-y')^2}} dx' dy' \quad (3-3)$$

while the roughness function gives the micro-geometry of the contacting bodies

$$R(x, y) = \delta_1(x, y, t) + \delta_2(x, y, t) \quad (3-4)$$

For moving roughness, the roughness functions are described as

$$\delta_1(x, y, t) = \delta_1(x - U_1 * t, y)$$

$$\delta_2(x, y, t) = \delta_2(x - U_2 * t, y)$$

Load balance equation

$$W = \int_{-\infty}^{+\infty} \int_{-\infty}^{+\infty} p(x', y') dx' dy' \quad (3-5)$$

Pressure-viscosity equation

The Barus equation

$$\eta(p) = \eta_o e^{\alpha p} \quad (3-6)$$

The Roelands equation

$$\eta(p) = \eta_o e^{\left((\ln(\eta_o) + 9.67) \left(-1 + \left(1 + \frac{p}{p_o} \right)^z \right) \right)} \quad (3-7)$$

Density pressure equation

$$\rho(p) = \rho_o \frac{5.9 \times 10^8 + 1.34p}{5.9 \times 10^8 + p} \quad (3-8)$$

The Reynolds equation (3-1) describes the fluid film formation in the EHL conjunction while the elastic deformation equation (3-3) represents the contact mechanics of the problem. The ML problem essentially combines both the fluid flow and elasticity equation in a single domain making it much more challenging to obtain converged solutions for the mixed physics problem. The load balance equation (3-5) ensures that the calculated pressures are actually the correct pressures by balancing pressures and load. In the EHL conjunction, the pressure might be several orders of magnitude higher compared to ambient conditions and thus it is essential to consider the effect of pressure on viscosity to correctly model the rheology of the lubricant. Several equations are presented to relate viscosity to pressure. The Barus law (3-6) is the most commonly used due to its simplicity and ease of implementation but does not represent true viscosity-pressure phenomenon. At pressures above 1 GPa, the

pressures predicted by the Barus may be quite overestimated [20]. Thus, the Roelands equation (3-7) is used in the current study. Due to the high pressures in the ML conditions, the fluid cannot be considered incompressible and the change in density with pressure is important. The change in density is represented by the Dowson and Higginson formulation given in equation (3-8).

3.2 Non-dimensionalization

In the above section, the EHL / ML equation set is presented. From a computational point of view, it is always advisable to non-dimensionalize the problem equations. The film thickness values range from micrometers to nanometers while the pressure ranges from megapascals to gigapascals. Thus non-dimensionalization removes any numerical inconsistencies that might occur due to the very large and very small numbers. Secondly, comparative analysis can be performed quite easily without actually having to deal with the magnitudes of quantities. And it has been a standard practice among the EHL community to non-dimensionalize the equation set. The same practice is followed here. Thus, the following variables can be used to non-dimensionalize the above equations.

$$X = \frac{x}{a}, Y = \frac{y}{a}, P = \frac{p}{p_h}, H = \frac{hR_x}{a^2}, \rho = \frac{\rho}{\rho_o}, \eta = \frac{\eta}{\eta_o}, T = \frac{tUr}{a}$$

Here, a is the half width of the Hertzian contact.

The Reynolds equation becomes

$$\frac{\partial}{\partial X} \left(\xi \frac{\partial P}{\partial X} \right) + \frac{\partial}{\partial Y} \left(\xi \frac{\partial P}{\partial Y} \right) - \frac{\partial(\bar{\rho}H)}{\partial X} - \frac{\partial(\bar{\rho}H)}{\partial T} = 0 \quad (3-9)$$

for $X \in [X_a, X_b]$ and $Y \in [-Y_a, Y_a]$. In this equation, $\xi = \frac{\bar{\rho}H^3}{\bar{\eta} \bar{\lambda}}$ and $\bar{\lambda} = \frac{12Ur\eta_o R_x^2}{a^3 p_h}$

The solution should obey the following boundary conditions

$$P(X_a, Y) = P(X_b, Y) = P(X, -Y_a) = P(X, Y_a) = 0 \quad (3-10)$$

And imposing $P(X, Y) > 0$ satisfies the general cavitation boundary condition.

The film thickness equation becomes

$$H(X, Y) = H_o + \frac{X^2}{2} + \frac{Y^2}{2} + \frac{2}{\pi^2} \int_{-\infty}^{+\infty} \int_{-\infty}^{+\infty} \frac{P(X', Y')}{\sqrt{(X-X')^2 + (Y-Y')^2}} dX' dY' - R(X, Y) \quad (3-11)$$

The dimensionless load balance equation is

$$\int_{-\infty}^{+\infty} \int_{-\infty}^{+\infty} P(X, Y) dX dY = \frac{2\pi}{3} \quad (3-12)$$

The load balance condition is implemented by adjusting the non-dimensional gap H_o in the film thickness equation.

The Roelands pressure-viscosity equation becomes

$$\bar{\eta}(P) = e^{\left((\ln(\eta_o) + 9.67) \left(-1 + \left(1 + \frac{p_h P}{p_o} \right)^z \right) \right)} \quad (3-13)$$

and finally the density pressure equation becomes

$$\bar{\rho}(P) = \frac{5.9 \times 10^8 + 1.34 p_h P}{5.9 \times 10^8 + p_h P} \quad (3-14)$$

3.3 Discretization

The non-dimensionalized equation set (equation (3-9) to equation (3-14) is discretized on a regular grid $\Delta X = \Delta Y$ using finite differences, though irregular grids can also be used. Central differences are used for the pressure flow terms (Poiseuille terms) and first order backward differences for the wedge (Couette flow) and squeeze

flow terms (the transient derivative). This particular difference scheme is chosen based upon the detailed study by Liu et al [80, 81]. The discrete versions of the mixed lubrication equation set is presented in the next sections.

3.3.1 Discrete Reynolds Equation

The discrete version of the Reynolds equation is given below:

$$\left[\frac{\xi_{i-\frac{1}{2},j} P_{i-1,j} - \left(\xi_{i-\frac{1}{2},j} + \xi_{i+\frac{1}{2},j} \right) P_{i,j} + \xi_{i+\frac{1}{2},j} P_{i+1,j}}{\Delta X^2} \right] + \left[\frac{\xi_{i,j-\frac{1}{2}} P_{i,j-1} - \left(\xi_{i,j-\frac{1}{2}} + \xi_{i,j+\frac{1}{2}} \right) P_{i,j} + \xi_{i,j+\frac{1}{2}} P_{i,j+1}}{\Delta Y^2} \right] - \left[\frac{\rho_{i,j} H_{i,j} - \rho_{i-1,j} H_{i-1,j}}{\Delta X} \right] - \left[\frac{\rho_{i,j}^k H_{i,j}^k - \rho_{i,j}^{k-1} H_{i,j}^{k-1}}{\Delta T} \right] = 0 \quad (3-15)$$

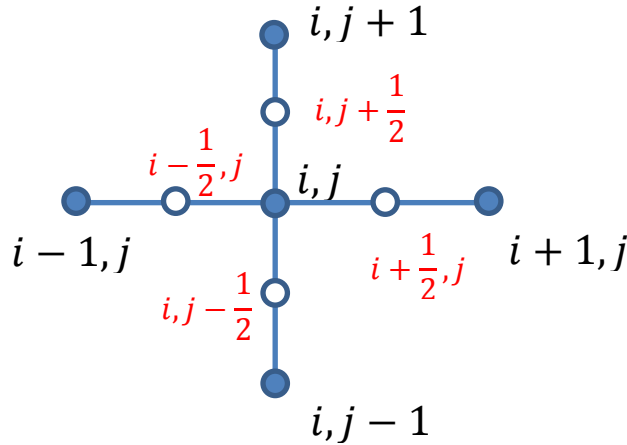


Figure 3-2: The distinction between the stencil of pressure differences and the stencil for discretizing the Reynolds coefficients. The open points and red indices refer to the stencil for Reynolds coefficients.

The discretization of the term ξ requires attention. This term is discretized on a grid that is different from the actual grid for solving the Reynolds equation and its value at a particular node is the average of values at the surrounding nodes halfway through the grid and is defined as $\xi_{i,j} = \frac{\xi_{i-\frac{1}{2},j} + \xi_{i+\frac{1}{2},j}}{2}$ (where $\xi_{i\pm\frac{1}{2},j} = \xi_{i,j} + \xi_{i\pm 1,j}$) as shown

in Figure 3-2. The indices labelled red and with hollow circles correspond to the grid for evaluating $\xi_{i,j}$ values.

To write the discrete version of the film thickness equation, the Boussinesq integral for the half space elasticity needs to be represented as a discrete operator. The denominator in this integral has a discontinuity at the point where the deformation is being calculated. This discontinuity can be avoided by writing the problem in polar coordinates [141]. In rectangular coordinates,

$$V(X, Y) = \frac{2}{\pi^2} \int_{-\infty}^{+\infty} \int_{-\infty}^{+\infty} \frac{P(S, T)}{\sqrt{(X-S)^2 + (Y-T)^2}} dSdT \quad (3-16)$$

The denominator gives the distance between the points (X, Y) the point where deformation is being calculated and (S, T) the point where pressure is acting. It becomes singular when $X = S$ and $Y = T$. To avoid this singularity first the coordinates are transformed by shifting the origin to (S, T) and substituting $X' = X - S$ and $Y' = Y - T$.

$$V(X', Y') = \frac{2}{\pi^2} \int_{-\infty}^{+\infty} \int_{-\infty}^{+\infty} \frac{P(X', Y')}{\sqrt{X'^2 + Y'^2}} dX' dY' \quad (3-17)$$

Using polar coordinates to represent this equation successfully eliminates the singularity. Thus, substituting $X = r \cos \theta$ and $Y = r \sin \theta$, the above equation becomes,

$$V(X, Y) = \frac{2}{\pi^2} \int_0^r \int_0^{2\pi} P(r, \theta) drd\theta \quad (3-18)$$

Now this integral can be evaluated by numerical integration procedures but the computational effort required to solve this for the point contact problem restricts its

use. Thus, the integral is converted into the **deformation matrix**. The solution domain is discretized and the pressures in the deformation integral are decoupled. Thus, the deformation at a node can be evaluated by considering pressure acting at a single node and this is repeated for the whole domain for every single point. The resulting summation is a convolution in real space.

3.3.2 Discretized deformation integral

The discretized version of the deformation integral is given below

$$V_{ij} = \frac{2*\Delta X}{\pi^2} \sum_{k=1}^N \sum_{l=1}^N D_{ij}^{kl} P_{kl} \quad (3-19)$$

In this equation, D_{ij}^{kl} is the non-dimensionalized deformation coefficient matrix. It relates the deformation at node (i, j) , the point at which deformation is being calculated to the node (k, l) , the point of application of pressure. The above equation is valid for a regular grid ($\Delta X = \Delta Y$) and for such grids

$$D_{ij}^{kl} = D_{kj}^{il}$$

$$D_{ij}^{kl} = D_{il}^{kj}$$

Resulting in N*N calculations for a single evaluation. The formula used to calculate deformation coefficient is as follows [141]:

$$D_{ij}^{kl} = (|j - l| + 0.5) \ln \left[\frac{f(|i-k|+0.5, |j-l|+0.5)}{f(|i-k|-0.5, |j-l|+0.5)} \right] + (|i - k| - 0.5) \ln \left[\frac{f(|j-l|-0.5, |i-k|-0.5)}{f(|j-l|+0.5, |i-k|-0.5)} \right] + (|j - l| - 0.5) \ln \left[\frac{f(|i-k|-0.5, |j-l|-0.5)}{f(|i-k|+0.5, |j-l|-0.5)} \right] + (|i - k| + 0.5) \ln \left[\frac{f(|j-l|+0.5, |i-k|+0.5)}{f(|j-l|+0.5, |i-k|+0.5)} \right] \quad (3-20)$$

The interpolation function used is $f(x, y) = x + \sqrt{x^2 + y^2}$.

3.3.3 Discretized Load balance equation

The discretized version of the load balance equation is given by

$$\Delta X \Delta Y \sum_{i=1}^N \sum_{j=1}^N P_{ij} = \frac{2*\pi}{3} \quad (3-21)$$

This equation is evaluated in every iteration and the resulting difference is used to update the value of the undeformed film thickness, H_o in the film thickness equation.

3.4 Numerical procedure for solving the Reynolds Equation

The numerical solution procedure for solving the above equation system is based upon solving the Reynolds equation and using the calculated pressures to update the deformation which is used to calculate the film thickness.

The film thickness is again used in the Reynolds equation to update the coefficient matrix for the Reynolds equation. This procedure is iterated until a desired pressure and load balance convergence is achieved. The complete flow chart is given in Figure 3-3

The steps involved in the solution procedure are clearly identified in the flow chart. The calculation starts with an initialization of the problem. The material properties like the elastic modulus, poisson's ratio etc. and the geometrical properties like the radius of curvature of the ball and the diameter of disc and the initial guess of pressure (generally Hertzian) are defined. This pressure goes into updating the deformation and film thickness equation and to build up the coefficient matrix for the Reynolds solver. The viscosity and density are also update based upon the pressure as these are a function of pressure and need to be updated every time the pressure is updated and are also used to update the Reynolds coefficients. The Reynolds coefficients are then used to solve the Reynolds equation and the error is checked. If the error is within the range specified, the simulation is stopped and the pressure and film thickness profiles are given as output. Otherwise, the pressure and the rigid body interference are adjusted for the next iteration and the procedure repeats until convergence.

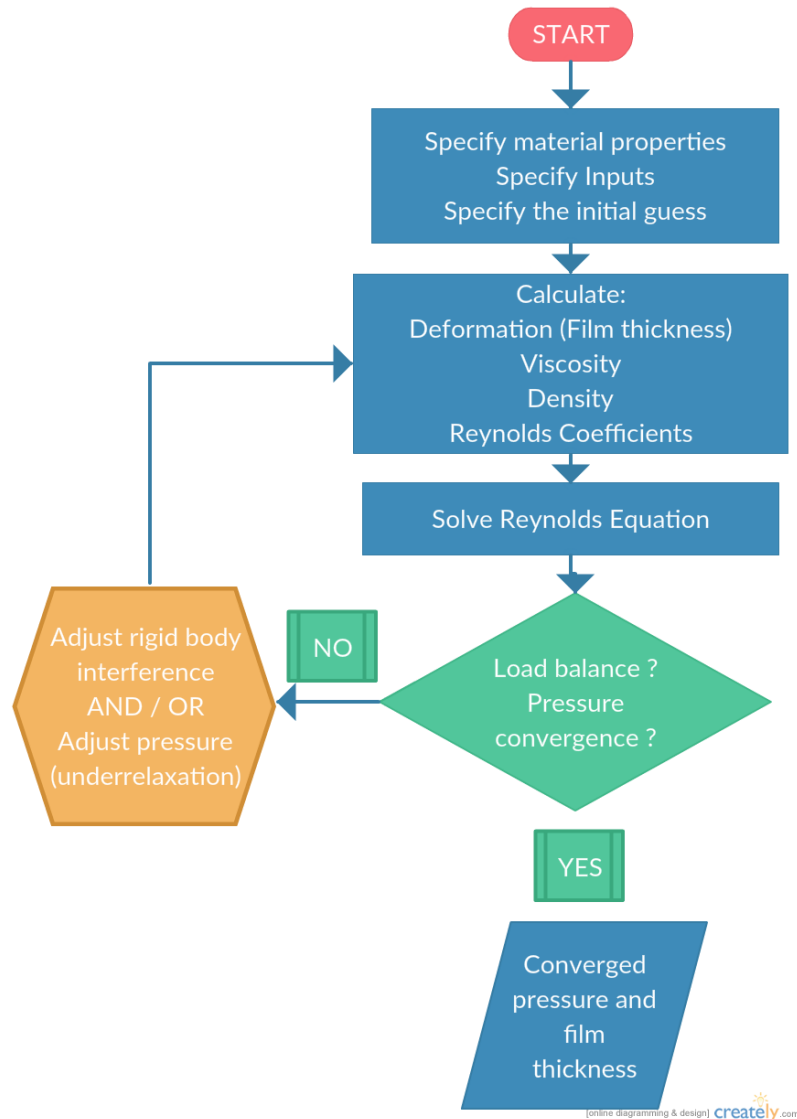


Figure 3-3: Flow chart to illustrate the numerical algorithm for solving the unified mixed lubrication problem.

3.5 Constructing coefficient matrix for the Reynolds Equation

The Reynolds equation (3-9) once discretized forms a system of equations that is solved simultaneously. This equation system is

$$A_{ij}P_{i-1j} + B_{ij}P_{ij} + C_{ij}P_{i+1j} = \delta_{ij} \quad (3-22)$$

The indexed notation in this equation is based upon the numerical solution domain. The coefficient matrix is built by fixing the index in one direction and populating the coefficient matrix by varying the index in the other direction. Once the system of equations is solved, the pressure and film thickness values are updated. In this way the solver moves from one end of the solution domain to the other. This procedure can also be repeated several times starting from one direction and reaching the other direction as in alternating direct implicit (ADI) technique but in the current study, this was not explored.

3.5.1 Conventional solution procedure

The conventional numerical procedure for solving the Reynolds equation considers the pressure flow terms to be unknown at each iteration and thus the coefficient matrix for solving the system of equations (3-22) is formed entirely by the pressure flow terms. This means that the entrainment terms are considered known and are updated based upon information from the previous iteration. The conventional procedure has some limitations especially at higher loads and extreme conditions which will be discussed in detail in the next sections.

The contribution of each term in the Reynolds equation (3-9) (discretized version is equation (3-15)) is considered independently and is included into the discretized equation (3-22). For a rectangular grid, the contribution of each of the terms in the Reynolds equation in building the coefficient matrix is given next.

Poiseuille flow contribution

$$[A_{ij}]_p = \frac{\xi_{i-\frac{1}{2},j}}{\Delta X^2}$$

$$[B_{ij}]_p = -\frac{\left(\xi_{i-\frac{1}{2},j} + \xi_{i+\frac{1}{2},j} + \xi_{i,j-\frac{1}{2}} + \xi_{i,j+\frac{1}{2}}\right)}{\Delta X^2}$$

$$[C_{ij}]_p = \frac{\xi_{i+\frac{1}{2},j}}{\Delta X^2}$$

$$[\delta_{ij}]_p = -\frac{\left(\xi_{i,j-\frac{1}{2}}P_{i,j-1} + \xi_{i,j+\frac{1}{2}}P_{i,j+1}\right)}{\Delta X^2}$$

Shear flow / Couette flow contribution

$$[A_{ij}]_s = 0$$

$$[B_{ij}]_s = 0$$

$$[C_{ij}]_s = 0$$

$$[\delta_{ij}]_s = \frac{\rho_{ij}H_{ij} - \rho_{i-1j}H_{i-1j}}{\Delta X}$$

Squeeze flow contribution

$$[A_{ij}]_t = 0$$

$$[B_{ij}]_t = 0$$

$$[C_{ij}]_t = 0$$

$$[\delta_{ij}]_t = \frac{\rho_{ij}^k H_{ij}^k - \rho_{ij}^{k-1} H_{ij}^{k-1}}{\Delta T}$$

Thus, the coefficient matrix for the complete system of equations can be written as the sum of the contribution from individual terms as

$$A_{ij} = [A_{ij}]_p + [A_{ij}]_s + [A_{ij}]_t \quad (3-23)$$

$$B_{ij} = [B_{ij}]_p + [B_{ij}]_s + [B_{ij}]_t \quad (3-24)$$

$$C_{ij} = [C_{ij}]_p + [C_{ij}]_s + [C_{ij}]_t \quad (3-25)$$

$$\delta_{ij} = [\delta_{ij}]_p + [\delta_{ij}]_s + [\delta_{ij}]_t \quad (3-26)$$

Using the above formulation the EHL / ML system of equations formed by equations (3-9), (3-11), (3-12) (3-13) and (3-14) can be solved subject to the boundary conditions given by equation (3-10) using appropriate numerical schemes (discussed in next section). The important thing to note here is that the complete coefficient matrix is built from the Poiseuille flow terms as the terms δ_{ij} are considered to be known from the previous iteration. The solution is expected to be stable at low pressures / high speeds. The numerical convergence and stability will be discussed in detail in the next section.

3.6 Design and development of a robust solver for the mixed lubrication problem

Once the mathematical problem is discretized using finite differences, it is now a linear algebra problem, $AY = B$, where Y is the vector of unknowns, A is the coefficient matrix of order $N \times N$ and B is the vector of known values. There are two types of linear algebra solvers to solve this problem: the direct solvers and iterative solvers. The direct solvers solve the problem exactly (to machine precision) and are most accurate but are only practically applicable to simplified and small problems. For large problems, the direct solvers cannot be used due to high computational cost and huge memory requirements. Thus, most practical problems are solved by the iterative solvers. The iterative solvers find successive approximations to the solution by starting from an initial guess [142]. The iterative solvers are much more flexible

and low cost and the accuracy of solution can be tuned by setting suitable convergence criteria. Iterations start with an initial guess $X^{(0)}$ and reaches a final solution X . In this process a series of solutions vectors is created $\{X^n\}_{n=0}^{\infty}$. This can be represented as

$$X_{i+1} = MX_i + c \quad (3-27)$$

3.6.1 Iterative approaches in EHL / ML solutions

The EHL equations are traditionally solved by using the Gauss-Seidel and Jacobi techniques. These techniques have been well documented and the more interested reader should consult the book by Venner and Lubrecht [29]. The difference lies in the way in which the new values are calculated for successive iterations. If only the old values are used to update the guess, it is essentially a Jacobi solver. The Jacobi solver is based upon the idea of simultaneous displacement where values are only updated once a complete iteration sweep has been taken so the order in which values are updated does not matter. If the values are updated dynamically and some newly updated values are used to update the guess, it is a Gauss-Seidel solver. Thus, it should be done in a lexicographic (increasing grid numbering) order and the values updated during the iteration sweep.

3.6.2 A survey of numerical approaches

Mixed lubrication has primarily remained a numerical analysis method due to the experimental difficulties. Simulations have been an invaluable tool to study ML. The fluid under study can be either Newtonian or non-Newtonian. For a non-Newtonian fluid, the shear behaviour becomes important. The distinction of various numerical approaches and the improvements introduced in the direct iterative approaches is shown in Figure 3-4 highlighting the semi-system approach.

The solution of the ML problem is very challenging as the equations exhibit strong non-linearity. The algorithm presented in above flowchart is for the direct iterative approach where the elastic deformation is first evaluated based upon the initial pressure guess (Hertzian in this study unless otherwise mentioned). This deformation $V(X,Y)$ is then used to calculate the film thickness $H(X,Y)$, and nodal values of viscosity and density. These values are input to the discretized Reynolds equation to get the system of equations that can be readily solved as everything on the right hand side (δ_{ij} given in equation (3-26)) is known. The pressures obtained are used again to calculate deformation, film thickness, density, viscosity and again the Reynolds equation is solved. This procedure repeats until a desired convergence of both pressure and load balance has been achieved.

The direct iterative approach has some limitations. The solution convergence is very slow and it is numerically unstable under heavily loaded conditions. Some other approaches have been put forward but since only the direct iterative approach (with improvements to overcome the limitations) is used here, the other approaches are just briefly introduced. The inverse solution approach [143] solves pressures inversely in the severe conditions. This enabled quicker solutions and could handle heavy loading conditions however is not automatic and requires manual input. The system analysis approach [144, 145] uses the Newton-Raphson iterative approach and is limited due to huge memory requirements and time step limitations. The coupled differential deflection technique was first applied to solve line contact problems [146] in 2000 and then extended to point contact problems [147], later in 2003. This approach introduces a new way to evaluate the deflection with very localized formulation. Thus the resulting discretized equations can be solved with banded matrix techniques which are well established among the computational fluid dynamics (CFD) and finite

element method (FEM) communities and rapid optimized solvers are available. The differential deflection methods are rapid and stable even under heavy loaded conditions.

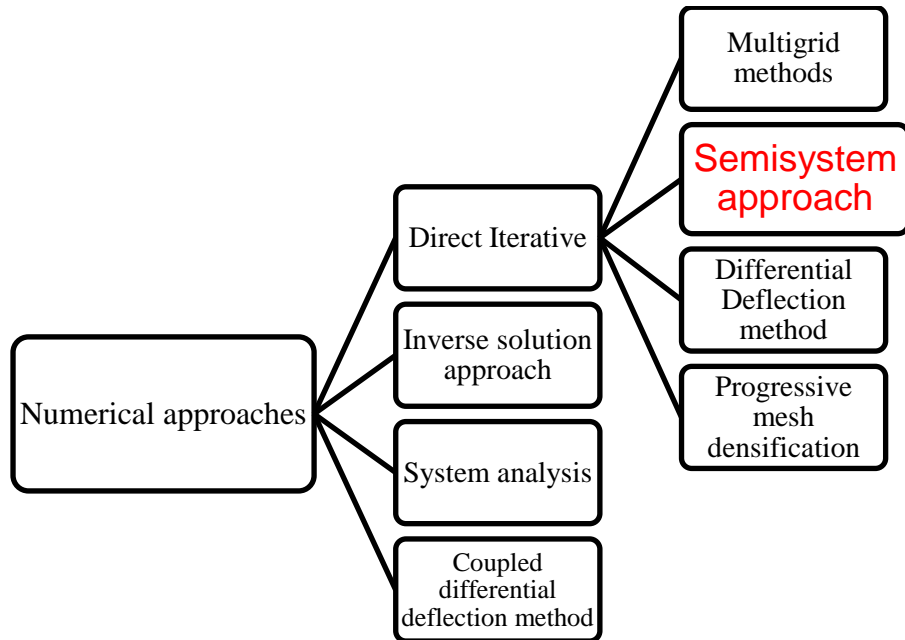


Figure 3-4: Various approaches for solving the EHL / mixed lubrication problem.

The direct iterative approach is the first approach used in EHL modelling. This is mainly due to its simplicity of development and implementation and secondly due to its low memory requirement. Once the issues of convergence and stability have been overcome, the direct iterative approach can be readily applied to solve practical problems. The first breakthrough in EHL theory came with the introduction of the multigrid methods by Lubrecht in 1987 [148] and application by Venner [56] in 1991 and Ai [77] in 1993. There are two variations of the multigrid method: algebraic multigrid and geometric multigrid and in EHL the multigrid methods refer to geometric multigrid methods. In algebraic multigrid, the degree of polynomial used to approximate the function is switched between higher and lower levels to reduce the errors correspondingly while in geometric multigrid methods, the computational grid

is switched between coarser and finer levels to reduce errors correspondingly. This switching is based upon the observation that the errors whose wavelength matches the grid size converge fast. These methods have enjoyed widespread acceptance and application.

In the above discretization given in section 3.5, it is clear that the coefficient matrix for the system of equations is built only from the pressure flow terms. All other terms (Couette and squeeze) are considered known and put onto the right hand side in the known vector (calculated based values from previous iteration). Under heavily loaded conditions, the Reynolds coefficients forming the coefficient matrix become very small due to high viscosity and small film thickness. Thus the coefficient matrix loses its diagonal dominance and the solution process suffers from severe instability and poor convergence. The solution to this problem was proposed by Ai [77]. He proposed the semisystem approach where the entrainment flow terms (Couette and squeeze) are also used to build the coefficient matrix. This ensures numerical stability even under extreme conditions when the pressure flow vanishes.

When the EHL film thickness approaches nanometer scale (especially below 20 nanometer [80]), the effect of mesh density on the EHL film thickness becomes significant. Although proposed earlier as well [82], the progressive mesh densification method has recently emerged [149] as a very promising new method to solve the mixed lubrication problems. Unlike the multigrid methods, this approach relies on starting with a coarser mesh and refining the mesh once a loose criterion for convergence is met. This significantly reduces the required computational effort and the inconsistencies regarding the mesh dependence of film thickness results.

A numerical improvement to the direct iterative approach was also given by Li and Kahraman [79]. Using the asymmetric integrated control volumes, the mesh

dependence of the film thickness can be removed altogether and coarser meshes are accessible.

All the above methods can be broadly classified into direct and inverse methods. The inverse methods are very powerful but require tricky manual tuning to get converged pressures at higher pressures. The direct methods are easily implemented and automated. Gauss-Seidel, Jacobi, Newton-Raphson, multigrid and semisystem method are all variations of the direct iterative approach.

3.6.3 The Semisystem approach: insights into numerical stability

As mentioned in section 3.5.1, the convergence is very slow under heavy loading conditions when the Gauss-Seidel or Jacobi methods are used where the coefficient matrix for the Reynolds equation solver is built only from the pressure flow terms.

The Reynolds coefficient ($\xi = \frac{\bar{\rho}H^3}{\bar{\eta}\bar{\lambda}}$ where $\bar{\lambda} = \frac{12Ur\eta_0R_x^2}{a^3p_h}$) due to reduced film thickness and increased viscosity at higher pressures will become insignificant. This will happen even under normal conditions, near the centre of the contact, where the pressure is high. This can be mathematically explained as

$$\lim_{P \rightarrow \infty} \xi_x \approx 0 \text{ and } \lim_{P \rightarrow \infty} \xi_y \approx 0$$

Asymptotically, Reynolds equation reduces to

$$\frac{\partial(\bar{\rho}H)}{\partial X} + \frac{\partial(\bar{\rho}H)}{\partial T} = 0 \quad (3-28)$$

This means that the pressure flow becomes insignificant and the equation for the fluid flow reduces to a wave equation [29]. Thus, if the Reynolds equation solver is based solely upon the pressure flow terms, the solution will not converge. So, we have to

develop the system of equations $AY = B$ again. The discretized Reynolds equation remains the same. We only reformulate the coefficient matrix.

The idea is to build the coefficient matrix with contributions from the pressure flow terms as well as the shear and squeeze flow terms. The pressure flow terms have already been included as explained in the previous sections. To include contribution from the entrainment flow terms (squeeze + shear), the nodal value of film thickness is expressed as:

$$H_{i,j} = H_{i,j}^{n-1} - (D_{i-1,j}^{ij}P_{i-1,j}^{n-1} + D_{i,j}^{ij}P_{i,j}^{n-1} + D_{i+1,j}^{ij}P_{i+1,j}^{n-1}) \\ + (D_{i-1,j}^{ij}P_{i-1,j}^n + D_{i,j}^{ij}P_{i,j}^n + D_{i+1,j}^{ij}P_{i+1,j}^n)$$

In this equation, n is the iteration number. The film thickness $H_{i,j}$ includes the deflection due to all the pressures from the previous iteration $n - 1$. The influence of pressures in the row being solved at point i is given by

$$D_{i-1,j}^{ij}P_{i-1,j} + D_{i,j}^{ij}P_{i,j} + D_{i+1,j}^{ij}P_{i+1,j}$$

The terms that are to be evaluated in the current iteration, n (the unknown values) are taken to the left side of the equation 3-22 to populate the vectors A_{ij} , B_{ij} and C_{ij} while the terms that are from the previous iteration are kept on the right hand side to develop the vector, δ_{ij} of known values. It is to be noted that due to the way the algorithm has been implemented, the pressure approximation term $P_{i-1,j}$ is known from the previous step in the current iteration. Based upon this approximation, the system of equations, equation 3-22 is built in the following:

Poiseuille flow contribution

$$[A_{ij}]_p = \frac{\xi_{i-\frac{1}{2},j}}{\Delta X^2}$$

$$[B_{ij}]_p = -\frac{\left(\xi_{i-\frac{1}{2},j} + \xi_{i+\frac{1}{2},j} + \xi_{i,j-\frac{1}{2}} + \xi_{i,j+\frac{1}{2}}\right)}{\Delta X^2}$$

$$[C_{ij}]_p = \frac{\xi_{i+\frac{1}{2},j}}{\Delta X^2}$$

$$[\delta_{ij}]_p = -\frac{\left(\xi_{i,j-\frac{1}{2}}P_{i,j-1} + \xi_{i,j+\frac{1}{2}}P_{i,j+1}\right)}{\Delta X^2}$$

Shear flow / Couette flow contribution

$$[A_{ij}]_s = -\frac{\bar{\rho}_{ij}D_{i-1j}^{ij} - \bar{\rho}_{i-1j}D_{i-1j}^{i-1j}}{\Delta X}$$

$$[B_{ij}]_s = -\frac{\bar{\rho}_{ij}D_{ij}^{ij} - \bar{\rho}_{i-1j}D_{ij}^{i-1j}}{\Delta X}$$

$$[C_{ij}]_s = -\frac{\bar{\rho}_{ij}D_{i+1j}^{ij} - \bar{\rho}_{i-1j}D_{i+1j}^{i-1j}}{\Delta X}$$

$$[\delta_{ij}]_s = \frac{1}{\Delta X} \bar{\rho}_{ij} [H_{ij} - (D_{i-1j}^{ij}P_{i-1j} + D_{ij}^{ij}P_{ij} + D_{i+1j}^{ij}P_{i+1j})] \\ - \bar{\rho}_{i-1j} [H_{i-1j} - (D_{i-1j}^{i-1j}P_{i-1j} + D_{ij}^{i-1j}P_{ij} + D_{i+1j}^{i-1j}P_{i+1j})]$$

Squeeze flow contribution

$$[A_{ij}]_t = -\frac{\bar{\rho}_{ij}D_{i-1j}^{ij}}{\Delta T}$$

$$[B_{ij}]_t = -\frac{\bar{\rho}_{ij}D_{ij}^{ij}}{\Delta T}$$

$$[C_{ij}]_t = -\frac{\bar{\rho}_{ij}D_{i+1j}^{ij}}{\Delta T}$$

$$[\delta_{ij}]_t = \frac{1}{\Delta T} \bar{\rho}_{ij} [H_{ij} - (D_{i-1j}^{ij} P_{i-1j} + D_{ij}^{ij} P_{ij} + D_{i+1j}^{ij} P_{i+1j})] - \frac{\bar{\rho}_{ij}^{n-1} H_{ij}^{n-1}}{\Delta T}$$

The individual contributions from all the terms in the Reynolds equation are summed up to build coefficients A_{ij} (equation (3-23)), B_{ij} (equation (3-24)), C_{ij} (equation (3-25)) and δ_{ij} (equation (3-26)) of the system of equations (3-22). Now the coefficient matrix is built from the entrainment terms as well and when the pressure flow becomes weak, the coefficient matrix still holds its diagonal dominance due to these entrainment terms. This is because the deformation matrix has its highest value at the point of application of pressure. Thus the semisystem approach ensures numerical stability even at higher pressures and severe conditions by ensuring that the coefficient matrix stays diagonally dominant.

3.6.4 The unified solution algorithm

The semisystem approach ensures numerical stability by including the dominant terms in developing the coefficient matrix. The idea behind the unified solution algorithm is to use the same Reynolds equation to handle the asperity contacts as well. This means that the pressures in the asperity-asperity contact regions is also calculated by the Reynolds equation. It is believed that when the film thickness approaches zero ($h \approx 0$) the same Reynolds equation will give the same pressures as the contact mechanics equations [75, 83].

The physical meaning of the Reynolds equation is a balance between fluid flows. The first two terms represent the fluid flow due to pressure while the third term represents the lubricant flow due to the movement of surfaces along tangential direction (wedge effect) and the last term represents the lubricant flow due to the vertical movement of the surfaces (squeeze effect). The constraint of zero film thickness can be mathematically written as

$$\lim_{h \rightarrow 0} \left[\left[\frac{\xi_{i-\frac{1}{2},j} P_{i-1,j} - \left(\xi_{i-\frac{1}{2},j} + \xi_{i+\frac{1}{2},j} \right) P_{ij} + \xi_{i+\frac{1}{2},j} P_{i+1,j}}{\Delta X^2} \right] + \left[\frac{\xi_{i,j-\frac{1}{2}} P_{i,j-1} - \left(\xi_{i,j-\frac{1}{2}} + \xi_{i,j+\frac{1}{2}} \right) P_{ij} + \xi_{i,j+\frac{1}{2}} P_{i,j+1}}{\Delta Y^2} \right] \right] = 0$$

Under this constraint, the Reynolds equation reduces to

$$\frac{\partial(\bar{\rho}H)}{\partial X} + \frac{\partial(\bar{\rho}H)}{\partial T} = 0 \quad (3-29)$$

At the border of the contact region, the squeeze terms are not zero. But once the node under consideration is essentially inside the contact, the squeeze terms are also turned off and the Reynolds equation further reduces to

$$\frac{\partial(\bar{\rho}H)}{\partial X} = 0 \quad (3-30)$$

This gives the idea that the same equation system can be used to calculate the contact pressures as well. The same loop goes through all the nodes of the Reynolds equation without distinction of whether the node is a fluid lubricated node or the solid contact node. Depending upon the film thickness constraint, the pressure flow terms are turned off from the solution procedure. If the node also satisfies the criteria that $\frac{\partial H}{\partial x} \approx 0$ the squeeze terms are also turned off. There is no need to define the boundary between the contact and fluid regions and the already existing algorithms for solving the Reynolds equation can be used by simply adding these constraints.

3.6.5 The line by line TDMA solver

As discussed before, two types of solvers are available to solve linear algebra problems: direct solvers and iterative solvers. The direct solvers being more accurate

are favoured if the limitations of memory and computational cost can be avoided. In this section, the objective of getting such a solver is outlined. If the discretized Reynolds equation can be formulated as a sparse banded system, the solution can be obtained by using the *Thomas algorithm* which is a special case of Gaussian elimination for banded systems.

The Thomas algorithm is also called the tridiagonal matrix algorithm [150] (TDMA). Implementation of the TDMA algorithm in different programming environments and are readily available. The TDMA algorithm has been implemented as part of the highly optimized lapack and blas libraries as well, which are a part of the intel MKL libraries. The developed FORTRAN program needs to be interfaced with the MKL libraries to use this default implementation.

The issues with the direct solvers i.e. higher memory requirements and huge computational costs can be very efficiently reduced by using the TDMA algorithm. It boasts the same accuracy as the elimination solvers yet requires very low memory due to its sparse banded nature. Instead of having one huge matrix with zeros all over except the middle banded region, the elements of individual bands are stored as vectors and passed over to the TDMA algorithm reducing the memory requirements significantly. The Thomas algorithm (although a simplification of Gauss elimination) requires far fewer operations to complete one calculation cycle as only one matrix entry is eliminated from a row during forward elimination. Finally a backward substitution step produces the vector of unknowns. Thus, the numerical cost of computing is reduced to $O(N)$ for N equations. The result is better accuracy at low cost. The TDMA algorithm is very famous among the Computational Fluid Dynamics (CFD) community.

The direct solution procedure adopted in this study to solve the ML problem forces the solution procedure to iterate between film thickness and pressure calculations. Thus, the solution to the problem can be obtained by iterating several times between the film thickness (deflection) and pressure (Reynolds equation) solution to get the pressure profile and film thickness with desired convergence of load and pressures.

3.7 Implications of reduced Reynolds equation: weak coupling

An inherent issue with the unified solution algorithm is the weak coupling under heavily loaded conditions when the reduced Reynolds equation (equation $\frac{\partial(\bar{\rho}H)}{\partial X} + \frac{\partial(\bar{\rho}H)}{\partial T} = 0$ (3-28) to equation (3-30)) is used. The mathematical character of the Reynolds equation changes from purely elliptical to a 1-D transport equation. The reduced Reynolds equation has two implications [29] that need to be considered to develop a robust solver for ML problems:

1. The reduction of the 2-D problem to a 1-D problem altogether removes the coupling in Y-direction. In reality the coupling does not vanish but becomes very weak. This is treated by solving the system line by line rather than on a point by point basis.
2. The equation becomes purely integral in character and this needs special treatment. The complete solution is governed by the film thickness derivatives. This requires special treatment to distribute the effect of this high pressure to surroundings.

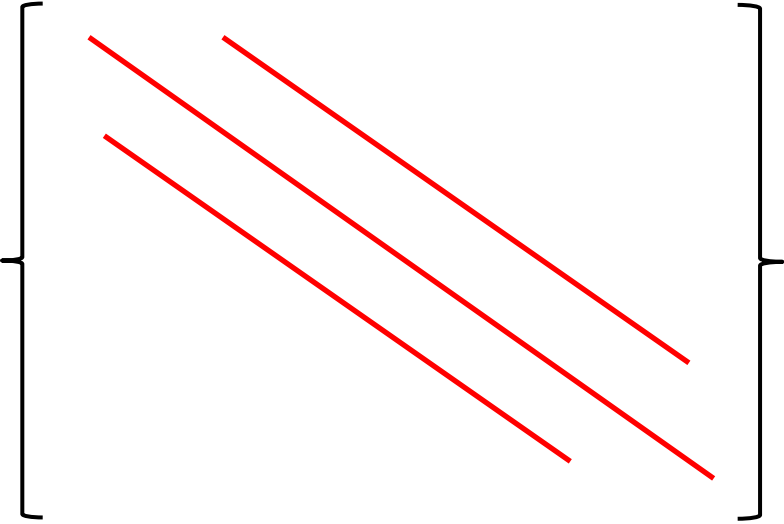
$$\sum \alpha_{i \pm k, j \pm l} P_{k,l} = \delta_{i,j}$$
A diagram illustrating the structure of a tridiagonal matrix. It consists of a large square bracketed area containing three parallel red diagonal lines sloping downwards from left to right. The lines are positioned such that they represent the main diagonal and the diagonals immediately above and below it, characteristic of a tridiagonal matrix.

Figure 3-5: Illustration of the tridiagonal matrix formation. This matrix forms for a single line in the solution domain.

Thus, the TDMA algorithm is applied in a line by line manner rather than on a point by point basis. The solution to a single grid line is obtained at once using the Thomas algorithm. The system of equations for a single line is of the form $AY = B$ and is represented in Figure 3-5. The coefficient matrix is a sparse matrix with the only non-zero entries on the main diagonal and the line just above and below it.

To represent the line by line application of the Thomas algorithm, the computational domain mesh needs to be visualized. A line means that the values for one of the indices is fixed and the system of equations is built by moving along the other index value. The algorithm can be applied along increasing or decreasing y-index values and is applied to each successive line along the Y-index. In the Figure 3-6, the action is

explained starting from a certain value of (i, j) index the system of equations is built for a complete line in lexicographic order.

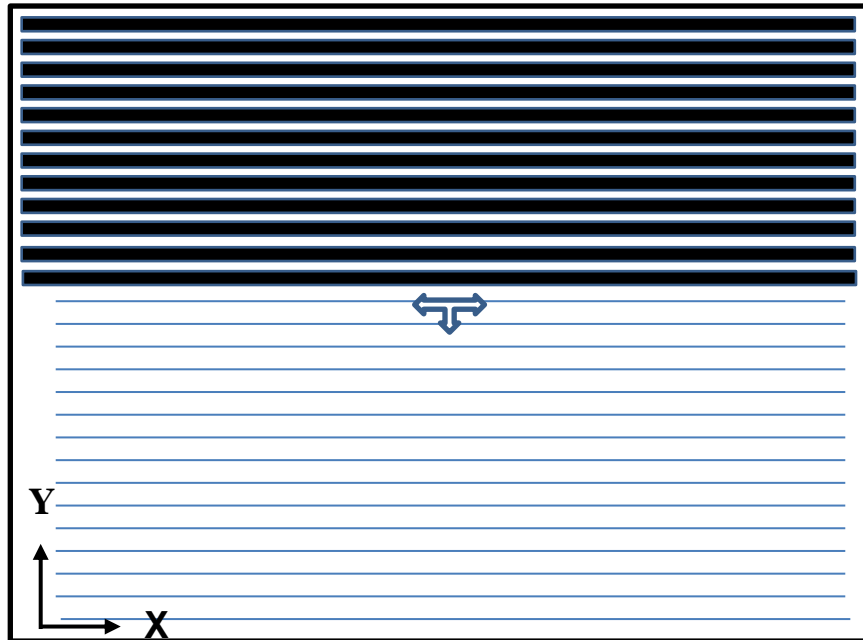


Figure 3-6: The line by line TDMA algorithm explained. The numerical flow of information is shown by arrows. Note: the information flow direction can be along other directions as well but the line by line solution should be performed.

Thus, the line in the computational domain is then solved by using the TDMA algorithm and then the solution moves to the next value of Y-index and another line is solved. This way the complete domain is scanned and a new pressure guess obtained. The pressure and film thickness values are updated as soon as the solution is obtained for a particular line. This ensures that more information is included into the solution procedure and the solution speed increases.

This technique of solving the system of equations gives a key advantage over the conventional Gauss-Seidel and Jacobi iterative solvers by giving greater coupling and

using more values from the current step. This can be appreciated by looking at the stencil of calculations formed by each as shown in Figure 3-7.

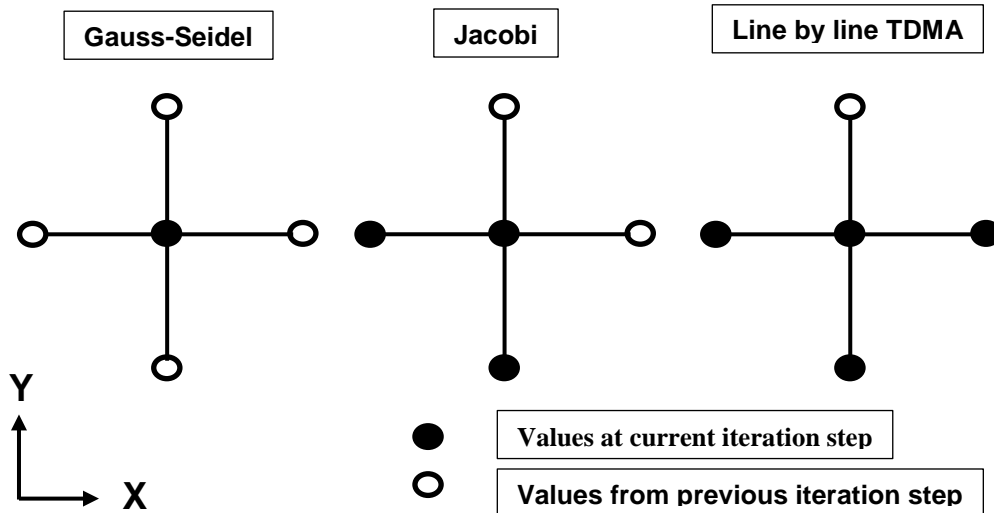


Figure 3-7: The superior performance achieved by the line by line TDMA algorithm explained for solution on a single node. For comparison, the nodal Gauss-Seidel and Jacobi stencils are also given.

3.7.1 Implementation of the unified solution algorithm

The details of implementing the unified solution algorithm are seldom found in the literature. Thus, in this section the details are presented for the way the solution scheme was implemented in this study.

The idea is simple and so is the implementation. The algorithm for the solution of the Reynolds equation stays the same. The implementation requires turning off the pressure flow terms when the film thickness hits zero. This is done by checking film thickness at every node. If the film thickness is zero or very close to zero (molecular dimensions), the coefficients of the Reynolds equation are put to zero and the film thickness also becomes zero. With minimal modifications, the direct iterative approach is very easily extended to mixed lubrication cases. This improves the

convergence and stability of the direct approach as whenever film thickness becomes less than a critical value the numerical overflow caused by the very small values of Reynolds coefficients is avoided by intentionally putting them equal to zero. Mathematically, if $H(I,J) < \epsilon$ where ϵ is comparable to molecular dimensions $\xi_{ij} = 0$ for the particular indices i, j .

3.7.2 Implementation of boundary conditions

The discussion about the TDMA algorithm is incomplete without the discussion of boundary conditions. The application of boundary conditions is crucial to get correct results. There are two boundary conditions to be applied. The zero pressure at the edges of the domain ($P(X, 0) = P(0, Y) = P(X, N) = P(N, Y) = 0$) and the general cavitation boundary condition ($P(X, Y) \geq 0$). The cavitation boundary condition is applied by enforcing the pressures to be always greater than zero. The implementation of zero pressure at the edges is slightly tricky. It is achieved by enforcing the first entry of the lower diagonal elements A_{ij} and the last entry of the upper diagonal elements C_{ij} to be zero for every single grid line in the computational domain. In this way the zero pressure boundary condition at the edges diffuses into the system along successive Y-indexed values. For one particular line, representing a system of equations, the application of boundary conditions is illustrated in Figure 3-8.

The application of boundary conditions in this way ensures that the zero pressure is applied to the boundaries and this pressure diffuses in towards the contact. Thus, the cavitation boundary forms automatically and is an indication of converged solutions.

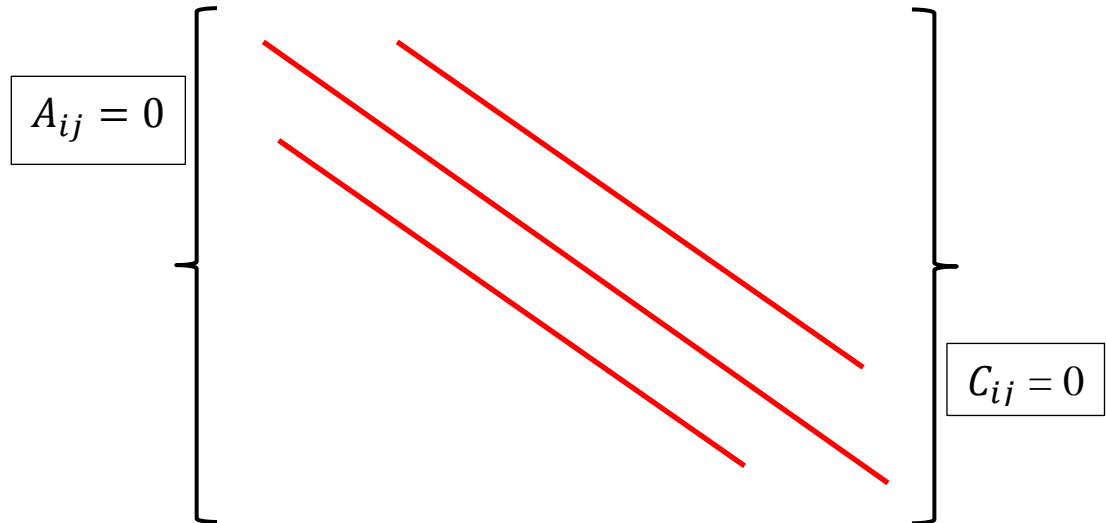


Figure 3-8: The application of boundary conditions for the TDMA algorithm. The boundary condition of zero pressure diffuses inwards to define the cavitation boundary.

3.7.3 Relaxation scheme and convergence criteria

The relaxation scheme used to update the pressure guess in each iteration is specified in this section. The relaxation scheme ensures smooth convergence of the solution from the initial guess to the final result and dictates the proportion of the updated value to be taken from the current iteration step and the previous iteration step. The relaxation scheme used is:

$$P_{new}' = P_{old} + f (P_{new} - P_{old})$$

In this equation, P_{new} is the pressure guess from the current iteration step while P_{new}' is the updated pressure after the current iteration. The pressure, P_{old} is taken from the previous iteration. The factor, f is called the relaxation factor and its value in the current study is kept between 0.02 and 0.2.

The updated pressures, P_{new}' are compared against the values from the previous iteration, P_{old} to calculate the pressure difference and the normalized value of this pressure difference is used as a convergence criterion.

$$Erp = \frac{\sum (P_{new}' - P_{old})}{\sum P_{old}}$$

The convergence of the pressure guess is fixed at $Erp \leq 1. \times 10^{-6}$ for all the results presented in chapter 3 and chapter 4. While performing the tribofilm growth calculations in the later chapters (chapter 5, 6 and 7) the pressure convergence is relaxed a bit to $Erp \leq 1. \times 10^{-4}$ and sometimes when the changes along iterations become smaller after the running in period, the convergence criteria is further relaxed to $Erp \leq 5. \times 10^{-4}$. I am using these values throughout the thesis unless otherwise stated.

The convergence of the load balance condition is also important as this condition ensures that the obtained solutions are the true pressure guess that balances the applied load. Due to the fact that the load balance condition is used to update the undeformed gap H_o in the film thickness equation, the error or the convergence criteria for the load balance condition is determined as,

$$Erh = \frac{H_o^{new} - H_o^{old}}{H_o^{old}}$$

In this equation, the “new” value of H_o is obtained at the current step within the pressure calculation iteration while the “old” value of H_o refers to the value obtained when the load balance loop was called the previous time during the same pressure calculation iteration / loop. In the current thesis, the error in the load balance criterion is set at $1. \times 10^{-5} \leq Erh \leq 1. \times 10^{-6}$ unless otherwise stated.

3.8 Deformation convolution using Fast Fourier Transforms (FFTs)

The deformation in contact mechanics is calculated with the Boussinesq formulation [151]. The nodal pressure is approximated with an interpolation function within small elements of the half space and a flexibility matrix is constructed. The flexibility matrix is also called deformation coefficient matrix / influence coefficient matrix etc. Finally, a linear combination of nodal pressures at every node gives the deformation at the node. This is mathematically written as

$$V(X_i, Y_j) = \sum_{k=1}^{M-1} K(X_i - X_k, Y_j - Y_l) * P(X_k, Y_l) \quad (3-31)$$

This equation is in fact a 2-D linear convolution. This equation cannot be used as such to calculate deformation using the FFTs because the application of FFTs requires that the convolution theorem is satisfied. This theorem is satisfied for cyclic convolutions but not for the linear convolutions of this type. Thus the equation (3-31) has to be converted to a cyclic convolution form to apply the powerful technique of FFTs. This fact was explained by Liu et al [152] although the idea of using FFTs to calculate the deformation convolution was first introduced by Ju and Farris [153]. Liu et al. suggested that the flexibility matrix and pressure are *pre-treated* so that the above equation could resemble a cyclic convolution.

Linear convolutions occur quite often in tribology e.q. in temperature rise calculations and stress calculation. The linear expressions as such require N^2 multiplication operations for an N numbered series if direct multiplication method is used [152]. This poses severe limitations to the use of refined grids and the process is computationally very expensive. Brandt and Lubrecht introduced and applied the multilevel multi-integration methods to significantly improve the computational efficiency of

deformation calculation [154]. Ju and Farris [153] realized that the FFTs could reduce the computation significantly but they observed that large errors occurred near the border of the solution domain which could be avoided by having a large ratio of five to eight between the computational and physical domain of the problem [155]. Liu et al performed a detailed study of these errors and presented a robust approach to apply FFTs without sacrificing the solution accuracy [152].

The pre-treatment involves doubling the computational domain for both pressure and flexibility matrix. For a point contact with $N \times N$ nodes, this means extending the domain to $2N \times 2N$. The extended pressure matrix contains the original pressure matrix for the corresponding indexed values and for the rest of the terms in the $2N \times 2N$ matrix, the domain is zero padded. For the flexibility matrix, the process is a more complex. The extended flexibility matrix is filled first with values of the corresponding indices in the first quadrant. Then for all $i = N, \forall j$ and $j = N, \forall i$ the corresponding entries are zero and this is referred to as zero padding. Then for the remaining entries in the second, third and fourth quadrants, the corresponding values of the original flexibility matrix are input in reverse order as shown in Figure 3-9.

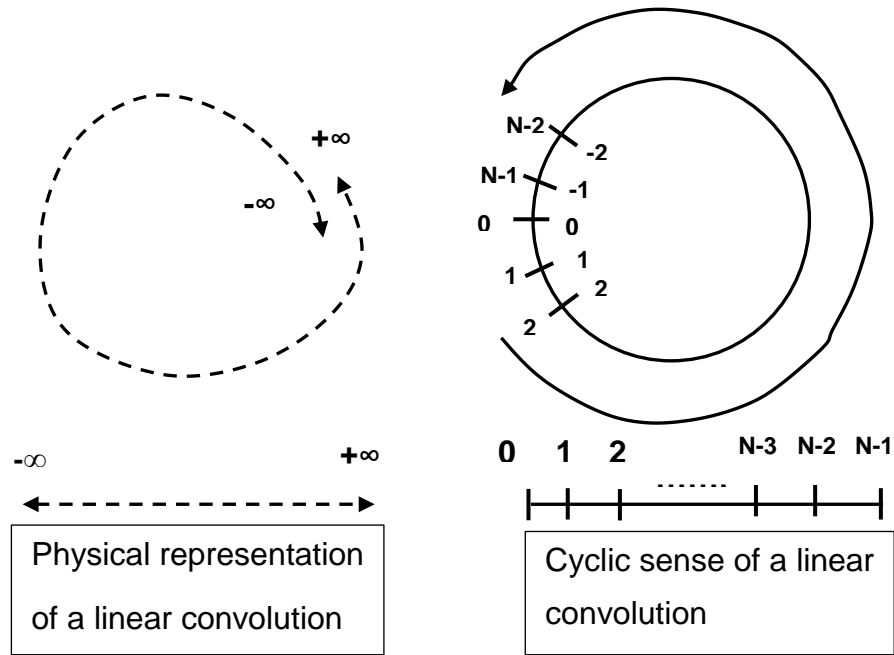


Figure 3-9: Modifications required to change the linear convolution to the cyclic convolution. These modifications are necessary for applying the FFT procedure to solve convolution.

The procedure has been simplified by Liu et al. [152] in the following steps:

1. Determine the influence coefficient matrix $\{K_{ij}\}_{N \times N}$
2. Expand the matrix $\{K_{ij}\}_{N \times N}$ to $\{K_{ij}\}_{2N \times 2N}$
 - $\{K_{ij}\}_{2N \times 2N} = \{K_{ij}\}_{N \times N} \forall [0, N - 1: 0, N - 1]$
 - $\{K_{ij}\}_{2N \times 2N} = 0 \forall [N, 2N - 1: N, 2N - 1]$ (zero padding)
 - $\{K_{ij}\}_{2N \times 2N} = \{K_{ij}\}_{2N - i * j} \forall [i \in N + 1, 2N - 1]$ (wrap around)
 - $\{K_{ij}\}_{2N \times 2N} = \{K_{ij}\}_{i * 2N - j} \forall [j \in N + 1, 2N - 1]$ (wrap around)
3. Apply FFT to $\{K_{ij}\}_{2N \times 2N}$ to get $\{\widehat{K}_{ij_s}\}_{2N \times 2N}$ in Fourier space
4. Expand the pressure array $\{P_{ij}\}_{N \times N}$ to $\{P_{ij}\}_{2N \times 2N}$. Apply zero padding to all additional terms

- $\{P_{ij}\}_{2N*2N} = P_{ij} \forall [0, N - 1: 0, N - 1]$
 - $\{P_{ij}\}_{2N*2N} = 0 \forall [N, 2N - 1: N, 2N - 1]$
5. Apply FFT to $\{P_{ij}\}_{2N*2N}$ to get $\{\widehat{P}_{ij_s}\}_{2N*2N}$ in Fourier space
 6. Multiply the two series term by term in the Fourier space to obtain a temporary series
 - $\{\widehat{V}_{ij_s}\}_{2N*2N} = \{\widehat{K}_{ij_s}\}_{2N*2N} * \{\widehat{P}_{ij_s}\}_{2N*2N}$
 7. Apply Inverse FFT to this temporary series to obtain the extended series in real space
 - $\{V_{ij}\}_{2N*2N} = IFFT(\{\widehat{V}_{ij_s}\}_{2N*2N})$
 8. Discard the extended terms (all except the corresponding values to get the actual deflection
 - $\{u_{ij}\}_{N*N} = \{V_{ij}\}_{2N*2N} \forall (0, N: 0, N)$

The influence coefficient produced by this implementation in this study is presented in Figure 3-10 along with the modified, pre-treated coefficient matrix.

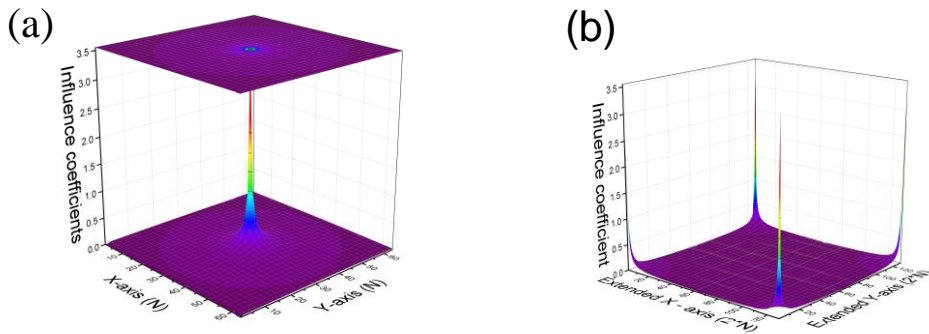


Figure 3-10: The influence matrix plotted over the entire domain. (a) shows the original influence matrix (b) shows the influence matrix after pre-treatment, modified to account for cyclic convolution as explained.

3.9 Implementation of `fftw`¹ library in FORTRAN

FFTW is a free software tool under the GNU public license. It stands for “Fastest Fourier Transforms in the West”. This library was developed at MIT by Matteo Frigo and Steven G Johnson [156]. FFTW is a C library for computing discrete Fourier Transform (DFT). The FFTW library can compute DFT in single and multiple dimensions and for any input size and can handle real as well as complex input. The FFTW library has superior performance over other public FFT utilities as well as some commercial optimized applications. But the key advantage of using FFTW library is that it gives high *portability*.

The FFTs can be computed by either adding a small subroutine into the FORTRAN program as given in Numerical Recipes in FORTRAN [157, 158] or by using the highly optimized FFTW library.

FFTW is a C library. It has different ways to interface to either FORTRAN or C programming languages. For FORTRAN programming the interface is different for the post-2003 FORTRAN standard and the pre-2003 FORTRAN standard. Only the pre-2003 interface will be explained as this was used in the current work. In the following paragraphs, the specific lines from the FORTRAN computer code developed in this study are given.

First of all the FFTW library is to be loaded as a module in ARC2² high performance computing (HPC) facility at Leeds. Once loaded the library can be used inside a FORTRAN program by using compiler flags

¹ www.fftw.org

² <http://arc.leeds.ac.uk/systems/arc2/>

```
ifort -o run.exe testworking_64.f90 -lfftw3
```

The last part in the above command “-lfftw3” is the compiler flag to specify the use of FFTW library. In addition to this there are some constants used by FFTW FORTRAN interface that need to be included into the main program before calling any FFTW functions. A file containing these constants can be found from the library homepage. This file is placed in the same folder where the program is being compiled and executed, and is included via the instruction:

```
Include fftw3.f90
```

All the FFTW functions have equivalent calling functions in FORTRAN. Extra care should be taken to ensure data type compatibility. The usage of FFTW library requires steps

- Allocating the input and output arrays
- Creating the plan
- Execution of plan: Computing the Discrete Fourier Transform (DFT)
- Destroy the plan (deallocation)

These steps are illustrated in Figure 3-11

STEP1: Allocating input and output arrays	
real (kind = 8) PFFT(nx,ny)	Pre-treated pressure array
real (kind = 8) AKTEMPin(nx,ny)	Pre-treated flexibility matrix
complex (kind = 8) out1(nh,ny)	Output array to hold transformed pressures
complex (kind = 8) out2(nh,ny)	Output array to hold transformed flexibility matrix
STEP2: Creation and execution of plan (execution: computing transforms)	
integer (kind = 8) plan_forward1	Declaration of plan
call (plan_forward1,nx,ny,AKTEMPin,out1,FFTW_ESTIMATE)	dfftw_plan_dft_r2c_2d_ Creation of plan
call dfftw_execute_ (plan_forward1)	Execution of plan
STEP3: Destroy plan	
integer (kind = 8) plan_forward1	Declaration of plan
call (plan_forward1,nx,ny,AKTEMPin,out1,FFTW_ESTIMATE)	dfftw_plan_dft_r2c_2d_ Creation of plan
call dfftw_execute_ (plan_forward1)	Execution of plan

Figure 3-11: The application of the fftw library to numerically solve the convolution of pressure and deformation matrix using FFTs. The actual lines from the Fortran code used are given.

FFTW allows computation of either in-place (real) FFTs or out-of-place (complex) FFTs. Both give the same end result. The application of in-place FFTs is complex and the actual input array is modified but this technique pays off in terms of lower memory requirement. This is important as the extended domain for cyclic representation of the linear combination increases memory requirements. The use of in-place FFTs can reduce further memory increase during transformation. In this study, in-place FFTs were implemented and all subsequent results were also obtained using in-place FFTs.

3.10 Validation of the Mixed lubrication model

3.10.1 Criteria

The model needs to be tested. The model should be able to reproduce the film thickness (minimum and central) for specific cases. The cases chosen are from the published studies. For comparison of steady state results, the model is tested against the work of Liu et al. [80] and for transient cases, the model is tested against the work of Pu et al. [149]. The ability of the numerical model to reproduce the central and minimum film thickness comparable to these simulation studies is considered as the criteria to confirm the quality and validity of the current approach.

It was reported by Morales-Espejel et al [159] that at ultra-low speeds, the EHL / ML models are prone to mesh dependence, see Figure 3-12. As the speed decreases, the film thickness predictions become more and more dependent upon the mesh density used. To understand this, let us visualize the inlet region (The same applies to the exit region as well).

It can be seen that the gradient of pressure at the inlet varies. At higher speeds, the pressure profile builds slowly over the correspondingly large inlet area while at lower speeds, the inlet region is small and a very large change in pressure takes place over this small region. Thus, coarser meshes will not be able to capture this.

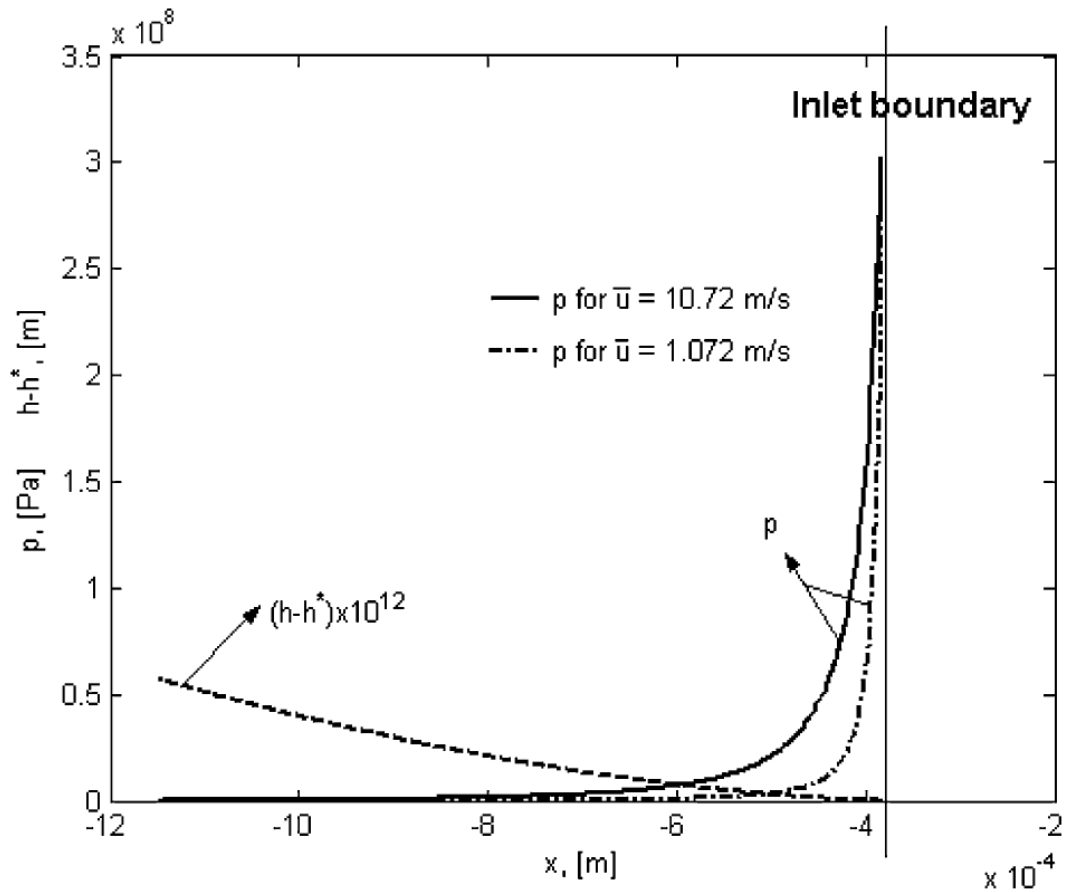


Figure 3-12: The discontinuities at the entrainment of contact leading to the grid dependence of the mixed lubrication / EHL solutions [159].

Therefore, the build-up of film thickness in the central region depends upon the entrainment action. To capture the inlet region either the mesh needs to be refined or higher order of integration methods used. For detailed analysis, see references [159, 160].

In the following paragraphs, the effect of mesh density on the film thickness in the ML / EHL model is presented. These results are for the separate first order backward differencing scheme for the Couette and Squeeze flow terms. The results are presented for three different speed groups: High speeds, intermediate speeds, low speeds.

This has been previously studied in detail by Liu et al [80]. The purpose of repeating these simulations is to first of all justify the mesh sizes that are going to be used in the current study and secondly to validate the results from the current method with the published work.

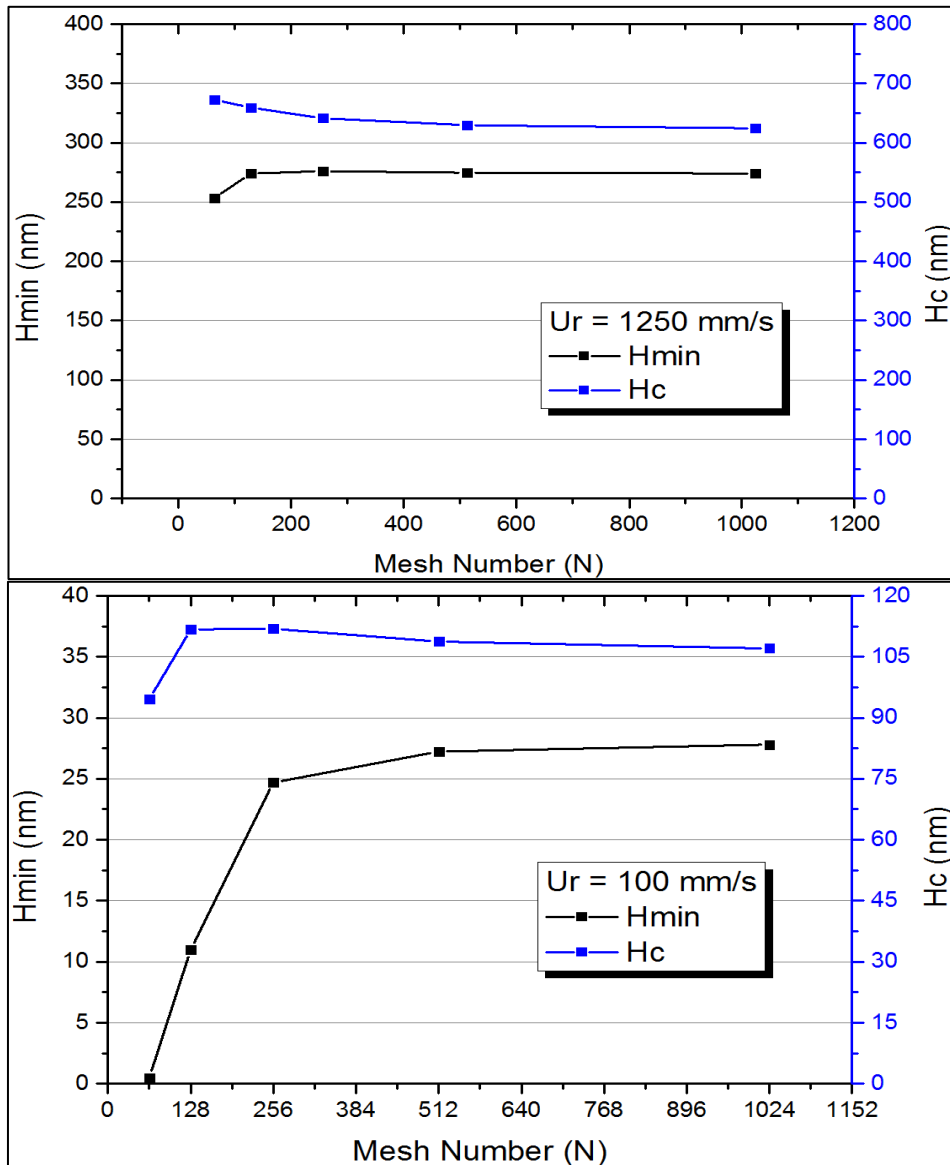


Figure 3-13: Grid justification for high to medium speed simulations in a mixed lubricated contact. The increase in film thickness with grid refinement is noticeable.

For higher speeds, as shown in Figure 3-13, the effect of mesh density on the minimum film thickness is rather small but the central film thickness is affected

considerably. There is an increase in the value of minimum film thickness initially while moving from a mesh of $N=64$ to $N=256$ but with further refinement in mesh density, the change is very small. For the speed of 1.25 m/s, the central film thickness value decreases from a large value to a limiting value of approximately 550 nm (which is the Hamrock and Dowson value for the same working conditions). The central film thickness, on the other hand, continues to vary with mesh refinement. When the speed is 312.5 mm/s, the central film thickness value increases first when changing N from 64 to 128 but with further mesh refinement it decreases asymptotically to the value of 240 nm (the Hamrock and Dowson value being approx. 220 nm). The same trend is also observed for the rolling speed of 100 mm/s. The central film thickness value increases first and then decreases asymptotically to a value of 108 nm (the Hamrock and Dowson value is 101 nm). For very high speed case (1250 mm/s) the central film thickness only decrease with increase in mesh density but for the other two speeds, 312.5 mm/s and 100 mm/s, the central film thickness increases first and then decrease. On the other hand, the minimum film thickness only increases for all speeds.

For the intermediate speed range (less than 100 mm/s) the effect of mesh density on the minimum film thickness is quite obvious and cannot be neglected. Two cases of speeds are shown in the Figure 3-14. The higher speed case, 30 mm/s shows that the central and minimum film thickness values approach an asymptotic value with the range of mesh sizes used. For the speed of 10 mm/s, the mesh dependence of the minimum film thickness is obvious even for the finest mesh used. This indicates increased sensitivity of the results upon mesh size.

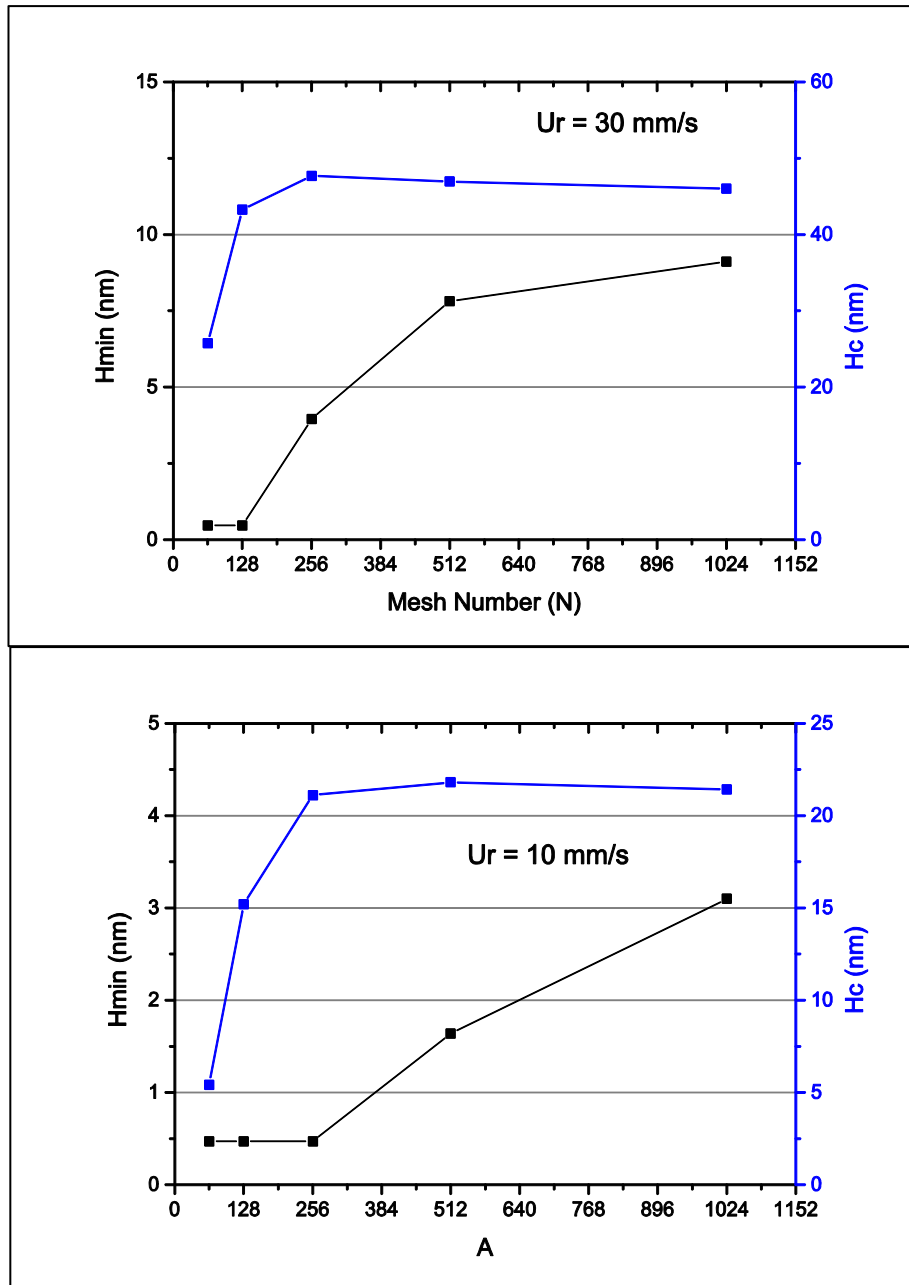


Figure 3-14: Grid justification for medium speed simulations in a mixed lubricated contact. The dependence of film thickness results on the grid density is more pronounced.

The low speed cases all represent the characteristic mesh dependence of the finite differencing scheme. For 1 mm/s rolling speed, the minimum film thickness is 0.47 nm (in these computational experiments minimum film thickness for the application of unified solution algorithm was set to 0.47 nm) no matter what mesh density is used

while the central / average film thickness is a function of mesh density and reaches an asymptotic value as the mesh is refined. The same trend is observed when the speed is 3 mm/s, the only difference being the very small value of film thickness developed towards the finest mesh of $N=1024$ as seen in Figure 3-15. It is to be noted that the minimum film thickness value stays zero for almost all the rest of the cases for both the ultra-low speeds.

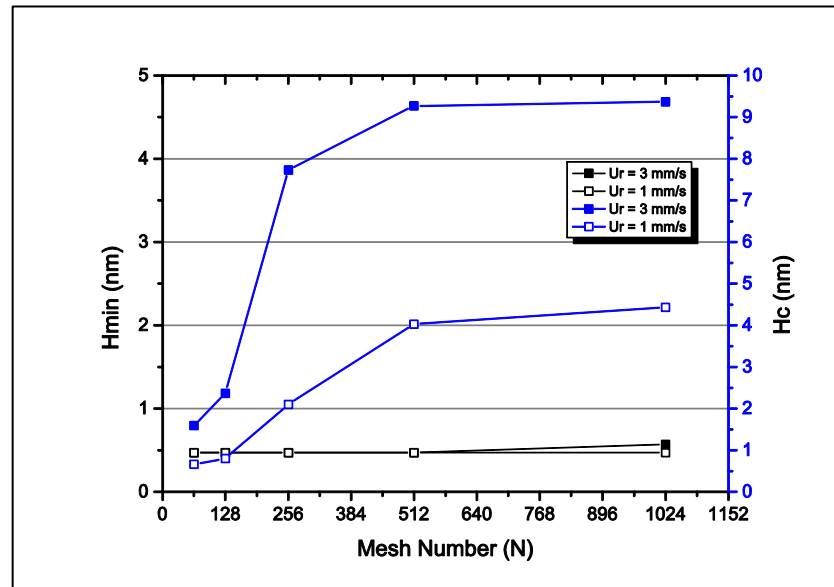


Figure 3-15: Grid justification for ultra-low speed simulations in a mixed lubricated contact. The choice of grid density strongly affects the results at such low speeds.

Next a comparison is made between the mesh justification results from the current study with the results presented by Liu et al [80]. They have presented calculations for varying mesh density for different speeds using seven different discretization schemes for the Couette and squeeze terms. We use the first order backward scheme that is consistent with scheme-1 in their results. A comparison is presented in the Figure 3-16 and Figure 3-17 . The correlation is very good for all speeds. But there are quantitative differences in values at higher speeds with our methodology producing slightly larger values of central film thickness. This may be because of

transient calculations performed in this study while it was not mentioned in the work of Hu and Zhu [76] if the calculations were transient or steady.

To further demonstrate the validity of the model, a series of simulations have been performed to compare the predictions of the model against the existing literature [75]. The working conditions, computational domain and the mesh density are kept the same and simulations are run by varying the speed from very high values of 15000 mm/s down to very low values of 0.001 mm/s. This large range of speeds is used for two reasons. First of all to simulate the transition from pure EHL through mixed down to boundary lubrication and secondly to check the robustness and stability of the present technique. The simulations were performed for a smooth surface contact. The part (a) in Figure 3-16 is compared against part (a) in Figure 3-17, and similarly Figure 3-16 (b) is compared against Figure 3-17 (b). The comparison is made against the work of Zhu and Hu [75, 76]. The agreement is excellent not only qualitatively but quantitatively as well.

These simulations were performed by using the transient mode calculations. The system was allowed to move to steady state by taking up values of the initial guess from the previous step. Thus, the plots are showing the results of pressure profile and film thickness that are obtained after a certain number of steps required for the system to settle down. Another important point to be noted is that these calculations correspond to static surfaces i.e. the surfaces of ball and disc are not moved due to their speeds. This simplification was introduced earlier in this chapter and is explained in Figure 3-1.

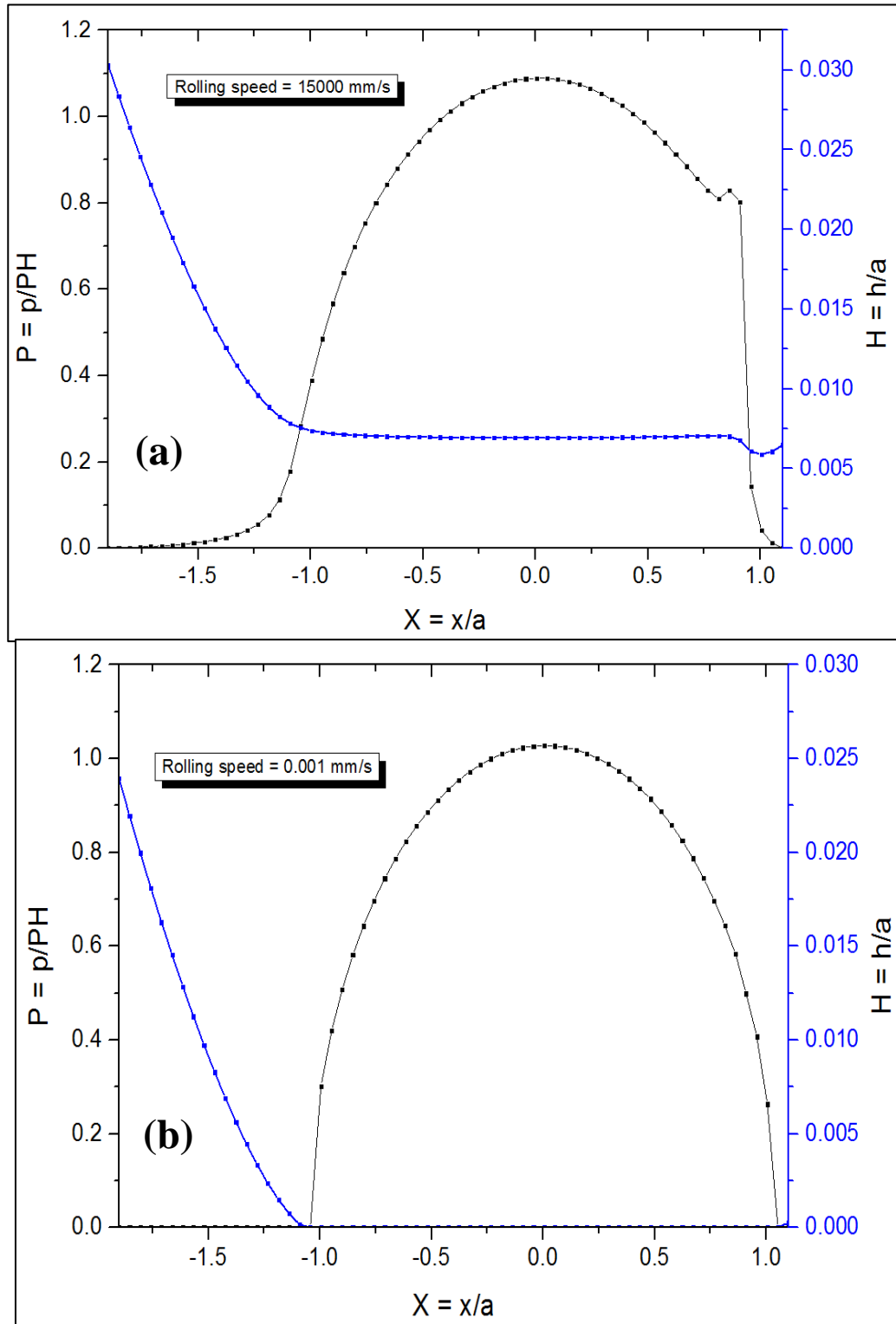


Figure 3-16: The pressure and film thickness profiles at the middle cross-section of contact from current study. (a) speed 15000 mm/s (b) speed 0.001 mm/s. Current study.

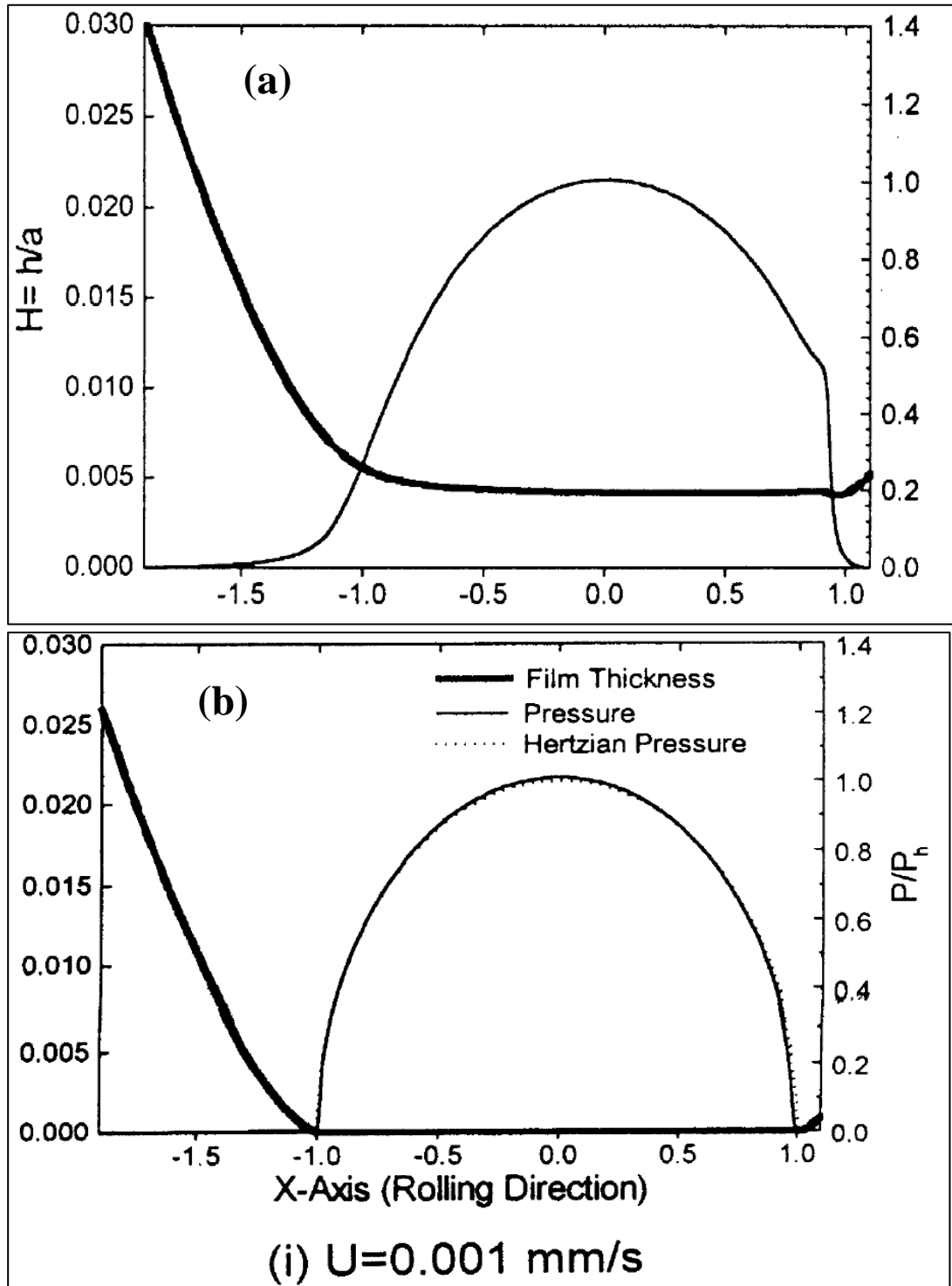


Figure 3-17: The pressure and film thickness profiles at the middle cross-section of contact. (a) speed 15000 mm/s (b) speed 0.001 mm/s. These plots are from ref. [76].

Next, results are presented for the complete range of speeds to see the transition of film thickness values from the full film to zero film thickness. The contact area ratio

as a function of speed is also presented. The results give a clear indication of the ability and robustness of the model to predict the transition of lubrication states from full film down to boundary lubrication.

These simulations correspond to smooth surfaces. The solution domain is defined as $-1.9 \leq X \leq 1.1$ and $-1.5 \leq Y \leq 1.5$. This domain is divided by a uniform grid of 129×129 nodes. Thus, the non-dimensional grid size is $\Delta X = \Delta Y = 0.023$. The non-dimensional time step is chosen to be half of the spatial time step $\Delta T = \frac{\Delta X}{2} = 0.0117$. The operating conditions are kept the same as those taken by Zhu and Hu [76]. A load of $W = 800 \text{ N}$ is applied and the combined material elastic modulus is $E' = 219.78 \text{ GPa}$. A value of $\eta_o = 0.096 \text{ Pa}\cdot\text{s}$ is used for the ambient viscosity and the pressure viscosity coefficient is fixed at $\alpha = 18.2 \text{ GPa}^{-1}$. The equivalent radius is $R_x = 19.05 \text{ mm}$ is used. The resulting Hertzian pressure is 1.711 GPa and the half width of Hertzian contact is $\approx 470 \mu\text{m}$. The entrainment speed, U_r is changed from a very large value of 5000 mm/s to 0.001 mm/s .

The entrainment speed is changed throughout the simulation to simulate the transition of lubrication from full film down to boundary lubrication. The simulation starts with the highest speed of 5000 mm/s and the solution is allowed to reach a steady state. Then the speed is reduced to a lower value and the simulation is again allowed to reach a steady state. Thus, the speed is reduced in steps and then the system is allowed to stabilize and the results are written and plotted.

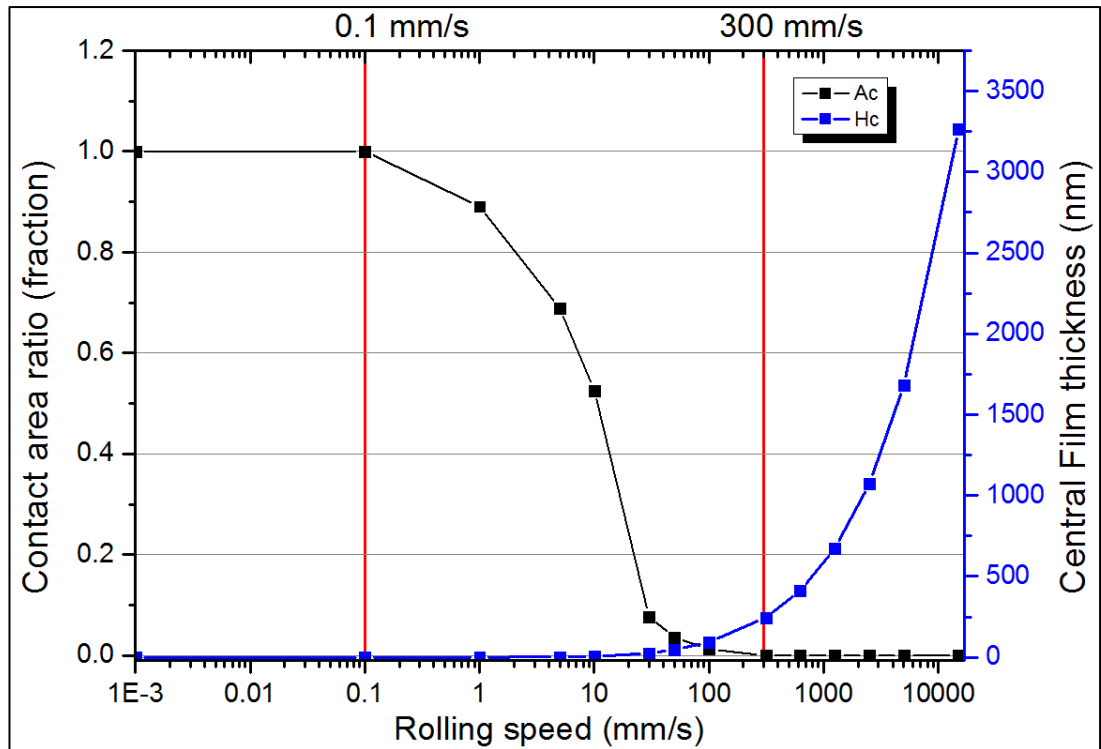


Figure 3-18: The mixed lubrication parameters contact area ratio (normalized) and the central film thickness plotted against the rolling speed. The entire transition of lubrication from full film down to boundary lubrication can be seen. The speeds corresponding to transition from full film to mixed and from mixed to boundary have been marked by the vertical lines.

The results presented in Figure 3-18 show that the central film thickness value reduces significantly coming down from 5000 mm/s to about 300 mm/s while the contact area ratio is zero. As soon as the speed approaches 300 mm/s, the solid contact starts to occur and the lubrication regime transits from full film EHL to mixed lubrication state. This has been clearly indicated in the graph with a red line for clarity. With further reduction in speed, the decrease in central film thickness reduces further and the contact area ratio starts to increase. The increase in contact area ratio is slow in the beginning but it increases abruptly below ≈ 50 mm/s reaching full 100 % solid contact state at 0.1 mm/s. The second red line at 0.1 mm/s indicates the transition from mixed lubrication regime to full boundary lubrication state where the complete contact

area is solid contact area. It is important to note that the model developed in this study gives smooth transition from the full film to boundary lubrication state as shown in Figure 3-18.

3.11 Summary

A computer program was written in Fortran 90 programming language from scratch to implement the mixed lubrication model. The numerical grid was justified for different speeds to address the key issue of grid dependence of numerical solutions of EHL results. The model was validated against published results, and successfully produces results through the complete range of speeds tested and the lubrication transition studies can be performed. The model successfully predicts the transition from full film down to complete boundary lubrication.

The equation system applicable to the mixed lubrication problem is the same as the EHL problem. But solving the system of equations to handle mixed fluid and solid contact spots requires the design of a robust solver. The Reynolds solver based upon traditional approaches like Gauss-Siedel and Jacobi are not applicable to high pressure, especially when actual asperity-asperity contact starts to occur. The coefficient matrix is constructed based upon the conventional approaches and it was suggested that the if the coefficient matrix is based solely upon the pressure flow terms the diagonal dominance is lost and the convergence halts. To overcome this, the semi-system approach is selected, which requires the coefficient matrix to include terms from the entrainment flow terms of the Reynolds equation as well. Thus, when the pressure flow terms become too small, the entrainment flow terms become dominant and keep the dominance of the diagonal terms in the coefficient matrix.

The pressure flow terms (2-D) are dominant at low pressures while the entrainment flow terms (1-D) are dominant at higher pressures. This results in changing the nature

of the problem from a purely differential to purely integral. The situation becomes more complex for rough surfaces. To address this issue, the unified solution algorithm is introduced, which enables the solution of the complete mixed lubrication problem by solving the solid and fluid contact pressures simultaneously by only solving the Reynolds equation. Thus, the developed model is suitable for performing lubrication transition studies and it was shown that the contact parameters can be readily identified for the transition from EHL to mixed and mixed to boundary lubrication.

Inspiration was taken from the CFD literature and a TDMA solver was designed to solve the Reynolds equation. This solver is a simplified form of the Gauss elimination applied to the sparse matrices, especially the tridiagonal matrices as the name suggests. This method requires very low memory compared to the direct solvers as the matrix can be stored as three vectors which are solved by the Thomas algorithm to get the pressures. The TDMA algorithm has been implemented in almost all numerical libraries like NAG³, BLAS⁴ and LAPACK⁵ and highly efficient implementations are readily available which can be scaled on parallel platforms as well.

At high pressures or low velocities, the pressure flow terms lose their dominance and thus the flow equation (Reynolds equation) loses its coupling in the y-direction. This is also one of the key reasons for the slow convergence of the mixed lubrication / EHL solvers. This issue was addressed by devising and implementing the TDMA solver in a line by line fashion. The discretized Reynolds equation is written in a sparse matrix

³ www.nag.co.uk

⁴ <http://www.netlib.org/blas/>

⁵ <http://www.netlib.org/lapack/>

form and the equation system is solved for each line in the numerical domain separately. These lines are coupled by the information that is transferred from one to the other during a single iteration. Thus, making solution quicker and convergence faster.

The EHL / mixed lubrication solvers require the calculation of deformation which is integral. Thus, it requires the convolution of the influence coefficient and pressure as the influence of pressure at each point is to be taken on all other points inside the numerical grid. This requires N^2 multiplication operations and as a result bottlenecks the solution procedure as it requires huge times for performing these convolutions in real space. Moreover, the problem scales as N^2 . Therefore the solution of EHL / mixed lubrication problems that require many iterations or where finer meshes (more grid points) are required cannot be accessed. But performing these convolutions in the frequency domain, using FFT (fast Fourier transforms), scales as $N \log(N)$ and requires comparatively less computational effort. The influence coefficient matrix and the pressure matrix are transferred to the frequency domain after pre-treatment and the multiplication is performed. Once the multiplication procedure is complete, the deformation is extracted from the frequency domain to the real domain. Although the pre-treatment increases the size of the matrices and more computer memory is required to store these matrices, the number of multiplication and addition operation operations are reduced significantly. The FFT method shows its true strength when accessing finer meshes.

The traditional method for applying the FFT method is to use a bespoke published code [158]. The current study uses the FFTW⁶ libraries to solve the convolution of the

⁶ www.fftw.org

influence coefficient and the pressure. These libraries are freely available and are highly optimized and portable, though the use of the FFTW tool required interfacing with the Fortran programming language. The linear convolution was first converted into a cyclic convolution using the method of wrap around and zero padding. The cyclic convolution was then coded using the specific interface for Fortran programming to apply the FFTW libraries.

The result is a highly optimized mixed lubrication solver that can handle the entire lubrication transition and is able to identify the transition parameters is developed. Grid sizes varying from very coarse to very refined mesh sizes are accessible and the problems involving larger number of iterations or longer simulations can be solved. The solver is coded in Fortran and all key issues that reduce computational efficiency are addressed. Great effort is made in ensuring portability and versatility of the code and wherever possible, the standard libraries and methods are adopted to ensure maximum efficiency of implementation.

Chapter 4

Elastic-Perfectly plastic deformation modelling in lubrication

This chapter presents the development and implementation of the plastic deformation model within the mixed lubrication model developed in Chapter 3. It starts by presenting the algorithm from Sahlin et al [161] to simulate elastic-perfectly plastic deformation in contact analysis in section 4.1.1. Their method and algorithm is discussed and its limitations are highlighted as their algorithm is based upon the dry contact model so it needs modifications to be used in the unified mixed lubrication algorithm. Thus some modifications are suggested and the resulting algorithm is significantly modified. The modified algorithm is presented and discussed in section 4.1.2. Then some sample simulations are presented to show the robustness and applicability of the algorithm in section 4.3. Finally, the model is validated by comparing against the work of Ren et. al. [162] in section **Error! Reference source not found.** and the results show very good match for the values of film thickness and plastic deformation.

4.1 Model and Algorithm

An elastic-perfectly plastic contact algorithm is developed and implemented for a lubricated contact. The existing unified mixed lubrication algorithm is modified and improved by extending it to include plasticity. The published work for elasto-plastic contact analysis is mainly for the dry contact cases. Ren et. al. [162, 163] presented elasto-plastic contact analysis for a lubricated contact in a series of papers. In the first paper, they give results for lubricated contact without actual solid to solid contact (they call it plastoelastohydrodynamic lubrication, PEHL). In such a situation the

lubricant pressure is high enough to cause permanent change. In the second set of simulations they present results for situations where the contact is mixed with load being carried by the surface asperities as well.

The approach used in this study is based upon the work of Sahlin et al [161, 164]. They developed a scheme to simulate the elastic-perfectly plastic contact. Their scheme is very efficient. It provides convenient way to integrate plasticity into the existing lubrication models. The contact algorithm presented by the authors is based upon the flow factor technique and considers elastic-perfectly plastic condition only for the dry contact part of the problem. The dry contact problem is solved by the potential energy minimization technique by enforcing the complementarity condition to find the pressures and deformation. The implementation of this algorithm, in practice, to the lubricated contact is not straightforward and requires some modifications to the algorithm. The modifications are essential as the complementarity condition is no longer applicable to the lubricated contact solution algorithms. There are mainly two differences. First of all, the lubricant also generates pressure resulting in situations where there is no solid to solid contact and film thickness (gap) is still positive but the pressure has a value $P \geq 0$ (contrary to the complementarity condition). The second difference lies in the fact that the lubricant pressure can be high enough to cause plastic deformation of the contact.

4.1.1 Sahlin et al. s' Approach (existing)

Among the very few methods to deal with the lubrication problem at engineering scales, the method of Sahlin et al [161] is an important step forward. They designed an algorithm to solve the elastoplastic contact problem based upon the hardness of material. The model could take real three dimensional roughness as input. This method relies on defining the deformation of the micro geometry in a specific way

and relating it to the overall displacement of the body. Instead of relying on the actual gap between the mating surfaces, the relative gap is considered. This gap is similar to the film thickness defined in the previous chapters and in mixed lubricated contacts it may be zero ($gap \geq 0$). They define the gap / film thickness as consisting of a global and a local component. The roughness is defined at the local scale. The strength of the model lies in integrating the information between the local scale of roughness to the global geometrical features of the contact. The undeformed film thickness is defined by simply adding the global geometry and the local roughness. It is to be noted that the index y in the current section corresponds to the local scale of roughness values and is not the y -axis in the Cartesian coordinate system.

$$h(x, y) = h_o(x) + h_1(y) \quad (4-1)$$

Adding the deformation on the local scale to the above equation, the deformed film thickness equation is defined as

$$h(x, y) = h_o(x) + h_1(y) + u(y) \quad (4-2)$$

Now this total displacement, ($u(y)$) consists of an elastic part ($u_e(y)$) and a plastic part ($u_p(y)$). With this definition of gap / film thickness in mind, it can be visualized that the points of zero film thickness form a plane. This plane is called the “contact plane”. The rigid body displacement / movement defines this contact plane. This is because by definition, the contact plane is the plane that moves into a deformable counter body and due to this movement the surfaces will interfere. Sahlin et al. [161] define this distance as the rigid body interference and it is a constant that relates to the load carried by the surface. Their algorithm to solve the problem of elasto-plastic contact analysis is based upon identifying the nodes that undergo plastic deformation

and limiting the value of load carried by these nodes to the yielding pressure value. The pressures are then truncated and the truncated pressures are then used to calculate the deformation again. The contact plane is identified and the resulting plastic deformation at is calculated throughout the computational domain. This plastic deformation is then used to update the geometry by introducing permanent changes and the updated geometry then goes into the next iteration.

4.1.2 The new algorithm: developed in current study

The plasticity is a non-linear phenomenon and the calculation of the plastic deformation is rather a complex problem. But as outlined in the beginning of this chapter, the calculation of plastic deformation for engineering applications can be done by a simplified algorithm that considers elastic-perfectly plastic behaviour. This gives conservative estimates about the material failure and can be complimented by suitable selection of factors of safety.

The integration of the elastic-perfectly plastic deformation calculation algorithm into the unified mixed lubrication algorithm is not easy due to the presence of lubricant and the calculation of lubricant and solid contact pressures by the same Reynolds solver. The main difference is that in the work of Sahlin et al. [161] the algorithm is applied to a boundary lubrication contact mechanics solver while in the current study an EHL model is solved using the advanced techniques to get solutions for extreme conditions of mixed fluid and solid contacts. Thus, the nodes corresponding to the “no contact” are no longer present and the condition of complementarity is no longer present.

In the current study, an algorithm is developed to account for the presence of lubricant in calculating plastic deformation pressures. This new algorithm is inspired by the algorithm presented in the last section but fundamental differences exist. The

developed algorithm is outlined here and the flow chart can be seen in Figure 4-2. The terminology used in the flow chart is kept similar to the terminology used in the previous section but some differences exist and are explained where appropriate. The term $[(h_1 + u_e)_e]_{min}$ requires attention as this is the key term that differentiates our methodology. This is the minimum value of film thickness after subtracting the undeformed film thickness value from it. This value is chosen as it ensures that in successive iterations, the contact reaches a final equilibrium geometry where only elastic deformation is present. The parameter g_{00} as used in the previous section is analogous to the minimum value of rigid body interference in our algorithm.

The Reynolds solver was described in the last chapter. The solver is modified to include the elastic-perfectly plastic behaviour as follows:

- The load balance condition is applied by only considering the pressures below the elastic yield limit to carry all the load. The plastically deforming spots are assumed to float to the surface forming a plane that penetrates the surface.
- Do not truncate the pressures at this point.
- The rest of the algorithm for the mixed lubrication problem stays the same and pressure and film thickness convergence criteria apply as well in exactly the same way.

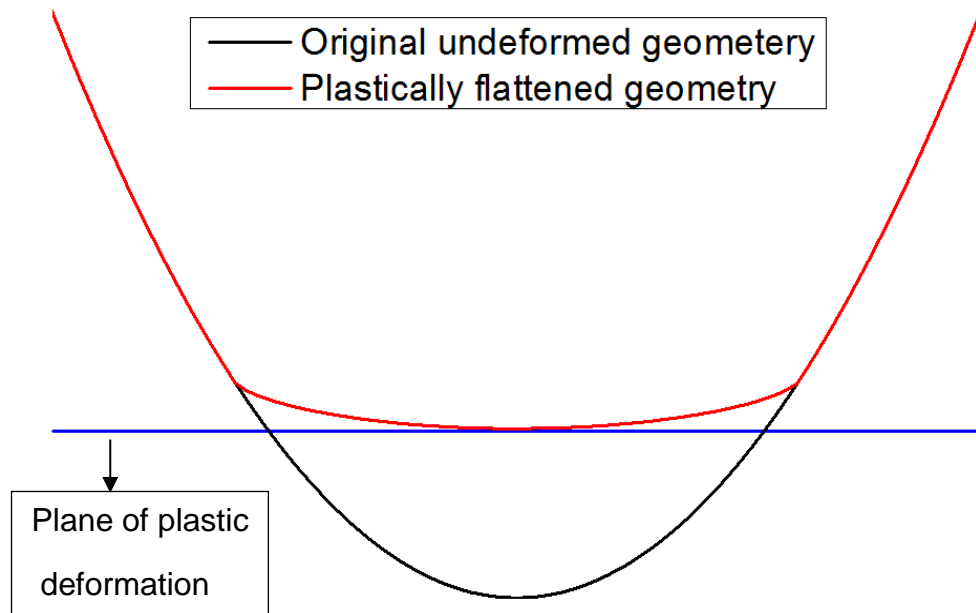


Figure 4-1: A schematic representation of the penetration of plane of plastically deforming points.

Once the converged pressure distribution has been achieved:

- The pressures are truncated to the yielding pressure values.
- Now the displacement is again calculated with this truncated pressure. This deformation contains both the elastic ($u_e(y)$) and the plastic ($u_p(y)$) component.
- The contact plane is calculated as shown in Figure 4-1 calculated. To calculate the contact plane, only the elastically displacing points are used to calculate the rigid body interference.
- The convergence of the contact plane is ensured. The criteria is not fixed and varies depending upon the applied load. For higher loads, this has to be relieved slightly.
- The elasto-plastic rigid body interference is evaluated and its minimum value is taken out.

- The plastic deformation ($u_p(y)$) is calculated by subtracting the rigid body interference from the maximum value of elastic displacement, only for the plastically deforming points.

The flow chart in Figure 4-2 gives the general procedure for the application of the elastic fully plastic behaviour into the lubrication models. The model is robust and no distinction is required as to whether the nodes are under elastic or plastic deformation or if the points are under fluid lubrication or solid contact condition. Thus giving an ideal opportunity to study the complete lubrication transition studies at all possible loads.

The steps in the algorithm have been labelled from 1 to 5 to highlight the key ideas necessary for the implementation of the model. The details of each step are provided below:

1. In this step the actual mixed lubrication problem is solved. The additional condition of limiting the load to plastic yielding values is applied by limiting the values of pressures in the load balance condition. This ensures that the nodes / points that have yielded float without carrying any further load.
2. Once the pressure and film thickness profiles have been obtained after applying step 1 above, the pressures are truncated and then the elastic deformation is calculated based upon these truncated pressures. This deformation is elastoplastic as it contains both the elastic and the plastic part.
3. In this step, the elastoplastic deformation is used to get the gap (film thickness in this work) and the contact plane formed by the plastically deforming points is obtained as well.

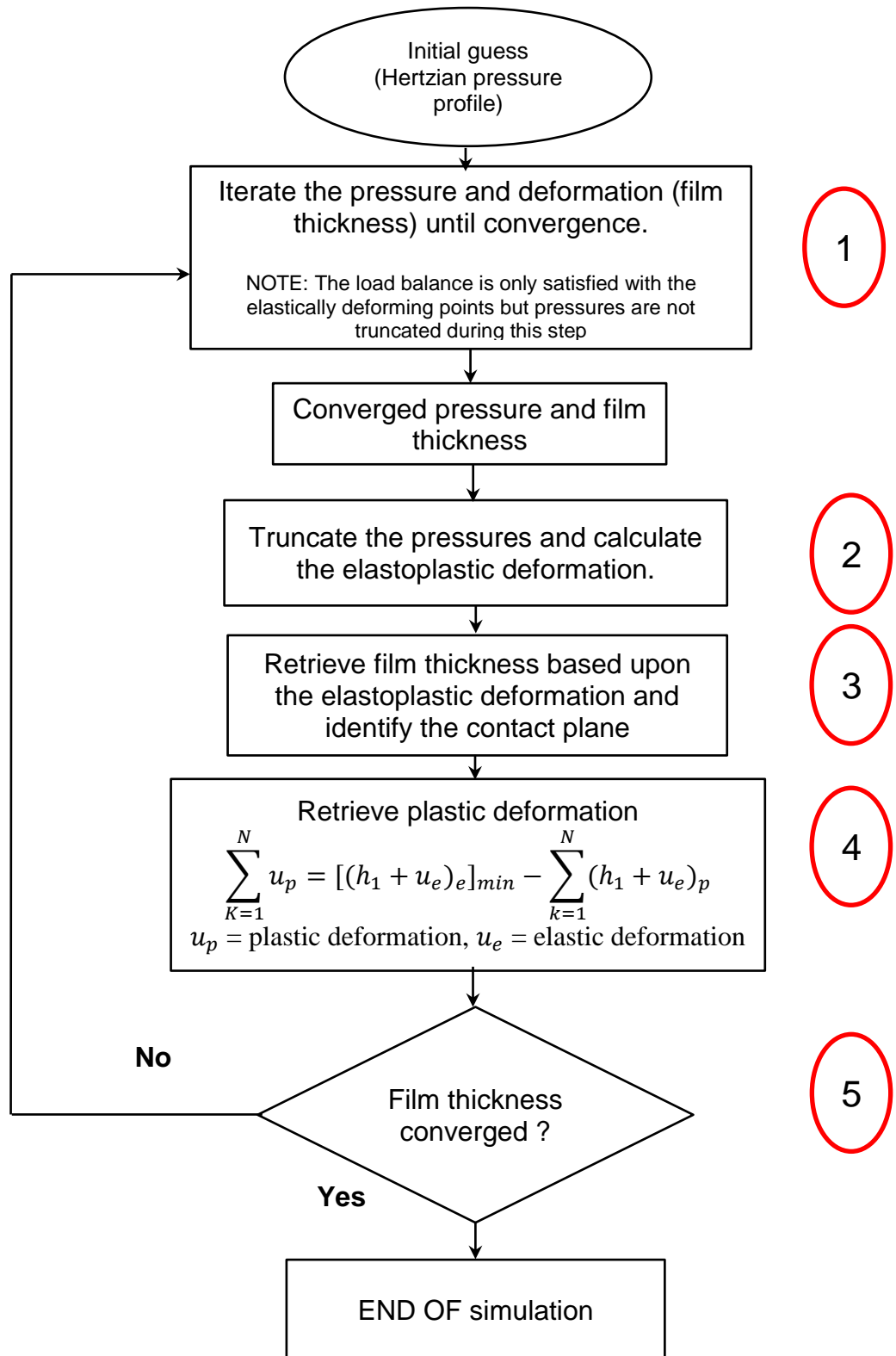


Figure 4-2: Flow chart and algorithm to extend the unified mixed lubrication solver to handle elastoplastic contacts as developed in the current study.

4. This step involves the extraction of the plastic deformation magnitude. This magnitude is the amount of material that is removed from the original geometry before the next iteration. In the equation, the subscript 'p' refers to the elastoplastic deformation calculated above.
5. In the end, the film thickness values are checked to ensure that all the plastically deformed material has been removed.

It was found that maximum of 5 iterations are sufficient to get completely converged plastically deformed geometry while in the first iteration, more than 90 % of the plastically deformed material is already identified. Whatever the case, when the evolution of the two contacting bodies is considered, the number of iterations to reach the final geometry do not matter as, based upon the way the algorithm is designed, the final geometry will always be the same.

4.2 Implementation Details

The strength of the model lies in the fact that plastic deformation can be evaluated from the model in the same way as elastic deformation with no harm to the computational efficiency and minimal algorithmic complexity. Although the computational time required to evaluate a single loading cycle is more compared to the simple elastic EHL case, the time to evaluate one convergence cycle stays pretty much same.

In terms of implementation, some modifications are required to the existing code. First of all nodes corresponding to elastic and plastic deformation are identified. Then the nodes that have undergone plastic deformation are considered to be freely floating. This means that once a particular node is identified as a plastically deforming node, it is assumed to carry no more load than the yielding pressure. The load has already

reached the yielding value at this node, so this point will keep deforming, along with other nodes that undergo yielding, forming a plane e.g. see part (a) in Figure 4-3. This distributes the load by increasing the contact area and more points come into contact. As our unified simulation strategy has no distinction between the fluid and solid contact regions, there is no need to distinguish between the fluid and solid contact spots. Thus the algorithm is very simple. The only change that needs to be made is that the nodes corresponding to the plastically deforming regions are considered not to be carrying any load by capping the pressure such that $P \leq 0$ as zero and $P \geq P_y$ as P_y . P_y is the pressure at which material starts to yield. The deformation in the film thickness equation is the sum of elastic and plastic deformation. The plastic deformation is taken out of this sum for the nodes corresponding to the plastically deforming region by subtracting the elastically deformed aperture from the rigid body interference.

4.3 Results

4.3.1 Smooth surface elastic-plastic contact

The contact between a smooth ball and flat is considered and the operating conditions applied, although unreal, are for the sake of verifying the robustness of the model. A stationary contact is assumed. The contact pressure, speed, equivalent radius and equivalent modulus are 1.45 GPa, 0.25 m/s, 9.525 mm and 439.5 GPa respectively. The plastic flow pressure is set to 0.807 GPa (far below the applied pressure) to ensure the lubricant can also cause plastic deformation of the contact. This yielding limit corresponds to the hardness of the material. In the top part of Figure 4-3, part (a), the convergence of the contact plane is presented. The initial contact is not a plane but the final deformed / plastically worn geometry forms a smooth plane. The lower part, part (b) represents the geometry of the contacting ball prior to and after the application of

plastic deformation. It is to be noted that the plastic deformation is not only caused by the solid-solid contact pressures. The lubricant pressure also deforms the surface and this deformation may be elastic or plastic.

4.3.2 Rough surface elasto-plastic contact

In the forthcoming paragraphs a glimpse of the ability of the above model to predict rough surface PlastoElastoHydrodynamic Lubrication (PEHL) is presented. The following results were taken by adding roughness to the ball and keeping the disc surface smooth and rigid. The results in Figure 4-4 show that the ball surface deforms significantly with deformation values reaching to about 100 nm at some points along the surface. The points of plastic deformation conform closely to the points of extreme pressure and these nodes deform permanently, changing the topography of the surface considerably due to flattening of corresponding asperities.

Roughness causes extreme pressure peaks that are far above the applied pressure so pressures do not need to be very high compared to the yield limit to deform the surface. Hence the operating pressure has been reduced in these simulations to a value of 0.645 GPa or 645 MPa. The R.M.S. roughness is fixed at 22 nm.

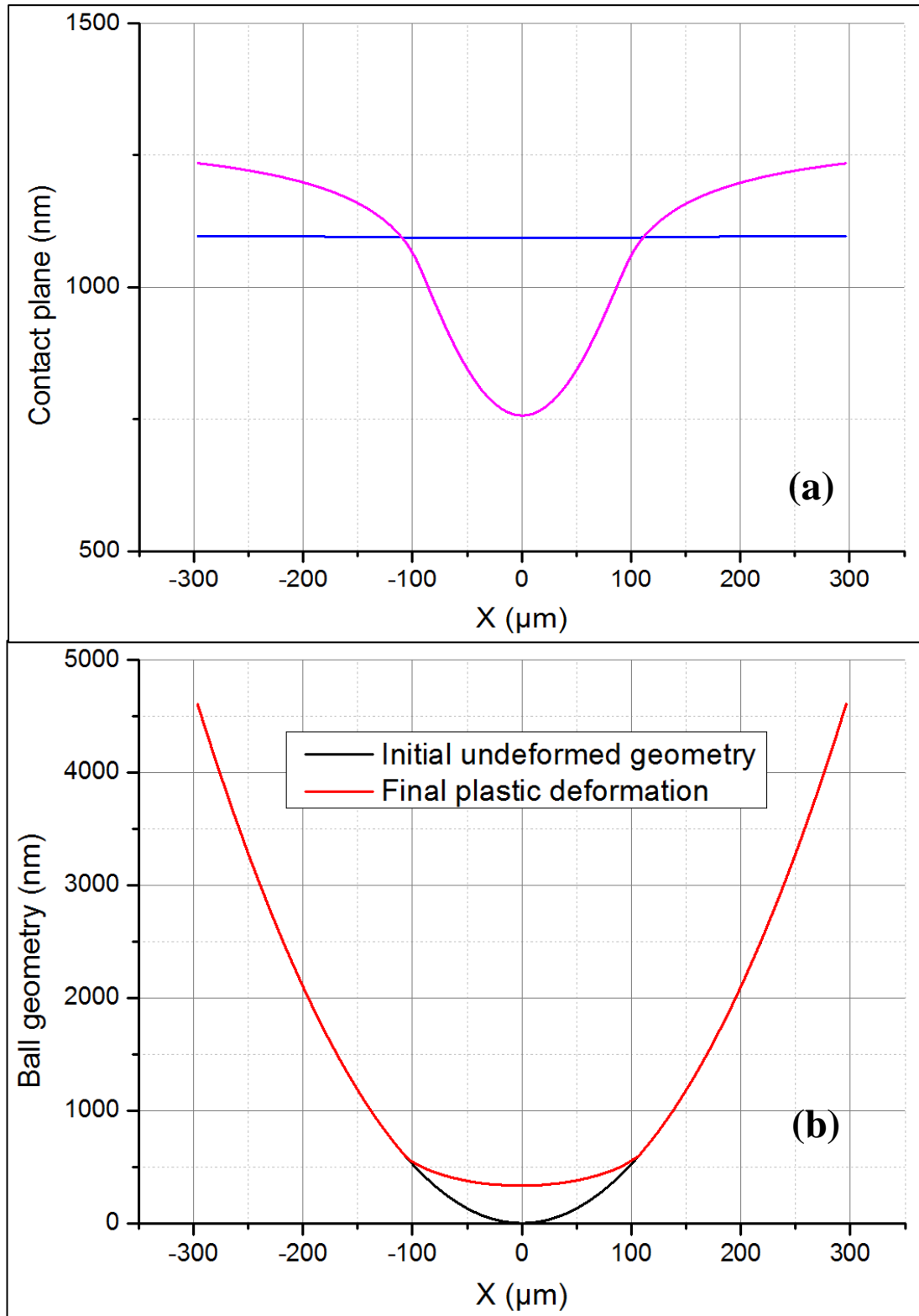


Figure 4-3: Smooth surface PEHL results. (a) The contact plane convergence. This plane converges by itself through the solution. (b) The undeformed and deformed geometry of the ball at the centre cross-section of the contact.

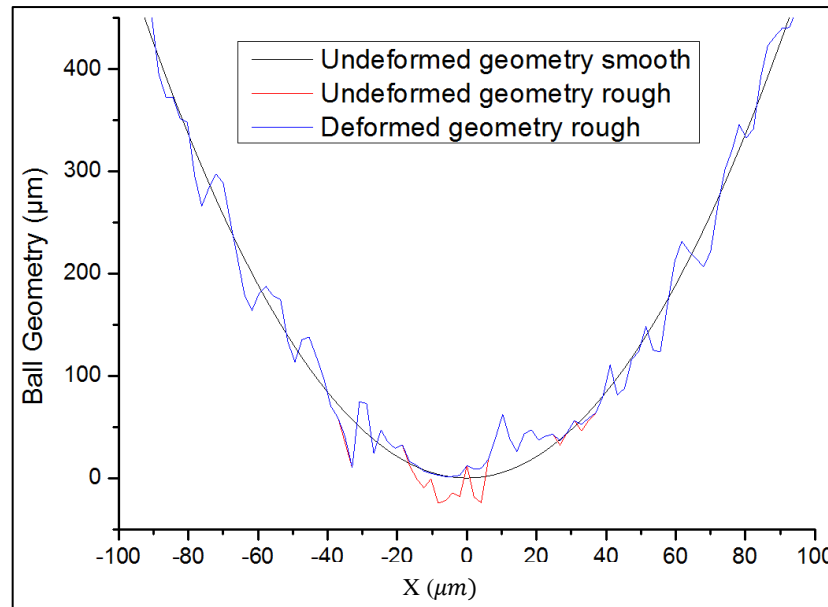


Figure 4-4: Rough surface PEHL results. The original smooth surface profile is also shown along with the undeformed rough surface and the corresponding deformed rough surface geometry.

The deformed geometry profile is one due to permanent deformation. It should be noted that the profile is flattened significantly at the points of peak pressure. This flattening also affects the pressure on the neighbouring points as shown in Figure 4-5. It is worth noticing that the pressure on the neighbouring points increases. This can be elaborated by examining the load-balance condition as applied to our case. The load is balanced by only the elastically deforming nodes and thus if some of the nodes undergo plastic deformation then the rest of the nodes will have to bear and balance more load.

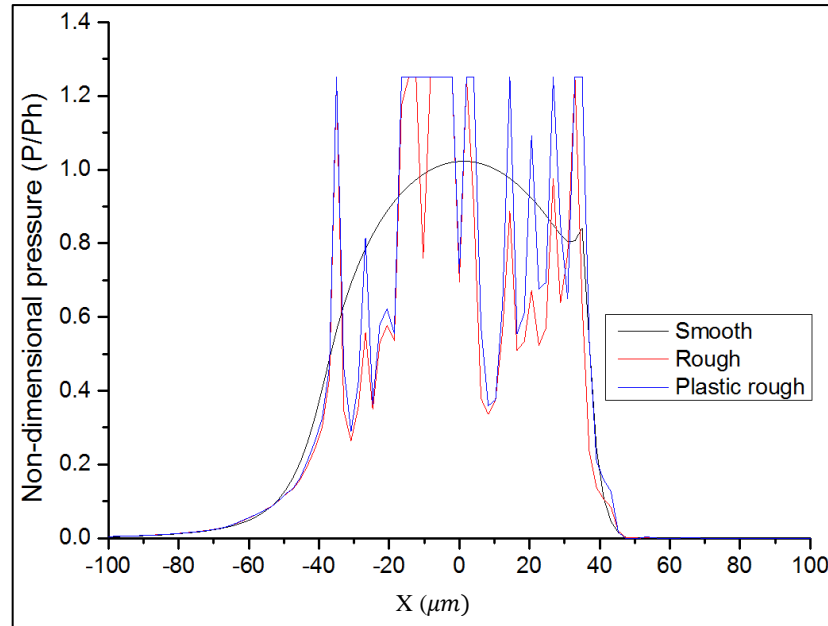


Figure 4-5: PEHL pressure profiles. The pressure profile for the original starting smooth surface solution is also given for comparison. The actual rough surface pressures without plastic deformation and with deformation show increase in area of contact. The starting pressure profile shows strong EHL by the presence of the pressure spike.

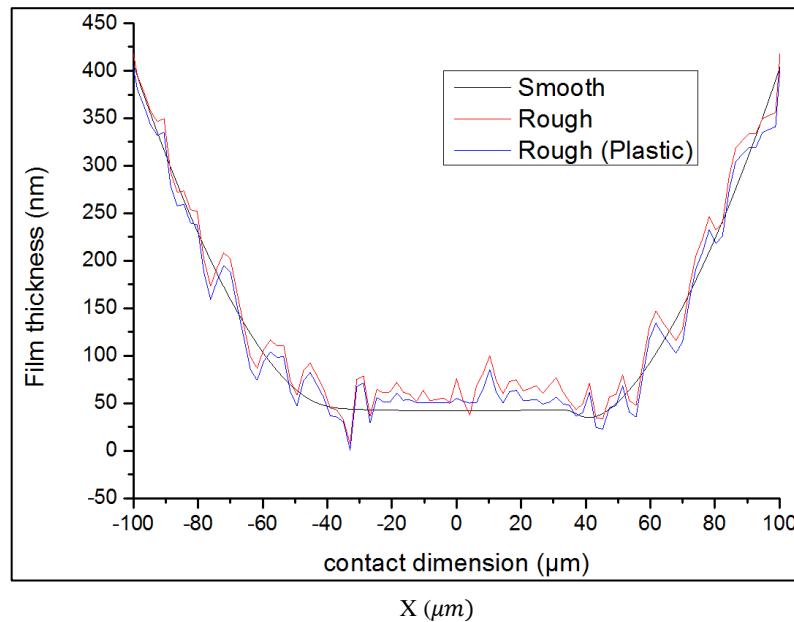


Figure 4-6: PEHL film thickness profiles. The presence of roughness effectively improves lubricant entrainment. The presence of plastic deformation flattens the film thickness profile.

The film thickness profile depicts similar characteristics (see Figure 4-6). The general profile of film thickness remains the same but at the points of plastic deformation, the film thickness also shows signs of flattening as seen in Figure 4-6. The overall film thickness, generally becomes thinner in case of plastically deforming surface.

4.3.3 Model validation and the effect of load on the elastoplastic contact performance

The model developed is validated against the work of Ren et al. [162]. In this section, the pressure profiles and plastic deformation profiles are presented in Figure 4-7 and the variation of film thickness with load for the plastically deforming contact is presented in dimensional form in Figure 4-8. The initial yielding pressure is 0.807 GPa corresponding to the yield limit of the material, 500 MPa. Although this value is not the actual plastic flow value but it is referred in this section to highlight the fact that the results are normalized against the Hertzian radius at the initial yielding and to illustrate the fact that the choice of the yielding pressure does affect the results. A discussion will follow in the next section on the effect of the plastic flow values on the PEHL results but in the current and the subsequent sections, the plastic flow value is taken as $2.3 \times \sigma_Y$ unless otherwise stated. The remaining parameters are kept the same as in previous sections but the applied pressure is different for different values of applied load.

The pressure profile has been normalized by the yield strength of the material and shows typical characteristics of plastically deforming contact as shown in part (a) of Figure 4-7. The contact area increases with increasing load as greater area is required to balance the greater applied load. The innermost profile shows the characteristic pressure spike that it retains as part of its EHL starting pressure profile. The remaining pressure profiles all show that the pressure is truncated at the yield pressure (as applied

in the algorithm) and this causes the increase in contact area compared to elastic contact. The pressure spike can be observed for all the loading cases where the truncated pressure was still higher than the value of pressure at which the pressure spike occurs. Moreover, when the pressure profiles are compared against the work of Ren et al., very good agreement is found (please refer to the top left graph in figure 9 of ref [162]).

The plastic deformation normalized to the Hertzian contact half width at initial yielding and shows smooth profiles corresponding to the smooth geometry of the ball, see part (b) in Figure 4-7. The comparison among the curves shows that the plastic deformation also increases with increasing load which is physical as the increased load should cause more plastic deformation. The deformation values at the centre of the contact varies almost linearly with applied load, from about 57 nm at the load of 25 N to a value of 1117 nm at the load of 125 N. It is interesting to note that no plastic deformation is observed for the load of 10 N.

The film thickness profiles in general show the key EHL characteristics but with plastic deformation incorporated, the profiles become flatter and thinner films develop inside the contact with a much deeper exit constriction. The parts (a) and (b) in Figure 4-8 have been plotted with different grid sizes to show the effect of grid size on the lubricant film thicknesses. There is a difference of about 5nm in the film thickness values plotted with both the grids.

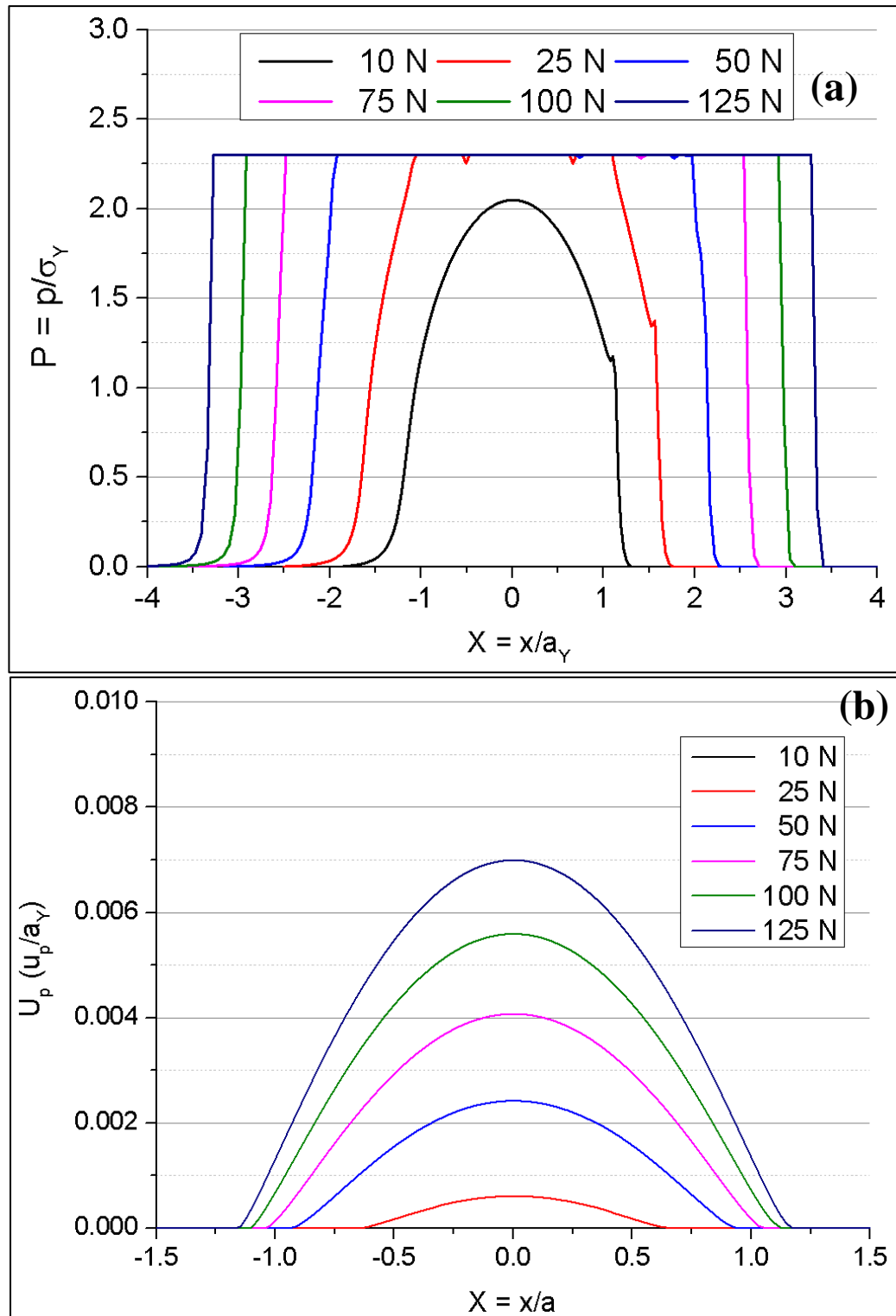


Figure 4-7: The results for PEHL from the current model. (a) pressure profile. (b) non-dimensionalized plastic deformation (cross-section at $Y=0$).

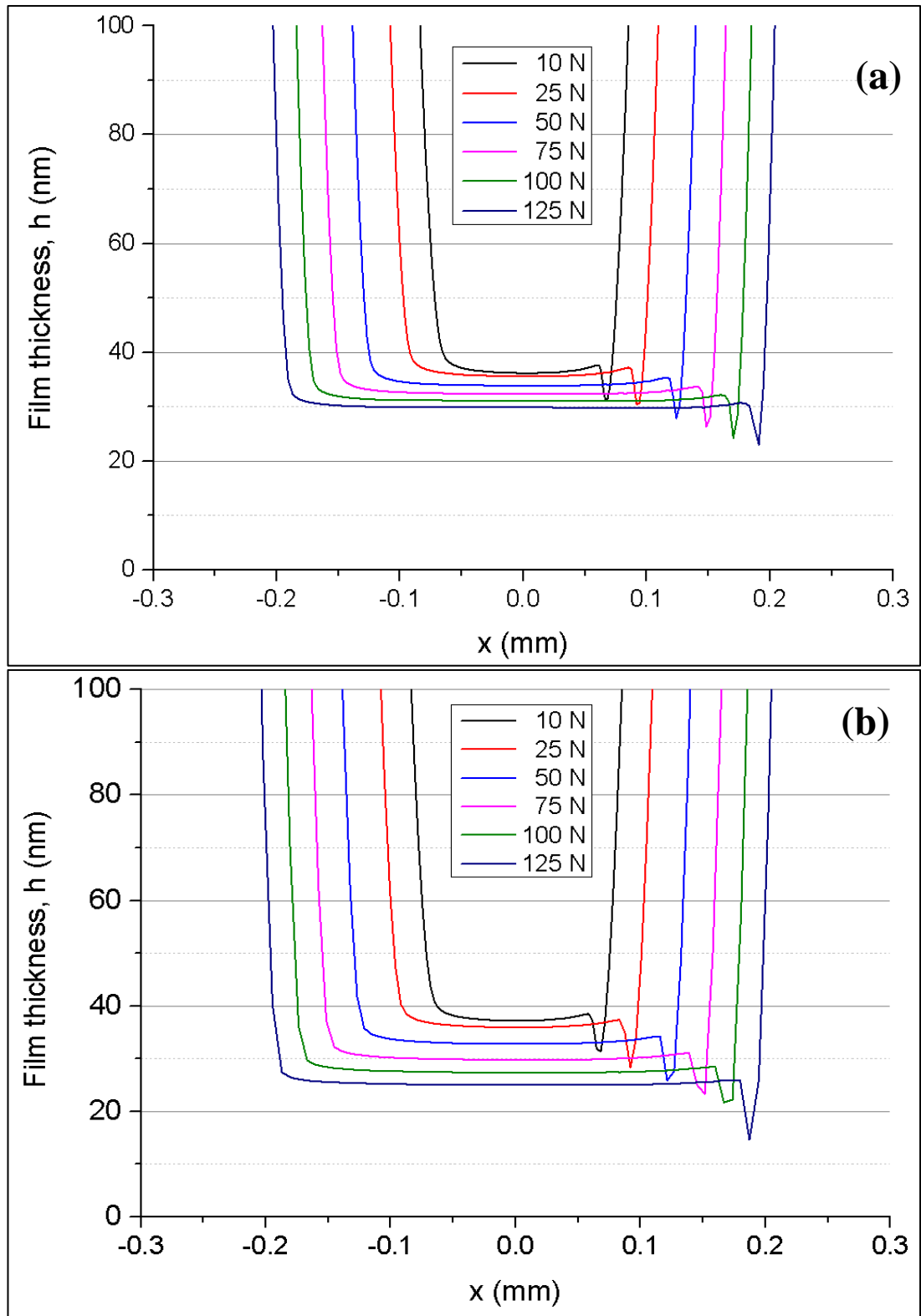


Figure 4-8: The lubricant film thickness results in nanometres for PEHL from the current model. (a) grid of 129 x 129 (b) grid of 65 x 65

The effect of geometry update is presented in Figure 4-9. Part (a) presents the lubricant film thickness values without updating geometry while part (b) presents the film thickness profiles when the geometry is updated every iteration until no more plastic deformation is present. It can be seen that the profiles become flatter and the exit constriction becomes thinner and deeper with geometry update. Moreover, due to the fact that the geometry update ensures that all the plastic deformation has occurred, the film thickness developed is thinner compared to the results without updating geometry. There is once again a difference of about 5nm in the values of film thickness predicted with or without geometry update.

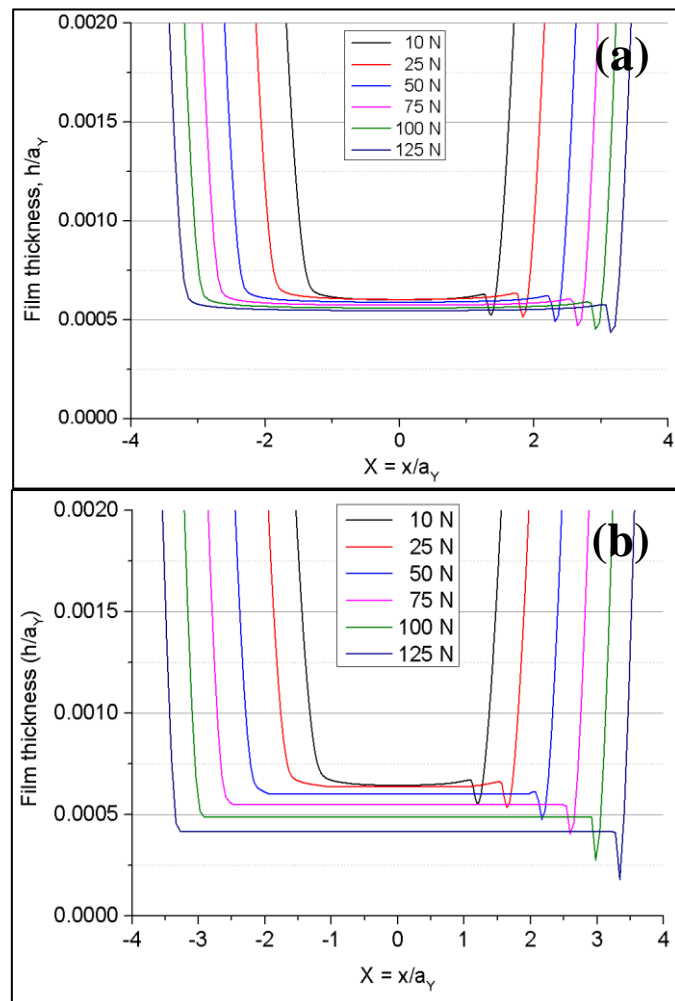


Figure 4-9: The effect of geometry update on the PEHL film thickness results. (a) non-dimensionalized film thickness profiles without geometry update. The plastic

deformation is allowed to accumulate in every iteration. (b) The geometry is updated every iteration until no more plastic deformation takes place.

The film thickness of the lubricant developed inside the contact is plotted in Figure 4-10. It can be seen that the film thickness values predicted by the current model are consistently higher. The values predicted by the current model are almost 5nm higher and this difference lies within the numerical error range as explained in the last paragraphs. Moreover, the film thickness values predicted by our model match almost exactly if $H \approx P_Y$. This will be further explored in the next section.

These results when compared against the film thickness results from the work of Ren et al. [162] give excellent qualitative agreement while quantitative differences do exist. The model is able to produce all key PEHL characteristics as shown in Figure 4-10 for comparison. The flattening of the film thickness profile and the increase in the depth of exit constriction is clearly observed, especially when the results are presented in dimensional form (see Figure 4-8, Figure 4-8 and Figure 4-10).

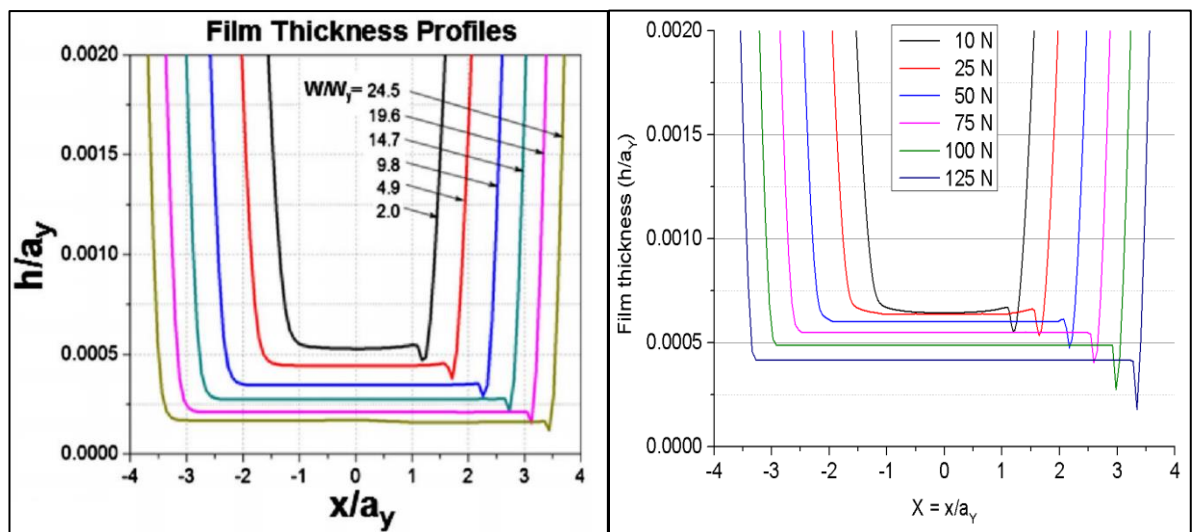


Figure 4-10: PEHL results. (Left hand side) solutions for different loads from Ren et al. [162]. (Right hand side) solutions for different loads from current study. Results are normalized by the half width of Hertzian contact radius at initial yield.

The film thickness variation follows precisely the same qualitative trend and shows all the properties of a plastically deforming contact. The increase in contact area with applied load is physically consistent: greater contact area with increasing load.

4.3.4 A note on the hardness value

The hardness value used in the above simulations (in the last section) is fixed to $2.3 \times \sigma_Y$ and this value is taken as it gives best fit with the simulation results of Ren et al. [162]. From the literature [151, 165-167] it can be seen that the relationship between the hardness of material and the yield strength is $H = 3.0 \times \sigma_Y$ i.e. the hardness scales as three times the yield strength and the general expression $H = c \times \sigma_Y$ holds which gives a linear relationship between hardness and yield strength. Here c is a constant. The value of this constant has been obtained in various studies through fitting to experimental data and it always comes out to be 3.

The results from the current model when compared against the results of Ren et al. [162] give a systematic difference. The pressure profiles give best qualitative match when compared a value of $c = 2.3$ is used while the film thickness predictions from the current model give best match against Ren's results when the value of 'c' is reduced to give hardness value close to the initial yield pressure value ($H \approx P_Y$). Thus, in the current section, a systematic study is performed to see the effect of hardness value on the pressure and film thickness profiles predicted by the current model by varying the value of 'c' from 1.6 to 3.0.

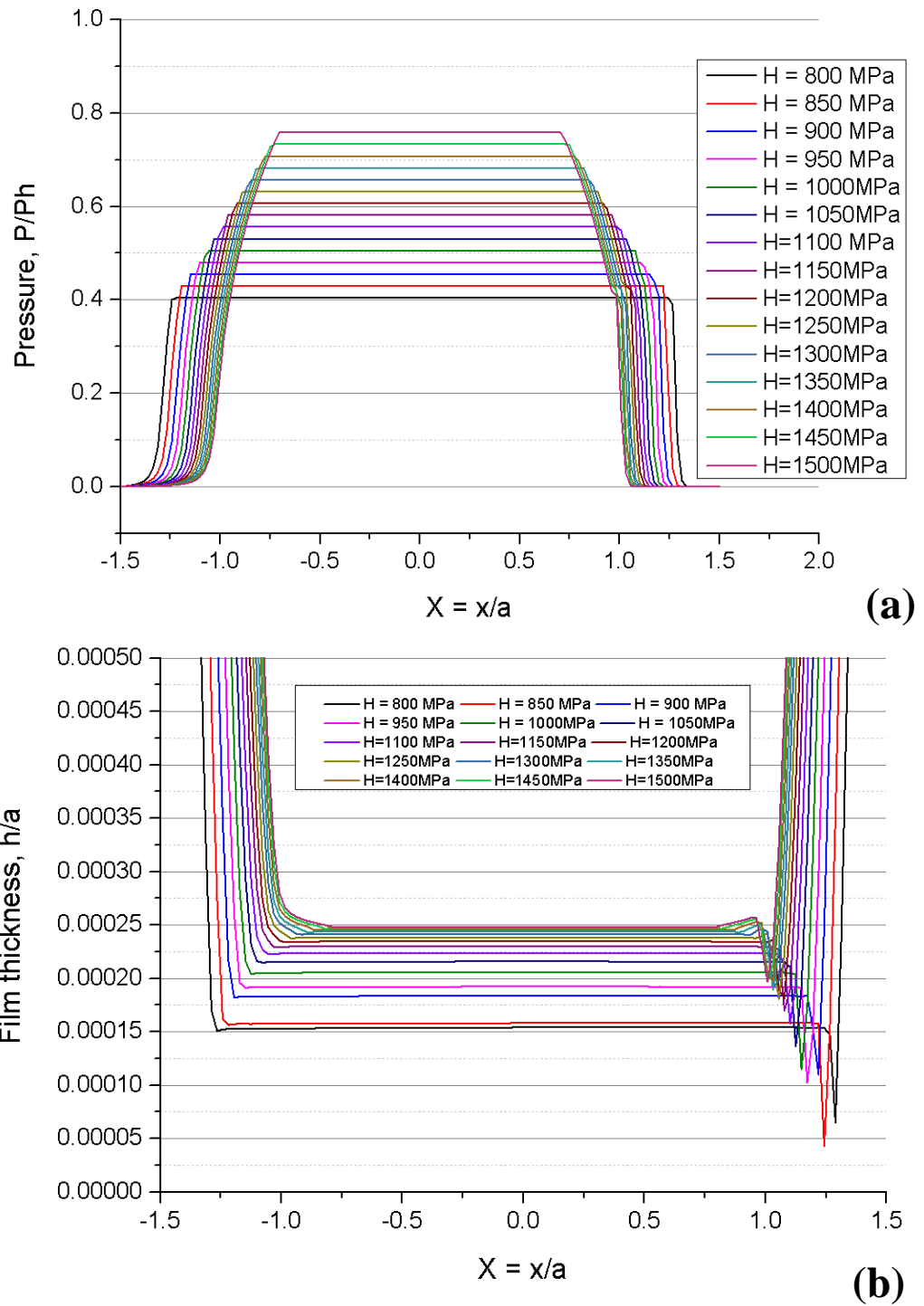


Figure 4-11: The effect of Hardness value used in the current model. (a) pressure profiles for varying hardness values. (b) film thickness profiles for varying hardness values.

The results are presented in part (a) of Figure 4-11 for the pressure profile while the film thickness profiles are presented in part (b) of the same figure. It can be seen that with increasing value of 'c', the contact area decreases as there is correspondingly lesser plastic deformation expected. The pressure profiles match the results of Ren et al. best when $H = 1150$ MPa corresponding to the value of $c=2.3$ while the value of film thickness matches best when $H = 800$ MPa to 850 MPa corresponding to the value of $c=1.6$ to 1.7 . These differences are expected owing to the approximate nature of the model. The model developed in the current study is of engineering value due to its simplicity and robustness. The slight differences can always be compensated by the use of a suitable factor of safety.

4.4 Effect of geometry update on plastic deformation

The results presented in the previous section are for the plastic deformation without any material removal due to plastic deformation. Our model is capable of giving results for contact evolution and thus, a comparison is presented in the following section to highlight the importance and the effect of material removal in changing the contact parameters.

In this section, the results are presented by running simulations for three different cases. The black curve corresponds to the starting EHL profile and is only presented here for comparison. The maximum number of iterations is fixed at 49 as this is sufficient to get stable values. The first case, *No removal_49* corresponds to the situation where the simulation is run up to 49 iterations but no material is removed at any point and the final results are plotted. The second case, *K=5_49* corresponds to the case where the plastic deformation is allowed to accumulate and is removed as soon as the 5th iteration is reached but no material is removed afterwards. The third case, *MOD(K,5)_49* corresponds to the situation where the plastic deformation is

allowed to accumulate and the geometry is updated every 5th iteration step. All the results are presented for the case of 75 N load with all the operating parameters kept the same as in the previous sections.

There seems to be no effect of geometry update due to plastic deformation on pressure as shown in part (a) of Figure 4-12. There is only very slight variation at the edges of the contact. The film thickness profiles are shown in part (b) of Figure 4-12 and it shows that the film thickness profile undergoes both qualitative and quantitative changes due to material removal. Qualitatively, the flattening of the film thickness profile is observed while the magnitude of film thickness values decreases as successive wear steps are introduced reaching a fixed and repeatable value. The minimum film thickness value also decreases and the difference between the central and minimum film thickness values also increases. For comparison purpose, the starting EHL pressure profile without any plastic deformation is also given. To explore this further, the plastic deformation values in each case are presented along with the evolution of central film thickness in Figure 4-13.

Although the film thickness in the case of no wear and a single wear step is different but the plastic deformation value is identical as both the curves overlap. But if the contact is evolved to its eventual state, there is some additional plastic deformation that is necessary to reach an equilibrium state where all the material that has yielded gets plastically removed and the contact geometry changes result in no further plastic deformation. This is also seen when the central film thickness profile is plotted, see part (b) of Figure 4-13. The steps in the profile correspond to each step of material removal.

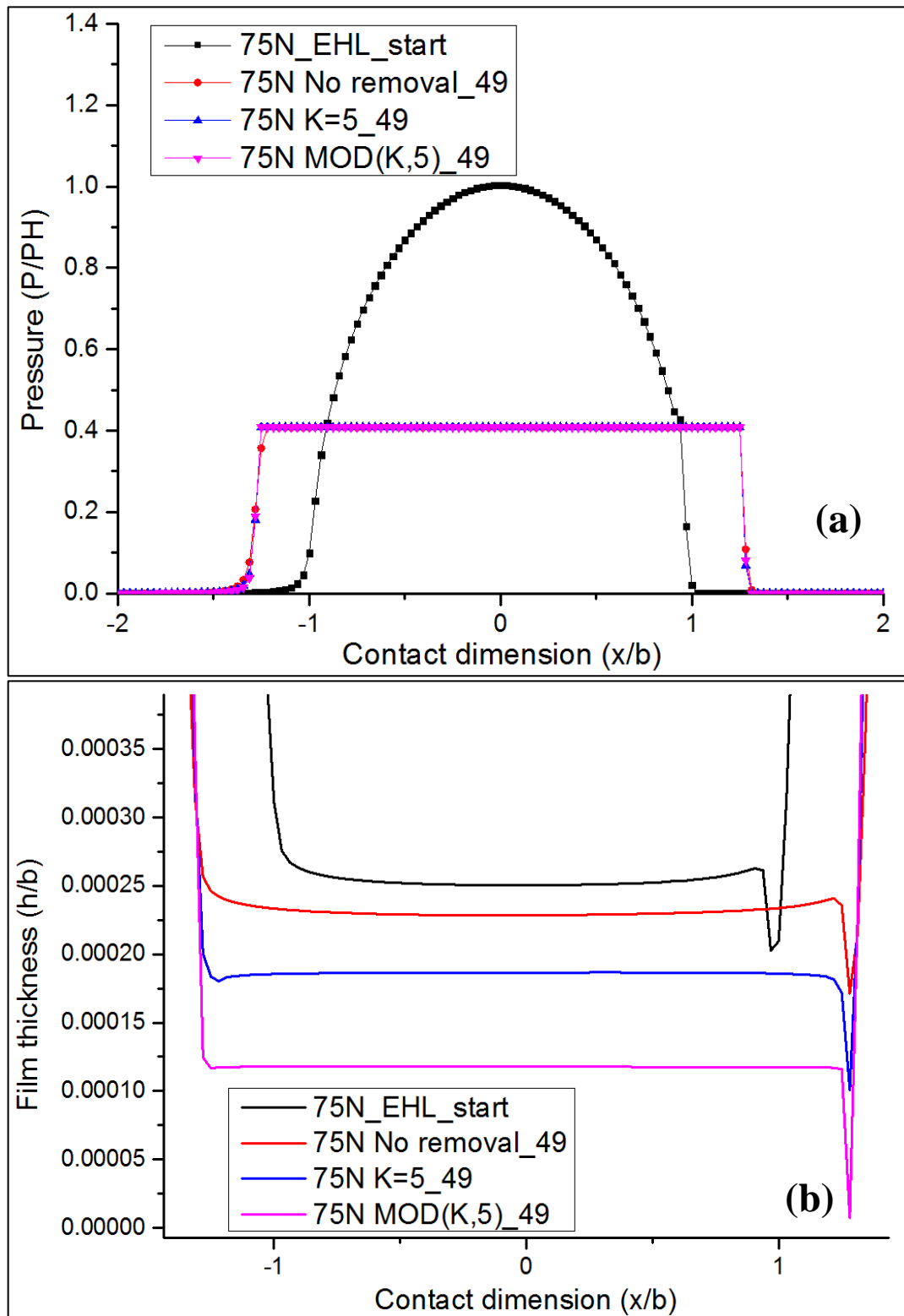


Figure 4-12: The effect of considering geometry update due to material removal. Various curves correspond to the iteration number at which the material was removed and if it was removed in a single step. (a) pressure profiles. (b) film thickness profiles

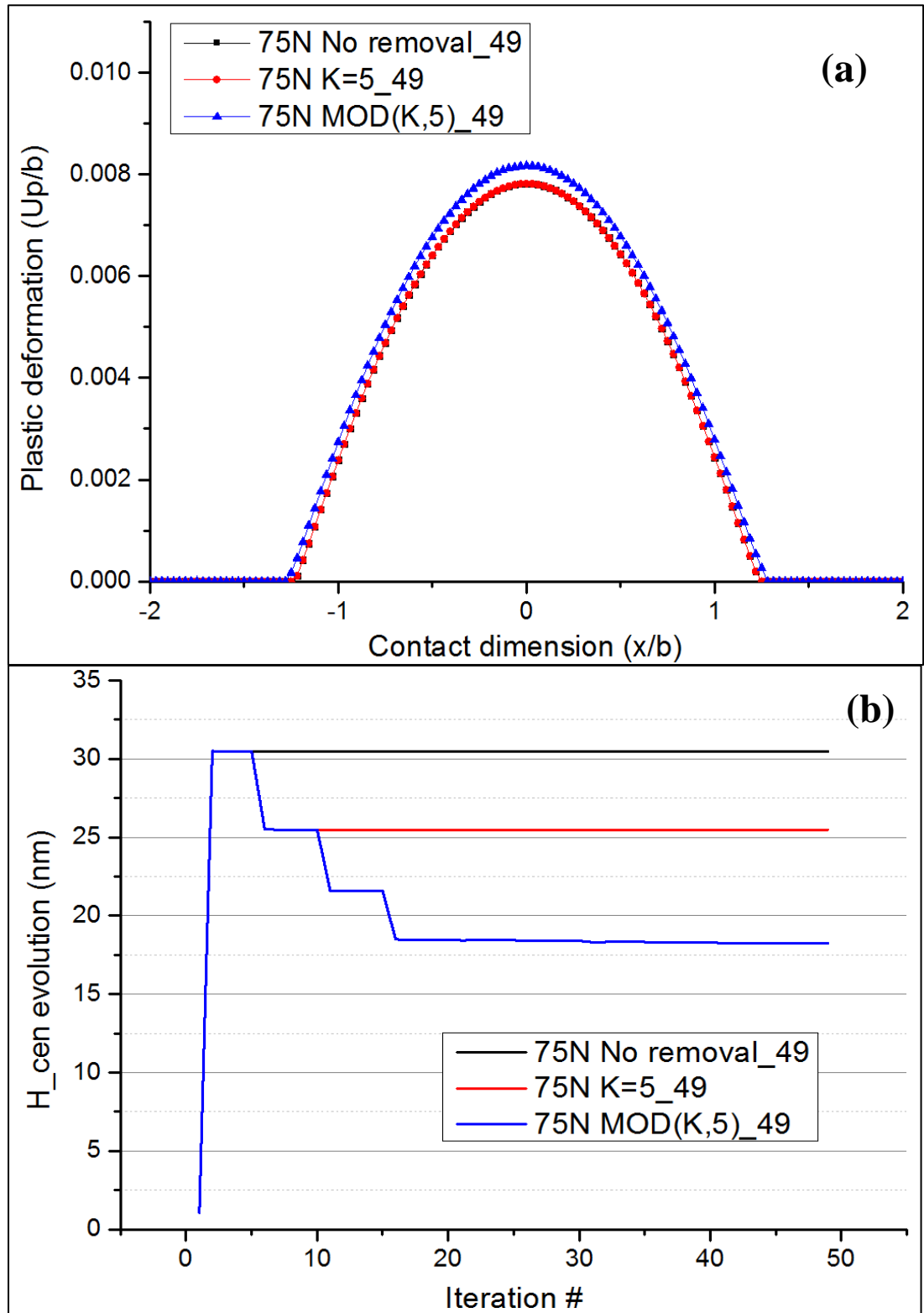


Figure 4-13: The effect of considering geometry update due to material removal. Various curves correspond to the iteration number at which the material was removed and if it was removed in a single step. (a) Plastic deformation profiles. (b) Central film thickness evolution with iteration number.

The present model is more robust compared to the method given by Sahlin et al.[161] as there is no need for a plane convergence criteria. The contact eventually reaches a stable state. The only thing that changes is the number of steps and amount of material removed in each step i.e. the intermediate state may be different but the final state is always the same and the results are repeatable.

4.5 Summary

In this chapter, a plastic deformation calculation procedure was developed and implemented into the unified mixed lubrication model. The model is robust enough to reach a steady state value without additional complications and is very simple and easy to implement. The results from this plastic deformation model are presented and compared against published plastic deformation models.

The unified mixed lubrication model gives pressures by solving the Reynolds equation to get the pressures in the entire solution domain. The solid contact and the fluid lubricated contact pressures are obtained successfully and entire lubrication transition studies can be performed. Due to the presence of roughness these nodal pressures have been observed to be very high and in most cases higher than the material yielding limit. Thus, the inclusion of plastic deformation is necessary.

The algorithm presented in the current study for plastic deformation calculation requires no identification of the nodes as either lubricated or solid contact. This enables the study of entire lubrication transition without actually going into the details of where the pressures came from. Thus, the plastic deformation can be calculated even if it has been caused by the lubricant pressures. This makes the model very useful for engineering applications.

The results are presented for smooth surface cases first and then for the rough surface cases to illustrate the working of the model. The results for the smooth surface case when compared against the published results give an excellent match. Not only the qualitative trends are produced accurately but the quantitative match is also very good. The edge of the current model is its simplicity and engineering value. The additional computational effort required to calculate plastic deformation is minimal but no comparison is possible due to not having sufficient comparable data from the literature.

In actual simulation to replicate experimental conditions, the material that undergoes plastic deformation is removed. This particular aspect is missing in the published plastic deformation models and thus is explored to see the effect of material removal on the contact performance. The film thickness is affected considerably but the pressures seem to be affected only slightly, especially at the edges of the contact domain.

PART III

Model Application

Chapter 5

Modelling tribochemistry in mixed lubrication

In this chapter, first, an overview of various factors driving the tribofilm growth is given in section 5.2 and section 5.3 presents different modelling approaches to simulate tribochemistry. First the methods used to study the tribochemistry under boundary lubrication conditions are summarized then the studies incorporating mixed lubrication are highlighted in section 5.4. A detailed section outlining various tribofilm growth models is presented in section 5.5 and finally, the tribofilm growth model from Ghanbarzadeh et al [23, 120] is chosen to simulate tribofilm growth. The mechanical properties of the tribofilm are implemented as variable hardness [22]. This tribofilm growth framework is then combined in our general mixed lubrication framework to get the tribofilm growth integrated with the plastic deformation and wear models and results are presented for an illustrative case in section 5.6. The wear of both the tribofilm (removal) and substrate (mild wear) are considered. Throughout this chapter, the relative importance of pressure and shear is emphasized.

5.1 Introduction and background

The mechanics under the mixed lubrication regime are governed by the mixed lubrication solver which gives pressure and film thickness profiles. The contact pressure and deformation is calculated by using the tridiagonal matrix algorithm. The pressures are calculated irrespective of the instantaneous state of the contacting asperity. *The deformation can be elastic or plastic and the pressures can be fluid or solid asperity contacting pressures.* The plastic deformation calculation procedure implemented in the previous chapter takes care of the plastic deformation. The model

is able to predict real areas of contact, the relative contact area and contact load ratios. The model is completely deterministic and can take the real engineering surface roughness as input. The lubrication regime can be varied from full film down to boundary lubrication and dry contact conditions.

All these mechanical parameters are directly linked to the tribochemical changes occurring in the contact. These tribofilm growth and the subsequent changes in the mechanical response of the contact have a significant influence in driving friction and wear in a tribosystem. The most important tribochemical parameters are the tribofilm growth behaviour, the mean tribofilm thickness, and the change in the mechanical properties of surface due to tribofilm growth. The tribofilm growth is a net result of formation and removal and the rates of formation and removal play a significant role in defining the contact performance. The changes occurring in the surface roughness of the contact in the presence and / or absence of the tribofilm are all crucial parameters that define the tribochemical performance of the contact. Thus, the next step is to include the tribochemical film growth into the mixed lubrication model. Before going into the details of the model, some key ideas related to the tribofilm growth and mechanics are discussed.

5.2 Factors driving the tribofilm growth

The growth of ZDDP tribofilms has been studied extensively and several key phenomena have been found to be responsible for the preferential growth of ZDDP and other phosphorous based additives [97] inside the rubbing contacts. The *flash temperature rise*, *pressure*, *triboemission* and *surface catalysis* are the most important parameters driving tribofilm growth. The nature of the rubbing phenomenon generates heat which is dissipated in the contact. This heat raises the bulk and flash temperature of the contacting surfaces. The flash temperature is the instantaneous rise in

temperature at the contacting asperities. It is a very rapid pulse of temperature and is a cause of ZDDP tribofilm growth on rubbing surfaces [94]. Due to the fact that the growth of ZDDP tribofilm has also been observed at relatively low sliding speeds (less than 0.1 m/s [113]) where the flash temperature rise is low, the flash temperature is not the main cause of tribofilm formation. The magnitude of flash temperature is strongly dependent on the sliding speed and is calculated using the theory of moving heat source [168]. Based upon theoretical calculations, Mosey et al. [108] suggests that the phosphate polymer network undergoes a cross-linking phenomenon due to the presence of very high pressures inside the contact, giving surface films with superior tribological performance. The pressure led tribofilm formation process is specific to non-conforming contacts involving high pressures. The main discrepancy in this idea is the prerequisite of having unrealistically high pressures [169] which are not in actual experimental conditions. Thus, pressure is also considered a key cause of tribofilm growth. The severe contact conditions can lead to plastic deformation and fracture of the contacting surfaces which result in the formation of charged regions on the local scale. This results in emission of particles like electrons and ions [170]. These active particles are considered to be one of the causes of tribochemical interactions [171] and the formation of ZDDP tribofilms [172]. The presence of triboemission in a lubricated contact is very difficult to detect. Therefore triboemission is not considered to be the cause of tribofilm formation in mixed lubricated contacts modelled in this study. The stress-promoted thermal activation of the tribofilm formation was very recently presented by Zhang and Spikes [97]. They studied tribofilm growth by a ZDDP containing lubricant in the absence of any asperity contacts and low sliding speeds. The concept of chemical reactions occurring due to mechanical force is emphasized by performing experiments using oils with very different friction properties and conducting experiments in the full film lubrication

regime. This idea is relevant as shear stress is ubiquitous in rubbing contacts [173]. The effect of shear stress is to reduce the activation barrier for the forward reactions.

5.3 Numerical simulation of tribofilm growth in boundary lubrication

Tribochemistry has been included into contact mechanics simulations by several researchers. These studies are discussed in this section and the gaps are highlighted. Tribofilm formation and growth in contacts has been modelled mainly in dry contact conditions. The first attempt to capture the ZDDP antiwear tribofilm growth in contact mechanics simulations was made by Andersson et al. [22]. A model for tribofilm growth based upon the thermal activation was given. This model was combined with a contact mechanics simulation to study the mutual effect of chemistry and contact mechanics. The tribofilm growth model was tuned to experiments and used in simulations. The model only simulated short-term tribofilm growth and did not consider the tribofilm removal but tribofilm growth on real rough surfaces could be simulated. Ghanbarzadeh et al. [120] developed a local tribofilm growth model that considers local formation and removal of the tribofilm. Their model was based upon the thermodynamics of interfaces. A linear reduction in the wear coefficient from the “no tribofilm” wear coefficient to the wear coefficient for “maximum tribofilm” height was assumed. They developed a contact mechanics model based upon the principle of minimization of potential energy [174] and integrated their tribofilm growth (formation/removal) and wear model into it. In the following study, Ghanbarzadeh et al. [175] performed tribofilm growth and wear experiments using the mini traction machine (MTM) equipped with spacer layer interferometry method (SLIM) and validated their model in real applications. Gosvami et al. [96] performed AFM single asperity experiments to study the effect of temperature and pressure on

tribofilm growth. The experimental data was fitted to the stress-dependent kinetic growth model and a functional relationship to give the rate of growth of tribofilm with time was given. This stress-active tribofilm growth model was used by Akchurin and Bosman [176] to simulate tribofilm growth on rough surfaces in dry contact. They combined this growth model with a contact mechanics model with a boundary element based contact mechanics solver. They model mild wear as diffusion of substrate atoms into the tribofilm. The steady state tribofilm thickness and tribofilm thickness evolution was simulated and validated against experiments. All these models consider dry contact with no effect of lubricant.

5.4 Mixed lubrication models with tribochemistry

The integration of tribochemistry into the mixed lubrication models is a fairly new concept. All approaches mentioned above are for boundary lubrication conditions where the importance of lubricant in changing the tribofilm growth and mechanics is absent. The first attempt to consider the tribofilm growth and wear under mixed lubrication conditions was a very recent study by Brizmer et al. [24]. They performed experiments to study the growth of ZDDP tribofilm on rolling / sliding rough contacts running under mixed lubrication conditions using MTM-SLIM. The tribofilm formation was studied as a function of applied pressure, temperature and roughness of the counter-part. They used the stress-activated thermal activation model for ZDDP tribofilm growth given, very recently, by Zhang and Spikes [97]. They designed a thermomechanical model and tuned it to experimental results of tribofilm growth. This specifically designed setup was validated against experiments and finally used to predict micro-pitting performance in a tribochemically active system.

The model from Brizmer et al. [24] does not take into account the topography evolution due to the tribofilm and the mixed lubrication model is based upon the semi-

analytical method [177]. There is no account of the removal of the tribofilm and only mild wear and fatigue damage are considered. The mild wear is simulated by using spatially varying wear coefficients in the Archard's wear equation that changes every time step as well. Moreover, no account of the effect of tribofilm growth in modifying the lubrication parameters was taken. The effect of tribofilm growth on the contact characteristics is very important and should be considered. The main difficulty is that the lubrication effectiveness varies from full film down to boundary lubrication and to simulate the effect of tribofilm on lubrication performance, the mixed lubrication models should be capable of simulating the entire transition from full film down to boundary lubrication.

There is no other study that captures tribochemistry and mixed lubrication in a single framework. Therefore, the current chapter outlines the tribochemical film growth in the presence of additives and the procedure to integrate it with the unified mixed lubrication model is given. The current chapter outlines mainly the capability of the model to simulate the tribofilm growth and the effect of this tribofilm in modifying the lubrication behaviour is presented in the next chapter. The results for the instantaneous tribofilm growth as a patchy tribofilm are presented. Then the mean tribofilm growth to steady state values is simulated and validated against the existing numerical studies. The current model is capable of simulating the tribofilm growth on both the counterparts and thus, the result will be presented for the smooth and rough counterpart separately. The movement of both the ball and the disc is controlled independently and different slide-to-roll ratios achieved.

5.5 Selection of the tribofilm growth model: A short survey

Several models have been presented in the past to simulate the tribofilm growth. Some studies consider the formation and removal aspects independently while others

consider the removal as a part of wear. These studies will be discussed and the advantages and disadvantages highlighted. Finally, a tribofilm growth model is selected.

The first model to describe kinetic growth of the ZDDP tribofilm was given by Fujita and Spikes [178] who performed extensive experiments and monitored the tribofilm thickness and fitted this model to the experimental tribofilm thickness values.

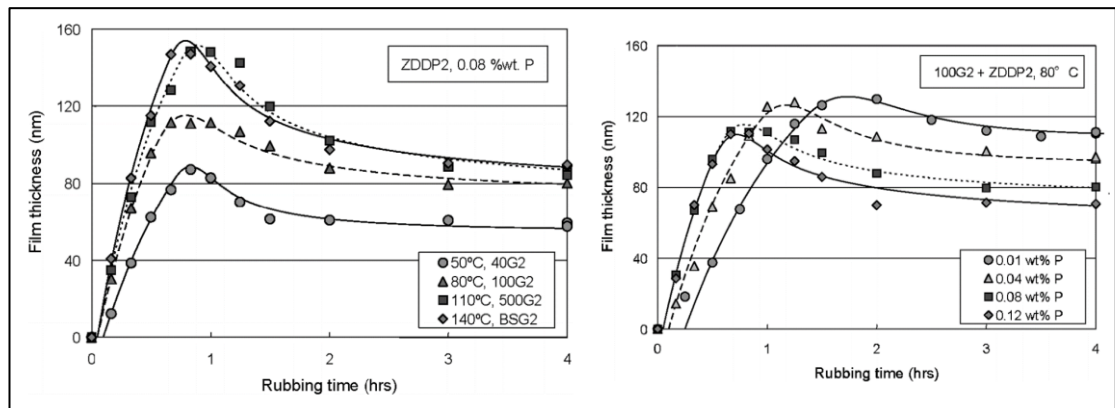


Figure 5-1: Tribofilm growth model from Fujita and Spikes [92]. (a) Results for different temperatures. (b) Results for different concentrations.

They considered a coverage model that relates the tribofilm formation rate to the area of substrate not yet covered by the tribofilm while the removal of tribofilm was incorporated by assuming the rate of removal proportional to the fourth power of the area of substrate that is actually covered by the tribofilm.

$$h_{mean} = h_{max}(1 - e^{-k_1(t-t_i)}) \quad (5-1)$$

Where h_{mean} and h_{max} are the mean and maximum tribofilm heights, k_1 is a constant while t is the time in the model. The term t_i represents the lag in the tribofilm growth, observed experimentally. The model can predict the self-limiting behaviour of ZDDP tribofilms with good accuracy. Some key results from their modelling study

are presented in Figure 5-1. They also developed some models for the change in the maximum and mean film thickness with temperature and concentration. It was an experimental work and no numerical simulations were presented.

Andersson et al. [22] proposed that the tribofilm formation was a chemical reaction happening between the substrate and the lubricant at the contacting asperities due to the severe temperature peaks called the flash temperature. They assumed a phenomenon of Arrhenius type and described the tribofilm growth rate as:

$$\left[\frac{dh}{dt}\right]_{growth} = C_6(h_{max} - h)e^{\frac{-C_5}{\mu p v}}$$

and the final nodal tribofilm growth equation used was,

$$h_{n+1}(i, j) = h_n(i, j) + \Delta t C_6 (h_{max} - h_n(i, j)) e^{\frac{-C_5}{\mu p_n(i, j) v}} \quad (5-2)$$

where h_i and h_{max} are the nodal and maximum tribofilm thickness, the terms μ , $p_n(i, j)$ and v are the friction coefficient, nodal normal pressure and the sliding velocity respectively. The constants C_5 and C_6 are tuned to experiments making it a semi-deterministic model for tribofilm growth simulation. The results for the tribofilm growth from their model are presented in Figure 5-2 for the tribofilm growth simulation for very short times. The term $\mu p_n(i, j) v$ collectively refers to frictional energy dissipation which is related to the flash temperatures.

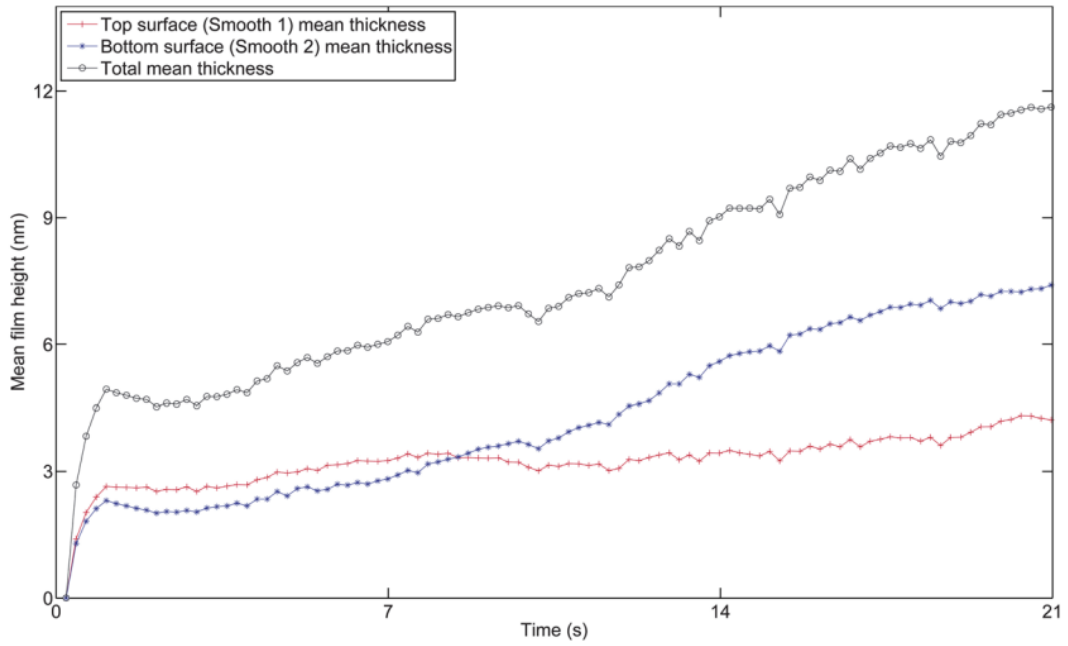


Figure 5-2: Mean tribofilm thickness results from the tribofilm growth model of Andersson et al. [22].

Only substrate wear via Archard's wear model was considered. This model was numerically simulated in a boundary lubrication solver to simulate the tribofilm growth for the initial couple of seconds of experiment. No tribofilm removal was considered in this model. This was a modelling study and they fitted their results to the experimental results of Naveira-Suarez [114].

The growth of ZDDP tribofilm as a diffusion process was also modelled. These models consider the formation of ZDDP tribofilm as a diffusion process at high temperatures [179]. The theory does not consider the actual formation of the chemical film. The effect of chemical film growth is modelled. An elastic modulus is set up that can achieve the same antiwear performance as a critical value of tribofilm thickness. Whether the tribofilm will form or not, at a point, is determined by the hardness and roughness of the samples. The decomposition of ZDDP was considered to start at a particular threshold temperature and the decomposition products are adsorbed onto

the surface. Then based upon the roughness and hardness, a chemically adsorbed film forms. The diffusion model has some parameters that are curve fitted to experiments. Tribofilm removal is also included. Some more complex models for the diffusion based theory of ZDDP antiwear additive have also been presented but these are very complex and considered not suitable for engineering applications and to be included into numerical solvers.

The thermodynamics of friction and wear process are complex and irreversible. The irreversibility is linked to the entropy generation during the friction process. The way the entropy increases can characterise the changes occurring in thermodynamic systems. Some authors have tried to correlate this idea of entropy change by studying the process of tribofilm formation as a non-spontaneous reaction that actually takes place due to the entropy generated in the contact due to friction [180]. The results suggested that if enough energy is present, the tribofilm formation process is independent of time and mainly depends upon speed. To express this functional relationship, they used the theory of activated complexes. An activated complex is a system where dynamic bond formation and breakage takes place. In this theory, the chemical and tribo-chemical (mechano-) reactions have a different rate. The rate of the former being dependent on temperature while the rate of the latter does not depend upon temperature. The key parameters driving the rate of tribochemical reactions was the sliding speed (shear). Based upon this, Bulgarevich et al. [119] proposed that the formation of chemical films on rubbing surfaces is primarily a mechanically activated phenomenon rather than only a thermal activated one. The effect of pressure was to change the equilibrium in the adsorption of additives in the lubricant. This study revealed that even at higher temperatures, mechanical activation plays a major role in causing tribochemical phenomenon. The thermal contribution is generally very low

in tribological applications. In another study, Bulgarevich et al. [118] have confirmed that population of transition states for a chemical reaction to occur are dependent upon the mechanical action. The mechanical action in a sliding contact is mainly “shear”. The rate of reaction can be expressed as a combined thermo- / mechano- activated process

$$k_{tribo-thermo} = \frac{x_{tribo}}{x_{thermo}} k_{thermo}$$

where x_{tribo} is the factor accounting for tribo-/mechano-activation and x_{thermo} accounts for thermal activation. k_{thermo} is the rate of thermal reaction given as

$$k_{thermo} = \frac{k_1 T}{h'} e^{\frac{\Delta E}{RT}}$$

And considering Boltzmann energy distribution, thermo-activation is given by

$$x_{thermo} = e^{\frac{\Delta E}{RT}}$$

Here, k_1 is Boltzmann constant, h' is Planck's constant and ΔE , R and T are the activation energy, universal gas constant and the temperature, respectively. Putting these expressions into $k_{tribo-thermo}$ gives,

$$k_{tribo-thermo} = \frac{K_1 T}{h'} x_{tribo}$$

It can be seen that the rate of tribochemical reactions is independent of activation and mainly depends upon temperature.

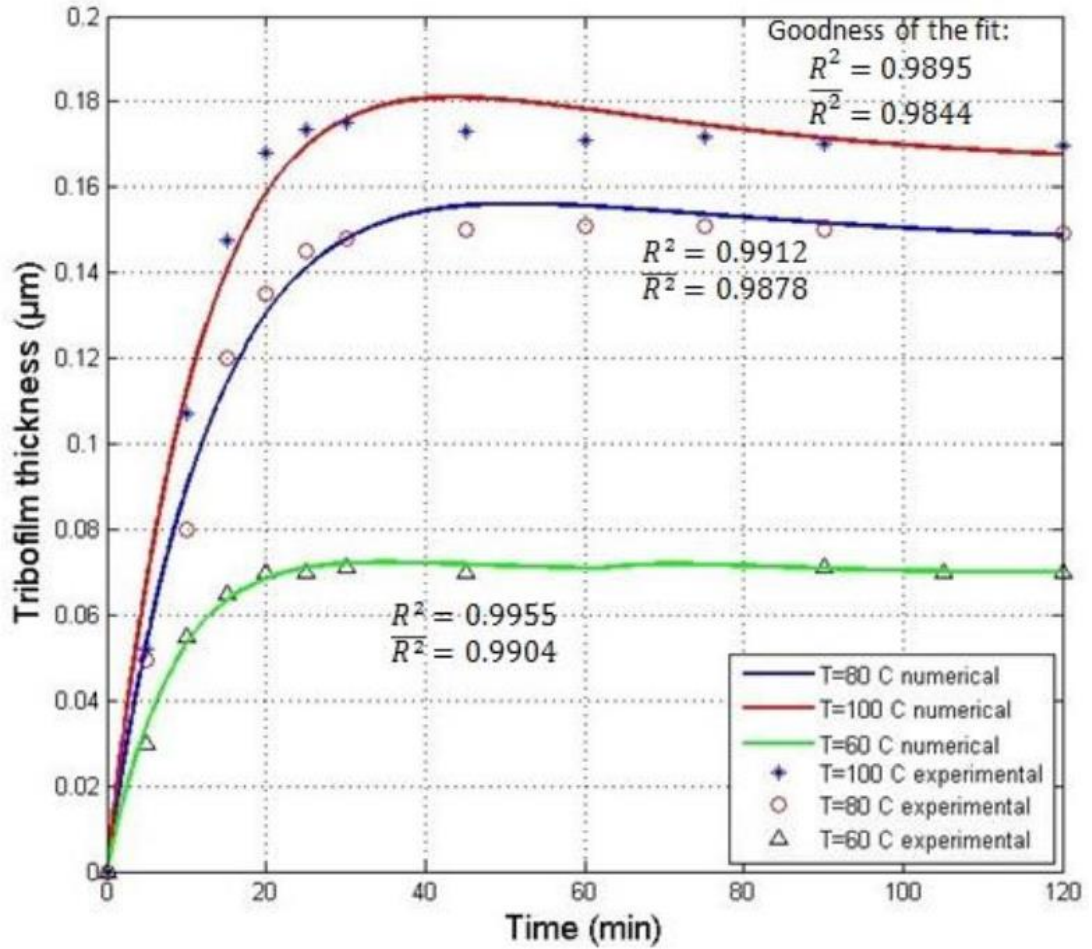


Figure 5-3: Tribofilm growth model results. The plots show the experimental results of tribofilm growth and the corresponding model fitted tribofilm profiles for different temperatures [175].

These ideas were used by Ghanbarzadeh et al. [120] to develop a tribofilm growth model. The term x_{tribo} was fitted to experiments to develop a semi-analytical model for tribofilm growth. As the rate of tribochemical reactions happening between the lubricant and substrate are complex [28, 85], they assumed a second order reaction for developing the model. Therefore, considering the lubricant as substance A and the substrate steel as substance B, the rate of the tribochemical reaction is given as

$$\frac{dC}{dt} = k_{tribo-thermo}AB$$

where A and B are the concentrations of reactants while C is the concentration of product. It was further assumed that the lubricant, substance A, is abundant and thus is not the rate limiting concentration. This assumption is valid as the formation of tribofilm will reduce the amount of nascent surface area that is available for chemical reaction. To incorporate the effect of self-limitation of the mean tribofilm thickness that is observed experimentally, Ghanbarzadeh et al. [23] introduced the following equation for the substance A,

$$A = A_1(h_{max} - h)$$

Thus, substituting this expression for substance A, the tribochemical reaction rate becomes,

$$\frac{dC}{dt} = k_{tribo-thermo} A_1(h_{max} - h)B$$

$$\frac{dC}{dt} = \frac{KT}{h'} x_{tribo} C_1(h_{max} - h)$$

Expressing the tribochemical reaction as the tribofilm formation process,

$$\frac{dh}{dt} = \frac{KT}{h'} x_{tribo} C_2(h_{max} - h)$$

Where C_1 and C_2 are constants. Integrating the above equation, the tribofilm growth is obtained as a function of time and mechano-activation.

$$h = h_{max} \left(1 - e^{-\frac{k_1 T}{h'} x_{tribo} t} \right) \quad (5-3)$$

In this equation, the term h_{max} and x_{tribo} are obtained through experimental fitting. Ghanbarzadeh et al. [120] also included removal to account for the wear of the tribofilm separately along with substrate wear. An exponential form very similar to

the formation model is assumed and when added to the formation part, the final tribofilm growth is obtained.

$$h = h_{max} \left(1 - e^{-\frac{k_1 T}{h'} x_{tribo} t} \right) - C_3 (1 - e^{-C_4 t}) \quad (5-4)$$

The constants C_3 and C_4 are also fitted to experimental data. The model results from this tribofilm growth model for replicating a typical experiment are presented in Figure 5-3.

From the above studies and the experimental results from Gosvami et al. [96], it is clear that the “shear” plays a critical role in the formation for tribofilms. Thus, it is not a surprise that the most recent model for tribofilm growth, given by Zhang and Spikes [97] considers tribofilm growth as a stress-promoted chemical reaction. This model is based upon the concept of physical and chemical processes driven by the applied mechanical action. The rate of thermo-activated chemical reaction is proportional to the probability of the species undergoing many chemical and physical processes. If the Boltzmann energy distribution is assumed, this probability is given by the Arrhenius expression as

$$P = A e^{-\frac{E_0}{k_b T}}$$

In this expression, E_0 is the activation energy barrier, k_b is the Boltzmann constant and T is the absolute temperature of the process and A is a pre-factor.

The stress-promoted thermal activation barrier states that an applied force, f, tends to reduce the activation energy for the forward reaction. Thus, under mechano-chemical conditions, the probability equation changes to

$$P = Ae^{-\frac{(E_0-f\Delta x)}{k_bT}} \quad (5-5)$$

where Δx is the activation length. This length corresponds to atomic scale phenomena like the distance a particle is moved or the distance a bond is stretched etc. The term $f\Delta x$ effectively represents mechanical work. In terms of macroscopic variables, the force can be represented as shear stress, τ , resulting in the following expression for the probability equation

$$P = Ae^{-\frac{(E_0-\tau\Delta v)}{k_bT}} \quad (5-6)$$

Here, τ is the shear stress at the interface, Δv is the activation volume and the pre-factor A needs to be obtained through experimental fitting. This expression is more suitable for applying to macroscopic experimental results. It is to be noted that the shear stress in this equation can either be fluid or solid shear stress depending upon the state of lubrication at a particular point inside the contact zone.

These expressions have been derived for the simplest form of stress-promoted chemical reaction where the applied force has no effect on the shape of the activation barrier. Albeit, this model successfully explains several important phenomenon related to ZDDP tribofilm growth.

In the current study, the tribofilm growth model given by Ghanbarzadeh et al. [120] is used. This model includes the effect of both thermal activation and shear independently. The tribofilm growth is controlled by multiplication of a factor called x_{tribo} and is a complete representation of the tribofilm growth behaviour. This factor has the effect of speeding up the chemical reactions due to shear. They have fitted this model to various experimental conditions and the values of fitting parameters are available for a wide range of experimental conditions. Thus, there is no need to

perform further experiments. Once the tribofilm growth model has been implemented and validated, the fitting parameters can simply be chosen based upon needs.

5.5.1 The calculation of flash temperatures

Sliding bodies experience friction which can manifest itself in many ways. Frictional heating is the most feasible way in which this energy appears. The mechanical energy of the contacting bodies due to normal and transverse loads at the asperities colliding with each other goes into increasing the internal energy of the system. This results in increasing the surface temperatures of the contact pair. The rate of energy dissipation inside the contact is related to the friction coefficient, pressure and sliding speed as

$$q_{dissipation} = \mu PV$$

or

$$q_{dissipation} = \tau V$$

where τ is the shear stress at the sliding interface.

This energy dissipation is directly related to the temperature rise at the contacting asperities. The contact is so severe that the resulting temperature peaks can be several hundred degrees. This rapid increase in temperature is called flash temperature. It builds up and dies out very quickly like a pulse. The flash temperature is very important in contact analysis as it affects the surface chemical reactivity and helps achieve the tribochemical reactions at relatively low temperatures. The exact value of this flash temperature inside the sliding track is very difficult to obtain but the maximum flash temperature rise has been studied by several authors in the past. These studies are based on the single heat source analysis on a moving or stationary surface.

The results from these models have been summarized by Kennedy [181] for different heat source geometries and is given in Table 5.1.

Table 5.1: Maximum flash temperature rise for different geometries and heat flux distributions [181].

Shape of Heat Source	Heat Flux Distribution	Figure No.	Maximum Flash Temperature Rise (Steady State)		
			Stationary or Low Speed Pe < 0.1	High Speed Pe > 10	Approximate Expression for All Velocities
Band	Uniform	6.7	$\frac{2qb}{k\sqrt{\pi}}$	$\frac{2qb}{k\sqrt{\pi Pe}}$	$\frac{2qb}{k\sqrt{\pi(1+Pe)}}$
Square	Uniform	6.10a	$\frac{1.122qb}{k}$	$\frac{2qb}{k\sqrt{\pi Pe}}$	$\frac{2qb}{k\sqrt{\pi(1.011+Pe)}}$
Circular	Uniform	6.5	$\frac{qa}{k}$	$\frac{2qa}{k\sqrt{\pi Pe}}$	$\frac{2qa}{k\sqrt{\pi(1.273+Pe)}}$
Circular	Parabolic	6.10b	$\frac{3\pi\bar{q}a}{8k}$	$\frac{2.32\bar{q}a}{k\sqrt{\pi Pe}}$	$\frac{2.32\bar{q}a}{k\sqrt{\pi(1.234+Pe)}}$
Elliptical	Uniform	6.10c	$\frac{qa}{k\sqrt{Se}}$	$\frac{2qa}{k\sqrt{\pi Pe}}$	$\frac{2qa}{k\sqrt{\pi(1.273Se+Pe)}}$
Elliptical	Semi-ellipsoidal	6.10d	$\frac{3\pi\bar{q}a}{8k\sqrt{Se}}$	$\frac{2.32\bar{q}a}{k\sqrt{\pi Pe}}$	$\frac{2.32\bar{q}a}{k\sqrt{\pi(1.234Se+Pe)}}$

The flash temperature calculation in this study is done by using a slightly modified formulation. The asperity contact temperature is

$$T_a = T_{bulk} + T_{flash}$$

The bulk temperature is the temperature at which the experiment is performed. Chang et al. [182] used the expressions for flash temperature and reformulated them to include the macroscopic contact parameters, asperity radius r_a , asperity shear stress τ_a and sliding speed u_s . The expression that they developed and which is used in this current study to calculate the asperity flash temperature rise is given in equation (5-7).

$$T_{flash} = \frac{1.22 r_a \tau_a u_s}{\sqrt{\pi} \left[K_1 \sqrt{0.6575 + \frac{u_s r_a}{2k_1}} + K_2 \sqrt{0.6575 + \frac{u_s r_a}{2k_2}} \right]} \quad (5-7)$$

Here, $K_{1,2}$ and $k_{1,2}$ are the thermal conductivity and thermal diffusivity of the contacting solids.

5.5.2 Mechanical properties of tribofilm

The mechanical properties of the ZDDP tribofilm vary spatially along the plane of contact and through the thickness of the film. The mechanical properties of the tribofilm evolve with time as well. The presence of polyphosphates of varying chain lengths gives the ZDDP tribofilm the smart behaviour with properties responding to the environment. Several authors have referred to ZDDP tribofilms as smart materials [84]. The mechanical properties have been shown to vary from substrate to the surface of tribofilm as explained in Chapter 2.

The effect of pressure on elastic properties was reported in [109]. They also suggest that the variation in elastic modulus is related to a threshold value below which the change in elastic properties is not noticeable and gave the following relationship

$$E_f^* = \frac{E_{f0}^*}{H_0} H \quad (5-8)$$

Here E_f^* is the reduced modulus, E_{f0}^* is the constant value of elastic modulus before threshold pressure H_0 is reached. With temperature, no change in the value of threshold elastic modulus E_{f0}^* was observed and its value was fixed at 39 ± 4 GPa while H_0 was found to vary with temperature.

In the current study, only the change in hardness of the tribofilm with thickness is simulated. The hardness at the substrate / tribofilm interface is fixed as the hardness of the substrate while the hardness for the maximum tribofilm height is the minimum

and a linear variation is assumed in-between. The change in the elastic properties is not considered here.

Andersson et al. [22] developed an efficient method to simulate the effect of hardness variation with tribofilm growth. The method assumes a linear variation of hardness from the surface of the tribofilm to its interface with the substrate as

$$H(h) = H_{max} - (H_{max} - H_{min}) \frac{h}{h_{max}}$$

It is to be noted that the variation in hardness has a direct impact upon the plastic deformation inside the contact. Relating the tribofilm height at the contacting interface with the amount of plastic deformation, the contact is either under elastic or plastic deformation condition as

$$H_s - \frac{H_s - H_t}{h_{max}} (h' - U_p) \quad \text{if} \quad U_p < |h_1 - h_2|$$

$$H_s - \frac{H_s - H_t}{2h_{max}} (h_1 + h_2 - U_p) \quad \text{if} \quad |h_1 - h_2| \leq U_p \leq h_1 + h_2$$

$$H_s \quad \text{if} \quad h_1 + h_2 \leq U_p$$

Here, H_s , H_t , h_{max} are hardness of substrate, hardness of tribofilm and maximum tribofilm thickness, respectively. U_p is the plastic deformation and h' assumes the value of the thicker of the tribofilm value (on ball or disc). Thus, in every iteration, the hardness is updated based upon the value of plastic deformation as shown in Figure 5-4.

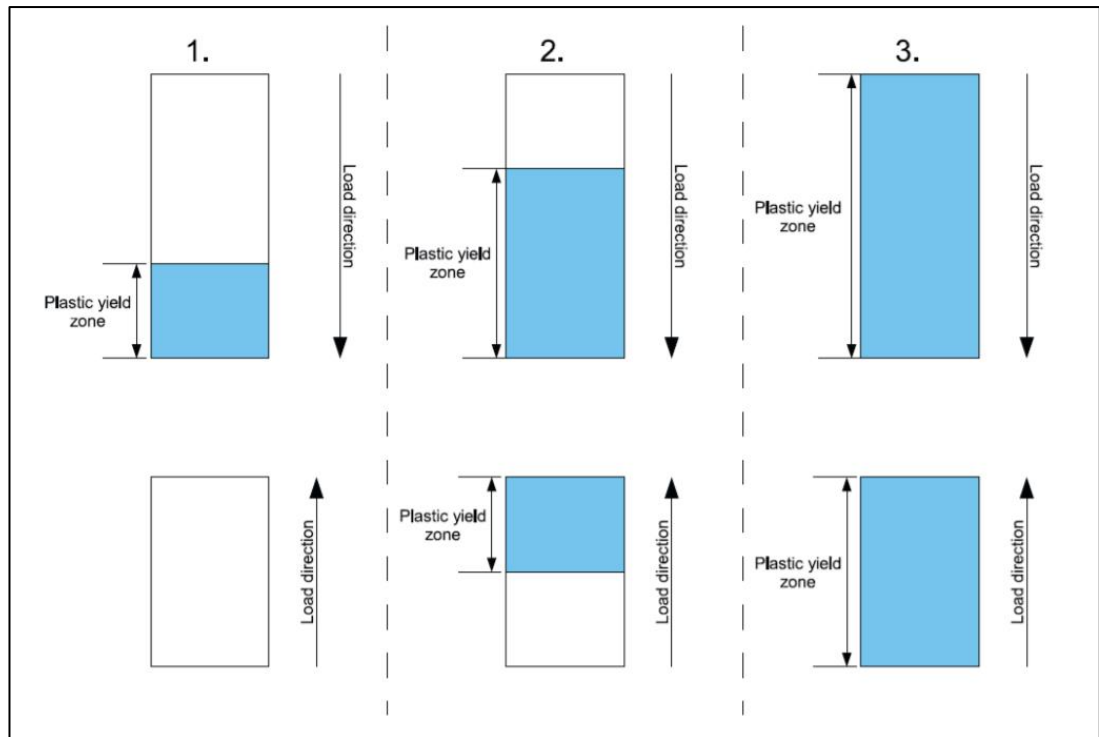


Figure 5-4: Variable hardness model for numerical simulation of mechanical behaviour of tribofilm. Case 1. Corresponds to the case where the tribofilm on one of the surfaces deforms. Case 2. Corresponds to the situation where the tribofilm deforms on both the contacting bodies. Case 3. Corresponds to complete tribofilm deformed on both the contacting surfaces. The plastic deformation has reached the substrate. Figure reproduced from [183].

5.6 Illustrative simulation of tribofilm growth

The tribofilm growth model is integrated with the mixed lubrication model to simulate tribochemistry. The model integration should take into account the scaling down of the experiments and the control of motion of individual surfaces to have different slide to roll ratios. At this stage of development, it is not possible to simulate the entire geometry of the ball and disc so the numerical domain is only capturing a snapshot of the experiment. For the results presented in this study, this snapshot corresponds to an area of 0.5mm by 0.5 mm unless otherwise stated.

The model algorithm is presented in Figure 5-5. The mixed lubrication problem is first solved to get pressure and lubricant film thickness profiles. These pressures are input to the tribofilm growth simulation model and wear model. The net effect of wear and tribofilm growth is used to modify the geometries of the contact pair. The geometry update is performed by subtracting wear and plastic deformation at each respective node while the tribofilm growth for each iteration is added to the nodal value of surface position. The updated geometry is input to the mixed lubrication model again. This process repeats for the duration of the simulation. The geometry of the ball and disc surface along with tribofilm growth on each surface are plotted with time. In every iteration the mean value of tribofilm thickness and wear on each of the counter parts is calculated and saved. The mean value presented is the arithmetic mean over the Hertzian zone unless otherwise stated. These values are used to develop the mean tribofilm thickness and wear plots presented in the following sections.

5.6.1 System and model configuration

In this section, the model is tested to generate tribofilm thickness plots. The details on how these plots are developed and the information they can give are presented in the previous section.

The mixed lubrication parameters are fixed first. A numerical grid of 129 x 129 is used. Based upon the grid justification given in chapter 3, this grid size is sufficient to get reliable results. Liu et al [80] performed detailed mesh density analysis and concluded that a mesh density of 129 x 129 is sufficient. The macro-geometry of the ball is fixed based upon the experimental values to compare with. In this particular example, the ball radius is fixed at 10 mm. The micro geometry (roughness) is generated by the method of Hu and Tonder [184] as a 129 x129 matrix of random numbers with desired R_a and R_q values. The roughness for individual surfaces is

directly input node by node to the macro-geometry of the ball and disc. Once both the surface geometries are ready, the contact between these rough surfaces is solved by the mixed lubrication solver developed in previous chapters.

The ball and disc material is assumed to be steel and the hardness for steel is fixed at 6 GPa. The hardness for the tribofilm of maximum thickness is 2 GPa. The applied pressure is 1.26 GPa and the equivalent radius of the ball, R_x is 10 mm. The wear track radius is taken as 39 mm (SKF bearing washer WS 81212). The entrainment speed is 0.25 m/s. A Newtonian lubricant with viscosity $\nu = 0.004$ Pa.s and a pressure viscosity coefficient of 14.94 GPa^{-1} is assumed. This value of viscosity is to ensure that the initial lambda ratio is 0.04. The equivalent Young's modulus, considering steel substrates is 230.47 GPa. The temperature in all simulations presented in this chapter is 90°C .

The solution to this rough surface mixed lubrication problem gives nodal pressures and lubricant film thickness values. The values of film thickness are used to determine asperity contact spots. The pressures are then compared with the yield limit for the material and truncated. These truncated pressures are then used to extract plastic deformation out of the total deformation. The plastic deformation at individual nodes is compared against the tribofilm grown on that individual node on the surface. It is to be noted that the tribofilm thickness value used for comparison is the one from the previous iteration step. This relative magnitude of tribofilm thickness and plastic deformation is used to adjust the hardness as discussed in the last section (see Figure 5-4). The final elastic pressures are input to the tribofilm growth and wear models to calculate tribofilm growth and wear of substrate. It is critical to model the interaction between the plastic deformation and tribofilm growth as this controls the contact mechanics to simulate the physics of the problem correctly.

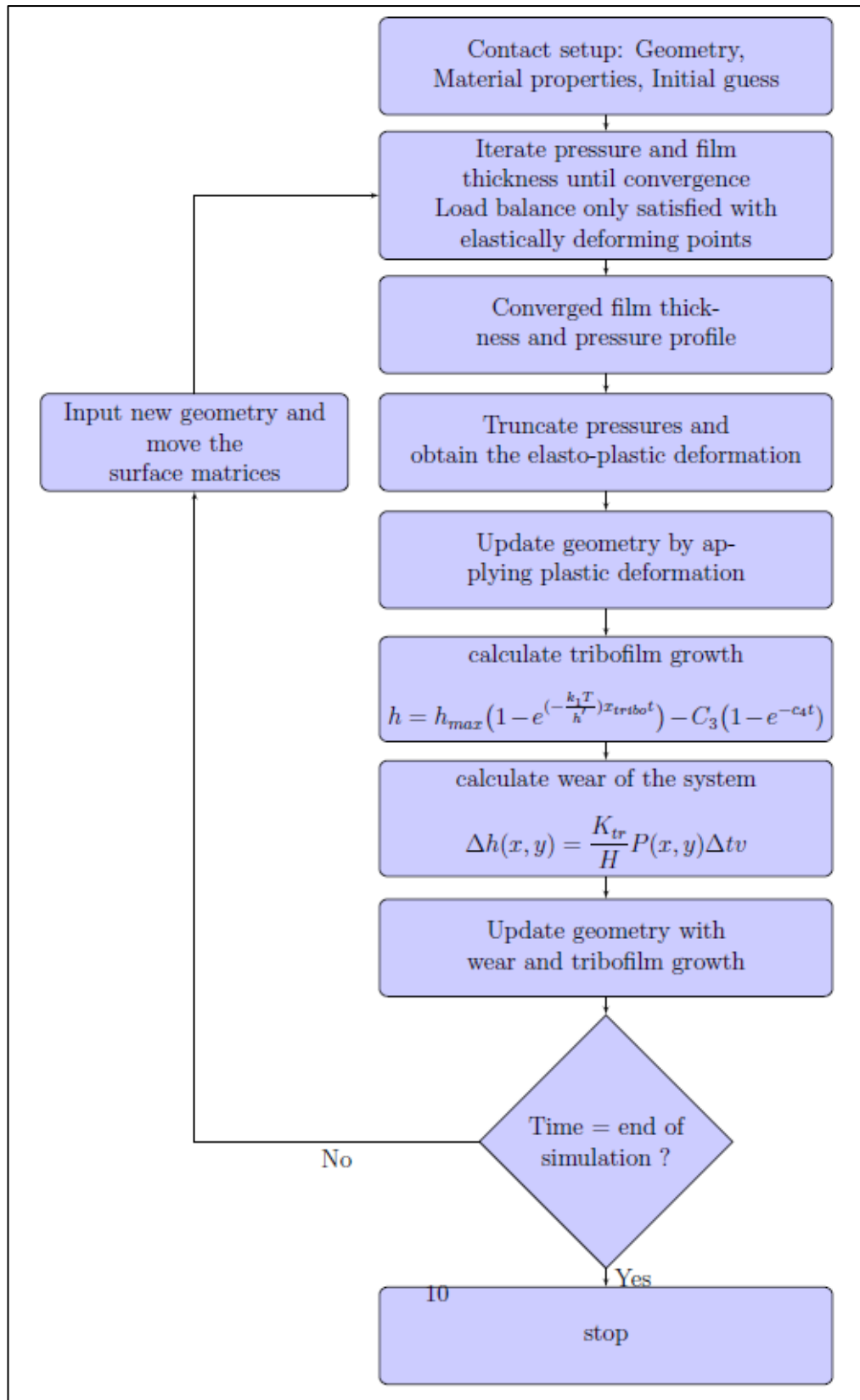


Figure 5-5: Flow chart to explain the numerical simulation of tribofilm growth / removal and wear of substrate in mixed lubrication conditions.

It is assumed that the tribofilm grows only on the asperity – asperity contacts. The effect of shear on the tribofilm growth is included through the factor x_{tribo} . The simulation results presented in this chapter are close to boundary lubrication with an initial lambda ratio (ratio of central film thickness to the composite roughness of both surfaces) of 0.04. Therefore the above assumption is valid. The geometry of both the contacting surfaces is changed before the next loading cycle by modifying two key aspects of the contact. First, the geometrical features are changed by the plastic deformation, wear and tribofilm thickness to evolve the system and the second change is actually an indirect change occurring because of the different speeds of movement of both surfaces. The movement changes the individual asperities inside the Hertzian contact region and controls the number of times the rougher surface moves through the contact.

The tribofilm growth calibration parameter values used are from the work of Ghanbarzadeh et al. [120]. They calibrated the tribofilm growth parameters h_{max} , x_{tribo} , C_1 and C_2 , based upon the experimental results of Naveira Suarez [114]. The roughness of the tribopair are kept the same in this study as well, 100 nm for disc and 10 nm for ball. Based upon the loading conditions, an area of 0.5 mm x 0.5 mm is simulated.

5.6.2 Tribofilm growth results and analysis

The tribofilm forms only on contacting asperities. The contacting asperities undergo high shear and pressure and an example of the tribofilm growth is given in the following Figure 5-6.

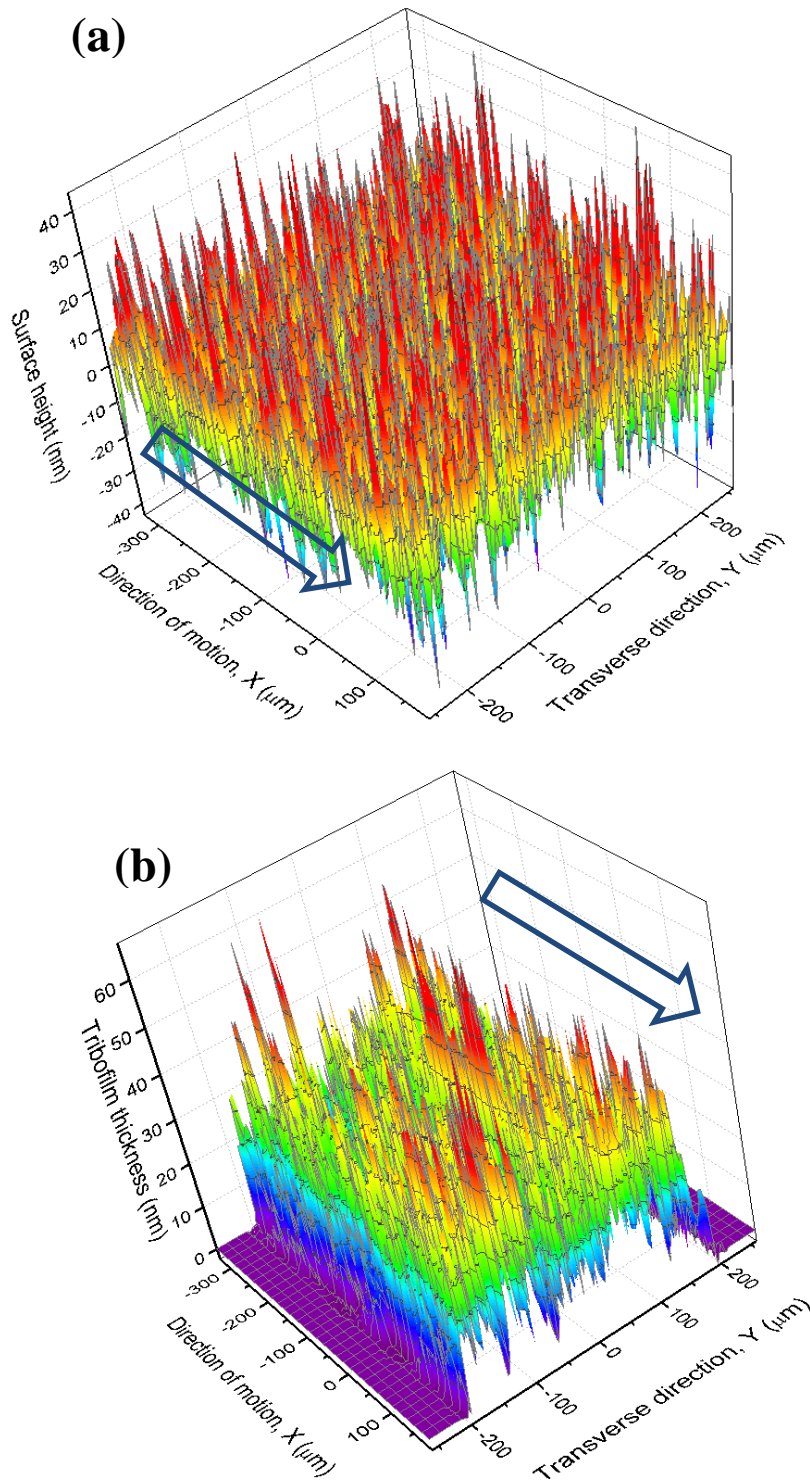


Figure 5-6: The growth of tribofilm on rough surface. (a) the original rough surface. (b) tribofilm formed on rubbing track. The rubbing track is aligned with the X-direction. The direction of flow is indicated by the arrow.

The results presented in Figure 5-6 show how the tribofilm grows only in the rubbing tracks. The tribofilm thickness can be monitored with time. The film thickness evolution can be monitored through time and space. The ability to observe the tribofilm behaviour at the local level is a big achievement.

In the next sections, some detailed results for tribofilm growth are presented.

5.6.3 The patchy growth of tribofilm (3-D evolution of tribofilm)

The tribofilm grows on surfaces in a patchy fashion. The tribofilm growth has been shown to be inhomogeneous and has been observed experimentally as well [96]. The inhomogeneity in the growth behaviour of ZDDP is linked to the roughness of the surface. When rough surfaces come into contact, the load is distributed among the lubricant and solid contacting asperities. The asperities carry load and undergo higher shear stresses. This results in more growth and different film formation and removal at different spots in the contact giving rise to inhomogeneous growth at different areas of the surface. Due to the relative movement of the contacting surfaces, the model predicts patchy and inhomogeneous tribofilm growth. This inhomogeneous growth gives rise to different wear behaviour at different areas of the surface. Figure 5-7 gives the evolution of tribofilm formation with time. A snapshot of tribofilm thickness and coverage for different instances is shown and the pad like structure of the tribofilm can be seen.

It can be seen that the tribofilm grows with time not only in thickness but the coverage area also increases. There are several reasons for why the area of tribofilm coverage increases. The process is dynamic. The tribofilm growth interacts with wear and plastic deformation. Thus more and more asperities come into contact due to flattening of the high asperities. From the results of tribofilm growth this can be observed clearly.

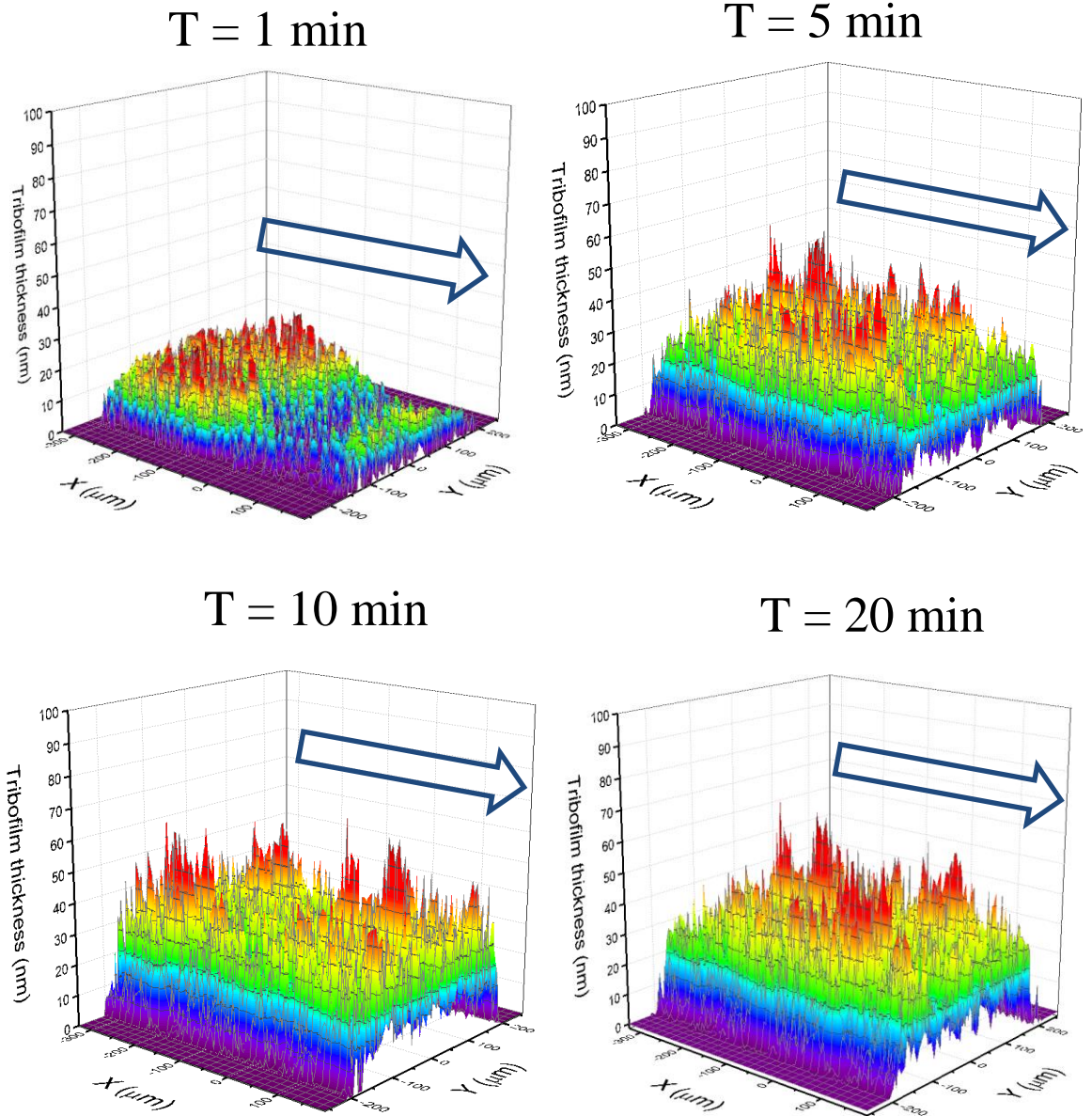


Figure 5-7: ZDDP tribofilm formation in the rubbing track. Coverage and thickness of tribofilm increases with time as well as the mean tribofilm thickness. Arrows point to the direction of flow. An area of **0.5 mm x 0.5 mm** is shown.

The severe loading inside the contact region results in asperities undergoing high plastic deformation and wear and consequently, this reduces the height of asperities. Thus more asperities come into contact and real contact area increases. Thus the tribofilm forms on a greater area and eventually covers the whole surface of the rubbing track. The ability of the model to capture this pad-like structure of ZDDP

tribofilm growth is great achievement as this fact has been experimentally observed as well [85].

5.6.4 Tribofilm growth on smooth counterpart surface (Ball, $R_a = 10$ nm, $R_q = 12$ nm)

The mean tribofilm growth on the surface is the sum of the tribofilm formed on all the rubbing track. The rubbing track is defined as the distance along the wear track with the width equal to the Hertzian contact diameter. It should be noted that the wear track width increases with time due to wear and plastic deformation of ball and disc. Thus, in the current model, the mean values of tribofilm growth are presented for all the points on which the tribofilm forms on either surface while the points with zero tribofilm thickness are excluded.

The tribofilm formation behaviour on the ball and disc is not very different. The tribofilm formation takes more time to reach a mean value on the ball compared to the tribofilm formation on disc. The main reason being the roughness of the counter bodies being very different. The ball is almost 10 times smooth compared to the disc and thus, experiences less severe pressures on individual asperities compared to the disc. The second reason to this difference is the different individual speeds of the two surfaces which gives rise to slide to roll ratios. Therefore, a stronger overshoot is observed in the mean tribofilm thickness value on the ball as seen in Figure 5-8. The SRR is fixed at -2.0 % for all the tribofilm growth graphs presented in this chapter. The tribofilm coverage was also studied and it was found that the smooth surface has a tribofilm growth pattern that gives full coverage of surface very quickly but the mean tribofilm thickness value is lower compared to the rough surface tribofilm thickness value.

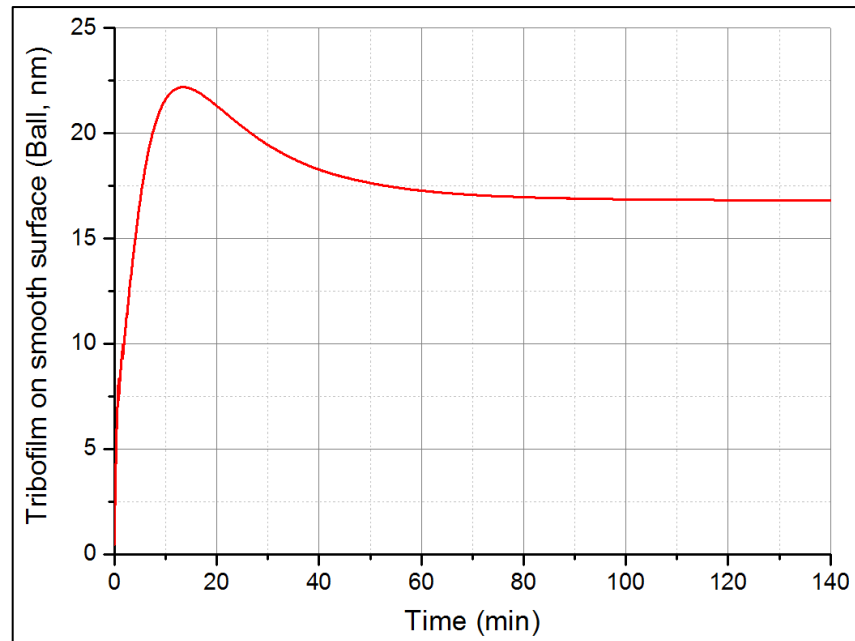


Figure 5-8: Mean tribofilm thickness on the smoother counterpart. (Ball surface roughness, $R_a = 10$ nm, $R_q = 12$ nm)

5.6.5 Tribofilm growth on Rougher counterpart surface (Disc, $R_a = 100$ nm, $R_q = 127$ nm)

The tribofilm growth on the rough counter-part is similar to that of the smooth surface case as shown in Figure 5-9 but some differences exist. The tribofilm coverage is low but the tribofilm mean thickness value is considerably high and establishes very quickly. This is expected as the rougher surface will have more inhomogeneity in the tribofilm growth behaviour and thus, the wear is also more non-uniform due to the wear reducing effect of tribofilm. The tribofilm grows to near maximum height at some of the contact points while the tribofilm growth at some of the asperities inside the contact is still very low and near zero. The overshoot in the mean tribofilm growth is less prominent for the rougher counterpart. Experimentally, the overshoot is linked to the removal of the tribofilm. The removal of tribofilm has been modelled in this study and thus, its effect on surfaces with different roughness values is also observed and is a very strong edge of our model. The overshoot can also be linked to the lower

coverage of the tribofilm on the rougher surface. The severity of the contact in case of rougher surface gives the tribofilm formation behaviour in which formation is dominant while for the smooth counterpart, the tribofilm coverage is more so more removal is observed.

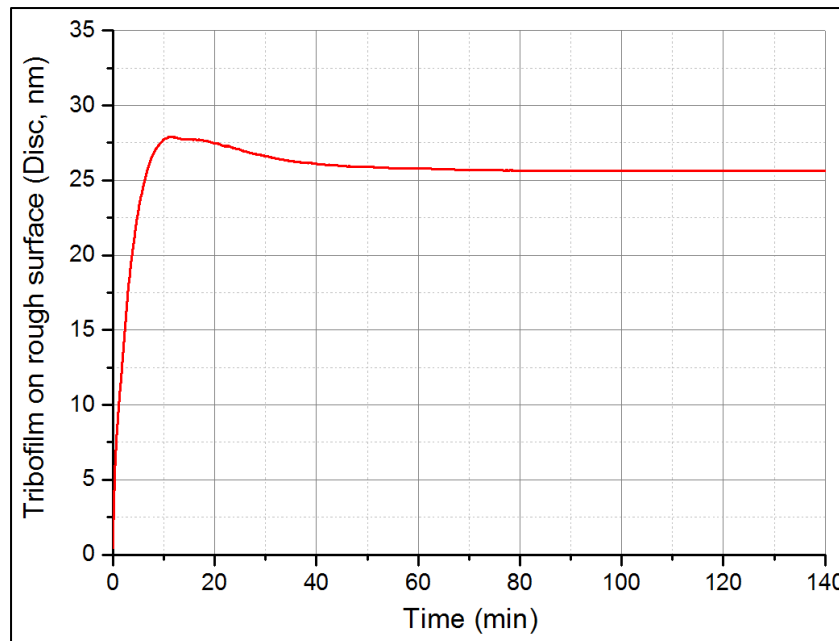


Figure 5-9: Mean tribofilm thickness on the rougher counterpart. (Disc surface roughness, $R_a = 100$ nm, $R_q = 127$ nm)

The tribofilm growth and removal can be simulated with confidence with the developed model.

5.7 Effect of slide to roll ratio on the tribofilm growth

In this section, the tribofilm growth on the smooth counterpart (the ball) is presented for different values of slide to roll ratio. The smoother counterpart in our case is the ball for which the roughness is fixed at $R_a = 10$ nm and $R_q = 12$ nm. It can be seen from the results presented in the last section that the tribofilm grows for a smoother counterpart with overall smaller values of mean thickness but more coverage and a more pronounced overshoot as was shown in Figure 5-8.

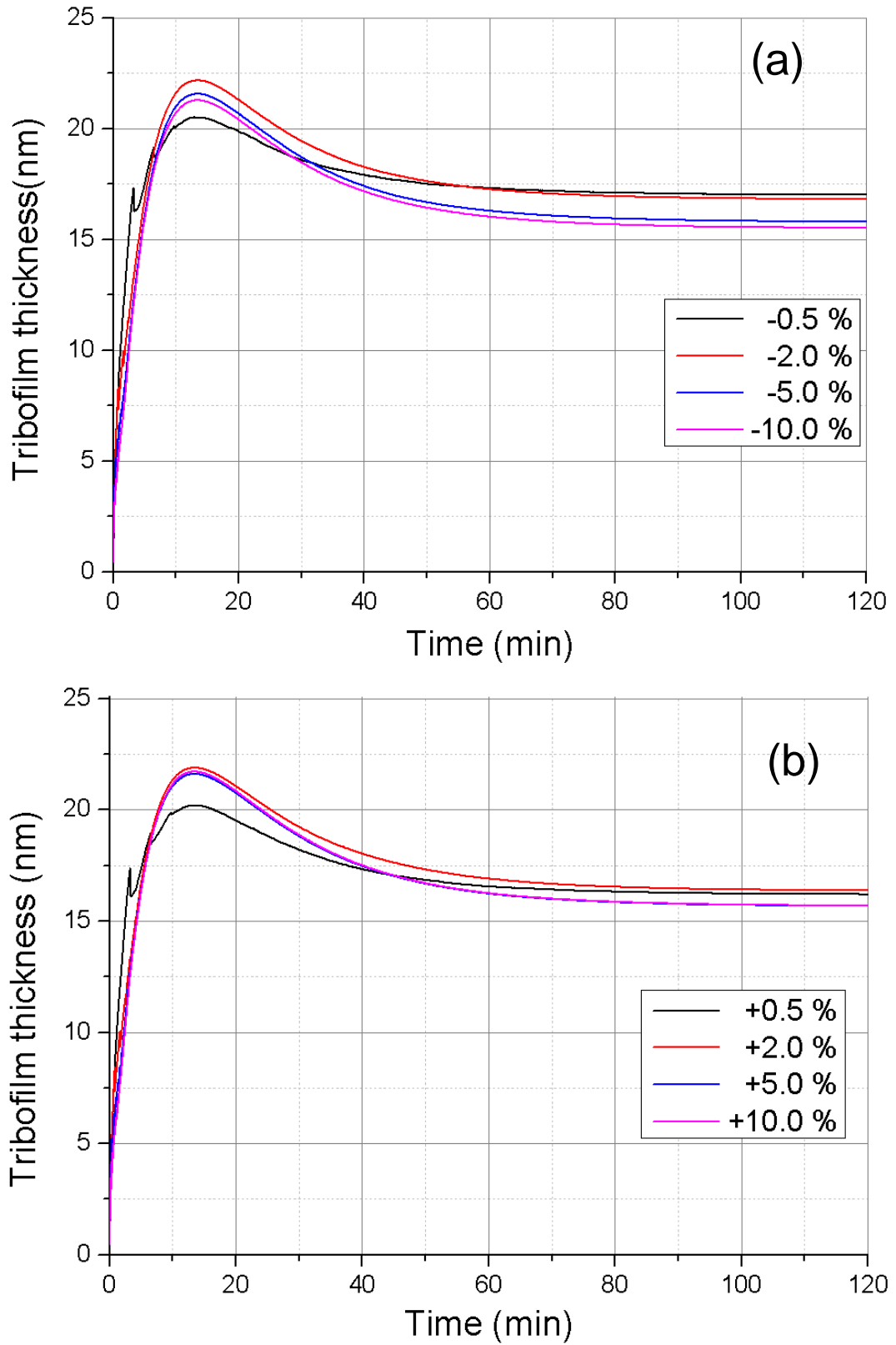


Figure 5-10: Tribofilm growth and mean tribofilm thickness as a function of time for different slide to roll ratios on the ball. (a) negative SRR values. (b) positive SRR values.

The slide to roll ratio represents the amount of sliding present in the contact configuration. This sliding results from the different speeds of the two surfaces.

$$SRR = \frac{2(U_{ball} - U_{flat})}{U_{ball} + U_{flat}} \quad (5-9)$$

According to this definition positive slide to roll ratios correspond to the ball moving faster while the negative slide to roll ratios correspond to the flat / disc moving faster. Thus, the results presented in this section should be analysed with this relative speeds in mind.

The numerical parameters are kept the same as defined in section 5.6.1. In the results presented in the previous sections, the slide to roll ratio was fixed at -2 %. Now the slide to roll ratio is changed from -10 % to +10 %. The results for the tribofilm growth are presented for four representative values of tribofilm growth in the positive and the negative range as shown in Figure 5-10. A trend in the tribofilm mean thickness values can be observed for different SRR values.

The mean tribofilm thickness is almost the same for both the positive and the negative SRR values and no matter what differences exist between the initial tribofilm growth behaviour, the mean tribofilm thickness values all reach a similar value. This behaviour has been reported by Naveira-Saurez [114] as well and will be discussed in the next section. Thus, the model produces the experimentally observed qualitative trends successfully. Observing the trend by moving from the negative SRR, -10 % to the positive SRR, +10 %, it can be seen that the tribofilm thickness values overshoot is linked to the SRR. For higher values of SRR, the overshoot is more obvious.

5.8 Model validation and discussion

The tribofilm growth model used in this work is adopted from the work of Ghanbarzadeh et al. [120]. The growth model requires fitting of experimental values and the values for the fitting parameters used in the current simulations were also adopted from their work and have been given in the previous section. They present their results in two forms: either taking the average over all the nodes in the simulation cell or taking the average over all nodes where the tribofilm thickness is greater than 80 % of the maximum value of tribofilm thickness in a single step. They refer to the latter as the mean over maximum tribofilm thickness values. The results presented in this section are for the average over all nodes.

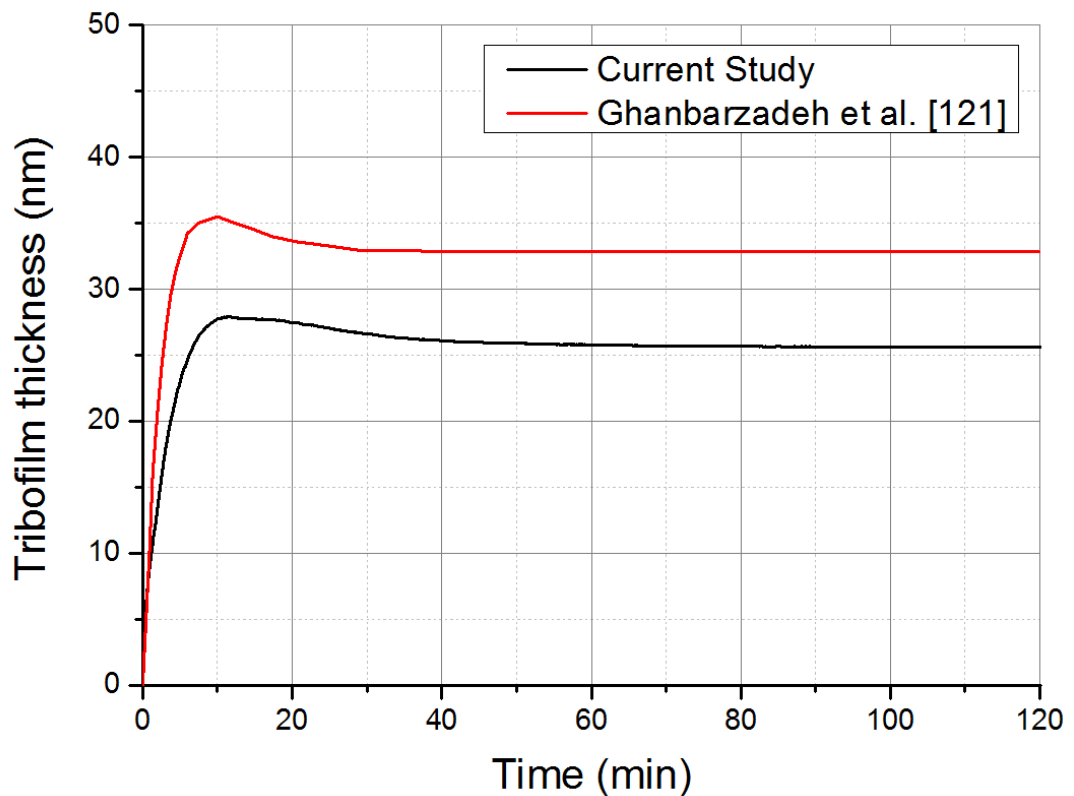


Figure 5-11: Comparison of tribofilm growth from current model against the work of Ghanbarzadeh et al. [120]

In the previous sections, the tribofilm thickness values presented are for the mean over the complete numerical solution domain by the tribofilm thickness at each node and taking their average over all nodes. But only the nodes with non-zero tribofilm thickness values are included.

The tribofilm thickness values from the current model compare and agree very well with the tribochemical models in boundary lubrication. The results in Figure 5-8 are reproduced along with the results from Ghanbarzadeh et al. [120]. A comparison of tribofilm thickness values for the slide to roll ratio of -2 % are presented. The values of tribofilm thickness from the current study agree very well with their results. The qualitative match is very good but the magnitude of predicted tribofilm mean thickness is lower, see Figure 5-11.

There can be many reasons to this difference. First of all, the presence of lubricant inside the rubbing track can carry a significant amount of load but based upon the assumption of tribofilm growing only on the contacting asperities, does not contribute to the tribofilm growth. Thus, the tribofilm growth and wear cause a reduction in the load carried by the asperities and tribofilm growth reduces with time. This reduction is in addition to the reduction in tribofilm growth due to the self-limiting nature of tribofilm. Thus, overall lower values of tribofilm thickness are expected. Secondly, the simulation area in the current study is orders of magnitude bigger compared to the existing boundary lubrication solvers. This causes differences in the values of tribofilm formation due to statistical inconsistencies. Here, the tribofilm is simulated in the entire wear track and averaging is performed for the complete wear track. Thirdly, the tribofilm growth model in the current study requires integration with the plastic deformation model. The plastic deformation model in the current study simulates plastic deformation irrespective of the state of contact i.e. the fluid pressure

can also cause plastic deformation. This may cause reduced tribofilm growth and ultimately, the tribofilm thickness values, due to differences in the plastic behaviour. The work of Ghanbarzadeh et al. [120] is centred around fitting the tribofilm growth model parameters to experimental parameters. They use experimental results from the study of Naveira-Suarez [114]. Andersson et al. [22] also developed a tribofilm growth model and fitted their results to the experimental values of tribofilm thickness values from Naveira-Suarez [114]. Thus, next results are plotted for the tribofilm thickness values from the current model against the values predicted by the model of Andersson et al. [22]. Comparison of Figure 5-12 and Figure 5-13 shows that the differences in the predictions from the current model and their results. It is to be noted that the geometrical and working conditions for the simulation results presented in figure Figure 5-12 are similar to the work of Andersson et al. [22] who performed simulations to capture the tribofilm growth behaviour observed by Naveira-Suarez [114]. The results agree well but again the predicted values are, once again, comparatively lower.

The key difference being the presence of overshoot in our model due to inclusion of removal of tribofilm. This feature was absent in Figure 5-13. A comparison of the plots also shows that the effect of SRR on the mean tribofilm thickness produced by the developed model give a very good quantitative match. The mean tribofilm thickness is lower for higher values of SRR and increases with decreasing values of SRR. This is confusing as the sliding is considered to be the main cause of shear and higher tribofilm growth in rubbing contacts.

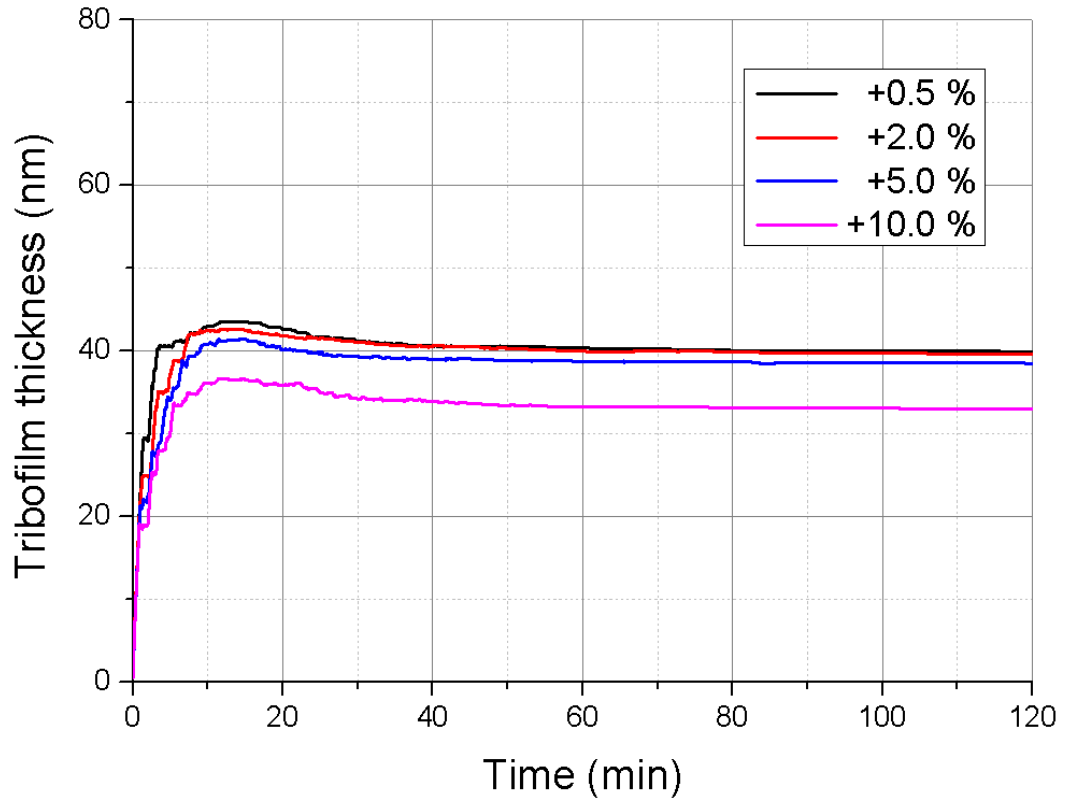


Figure 5-12: Tribofilm thickness values as a function of time for different values of positive SRR.

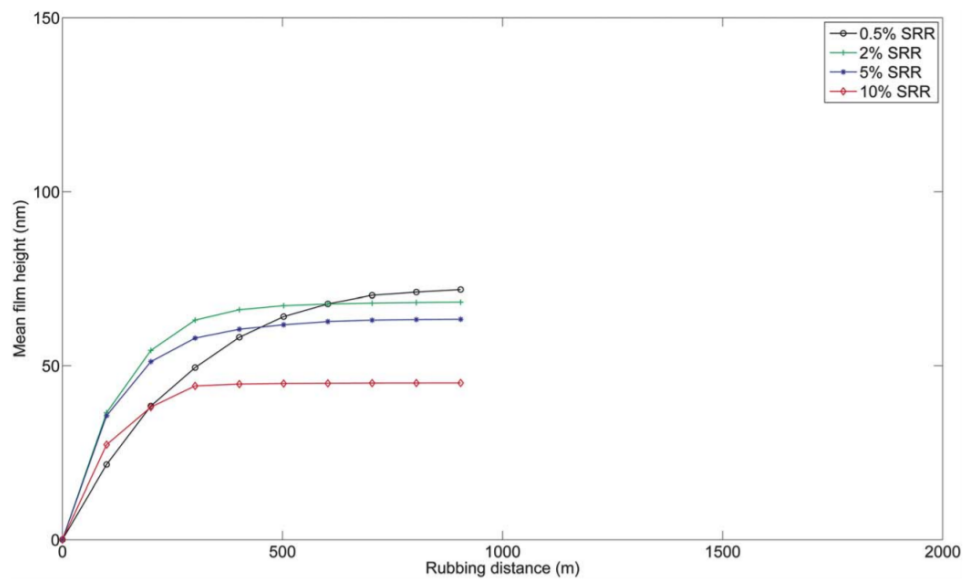


Figure 5-13: Tribofilm thickness results from Andersson et al. [22]

This may be true for contacts where the roughness of counterparts is the same. But the results in Figure 5-12 have been produced for the contact between a smooth ball and a rough disc and the results are presented for the smoother counterpart. Thus, the reason for the increased value of tribofilm thickness with decreasing SRR is not sliding. The main reason here is that positive SRR values correspond to faster movement of ball and thus, for a single loading cycle on the disc / flat, the ball undergoes more cycles and vice versa. A greater magnitude of positive SRR would mean the same. Thus, a smaller value of SRR means that the disc / flat undergoes a relatively greater number of loading cycles for the same number of loading cycles considered for the ball. Therefore, more passes of the rougher counterpart will result in higher values of tribofilm thickness.

Next simulations are performed to compare the tribofilm growth results from the current model against experimental results from Parsaeian et al. [185]. The tribofilm growth parameters for running current simulations have been taken from the work of Ghanbarzadeh et al. [175]. The tribofilm growth was simulated for different values of temperature. Three values of temperature were used i.e. $T = 60^{\circ}\text{C}$, $T = 80^{\circ}\text{C}$ and $T = 100^{\circ}\text{C}$ and the concentration was taken as 1% wt ZDDP.

The diameter of the ball and disc was 19.05 mm and 46 mm, respectively. The value of SRR is 5%. The roughness of the ball and disc is 20 nm and 130 nm, respectively. The Hertzian contact pressure is 1.15 GPa and the entrainment speed is U_r is 0.1 m/s. The lubricant viscosity and the pressure viscosity coefficient are fixed to get the lambda ratio of 0.04. The results for the tribofilm growth from the current model are presented in Figure 5-14 along with the experimental results. The model produces experimental results with good accuracy. These tribofilm thickness results also quantitatively compare very well against the modelling results of Ghanbarzadeh et al. [175] but the once again, the overshoot is not produced quite well. The experimental

tribofilm thickness values also show very subtle presence of the overshoot as shown in Figure 5-14.

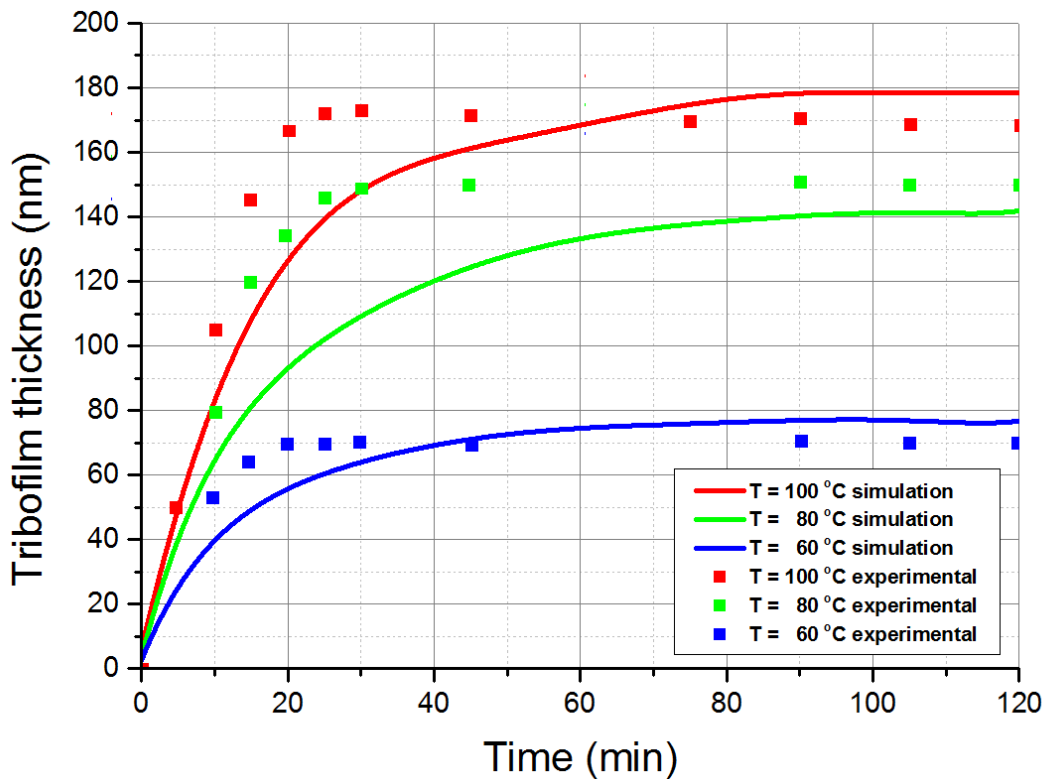


Figure 5-14: Experimental validation of tribofilm growth results. Experimental results are digitized from the work of Parsaeian et al. [185].

The tribofilm thickness values produced by the current model are within the experimental error range. Although the mean tribofilm thickness produced by the current simulation method are very similar to the experimentally observed values, the pathway to reach the mean tribofilm thickness is different. The simulation results show a steady growth of tribofilm over a longer period of time in the 2 hour experiment whereas the experimental results show very quick growth of tribofilm and the mean tribofilm values are established in the first 20 to 30 mins.

5.9 Summary

The current chapter outlines a robust numerical procedure for incorporating tribochemistry into a mixed lubrication model. The mixed lubrication model is based upon the unified solution algorithm and thus, the lubrication regime can be controlled as well as monitored from full film down to boundary lubrication. Therefore, the model enables the study of not only the effect of lubrication quality on tribochemical behaviour but the effect of tribofilm formation and wear on lubrication parameters as well. This latter part is the topic of next chapter.

The tribofilm model when integrated with the mixed lubrication model, enables the simulation of tribofilm growth. The tribofilm growth changes the local physical and mechanical properties of the surface locally. This local change in interfacial behaviour changes the macroscopic behaviour of the contact through friction and wear.

The tribofilm growth model requires fitting of key parameters to experimental data. In the current framework, the values of fitting parameters were used from the literature. The different factors driving ZDDP tribofilm growth are reviewed and discussed in the context of the model. The modelling studies until now mainly consider the growth under boundary lubrication conditions while the current model takes the lubricant physical properties into account. Several approaches to model the tribofilm growth are available in the literature but the current model is chosen as the fitting parameters are available for a range of experimental conditions. The ZDDP tribofilm growth can be simulated for different roughness and different slide-to-roll ratios, in fact, the model can be adapted to most experimental configurations. An inhomogeneous tribofilm growth was observed which is in line with experimental findings. The relative importance of surface coverage and plastic deformation and wear is highlighted and the reasons for inhomogeneous tribofilm growth discussed.

The experimental studies observe the growth of tribofilm using the spacer layer interferometry method (SLIM) and report the tribofilm growth on the ball surface. The tribofilm growth on the disc cannot be observed using the SLIM apparatus. The tribochemical mixed lubrication model developed is able to capture tribofilm growth and wear on both the counter parts. Thus the tribofilm growth on the smoother and rougher counterparts are presented separately and the reasons for the qualitative and quantitative differences discussed. The ball surface (smoother) covers faster to reach full coverage while the disc surface (rougher) covers slow and only reaches full coverage asymptotically.

The tribofilm formation and removal and the distinction between removal of tribofilm and wear of substrate will give exciting information about the internal working of the contact mechanics and its interaction with lubrication. The tribochemical model considers the mechanical properties of the lubricant, the tribofilm and the substrate. The difference in the lubricant additives and additive concentrations is controlled by experimental fitting. This makes the model semi-analytical. But this is also the strength of the model. The experimental fitting parameters make it possible to adapt the set up to experiments. The model can distinguish between the macroscopic as well as microscopic features of the contact. The microscopic contact parameters like the nodal pressures, lubricant film thickness and elastic and plastic deformation can be linked to the macroscopic parameters like friction and wear. The ability to scale down the experiments to simulate exactly similar conditions makes the model much more robust and useful. This is because by simulating a finite area, the key contact characteristics describing the contact mechanics, lubrication and tribochemical parameters can be calculated and matched to real experiments.

The growth of tribofilm in the mixed lubricated contact is simulated. A comparison of tribofilm growth behaviour for different values of SRR shows that not only the

presence of sliding but the relative roughness of each surface and their relative speeds of movement also affect the tribofilm growth behaviour. The tribofilm growth behaviour produced by the current method gives very good qualitative match with the published simulation results but quantitative differences exist. These differences are within the experimental error range of MTM-SLIM experiments. The tribofilm growth model was also compared experimental results of tribofilm growth and the current model produces mean tribofilm thickness values that are in good agreement with experimental values but the pathway to reach the steady mean values is not very well reproduced. Despite these differences, the current model gives a very powerful analysis tool to study the growth of tribofilm in the contact mechanics where the lubrication regime can range from full film to full dry contact conditions. The presence of lubricant and its effect on tribofilm growth can be studied and most importantly, the effect of tribochemical film growth on the lubrication parameters can be studied.

Chapter 6

Interfacial Mechanics:

The interaction between tribochemistry and

lubrication science

This chapter outlines the effects of tribofilm growth on the mixed lubricated contact. In section 6.1, a background to the interfacial mechanics concept is given. The most important parameters in mixed lubrication are the lambda ratio, contact area ratio, contact load ratio and the central film thickness as outlined in section 6.2. These parameters are significantly affected by the tribochemical film growth.

The experimental as well as numerical studies mainly present the starting values of the lambda ratio while these mixed lubrication parameters are not modelled and are experimentally not measurable. The results are presented in section 6.3 for an illustrative case. The results are presented using two sets of simulation cases. The first set of simulations and the corresponding results are presented in section 6.3.4 and are meant to illustrate the evolution of key lubrication parameters over time. The second set of simulations are performed with more realistic values closer to experimental conditions and aid discussion on the hypothesis presented in this chapter. This results from this second set of simulations are given in section 6.3.5.

To date there has been no study dealing with this problem and this is the first attempt to capture the interfacial mechanics of tribofilm growth to link the science of lubrication and contact mechanics with the tribochemical phenomenon.

6.1 Background to problem

The first successful EHL solution appeared in 1951 with the pioneering study of Petrusevich [186]. Since then for the last 60 years the field of EHL study has been continuously evolving. Although the mixed lubrication models have evolved from the study of EHL, conceptually, EHL and boundary lubrication are special cases of mixed lubrication.

Initially, the EHL models were mainly developed for smooth surfaces or artificial roughness. Full film conditions were considered and asperity contacts were not present in these models. Then stochastic models appeared that considered the effect of roughness and could only handle mild contact conditions ($\lambda < 0.5$). Real surfaces are rough and the roughness and lubricant film thickness are comparable. Thus, it is very difficult to have a full film contact in practice. Mixed lubrication is the state of lubrication where both fluid film and solid contacts are present. The machine elements generally operate in this lubrication regime or at least experience mixed contact conditions during start up and slow down of the contact.

The studies focusing on lubrication transition should consider mixed contact as a crucial element. Thorough understanding of the mixed lubrication behaviour is also critical for comprehending and eventually modelling the failure of machine components. The mixed lubrication analysis can give detailed information about the contact performance in terms of deterministic maximum pressures and minimum film thickness. These can be used to extract macroscopic variables like friction, flash temperatures and the surface and subsurface stress values. Developing experimental setups and numerical models to study mixed lubrication are therefore, the need of the time.

The mixed lubrication model developed in chapter 3 is based upon the unified solution algorithm. This model is capable of simulating the entire transition from no fluid film to full EHL film and the roughness can be input in every form ranging from the simplest cases of single asperity calculations to more complicated case of artificial sinusoidal roughness calculations to real random roughness calculations. The roughness can be computer generated, as done in this work, or real random roughness measured experimentally input to the simulation model as a collection of surface height values. The orientation of roughness can also be controlled by using appropriate mathematical functions. This is a great achievement. The idea for unified solution of EHL problems was first given by Zhu and Hu [75] in 1999. Then Holmes et al. [78] proposed a unified solution model to solve the mixed lubrication problem in gear applications. Li and Kahraman [79] presented a unified solution to the EHL problem based upon the asymmetric integrated control volume approach to overcome grid dependence of the previous EHL solutions methods. The basic idea is to solve the mixed lubrication problem by using the Reynolds equation to calculate the contact and fluid pressures.

The unified algorithm has been improved in many ways. During the last 15 to 20 years, there has been many refinements to the method. Wang et al. [187] implemented the DC-FFT method into the unified algorithm. This improved the calculation efficiency significantly. EHL solution algorithms are prone to mesh dependency and this issue was addressed by Liu et al. [80]. Then Zhu [82] clarified the concept of definition of contact as a limiting value of lubricant film thickness and suggested a range of acceptable mesh densities. These ideas were further discussed and clarified by Wang et al. [83] who compared the solutions from unified algorithm using Reynolds equation with the boundary lubrication solver. Then Wang et al. [188] devised a method to simulate interasperity cavitation in unified solution algorithms

by combining the concepts of fractional film defect given by Jacobsson and Flodeberg [189] and the mass conserving algorithm proposed by Elrod [190].

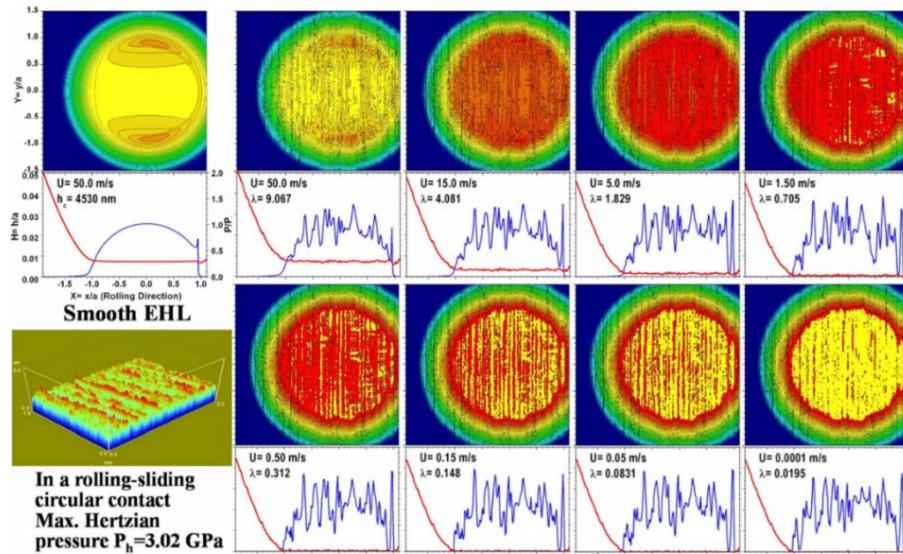


Figure 6-1: The state of the art in unified mixed lubrication models being able to predict the contact parameters through all the lubrication regimes [20, 76, 82].

The current status of the unified mixed lubrication models is presented in Figure 6-1 where the pressure and film thickness can be predicted deterministically through all lubrication regimes. No effort has been made until now to include the tribochemical effects into the unified algorithm. The potential reason behind this can be the definition of asperity contact. Boundary lubrication is defined as the state where contact characteristics are dominated by asperity contacts and the state of contact is considered as the absence of any lubricant hydrodynamic film. This concept requires a second thought as the dry contact condition is defined using continuum principles and the contacts are rough at the atomic scale where the atomic interactions control interfacial chemical phenomenon. The limitations on the use of continuum models to describe contact mechanics were studied and discussed by Luan and Robbins [191]. They suggest that the continuum assumption breaks down as the atomic dimensions are reached. The lubricant also loses its continuum nature and starts to dissociate at

the interface as suggested by the work of Spikes [192] and Luo et al. [193] and recently pointed out by Zhu and Wang [20]. Thus, the unified solution model is not suitable for representing any atomic scale effects in its conventional implementation. In the previous chapter, chemical interactions are included, in an approximate but clever way, in the unified solution model to solve the mixed lubrication problem. The growth of tribofilm under mixed lubrication conditions was presented and validated against published simulation results, in the previous chapter.

In engineering components, power is mainly transmitted through interfaces. Several complex phenomenon are taking place simultaneously at these interfaces and the problem is a true multiphysics problem requiring integration of relevant branches of science as shown in Figure 6-2. The ultimate goal is to include advanced theories to simulate such complex interface by releasing the assumptions one by one. A model enabling the study of complex interfacial phenomenon where several physical phenomenon occur simultaneously is required [20].

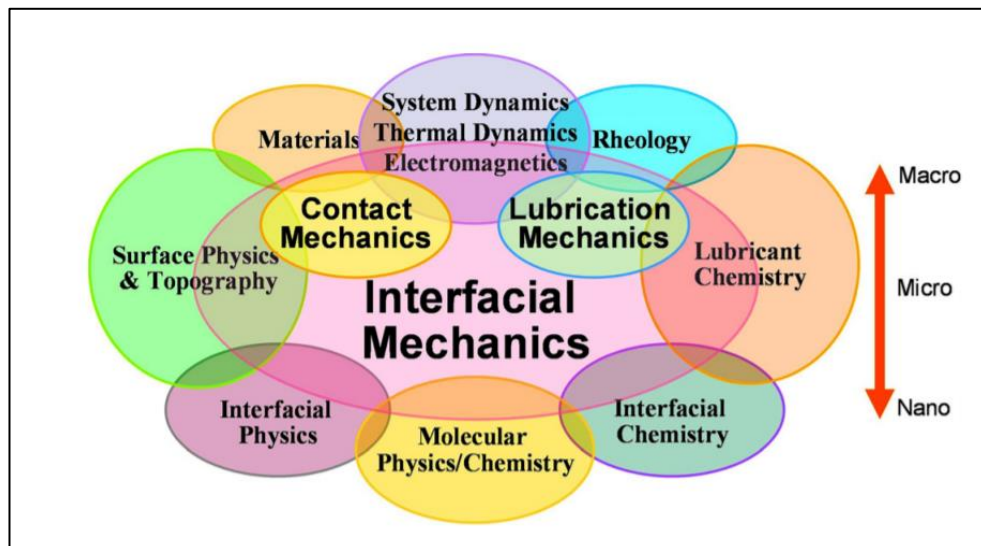


Figure 6-2: A glimpse of complex phenomena happening at the interface [20].

Zhu and Wang [20] in their recent review on EHL literature stress on the importance of including the micro- and nano-scale properties of interfaces as these strongly affect

the macroscale contact performance as shown in Figure 6-2 . Therefore, a multiscale analysis approach is required.

Some studies using molecular dynamics simulations have started to appear [194, 195] but these are limited to fundamental understanding of the interfacial phenomenon. An engineering model capable of bridging the gap between the micro- / nano-scale phenomenon and the macroscale contact performance parameters is still missing.

This gap is filled by the model developed in the current study. Our model successfully bridges the gap between **lubrication**, **contact mechanics** and **tribochemistry**. This overcomes the continuum restriction as described earlier. Thus a powerful tool capable of analysing interfacial phenomenon is developed. It enables design of lubricants considering interfacial mechanics and vice versa. Such models are the need of time and give a platform for future development by incorporating more physics.

6.2 Terminology update for describing mixed lubrication

The parameters to define the mixed lubrication regime are redefined to describe the results consistently with the EHL parameters. The commonly used terms like central film thickness, minimum film thickness and lambda ratio (ratio of central film thickness to composite roughness) are no longer defined in the traditional way as used in EHL literature. The lambda ratio has been defined by several authors in different ways. Thus, to describe mixed lubrication, lambda ratio has to be redefined to describe the comprehensive lubrication characteristics. In the following, some key parameters are defined and the importance of these changes is highlighted.

6.2.1 Minimum film thickness (h_m)

The term minimum film thickness is no longer valid. In EHL analysis this minimum film thickness parameter is given great importance as it is related to the design of

components. In mixed lubrication the coexistence of asperity contacts and lubricated regions means that the minimum film thickness is always zero. The asperity contacts are always present. It is important to note that this minimum film thickness is no longer fixed in space and is a highly localized transient parameter that changes in space with time. This complicates the design process. Therefore, the use of minimum film thickness is no longer a key parameter to describe global lubrication characteristics.

6.2.2 Central film thickness (h_c)

The conventional definition of central film thickness is based upon the formulae developed long ago. These formulae were developed for smooth surface EHL cases. Therefore this formulation needs modification to use it for rough surface EHL cases. Zhu and Ai gave an idea to describe the global lubrication characteristics in rough surface EHL and mixed lubrication cases by defining an average value of film thickness. Their definition of average film thickness assumes an average of film thickness values within a pre-set radius from the centre of the normalized Hertzian contact region. A value of $\frac{2}{3}$ times the Hertzian contact radius was suggested and this value has been consistently used in this study as well. It is to be noted that this radius actually defines the window of analysis and the size of this window of analysis is not fixed. To fix its size a general criteria proposed in this study is to include a sufficient number of data points in this window so that the calculated average values are smooth. But too large values should be avoided to avoid the effect of edges on the boundary of contact domain.

The advantage of using this type of formalism is that when a full lubricant film is present, this value is very close to the value of central film thickness obtained from the conventional formulae but when the contact is in a mixed or boundary lubrication

regime, this film thickness value is identical to the average gap that was defined by Jiang et al. [11]. There is a trade-off between choosing a sufficiently large value of this window to get better averaging and avoiding edge effects. The number of points should be enough to minimize the effect of small asperity movements but at the same time, edge effects should not dominate this average film thickness value [76]. The average film thickness can also be called average gap when the lubrication regime is close to boundary.

6.2.3 Film thickness ratio (lambda ratio / λ ratio)

The term λ ratio is defined as the ratio of average film thickness (defined above) to the composite roughness inside the contact. For the last 50 years, the lambda ratio has been used as a universal parameter to describe the global lubrication behaviour. The presence of roughness makes its definition complicated and the presence of asperity contact spots in a mixed contact situation requires redefinition of the long established λ ratio. In a recent experimental study, the need to define a new lambda ratio that more realistically considers current engineering trends has been developed and its need is emphasized [196]. In the current study, unless otherwise stated, the lambda ratio is the ratio of average film thickness value to the composite roughness value. This definition enables the comprehensive study of lubrication behaviour through all lubrication regimes and gives identical values under full film conditions. The lambda ratio is also referred to as the film thickness ratio.

It is to be noted that the average film thickness and composite roughness are variable as the contact is continuously evolving due to wear, tribofilm growth and plastic deformation and the relative movement of surfaces to maintain certain slide to roll ratios.

6.2.4 Conventional Film thickness ratio λ_{OLD}

The study of mixed lubrication sometimes requires a comparison between these modified parameters and the conventional parameters. To enable this, the conventional lambda ratio is also used frequently. In this study, it is sometimes also referred to as λ_{OLD} . By definition, it is the ratio of central film thickness to the composite roughness.

It is to be noted that in this definition, the central film thickness is calculated from the Dowson and Higginson equation while the roughness is modified with time. This definition enables comparison and to assess the relative importance of roughness in improving or reducing lubrication performance. If the conventional lambda ratio is smaller, the roughness has the effect of improving lubrication and roughness hinders lubrication effectiveness if this value is bigger than the actual mixed lubrication lambda ratio defined above.

6.2.5 Contact area ratio A_c

The contact area ratio and the contact load ratio were both defined first by Jiang et al. [11]. The apparent area of contact in a mixed lubricated or rough EHL contact is the Hertzian area of contact. In reality however, the area of contact is very small. First the contact is initiated at a single asperity and soon more and more asperities start to come into contact. The load carried by the asperity contacts keeps increasing. With increasing contact severity, more and more asperity contacts occur and soon support majority of load. Thus, it is critical to define a parameter to consider the change in real area of contact as the contact evolves. The ratio of real area of contact (defined by discrete asperity contact spots) to the nominal Hertzian contact area is called the contact area ratio, A_c . This parameter is directly related to the macroscopic friction,

wear and tribofilm growth. Therefore the effect of the tribofilm on this parameter gives the effect of tribofilm growth on the general mixed contact.

6.2.6 Contact load ratio, W_c

The contact load ratio is the ratio of the load supported by the asperity contacts to the total load. This parameter is very important for lubrication transition studies as the higher the contact load ratio, the higher the boundary lubrication contribution. Although roughness starts to change contact characteristics long before the actual asperity contact takes place, the contact load ratio is zero in full film conditions. When the contact load ratio has exceeded 0.8 or 80 %, it is believed that the lubricant has a negligible effect in changing the lubrication performance and the contact is assumed to be in boundary lubrication.

6.3 Illustrative tribochemical simulation of mixed lubrication

In the next sections, the tribochemical mixed lubrication model is used to study the effect of tribofilm growth on the lubrication mechanics and the results for the dynamic evolution of the key lubrication parameters identified and modified above is presented to analyse the effect of ZDDP tribofilm on lubrication behaviour. To illustrate the interfacial mechanics of tribofilm, simulations are run with the input and numerical parameters listed below. First the evolution of the central film thickness (h_c), lambda ratio (λ ratio), contact area ratio (A_c) and contact load ratio (W_c) is presented for a 2 hour simulation time to observe combined effect of wear and tribofilm growth. Then two representative simulation cases are performed. First case without any tribofilm growth and the second case with active tribofilm growth. First a comparison of conventional and modified mixed lubrication parameters is presented and then

comparative results for the two cases are presented by comparing h_c , W_c , A_c and λ values in the presence and absence of ZDDP tribofilm growth.

6.3.1 Numerical details

The mixed lubrication problem is solved on a uniform grid of 129 x129 nodes. The first set of simulations were performed with the same input and operational conditions as used in chapter 5 and are taken from the first study by Ghanbarzadeh et al. [120]. The second set of simulations are performed with input parameters taken from the second study by Ghanbarzadeh et al. [175] as this work was done alongside experimental work and more realistic parameters were used.

6.3.2 Input parameters for simulations to study the comparative effect of tribofilm growth and wear

A steel ball is in contact against a steel disc and both are assumed to yield at 6 GPa while the tribofilm yield pressure is set as 2 GPa for the tribofilm of maximum thickness. The applied pressure is 1.26 GPa. The radius of curvature for the ball is $R_x = 10$ mm and the wear track radius on disc is 39 mm and the equivalent modulus is 230.47 GPa. For a schematic representation of the wear track radius, please see Figure 6-3.

A Newtonian lubricant with viscosity, $\nu = 0.004$ Pa.s and pressure viscosity coefficient of 14.94 GPa^{-1} is flowing with rolling speed / entrainment speed, $U_r = 0.25$ m/s. The temperature is fixed at 90°C and the results are presented for an SRR value of -2.0 %. The tribofilm growth parameters used are $h_{\max} = 176$ nm, $x_{\text{tribo}} = 4.13 \times 10^{-16}$, $C_1 = 0.1125$ and $C_2 = 0.0006799$.

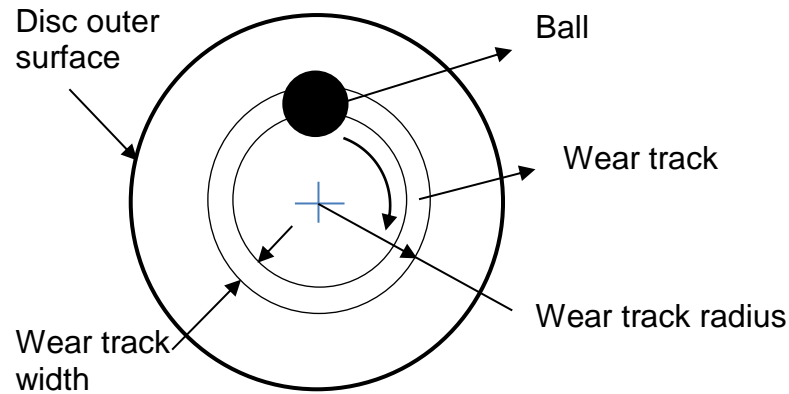


Figure 6-3: The illustration of the wear track and associated parameters.

6.3.3 Input parameters to study the effect presence and absence of tribofilm

A simplified MTM-SLIM experimental ball-on-disc configuration is simulated. The steel ball has a diameter of 19.05 mm. In the simulations, the wear track radius is taken to be 23 mm. The applied pressure is 1.15 GPa the roughness on the ball and disc is $R_q = 20$ nm and $R_q = 130$ nm respectively. The lubricant rolling speed / entrainment speed, U_r , is 0.1 m/s with an SRR value of 5 %. The temperature of the contact is fixed at 80 °C. The lubricant properties, the equivalent modulus and the material and tribofilm yielding limits are kept the same as above. The tribofilm growth parameters are $h_{\max} = 200$ nm, $x_{\text{tribo}} = 1.66 \times 10^{-16}$, $C_1 = 0.05432$ and $C_2 = 0.0004022$.

6.3.4 Results

First, the results are presented for the central film thickness evolution for a simulation experiment of 2 hours as shown in Figure 6-4. The central film thickness changes with time due to the dynamic evolution of the contact. Due to the gradual removal of the substrate material, the lubricant entrainment reduces. The lubricant entrapped inside the contact reduces due to reduction in roughness. In the first 5 to 10 minutes, the central film thickness increases due to increase in roughness inside the contact due to

tribofilm growth but as soon as the wear overcomes tribofilm growth the central film thickness reduces. This can be seen by close examination of the central film thickness evolution in time. It increases first and then decreases and finally reaches an asymptotic value of 18 nm in the current simulation test after 2 hours. As defined earlier, the central film thickness is defined over the normalized central $\frac{2}{3}$ times Hertzian contact region. This gives the dynamic changes in film thickness occurring in real time.

A close look at the central film thickness evolution results gives a very clear indication of the processes happening inside the contact. Whether wear or tribofilm growth dominates, can be quickly identified. But only examining the central film thickness does not give the complete contact characteristics.

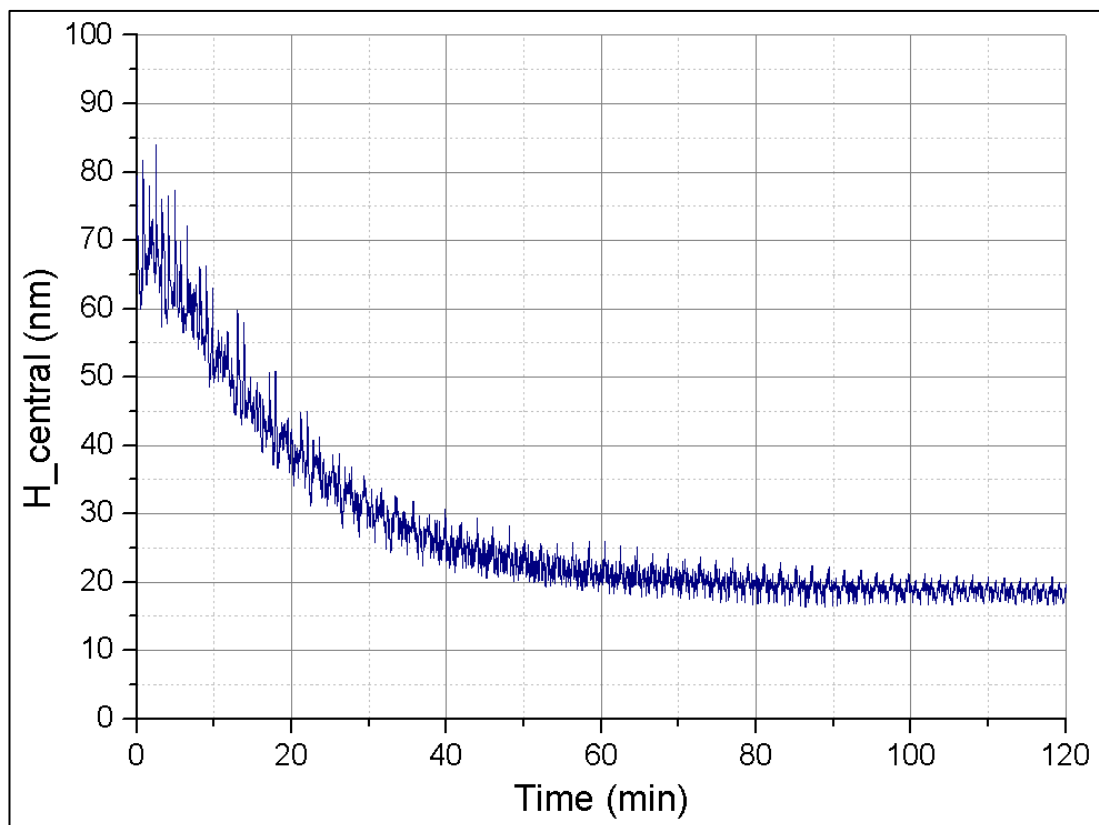


Figure 6-4: Central film thickness evolution in a 2 hour simulation. The relative importance of tribofilm growth and wear can be identified. The hump in the

beginning is where the tribofilm is dominating the contact characteristics. The latter part refers to the region where wear dominates the contact performance.

Next the results for the changes in lambda ratio are presented shown in Figure 6-5. The film thickness ratio / λ ratio gives the entire transition of lubrication characteristics over time. The relative changes in roughness and central film thickness are given by the λ ratio. The central film thickness changes and the roughness also changes over time. The roughness is also averaged over $\frac{2}{3}$ times normalized Hertzian contact region.

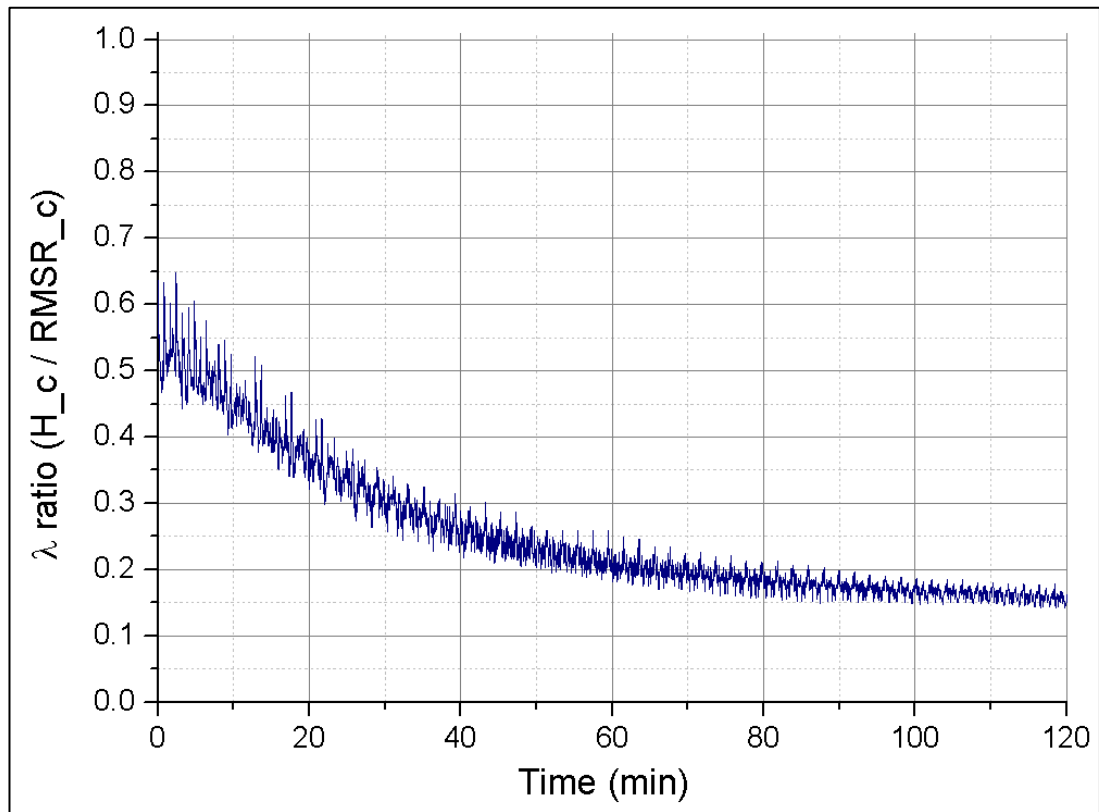


Figure 6-5: Film thickness ratio / λ ratio evolution in a 2 hour simulation. The relative importance of tribofilm growth and wear can be identified.

It can be clearly seen in Figure 6-5 that the rate of change of λ ratio is less pronounced compared to the rate of change of central film thickness. But the presence of a slight

increase in the first 5 to 10 minutes is visible in both the plots. But one thing is very clear that the lambda ratio is still decreasing even after 2 hours of simulation test but the rate at which the lambda ratio decreases is reducing with time. The roughness of the disc reduces while the roughness of the ball increases over time. Thus the overall composite roughness decreases.

The mechanics of the contact in a mixed lubrication state are best described through the contact area ratio A_c and contact load ratio W_c . A slight increase in the contact area ratio is observed during the first 10 minutes and an eventual reduction afterwards. This trend is similar to that observed in the plots of central film thickness and λ ratio but the contact area ratio curve seems expanded in time showing a comparatively slower change in area ratio. The phenomenon that was observed in the values of lubricant central film thickness and λ ratio in the initial 5 to 10 minutes is spread over 20 minutes in the case of contact area ratio. Thus the contact area ratio is less affected by the dynamic changes occurring inside the contact due to tribofilm growth / removal and plastic deformation and wear of the substrate.

The results presented in Figure 6-6 show that the growth of tribofilm seems to have no effect on the contact load ratio as the parameter W_c seems unaffected during the initial phase of simulation where tribofilm growth is dominating contact performance as shown in Figure 6-6. The contact load ratio decreases throughout the contact area indicating that the tribofilm growth and wear reduce the contact load ratio but it is not possible to see the competitive processes happening inside the wear track through W_c . In other words, whatever happens inside the tribochemically active contact, the contact load ratio W_c is not affected.

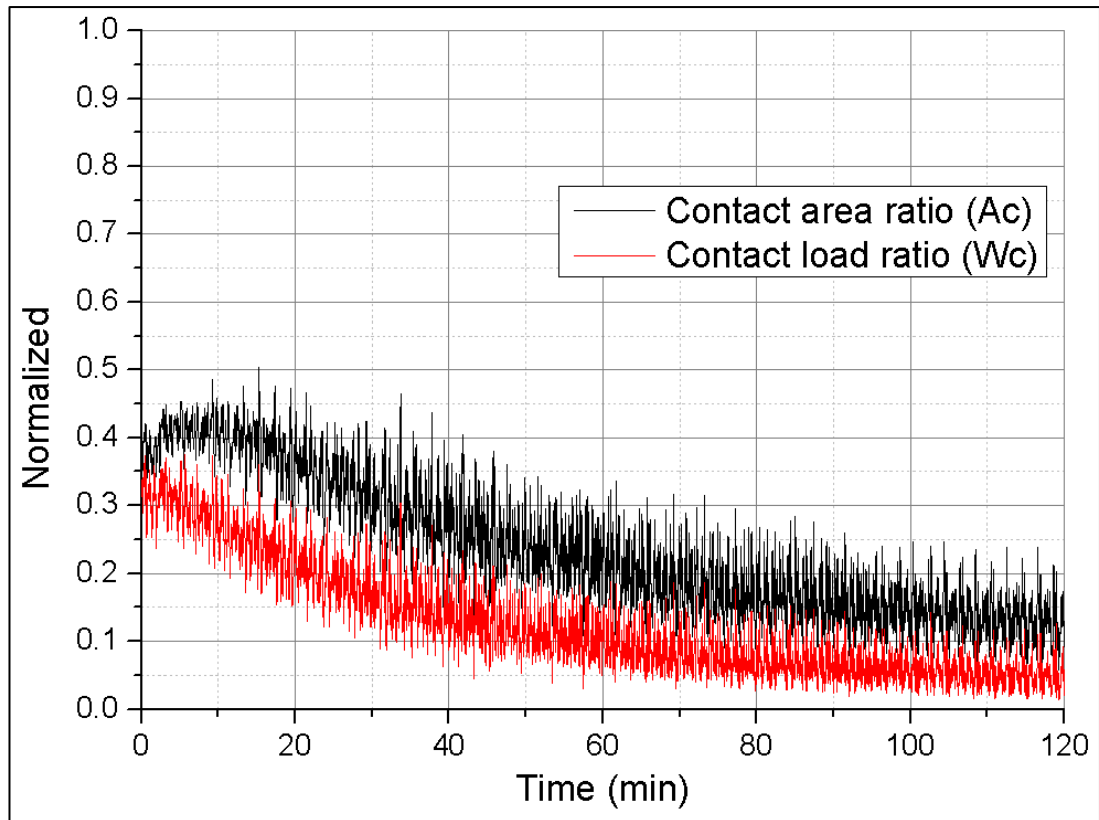


Figure 6-6: The changes in the contact area ratio and contact load ratio in a 2 hour simulation test. The relative importance of tribofilm growth and wear can be easily identified in the contact area ratio while the contact load ratio seems unaffected by the growth of tribofilm.

It is to be noted that the averaging procedure adopted for obtaining the values of A_c and W_c is the same as used for obtaining the values of central film thickness i.e. averaged over $r < \frac{2a}{3}$ (where a is half width of Hertzian contact). Therefore, the changes presented in Figure 6-6 are the real time changes occurring inside the wear track with time.

6.3.5 Discussion: The presence of tribofilm and its effects

The results presented in the above section clearly demonstrate that the tribofilm growth affects the mixed lubricated contact. The central film thickness H_c , the film thickness ratio λ , the contact area ratio A_c , and the contact load ratio W_c have been

presented in the previous section. In the current section, the presented results are discussed. These results are the first attempt to model the tribochemical effects in mixed lubrication and simulate the effects of tribofilm formation on the lubrication parameters. Therefore no direct comparison is available. Thus, the discussion is mainly based upon the interpretations of the effects seen in the plots of H_c , λ ratio, A_c and W_c . The effects of tribofilm due to its presence and its smart mechanical properties is highlighted.

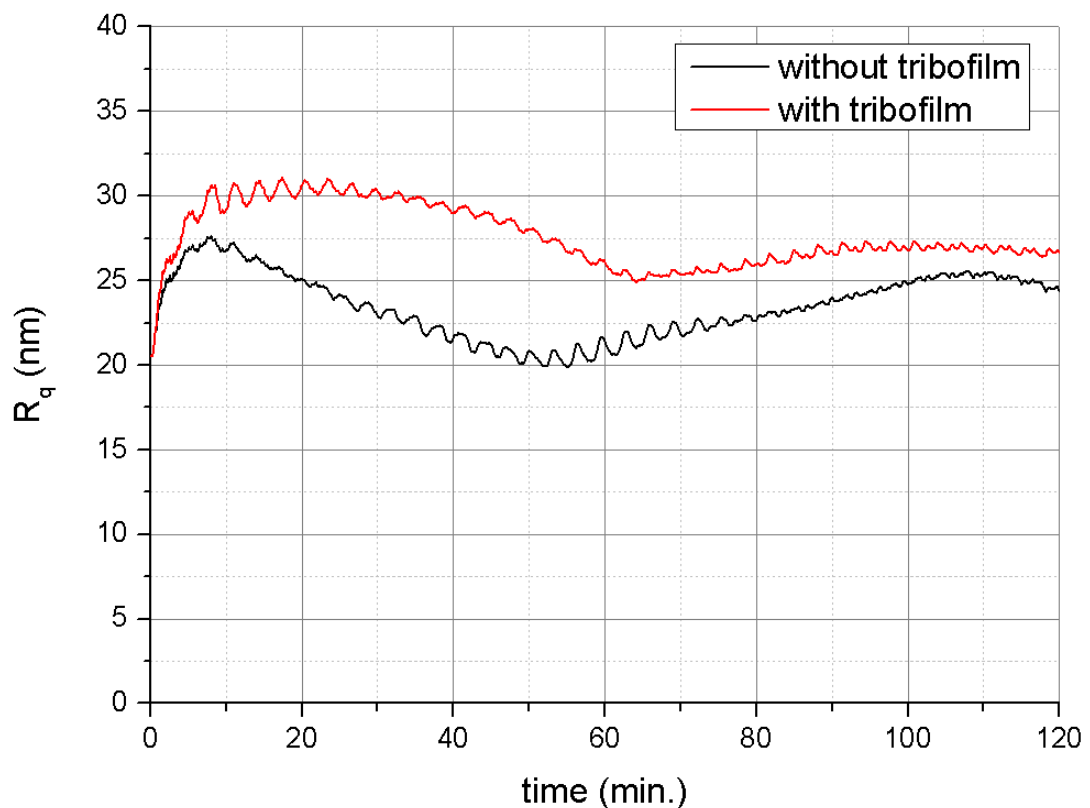


Figure 6-7: Assessment of the effect of tribofilm growth on roughness evolution. These plots correspond to the ball surface.

The presence of tribofilm roughens the contact. This can be observed in Figure 6-4 and Figure 6-5 as well but is clearly seen in Figure 6-7. The plot of roughness evolution with time over the simulation is plotted and the roughness in the presence of additive stays higher throughout the 2 hours simulation test. The tribofilm thickness

reaches its mean thickness very quickly in the first 20 minutes (see chapter 5). The wear rate is also very high initially but is quickly slowed down by the tribofilm. This is because the reduction in wear rate is linked to the presence of the tribofilm as well as the reduction in asperity heights and this eventually is linked to reduced plastic deformation. The tribofilm thickness eventually reaches its mean value and no more growth takes place. In fact the tribofilm formation and removal dynamically balance each other.

The tribofilm formation very quickly changes the mechanical properties of the surface. This is due to the reduction in the yielding pressure which makes the plastic deformation easier but on the other hand reduces the maximum local contact pressures inside the contact. The model development considered a linear reduction in the wear behaviour with tribofilm growth and thus, the wear also reduces significantly over time. The tribofilm growth in the current simulation was very small compared to the wear of the substrate. So, the effect of the tribofilm was seen only during the initial running-in period. Moreover, the presence of overshoot which is linked to the removal of tribofilm is also changing the contact microgeometry during this initial transient period.

In the current simulation set up, the yielding pressure for the steel substrate was taken as 6 GPa while the tribofilm yielding pressure was 2 GPa. The presence of roughness causes the contact pressures at certain points inside the contact to be even higher than 6 GPa resulting in the yielding of the steel substrate. Therefore, the contact transits first through the steel yielding limit and then the maximum pressures inside the contact reduce to somewhere between 6 GPa and 2 GPa towards the end of the simulation. In a similar fashion, for full tribofilm coverage, the local wear coefficient is always less than the wear coefficient for bare steel-steel contact. In the current

simulation setup, no wear was assumed on the fluid lubricated regions as the starting lambda ratio was 0.04 which signifies strong boundary lubrication effects.

IF h_c is constant but lambda keeps decreasing, roughness must be increasing and this is true when the conventional mixed lubrication parameters are observed. A plot of λ_{OLD} for two representative cases with the presence of tribofilm and the absence of tribofilm are plotted in Figure 6-8. The increase in roughness due to the tribofilm pushes the λ_{OLD} curve downwards to more severe contact conditions. This first of all means that the tribofilm roughens the contact and secondly the presence of tribofilm increases contact severity by reducing the lambda ratio.

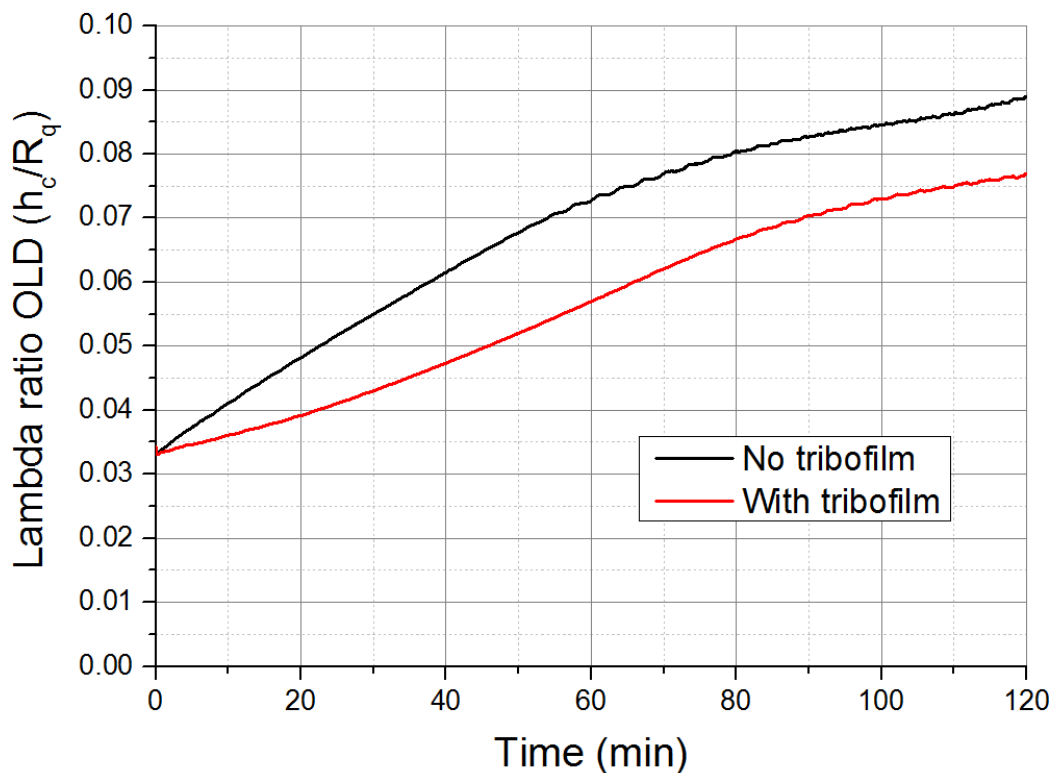


Figure 6-8: The effect of tribofilm growth on the conventional lambda ratio. The central film thickness value in this plot is a constant value based upon Dowson and Higginson formulation (equation (2-6)).

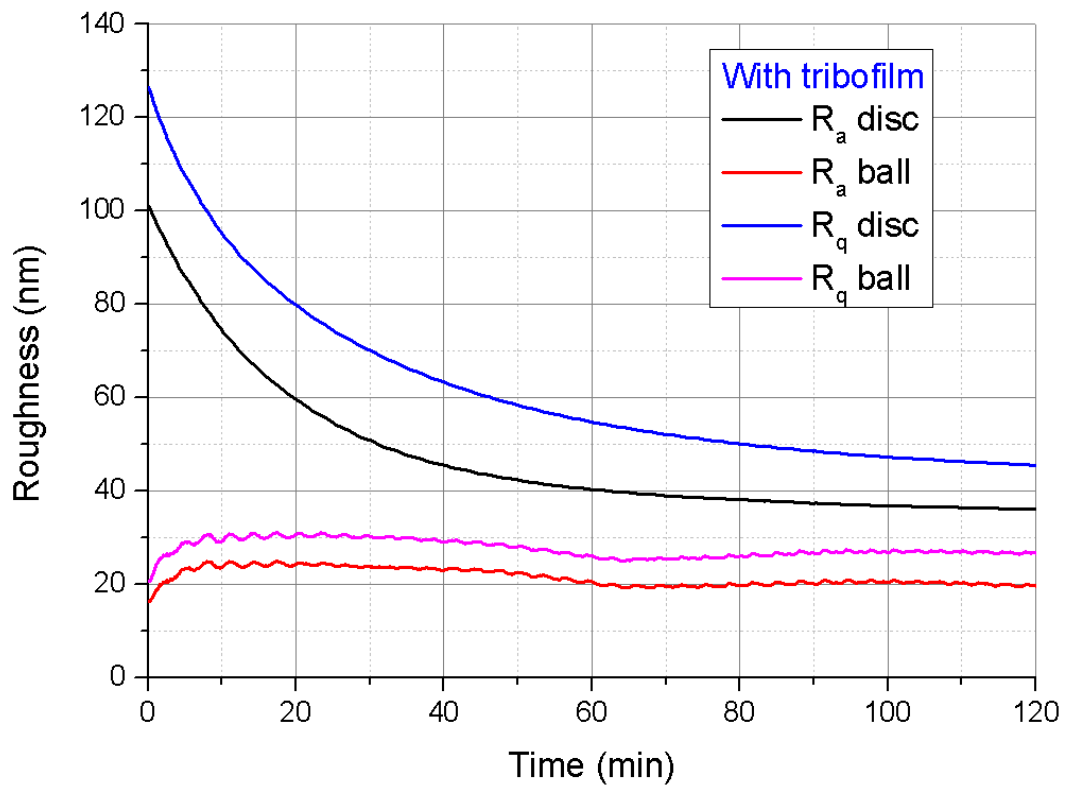
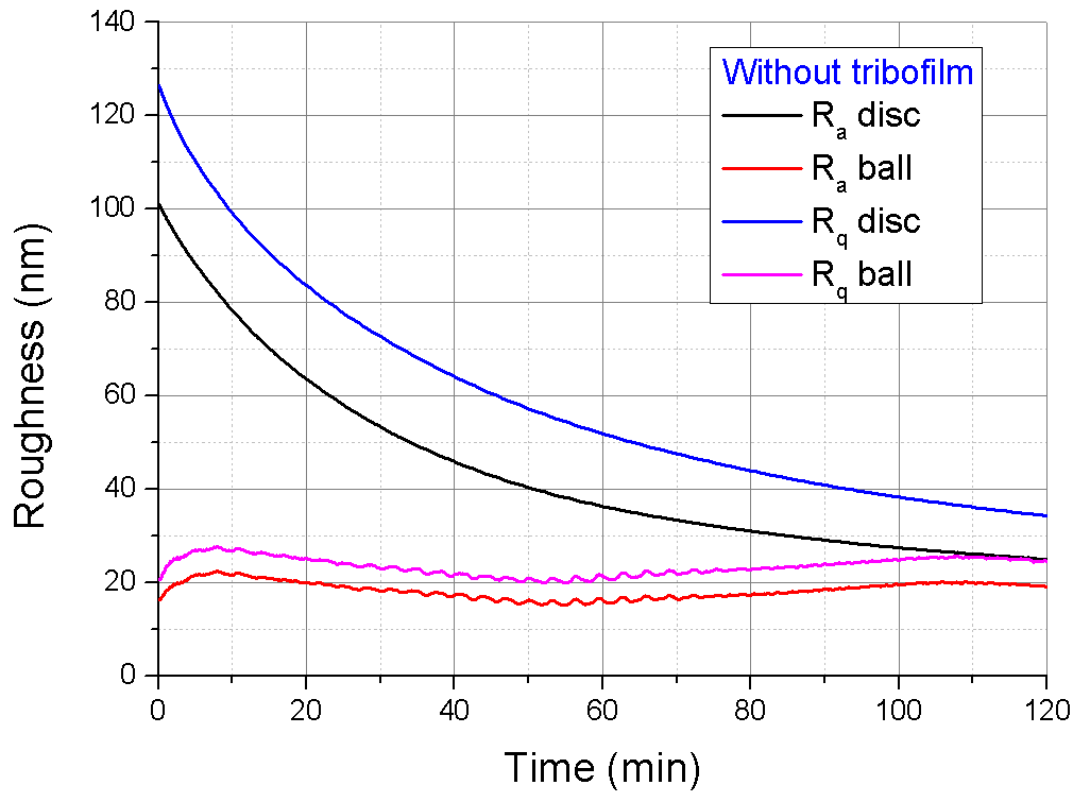


Figure 6-9: The effect of tribofilm growth on the R_q and R_a roughness values over time. The presence of tribofilm roughens the contact.

The mechanical properties of the contact, therefore, change the lubrication parameters significantly. The central film thickness and the λ ratio continuously decrease throughout the 2 hours simulation test, apart from the small peak observed in the first couple of minutes. The rate of decrease in both the cases is different which may be linked to the effect of reduction in roughness caused by wear. The central film thickness reaches a limiting value towards the end of simulation but the λ ratio keeps on decreasing with time and the rate of this decrease gradually becomes very small. The final gradient of this curve can be linked to the steady state wear of the substrate in the presence of the tribofilm.

The results for the roughness evolution with time are presented in Figure 6-9. The results give a more stronger explanation of why the lambda ratio decreases. The roughness in the presence of tribofilm is considerably higher both for the smooth and rough counterparts. This roughening of contact is believed to increase the contact severity. But just looking at the roughness values through the contact does not give the true picture of happenings inside the contact. This is because the lambda ratio is the ratio of central film thickness to the composite roughness.

The central film thickness is also very crucial in defining the contact performance. In Figure 6-8 , the central film thickness was fixed to the traditional values based on the Dowson and Higginson formulations. Thus, a plot of central film thickness values predicted by the developed tribochemical lubrication model is given in Figure 6-10. The film thickness values inside the contact changes dynamically through time and is sensitive to other simulation parameters. The sensitivity of the central film thickness to the presence of tribofilm can be clearly seen.

The increase in roughness due to the tribochemical film growth may seem detrimental but this increase in roughness helps entrain more lubricant inside the contact. This

results in the development of a thicker lubricant film inside the rough contact. Thus the tribofilm growth helps to improve the performance of the contact by improving the lubricant film formation and entrainment within the contact.

Thus, looking at these parameters individually does not give the complete picture of the contact performance. The key parameter connecting the roughness and the lubricant film thickness is the lambda ratio or the central film thickness ratio. Therefore the lambda ratio or more appropriately the central film thickness ratio is plotted and presented in Figure 6-11. The lambda ratio based upon the true, momentary values of central film thickness and composite roughness within the contact give an entirely different picture compared to that obtained based upon the Dowson and Higginson film thickness values (see Figure 6-8).

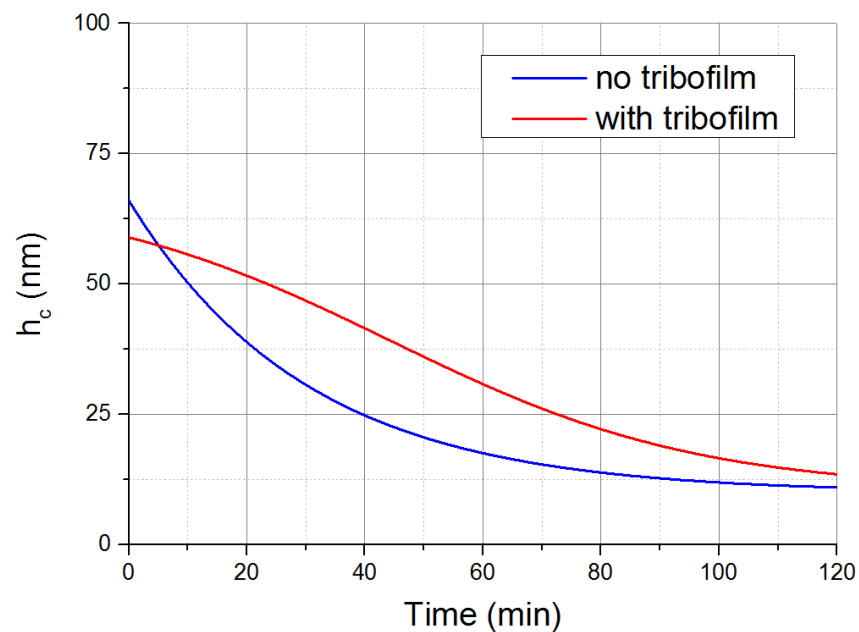


Figure 6-10: The effect of tribofilm growth on the central film thickness. The central film thickness value is the average of the instantaneous film thickness values within the contact region.

The lambda ratio stays higher throughout the simulation highlighting the importance of the tribofilm in improving the lubrication performance. Higher values of the central film thickness ratio mean that the contact moves to less severe conditions. Thus, from all these results, it can be seen that the lubricant additive derived reaction layers, in general and the ZDDP tribofilm formation specifically does not only perform due to their chemical nature to form antiwear and sacrificial layers to reduce wear but the formation of ZDDP derived reaction layer also helps the lubrication phenomenon by entraining more lubricant. This fact has not been identified until now due to the inability of experiments to capture the mixed lubrication phenomenon and not having a complete model that incorporates lubrication, contact mechanics and tribochemistry in a single framework.

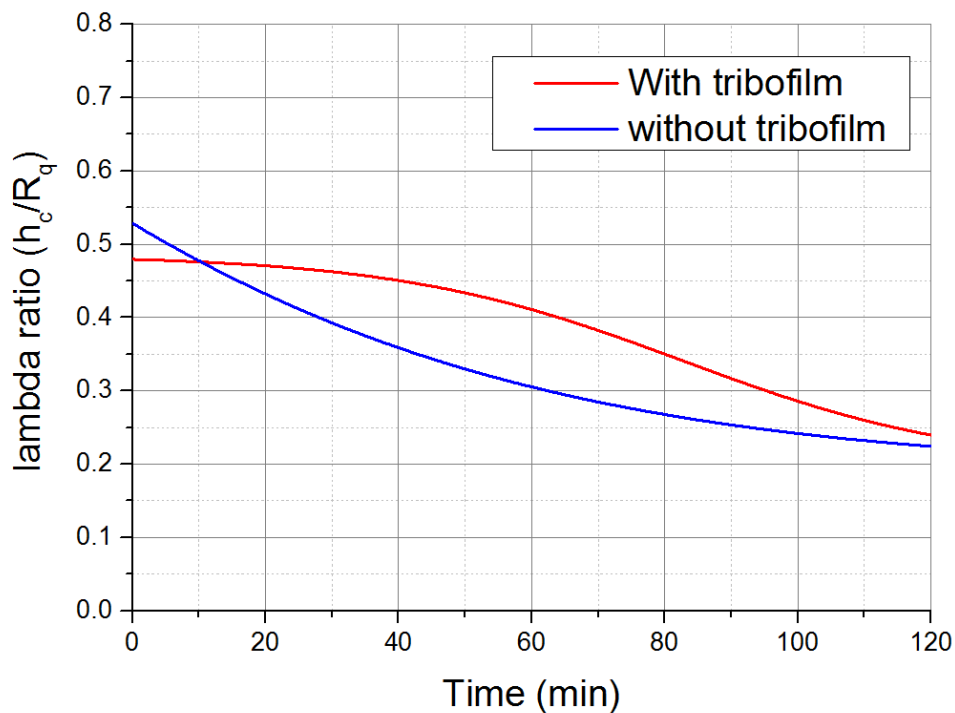


Figure 6-11: The effect of tribofilm growth on the film thickness ratio. The results are plotted over time and the presence of tribofilm improves contact performance.

The trend observed in the contact area ratio is more interesting. The tribofilm growth and wear initially increase A_c and then decrease it. This increase and decrease happens over an extended time of about 20 mins which is much higher. The tribofilm grows rapidly as soon as rubbing starts. As mentioned earlier, the tribofilm yields at a much lower pressure causing more area to come into contact. Then due to the removal of the tribofilm that is considered in our model, the contact area reduces gradually and keeps on reducing due to the smoothening of the higher asperities due to wear and plastic deformation as seen in Figure 6-6.

A closer look at the contact area ratio A_c and the contact load ratio W_c suggests that W_c keeps on decreasing with time as the contact evolves. This hints towards the lower load carrying capacity of the tribofilm. The tribofilm formation increases the number of asperity contacts but due to it being softer, the contact load ratio keeps on decreasing. This is a very important outcome and is expected. The sole reason for using additive derived reaction layers is to minimize the yielding pressure to provide a shearing interface that performs under extreme conditions of load and environment. This reduction in load bearing capacity is not harmful as the tribofilm formation on the other hand reduces wear due to its lower coefficient of wear and a lower value of resulting maximum pressure.

To date there has been no study directed at observing the effect of tribofilm growth on the contact lubrication behaviour. The only study that addresses the contact ratio and the effect of various parameters on the contact ratio is the work of Luo and Liu [197]. Figure 6-12 shows some key results from their work regarding the effect of polar additive in different base oils on the contact area ratio. They investigated the contact ratio using the relative optical interference intensity (ROII) technique. This method gives a vertical resolution of 0.5 nm and an in-plane resolution of 1 μm . They

investigated the effect of surface roughness, maximum Hertzian pressure and the combined elastic modulus on the contact ratio. The effect of viscosity and rolling speed was also considered and a threshold speed above which the effect of roughness is reversed was suggested. They used several base oils with different viscosities to see the effect of viscosity on the area ratio. They also added polar additives to some of the base oil. The results showed that the presence of polar additives tends to reduce the contact ratio as seen in Figure 6-12.

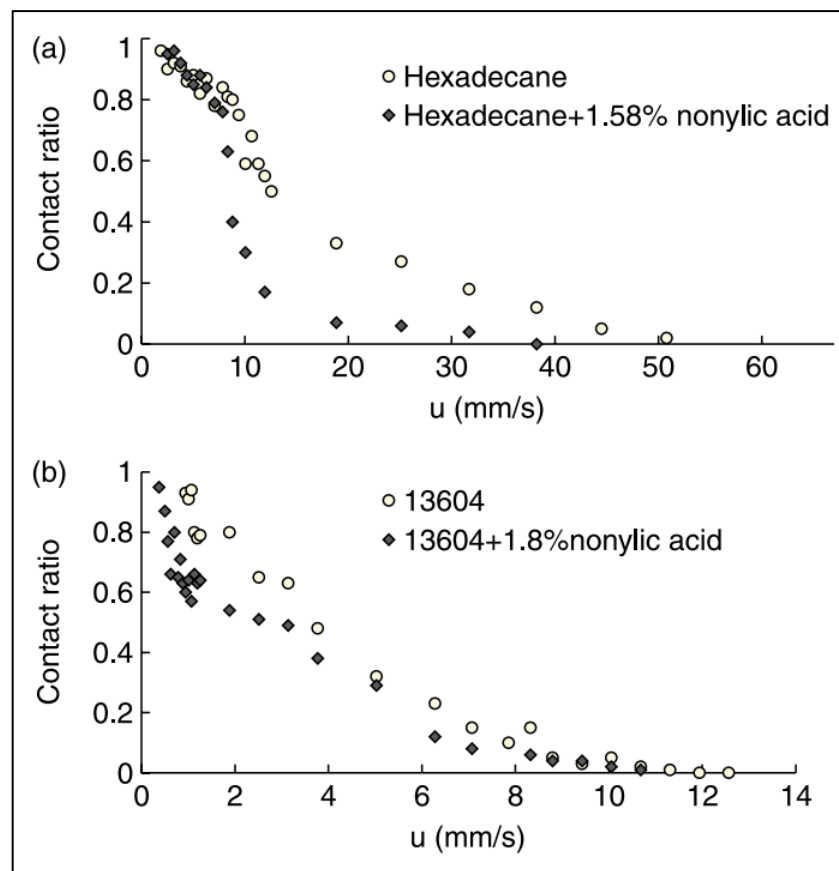


Figure 6-12: The effect of polar additives on the contact area ratio. Maximum Hertzian pressure is 0.292 GPa. (a) The effect of adding polar additive nonylic acid to Hexadecane. (b) The effect of adding polar additive nonylic acid to mineral oil [197].

Therefore, they concluded that the contact ratio (defined as A_c in this thesis) reduces if polar additives are present. Simulation findings from the model developed in the

current study are in line with this experimental outcome (see Figure 6-6) as with the growth of tribofilm through time, the contact area ratio keeps decreasing. As this study is a first attempt at predicting these effects of tribofilm growth on the lubrication behaviour, more work needs to be done. Unfortunately, it was not possible to perform simulations to do a quantitative comparison with their results as the nature and type of the additive as well as the base oil were different. Moreover, they do their calculations for static contact and give no definition of what they mean by having a static contact.

Thus, to address the issue completely and to understand the true impact of tribofilm on the contact parameters, two additional simulations were performed with two different scenarios. In the first set of simulations, no active additive was present in the lubricant. The second set of simulations was performed with ZDDP antiwear additive in the lubricant. Both the simulations are performed with everything the same except the presence or absence of tribofilm. This is to illustrate the capabilities of the model in predicting the interfacial behaviour. Some key results have been presented already in Figure 6-7, Figure 6-8, Figure 6-9, Figure 6-10 and Figure 6-11. In the following paragraphs, some more results are presented to study the effect of tribofilm growth on the contact area ratio and the contact load ratio by observing the effect of tribofilm on the key contact parameters affecting A_c and W_c .

First of all a comparison of roughness evolution for the smoother counterpart (ball) and the rougher counterpart (disc) is presented in Figure 6-13 to illustrate the comparative differences between each of the counterparts caused by the presence of tribofilm. In both the cases, the presence of tribofilm eventually roughens the contact. The slight differences can be linked to the differences in surface coverage of the tribofilm. The surface coverage for the ball reaches 100 % very quickly but for the

disc it takes much longer to reach full coverage. The slightly higher value of roughness in the R_q value of disc without tribofilm compared to that in the presence of tribofilm for the first 40 mins of the simulation may be due to the competition between tribofilm growth and wear. The tribofilm formation takes time to reach its steady state values and it may be that as soon as the average values of tribofilm formed and the wear become equal and the wear keeps increasing, the graphs crossover at or near to that point. But this requires more numerical and if possible experimental work to explore this fully and is left for future work.

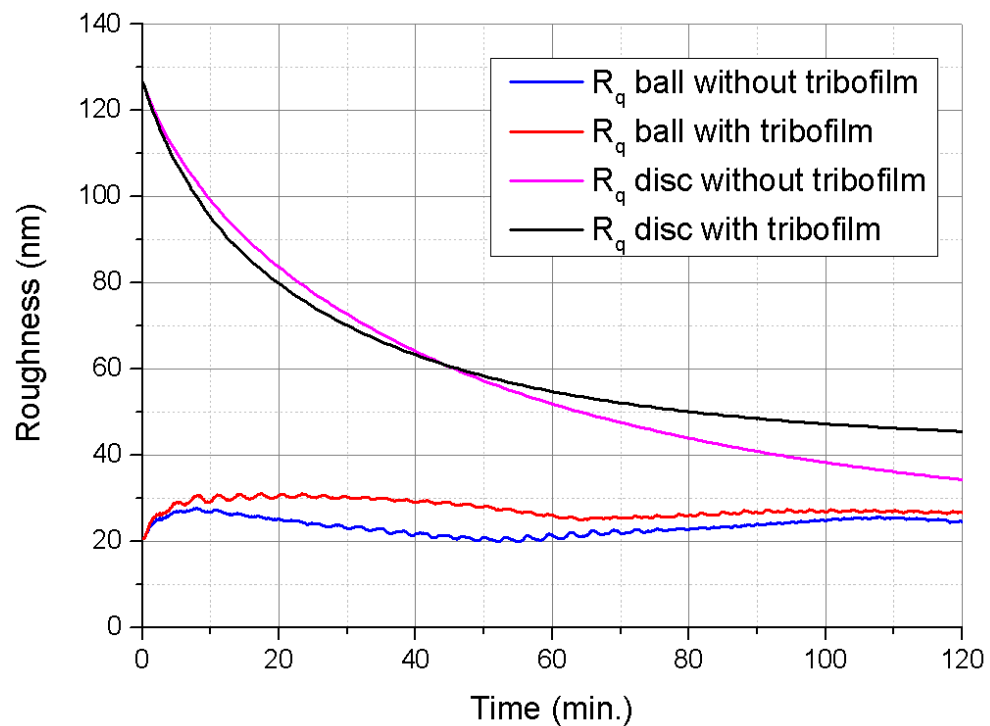


Figure 6-13: A comparison of the effect of tribofilm growth on the roughness evolution of the ball and disc.

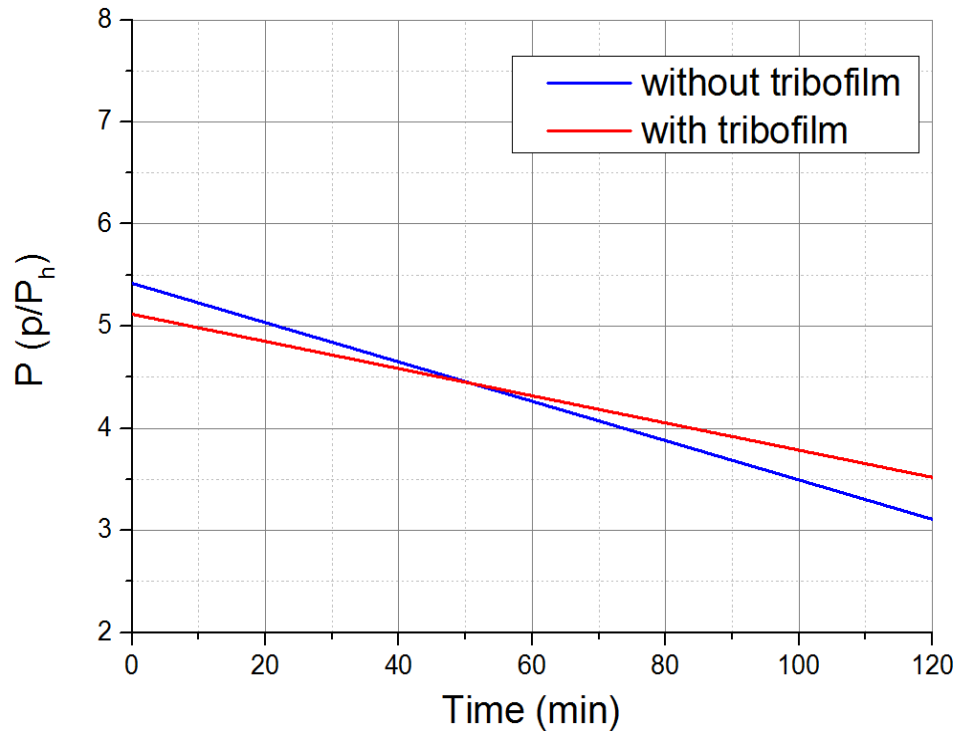


Figure 6-14: The effect of tribofilm growth on the maximum instantaneous value of pressure. The pressures are non-dimensionalized with the Hertzian pressure and the results are plotted over time.

The plot of the maximum nodal pressure with time is presented in Figure 6-14. The presence of the tribofilm seems to reduce wear and this eventually results in having asperities that are still high enough to cause pressures higher than the yielding pressure. This is why in the plot of maximum pressure, the maximum pressures stay higher and more steady throughout the simulation of two hours. This key feature once again has a crossover among the individual plots with and without the tribofilm at around 50 mins. This crossover point and the fact that the presence of tribofilm keeps the pressures higher is extremely important as experimental work suggests similar characteristics of the tribofilm that ultimately manifest as increased micropitting damage [198].

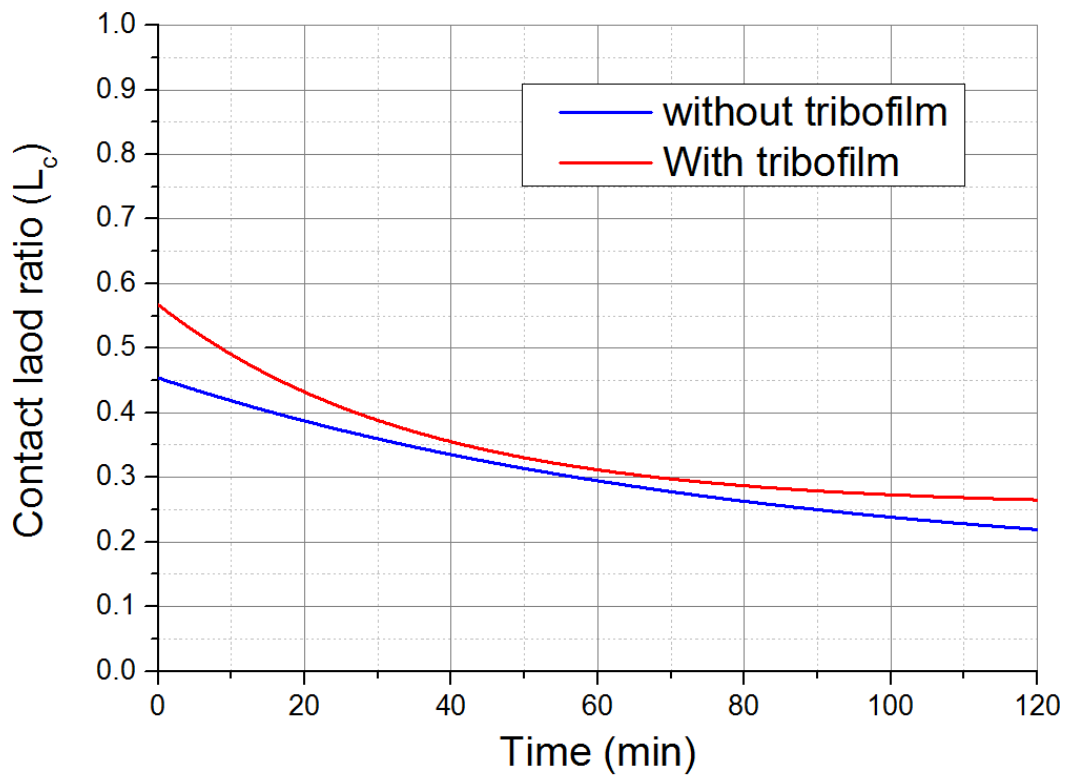
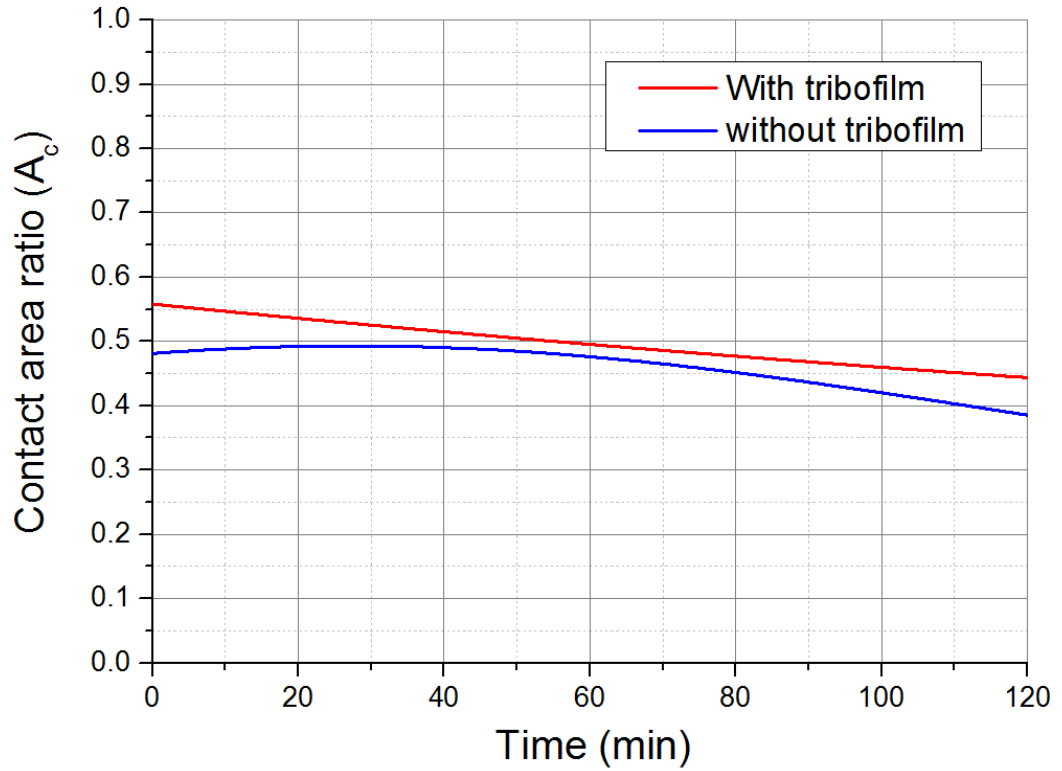


Figure 6-15: The effect of tribofilm growth on the contact area ratio (A_c) and contact load ratio (L_c). The results are plotted over time and the magnitude of both A_c and L_c increase due to the tribofilm.

Finally, the contact area ratio, A_c and the contact load ratio, W_c are presented in Figure 6-15. The presence of tribofilm on the contacting bodies increases both A_c and W_c . Whether tribofilm is present or not, A_c and W_c keep decreasing as the contact geometries evolve through time due to wear, plastic deformation and tribofilm growth but in the presence of ZDDP lubricant additive, the tribofilm growth increases both these parameters. This is clearly due to the increase in roughness as this leads to more solid contact within the nominal contact zone. The increase in W_c due to tribofilm growth is observed not only due to the increased number of solid asperity contacting nodes but also due to the sustained maximum pressure values as seen in Figure 6-14.

It is important to mention that the above results are presented for one particular case and only those properties and trends have been presented which have some experimentally established basis. A more detailed study needs to be done to explore the general behaviour and interdependence of the contact parameters. This will be included in future recommendations.

6.4 Summary

A contact mechanics model was successfully developed to link lubrication science and contact mechanics with tribochemistry. The model captures the effect of ZDDP additive derived reaction film growth on the lubrication performance by simulating the most important lubrication parameters. A continuum scale model to describe atomic scale phenomena in an approximate manner is realized.

A unified solution strategy was adopted to solve the mixed lubrication problem. Complete lubrication transition can be simulated and studied. Previous unified mixed lubrication models are lacking the presence and integration of tribochemistry. The current model fills the literature gap by providing such a model. This successfully

links the lubrication and contact mechanics with chemistry and enables the simulation of tribochemical effects. The term ‘interfacial mechanics’ best describes the model as it has the potential to give detailed information about the interfacial mechanics and tribochemistry and their mutual interaction. The localized details about contact pressures and tribofilm growth are obtained and simulations are conducted to see the behaviour of the contact when the tribofilm growth takes place. The model also enables the study of running-in behaviour as well demonstrated by the differences in the initial and the steady state values of contact parameters.

The conventional terms like minimum film thickness, central film thickness, lambda ratio were redefined and some new terms were adopted to represent mixed lubrication results more precisely and to provide global comparison tools. An averaging procedure was adopted to take the values of properties as average from its local values within $\frac{2}{3}$ times the Hertzian contact radius from centre of contact. This standardises the property values and enables comparison among different studies.

The results for the central film thickness, lambda ratio, contact area ratio and contact load ratio give useful insights into the interaction between tribochemistry and lubrication. The presence of tribofilm provides a shearing plane for asperities to slide over each other with lower damage and wear. The mechanical properties of tribofilms play a critical role in modifying these lubrication parameters and thus lubrication performance. To elaborate the key outcomes from the results, two sets of simulations were performed and the results plotted to see the effect of tribofilm growth. The overall composite roughness increases due to the increase in roughness of both the counter parts due to presence of tribofilm increasing severity of contact. But on the other hand the tribofilm formation helps entrain more lubricant due to this roughening as seen by the increase in the central film thickness values. Thus, to see the overall

effect of tribofilm in modifying the lubrication performance the central film thickness ratios are plotted. A comparison in the presence and absence of tribofilm show that the overall effect of tribofilm is to improve lubrication by improving the central film thickness ratio. The effect of tribofilm in roughening the contact is observed and its beneficial effects in improving lubrication discussed. Thus, based upon the results in this chapter, it can be concluded that the tribofilm not only reduces wear by forming an antiwear tribofilm on the contacting surfaces but it also improves lubrication performance by helping entrain more lubricant into the contact.

The ability of the tribofilm to sustain higher pressures in the contact compared to the case of no tribofilm suggests that the tribofilm formation might reduce mild wear but other phenomenon like micropitting might become active due to increased roughness and sustained high pressures.

The experimental studies addressing the effect of tribofilm or in general contact parameters on the lubrication performance are very few. The contact load and contact area ratios were compared against experimental results but a simple comparison was not possible due to incomplete information in the experimental results. Thus, results for contact area and contact load ratio were presented to see the effect of tribofilm and the effect of tribofilm in increasing both these parameters was identified.

The key idea in this chapter is to illustrate the ability of the developed model to address the mutual interaction between lubrication and tribochemistry. With these preliminary results, it can be seen that the role played by the tribofilm during the contact evolution, especially running-in stages is very important and it is expected to protect the contact and preserves its lubrication performance for longer times. But more work needs to be done to analyse the key concepts presented in this chapter and relate these to the actual experimental outcomes.

Chapter 7

Predicting wear and wear track profiles

This chapter presents the results on wear from the current model. The basic idea is to explore the applicability of the model to real experimental conditions and explore the capabilities of the system. The accuracy of predictions of the macroscopic wear of the system is tested and some microscopic features are extracted from the model results.

The chapter starts with a general introduction to wear in section 7.1. Some key studies incorporating wear into tribochemical film growth modelling frameworks are discussed in section 7.2 with emphasis on incorporating the tribochemistry into wear modelling. The predictive studies on wear track profiles are very rare and a review is given in section 7.3. Then the wear model implemented in the current study is given and the results of wear prediction presented. First results are presented in the averaged form in section 7.5.1 and then the asperity based detailed deterministic information is taken out by presenting 2-D wear track profiles in section 7.5.2. Then the 3-D wear track results are presented for different slide to roll ratios in section 7.5.3 and enable easy identification of features of wear of the contact pair and help identify the system behaviour in the simplest form.

7.1 Introduction

Mechanical forces of sliding and rolling result in material removal. This material removal was defined as wear by Whitehouse and Archard [199]. Wear can either be mild or severe depending upon the severity of contact conditions. Generally in the absence of lubricant, severe wear conditions exist. It is possible to achieve mild wear conditions by controlling material properties, selecting suitable lubricant and by choosing appropriate operating conditions. Surface roughness plays a key role in

defining and driving this transition of wear from mild to severe regime [200] as it has been observed that the transition to severe wear is almost always accompanied by an increase in roughness of the contact pair [201, 202].

The wear is significantly higher during the running in process. The contacting asperities smoothen out soon and the wear reduces significantly. The wear process generally results in generation of wear particles. If these wear particles are hard, these will cause an increase in wear due to abrasion and if softer particles form, indentation of these particles might result in formation of transfer layer [203].

The wear phenomena can be divided into four fundamental types depending upon the way material is being removed: adhesive wear, abrasive wear, fatigue wear and tribocorrosive wear [204]. The adhesive wear occurs primarily under severe dry contact conditions where adhesive junctions formed asperity contacts are removed due to the relative movement of the contacting surfaces. Abrasive wear as shown in Figure 7-1 is the primary mode of wear when harder and softer surfaces interact. The harder surface abrades the softer one. This type of wear is called two body abrasion. The presence of hard wear particles between contacting bodies can also cause abrasive wear. This type of wear is called three body abrasion. Figure 7-2 shows these two modes of abrasive wear.

Repeated cyclic loading can cause additional wear due to accumulation of stress inside the contacting materials and is called fatigue wear. This type of wear is accompanied by the formation of visible cracks inside the rubbing track. The cracks might be surface initiated or subsurface initiated and are progressive in nature. Whether surface or subsurface fatigue is observed depends upon the roughness of the contact pair. Lancaster [204] suggests that for lambda ratio much lower than unity, the formation of surface cracks is favoured while for lambda ratios typical of EHL conditions, the

formation of subsurface cracks is observed which finally grow to the surface. Fatigue wear is also called rolling contact fatigue. Spalling is the type of fatigue wear that is subsurface initiated.

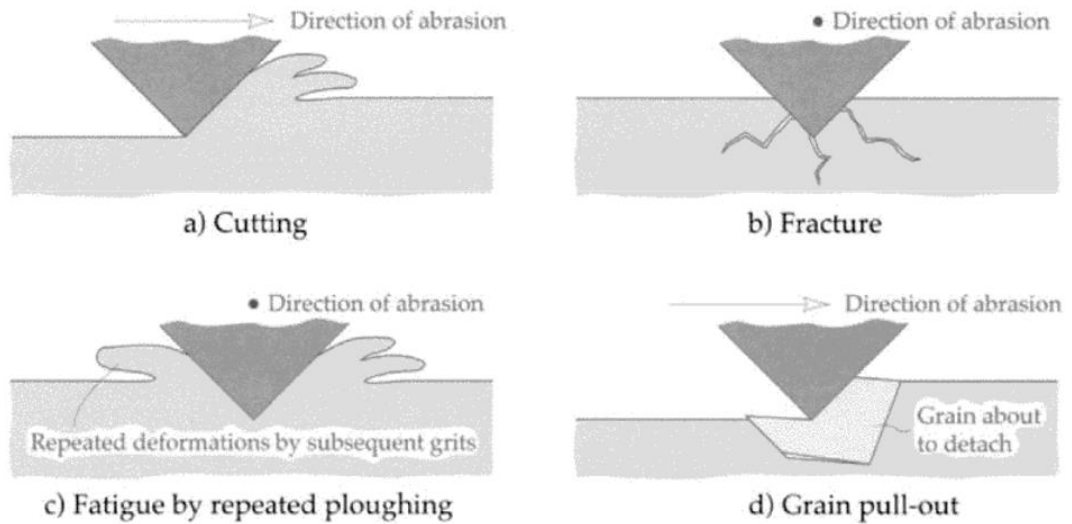


Figure 7-1: Various forms in which abrasive wear manifests itself [8].

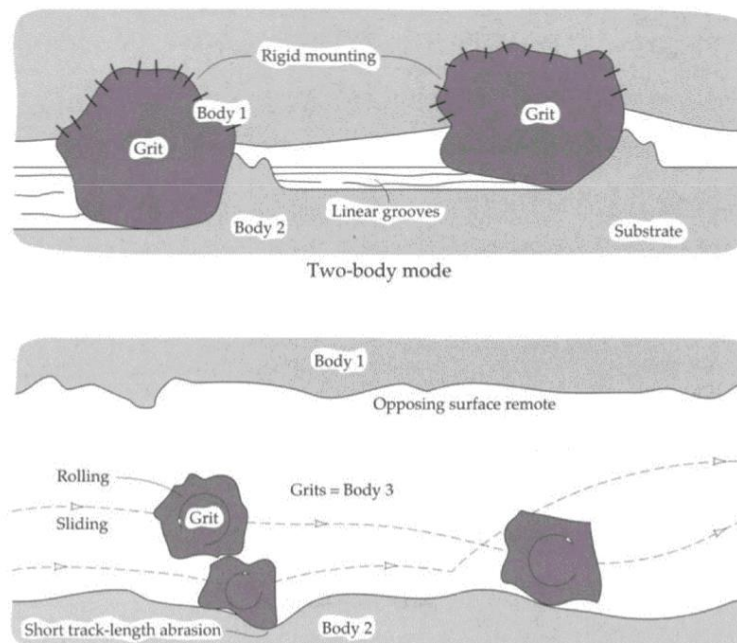


Figure 7-2: Modes of abrasion. (Top) Two body abrasion. (Bottom) Three body abrasion [8].

For hardened surfaces, the term subcase fatigue defines the wear phenomena. This is also called case crushing. If the cracks are surface initiated, the term pitting is used to describe the wear. Pitting failure has a very specific form, observed especially in ball bearings and related very strongly to the surface roughness, called micropitting. All these types of wear are characterized by crack formation and progress and are also called rolling contact fatigue wear.

7.2 Wear prediction and its significance

Wear is a complex phenomenon and its prediction is still a challenge in tribology. The literature on wear prediction is very broad and huge number of attempts at modelling wear are available as evidenced by over 300 equations developed to predict friction . It is still not possible to predict wear purely based upon the first principles.

Archard's wear model is one of the simplest and widely used model. This model has been applied to various contact and lubrication conditions. Some initial attempts at modelling wear by using the Archard's wear model were primarily for dry contact and pure sliding conditions [205, 206] but more and more studies have emerged in the recent years especially to include the effect of lubrication [24] and tribochemistry [120]. The presence of tribofilm has significant effect on wear. The ZDDP is an antiwear additive and its tribofilm reduces wear. The mechanism by which it reduces wear are strongly related to its mechanical properties.

The idea of considering the effect of tribofilm growth into the Archard's wear model comes from the ability to relate the wear coefficient in the Archard's equation to different experimental conditions [207, 208]. There has been several attempts to include the effect of tribochemistry into the Archard's wear equation by considering the wear coefficient to be a function of film growth. As mentioned before, the first

attempt at successfully simulating wear in the presence of tribofilm is the work of Andersson et al. [22]. They simulated the effect of tribofilm in modifying the wear by only considering the change in mechanical properties due to the tribofilm and the Archard's wear coefficient was only fitted to the data on wear of the system in the presence of tribofilm. Thus, this wear coefficient is different from the coefficient of wear in the absence of antiwear additive and is somehow giving a homogenized effect of tribofilm on wear coefficient. The coefficient of wear was assumed to be a fixed value which raised questions on the portability of their model results to different cases with different tribofilm behaviour. Ghanbarzadeh et al. [120] improved this wear model by incorporating the idea of having a variable wear coefficient that varies linearly from a maximum value for no tribofilm to a minimum value in the presence of the maximum tribofilm grown under given conditions. The idea of having different coefficients of wear was already invented but its variation with the growth of tribofilm enabled instantaneous observation of the wear behaviour. This model was validated against experimental results [175]. The wear of tribofilm is considered explicitly as the removal of tribofilm and is obtained by experimental fitting.

In the current study, the approach the variable wear coefficient is used to model wear. The simulated wear is based upon the Archard's wear equation that relates the wear volume to the material hardness, applied load and the sliding distance.

$$W_v = K \frac{F_N}{H} S \quad (7-1)$$

This equation states that the wear volume, W_v is proportional to the applied load, F_N and sliding distance, S and is inversely proportional to the hardness of the material, H . The proportionality constant, K is called the Archard's wear coefficient. It is obtained empirically and is related to the probability of a collision leading to removal

of material. The description of wear using equation (7-1) describes the macroscopic wear behaviour of the system. To apply it to the local asperity scale, the above equation is modified and expressed as the wear depth, h .

$$h = K \frac{P}{H} S \quad (7-2)$$

or

$$\frac{\Delta h}{\Delta t} = K \frac{P}{H} v \quad (7-3)$$

In equation (7-2) and equation (7-3), the local, microscopic variables are used. P is the pressure at the asperity scale and the term v is the sliding velocity of the contact pair. Thus, wear can be simulated over time with local information of the properties of the contact.

7.2.1 Inclusion of tribochemistry

The inclusion of tribochemistry into wear prediction has been the topic of interest in the recent years. The presence of different additives in the lubricant can affect the wear. The formation of reaction layers due to these additives, especially ZDDP reduces wear. It is very important to understand the effect of these additives in modifying wear. Several hypothesis exist and the main reason for the reduction of wear due the antiwear action of ZDDP has been attributed to the formation of a tenacious chemical layer on the surfaces of contacting bodies. The decrease in wear can be due to a reduction in pressure, asperity failure or the crack formation processes etc. It was suggested in the previous chapter that the presence of tribofilm reduces contact severity by allowing more lubricant to entrain the contact and therefore may

cause a reduction in wear. It was suggested by Spikes [85] that the formation of tribofilm reduces wear in one of the three ways:

- Preventing direct asperity-asperity contact by providing a barrier between the contacting bodies. Thus, adhesive wear can be significantly avoided.
- The process of formation of ZDDP tribofilm can digest the abrasive iron oxide particles, ultimately reducing the abrasive wear as well.
- The ZDDP undergoes several chemical processes at the interface and one of the mechanisms by which it can reduce friction is by inhibiting corrosive interactions in metallic systems by reacting with peroxides.

In the current study, another mechanism by which ZDDP reduces wear in mixed lubricated contacts is by improving contact severity. The roughening of the contact allows more lubricant to be entrained inside the contact and subsequently reduce wear.

The tribochemical interactions can be included into the Archard's equation by devising a wear coefficient that can accommodate spatial and temporal variations. A wear coefficient sensitive to the tribochemical interactions should be able to accommodate the change of mechanical properties with tribofilm formation and wear. To simulate this effect, two wear coefficient values are chosen and fixed. A higher value of wear coefficient, representative of the case where no tribofilm is present and a lower value of wear coefficient, representative of the case where the maximum tribofilm has formed. The variation of the wear coefficient between these two extremes is assumed linear as a starting point. Thus, with tribofilm growth the wear coefficient reduces from one extreme value to the other with tribofilm growth.

The simulation starts with the high value of wear coefficient and the wear coefficient reduces linearly (from the highest value for "no tribofilm" to the minimum value for the maximum tribofilm thickness) as soon as the tribofilm starts to grow on each

surface. The wear coefficient has a local instantaneous value for every node. If an average value over the rubbing track is calculated for every time step then this average value will reduce and reach a steady value towards the end of simulation.

7.3 Attempts at modelling and predicting wear tracks

The simulation of wear in a numerical framework is a relatively new concept. The integration of wear simulation into a boundary solver was done first by Andersson et al. [22]. They developed an approximate method to simulate wear both in the presence and absence of tribofilm. The tribofilm growth only alters the value of wear coefficient that they fit to the experimental data but the wear coefficient has a single value that is fixed. They have developed some wear plots over time for the wear on ball and they have been successful in predicting the qualitative trends in wear. Although the profiles they predicted were very idealized with no deterministic information. The second important parameter missing from their work is the presence of lubricant. They simulate a dry contact and the dry contact does not give a complete picture of the happenings inside the contact. With wear the contact parameters change and the effect of lubricant becomes important as seen in the previous chapter.

The current simulation set up gives the flexibility to access larger areas in the range of millimetres. Due to the fact that the equations have been formulated in non-dimensionalized form, a compromise between grid size and the accessible areas is possible. If the phenomena under observation does not require refined grids, then even larger areas are accessible. In the simulation results presented in chapter 5 and chapter 6, the areas under observation were ≈ 0.5 mm by 0.5 mm.

Thus, it is possible to simulate the wear track profiles. Even the distribution of tribofilm and the relative importance of wear and tribofilm removal at distinct parts

of the contact region can be identified. A comparison of wear track profiles in the presence and absence of the tribofilm can be identified and simulated deterministically. It is to be noted that this deterministic information may not be exact but it can help identify the key lubrication and wear processes occurring within the contact under different contact configurations and operating conditions. Thus, a tool able to help easy identification of contact performance is devised.

7.4 Operating and numerical parameters

The results are presented in the following sections by varying the slide to roll ratios from -10 % to 10 %. The ball and disc are assumed to be made up of steel 52100. The roughness, R_a of the ball and disc is 20 nm and 100 nm, respectively. The ball has a diameter of 20 mm and the wear track radius is 39 mm (see Figure 6-3 for the definition of wear track). A rolling sliding contact is assumed with rolling speed / entrainment speed, $U_r = 0.25$ m/s. The applied pressure is 1.26 GPa and the fitted tribofilm growth parameters are taken from Ghanbarzadeh et al. [120]. The values of h_{max} , x_{tribo} , C_1 and C_2 are 176 nm, 4.13×10^{-16} , 0.1125 and 0.0006799, respectively. The wear coefficient values are $K_{max} = 10^{-5}$ and $K_{min} = 10^{-6}$.

The simulations are run for different slide to roll ratios by moving the matrices of surface height information at relative speeds. The results for the tribofilm growth for these contact operating and numerical parameters were presented in chapter 5 and in this chapter mainly the results for the tribochemical wear are presented.

7.5 Results and discussion

The wear is generally reported as a mean value of material height removed inside the rubbing track. This approach is very well established and even numerical results are presented in this format. In this study, the aim is to go one step ahead and observe the

validity of the Archard's wear model in real systems and to what extent Archard's wear model can give accurate results.

7.5.1 Mean wear depth

The first set of results are presented for the average wear depth for the ball and disc surface. Figure 7-3 gives the mean wear depth for the smoother ball surface and the mean wear on the disc is presented in Figure 7-4.

A close examination of both the figures shows that the ball undergoes almost 4 times higher wear compared to that on disc. This is because the ball undergoes many more loading cycles for the complete duration of the simulation experiment. The positive and negative SRR values have different effect on the wear performance. The ball is moving faster for positive slide to roll ratios and the effect of positive slide to roll ratio on wear behaviour can be precisely identified as seen in part (a) of Figure 7-3. For the negative slide to roll ratios where the ball is moving slower than the disc, the wear behaviour for different SRR values is not clearly identifiable from the mean wear depth plots as shown in part (b) of Figure 7-4.

The dependence of wear on SRR for the disc is the same but some differences can be observed. Whether the SRR is positive where the disc is moving slower or SRR is negative where the disc is moving faster, the differences in the wear behaviour of discs with variations in SRR is not very clear. For positive SRR values, during the first hour of the simulation, a difference in the wear behaviour with SRR can be observed with higher SRR values corresponding to higher wear but all the average values merge in a narrow band of values with no specific correlation towards the end of 2 hours simulation test. The disc is moving faster and dominating contact wear characteristics for negative SRR values and thus, the SRR correlates with the wear behaviour with more negative values corresponding to higher wear.

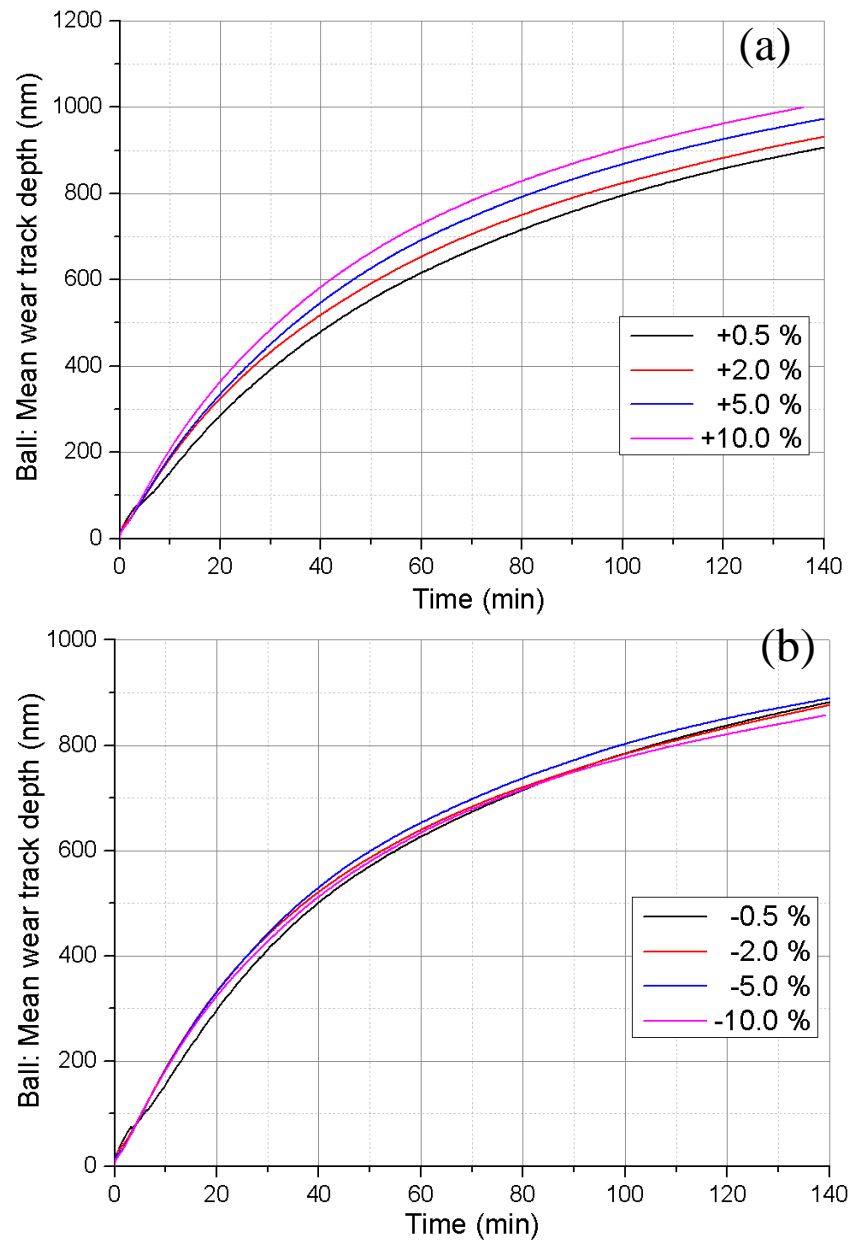


Figure 7-3: Mean wear depth on the ball surface calculated from the current model over time. The legends are the SRR values. (a) positive SRR. (b) negative SRR

It is to be noted that the wear model used is a simplified representation of the complex phenomenon happening at the interface, the differences in the values of disc wear for different slide to roll ratios is not considered important. The results for the wear on ball for the positive SRR values give an indication about the effect of SRR on wear i.e. higher SRR values mean higher wear. The same qualitative conclusion can be

reached by looking at the disc wear values for the negative SRR values where higher slide to roll ratios give more wear.

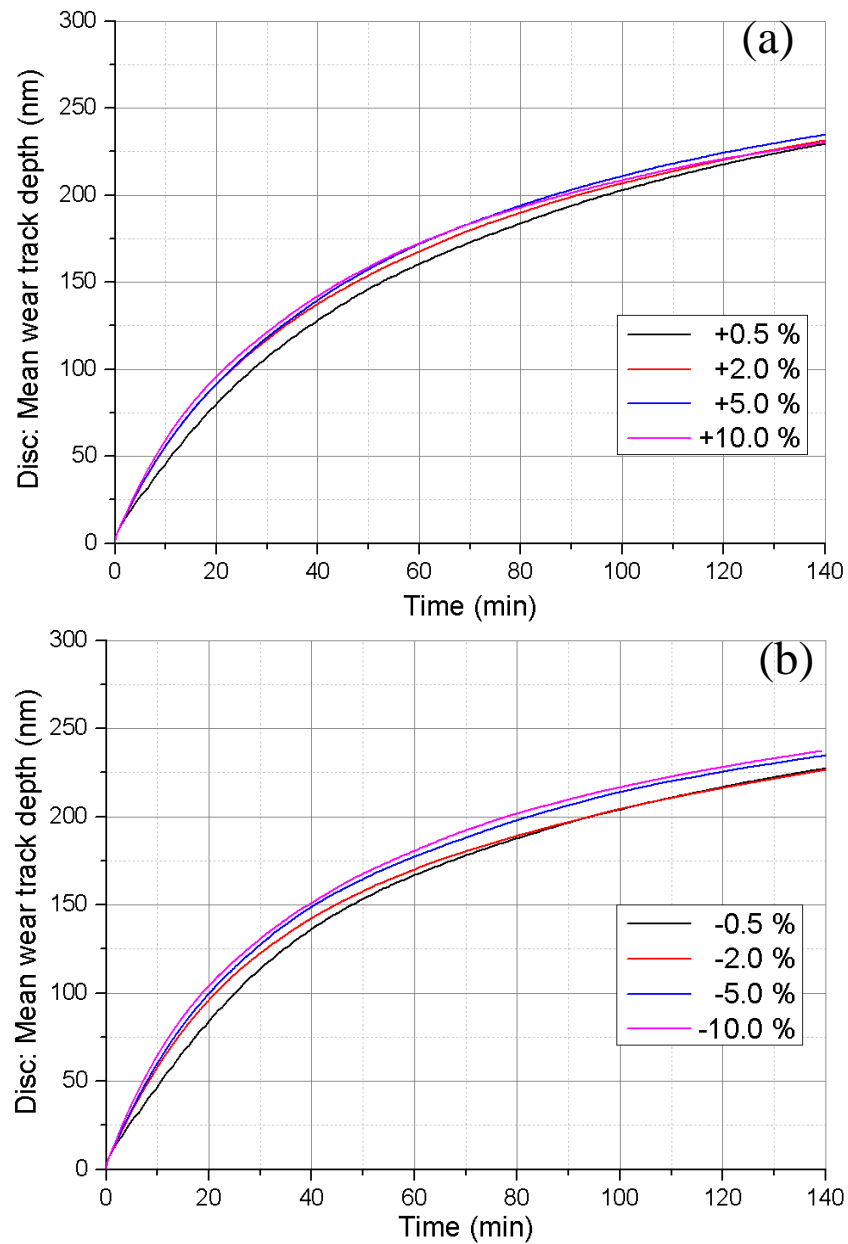


Figure 7-4: Mean wear depth on the disc surface calculated from the current model over time. The legends are the SRR values. (a) positive SRR. (b) negative SRR

Another important point to be noted from the results presented in Figure 7-3 and Figure 7-4 is that the features present in the plots of average wear depth are prominent if the ball moves much faster compared to the disc. Thus, contrary to the existing

approach where sliding is considered the main parameter affecting wear, the relative speeds of both surfaces is also very important. From these average wear plots, it can be seen that the difference in wear is not only because of sliding but the number of times the rough and smooth surface passes through the contact is also important. Thus, the movement of the rough surface through the contact is controlling the wear and contact performance. This will be discussed in more detail in the next section with deterministic local details to justify this hypothesis.

7.5.2 Wear track and worn surface profiles (2-D)

It was seen in the last section that the average wear depth despite being very useful in giving macroscopic properties of the contact lacks the ability to identify the wear performance of the contacting counterparts. Therefore, in this section the results for the final worn profiles of the ball and disc are plotted to see if these can help to identify the wear behaviour.

The wear profiles on the ball are plotted in Figure 7-5. These profiles are taken at the cross-section of the contact (at $Y=0$) and are representative of the wear that has taken place during the 2 hour simulation test. The plots indicate very clearly that the ball surface wear increases with increase in the SRR value. Thus the case of $SRR = -10\%$ gives the lowest wear and the case of SRR of $+10\%$ gives the most wear as indicated by the worn surface profiles in Figure 7-5. This figure indicates that not only the amount of wear increases but the wear track width and profile also change. Thus when the wear is under consideration, the increase in the speed of the ball within the contact can be related to the wear on the ball. For the SRR of -10% , the ball has the lowest speed of movement among the SRR values discussed and the wear is lowest. When the speed of the ball is the highest, the wear is also highest. This correlation is also valid when considering intermediate values of SRR .

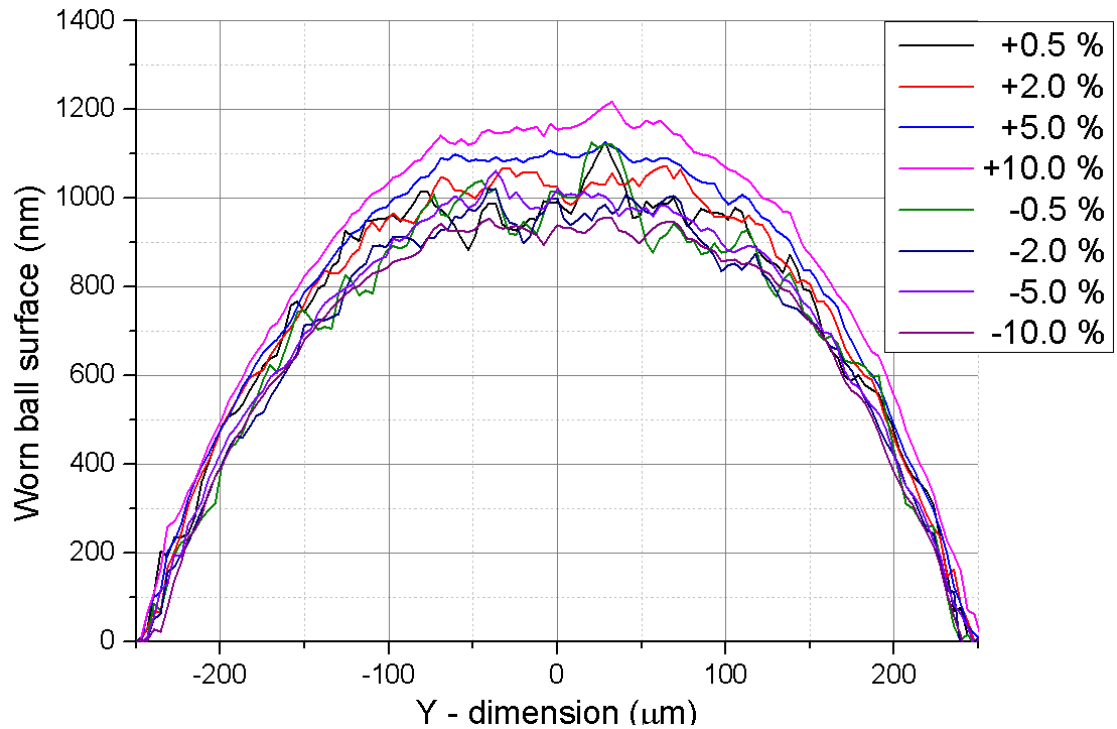


Figure 7-5: The profile of wear on the surface of ball for different SRR values. The plots present values for the worn geometry at the cross-section in the middle of contact at $Y=0$.

A plot of the actual worn surface of the ball is presented in Figure 7-6. The results are presented for different values of SRR and the original undeformed starting profile of the ball is also given for reference. A significant amount of material is removed during this 2 hour simulation test and the original ball curvature also changes. Once again the wear is lowest for the SRR of -10 % and is highest for the SRR of +10 % correlating with the speed of the ball. The difference in the amount of wear between these two representative SRR values is almost 250 nm at the middle of the contact. The model strength in capturing the differences in the wear rate can be readily seen by observing the fact that the wear profiles in Figure 7-5 and the actual ball geometry plots in Figure 7-6 for the intermediate SRR values all lie in between the minimum wear value given by SRR = -10% and the maximum wear value given by +10 %. The x-axis in both the

figures are in micrometres and thus, it can be seen that the contact width increases in the order of micrometres among different SRR values used.

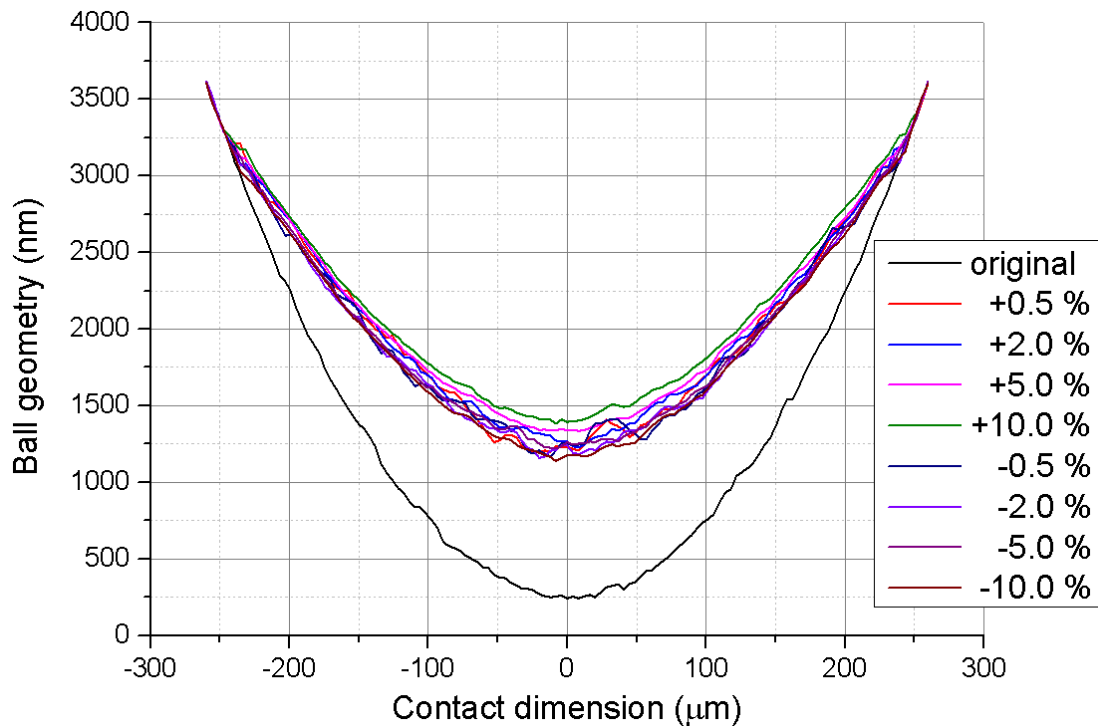


Figure 7-6: The profile of actual worn geometry of the surface of ball for different SRR values. The plots present values for the worn geometry at the cross-section in the middle of contact at $Y=0$.

Next, the worn surface profiles on the disc surface are observed as shown in Figure 7-7. The disc surface ($R_a = 100$ nm) is much rougher than the ball surface ($R_a = 10$ nm). Thus, a quick look at the worn disc profiles suggests that by comparing the roughness at the edges and the central region, the surface roughness of the disc has decreased significantly. It is not possible to extract a correlation in the data by simply looking at these worn disc surface profiles. It is seen that the data definitely shows that by varying the SRR values, the disc surface undergoes different wear not only in terms of quantitative wear volume but the qualitative wear profile is different as well for different values of SRR. The difference in the final roughness of the disc is also

seen in Figure 7-7. The differences in the wear track width can also be seen by observing that the point at which the roughness at the edges of the wear track and inside the middle of the wear track starts to differ is different for SRR values.

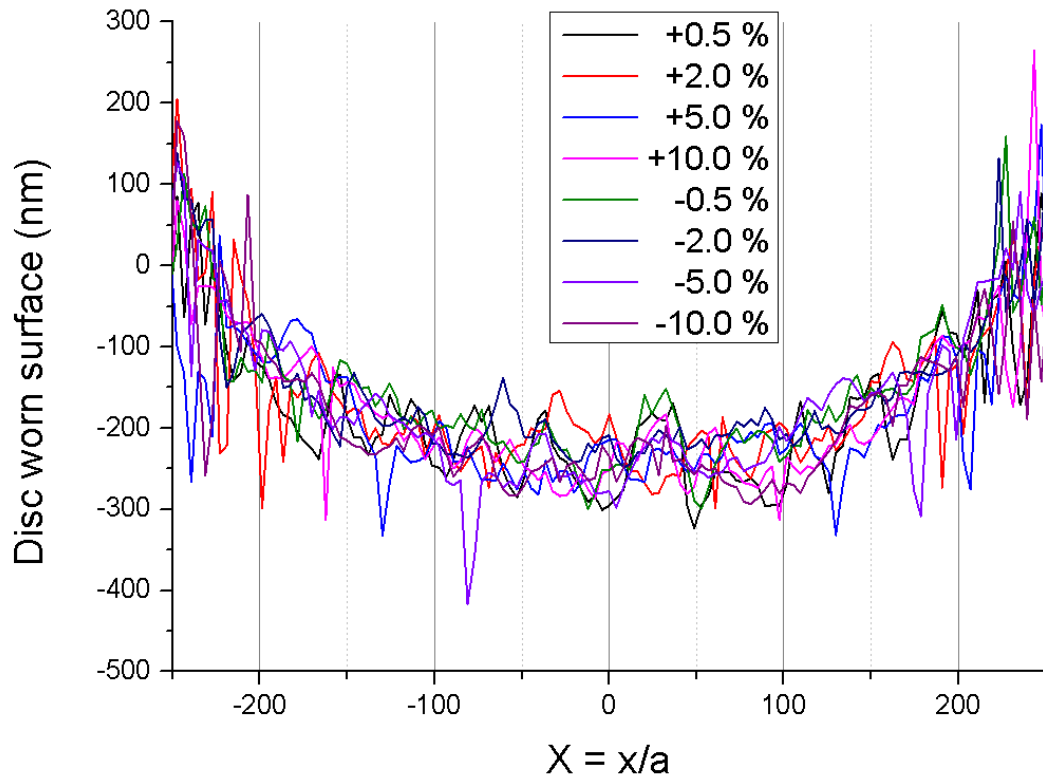


Figure 7-7: The profile of wear on the surface of disc for different SRR values. The plots present values for the worn geometry at the cross-section in the middle of contact at $Y=0$.

Thus, the 2-D wear track profiles for the ball and disc give very useful information about the wear performance of the contact. The contact configuration with the best and worst performance can be identified easily for the ball but in the current configuration it is not possible to identify differences in wear for different SRR values for the disc. To represent the results of wear to a wider audience, the 3-D wear plots are also presented with arrows indicating the increasing the increase in performance

of the contact. The wear of the system has been taken as the parameter to identify the performance of the contact.

7.5.3 Wear track profiles (3-D)

The 3-D wear track profiles are plotted by taking a snapshot of the top view of the contact at the end of the 2 hour simulation. The 3-D wear profiles are plotted for the ball in Figure 7-8. The darkness of the red colour correlates to more wear and in the final part in the bottom right of the figure, the white colour in the middle of the wear track corresponds to the worst case with the most wear. The arrows have been drawn in the plots to show the direction of increasing wear and decreasing performance of the contact. The contact performance can be readily identified. It can be seen that the wear is lowest for the SRR of -10 % and increases as the SRR is changed to +10 %. Similar behaviour was observed with the 2-D plots as well (see Figure 7-5 and Figure 7-6) but with 3-D plots, it is even possible to address public and non-specialist audience. The wear in the case of ball again correlates with the speed of the ball. The faster the ball moves through the contact, the more the loading cycles that it undergoes and subsequently more wear occurs. Thus shear is not the only parameter that affects wear and to address the topic in more detail, further work needs to be done.

The wear on the disc is expected to show similar characteristics and certain trends in wear behaviour with SRR. The 3-D wear profiles have been drawn for the disc in Figure 7-9. The amount of blue and green colour corresponds to the amount of wear. It is difficult to identify a pattern in the wear behaviour of the disc but a close examination clarifies that the disc undergoes more wear in the case of positive SRR values compared to the negative SRR values. This can be seen by comparing the results of wear for respective positive and negative SRR values with similar magnitude of SRR. It is easy to identify this behaviour for the smaller values of SRR

= $\pm 0.5\%$ and $SRR = \pm 2.0\%$ but for the higher values of SRR considered ($SRR = \pm 5\%, \pm 10\%$), it is difficult to identify whether positive or negative SRR values give better wear performance. Thus, these results indicate that the wear for a tribopair with different magnitudes of roughness in general correlates with the speed of the individual contact pair. An examination of the corresponding 2-D wear tracks on the disc show that for higher values of SRR, wear on the disc is approximately the same for both positive and negative SRR values but the wear track width is different. Thus, to address the topic more work needs to be done to analyse more parameters and perform a parametric study. As this chapter is mainly to address the strengths and capabilities of the modelling framework that was developed, so, a comprehensive study to deal with this topic of wear will follow as a future work.

7.6 Summary

This chapter presented the results on wear of the tribological setup for a ball-on-disc configuration simulated by the tribochemical mixed lubrication model developed in the current study for different values of SRR. The weakness of the average wear depth results in giving detailed information of the events happening at the contact is identified and the 2-D and 3-D wear track profiles are developed and plotted. It is relatively easy to identify the correlations in wear of the system with these resolved plots.

It was observed that the wear on the ball and disc wear exhibit similar characteristics. The wear was found to generally correlate very well with the speed of the ball or disc respectively. With increase in the slide to roll ratio moving from -10% to $+10\%$, the wear on the ball increases but for the disc it was difficult to extract a pattern but the wear was found to increase by moving from negative to positive SRR values with corresponding magnitude.

The idea in this chapter is to present the capability of the model in producing wear results and its ability to identify different wear characteristics by varying parameters.

It was identified that these results were not sufficient and more work needs to be done to generalize the outcomes of the current study on wear and explore this topic further.

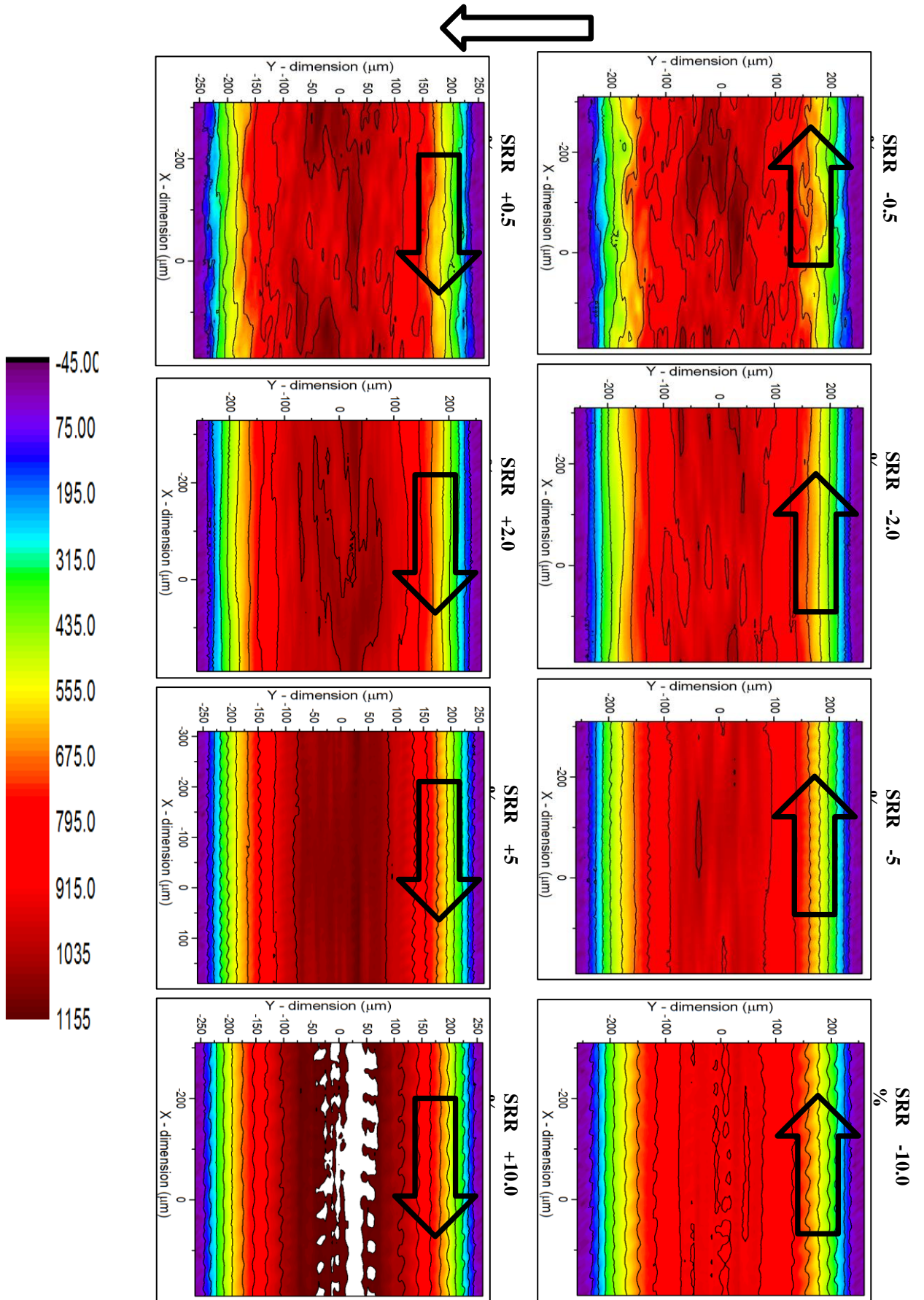


Figure 7-8: 3-D wear track profiles on the ball. Arrows indicate increase in wear.

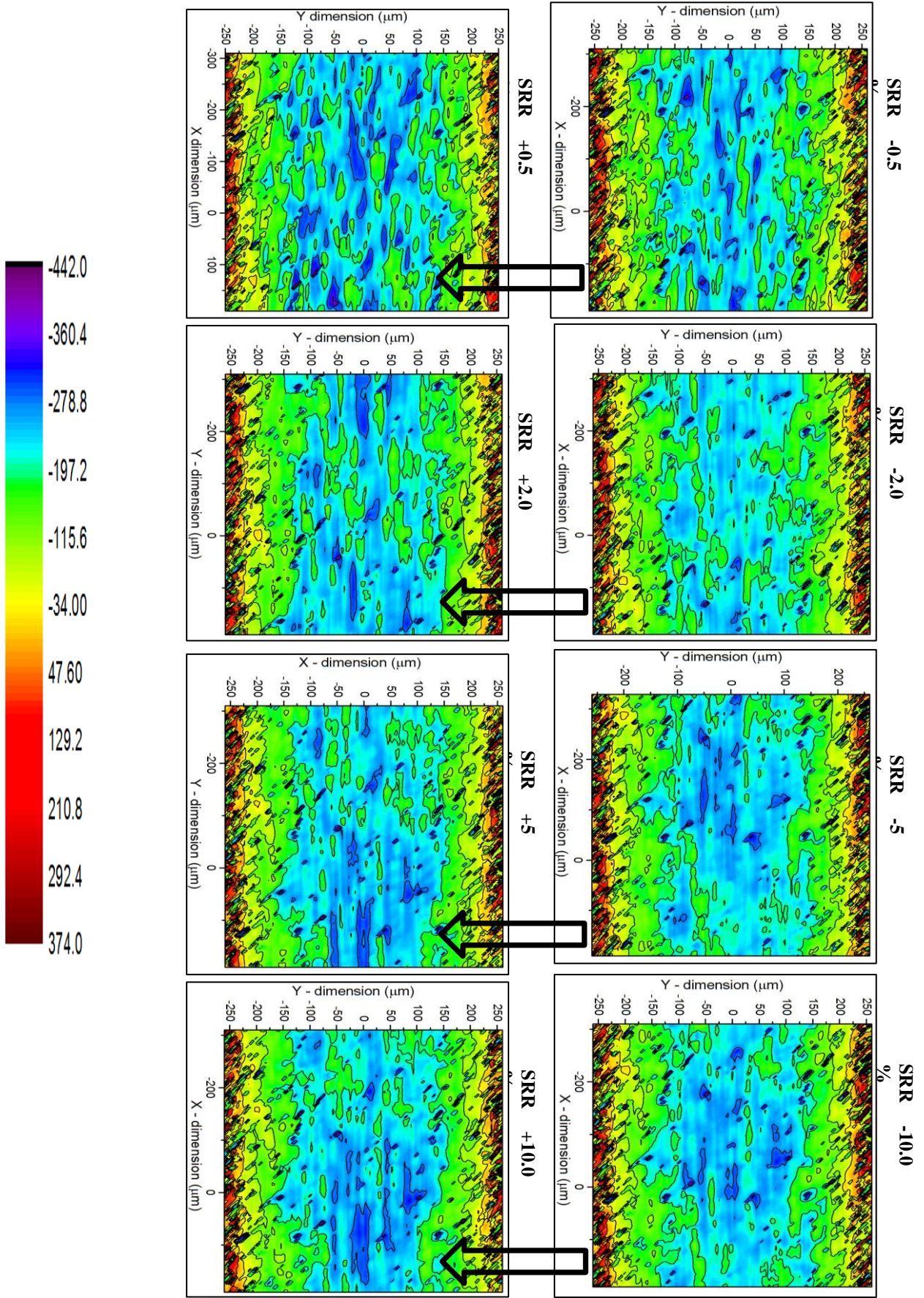


Figure 7-9: 3-D wear track profiles on the Disc. Arrows indicate increase in wear.

Chapter 8

Conclusion and Future Outlook

In this chapter the main conclusions reached by the current study are outlined. First a summary of the key developments is given and then the general conclusions are drawn. The final section presents the main directions in which this study can be extended.

8.1 Summary of key developments and advances achieved

A realistic model to incorporate tribochemistry in the mixed lubrication regime is developed. A robust solver was designed to solve the mixed lubrication problem and has been tested to simulate the entire transition from full film to boundary lubrication. Fast Fourier Transforms were used to solve the convolution of the deformation algorithm. The use of FFTs resolved the issue of numerical scaling of the EHL / ML results and enabled simulations over larger area and finer grids. A numerical algorithm was developed to simulate elastic perfectly plastic conditions and was integrated into the mixed lubrication solver. Thus, more realistic contact conditions can be simulated. The plastic deformation was designed to give minimum increase in computational burden and to simulation of plastic deformation irrespective of whether the contact is fluid or solid contact point. The mechanical properties of the tribofilm are considered in the model by using the variable hardness model. The hardness of the tribofilm changes with the thickness of the tribofilm.

The model captures the multi-physics behaviour inside the contact, linking the lubrication analysis to contact mechanics and tribochemistry. The mixed lubrication model can simulate the mixed contact condition and the tribofilm growth on the contacting asperities can be locally analysed. The model is able to capture the dynamic

growth and removal of the tribofilm and the wear of the substrate. The model is capable of not only simulating the tribofilm growth under different lubricating conditions but enables the study of mutual interactions between lubricant film formation and the tribofilm formation.

The wear of the tribological system was modelled using the Archard's wear equation and the model was tested to check its capability in predicting not only the average wear but the detailed 2-D and 3-D wear tracks were also predicted and correlations were outlined. The ability of the model to produce 3-D wear tracks within the limitations of Archard's wear model was tested.

The key capabilities of the model have been outlined below

- The entire transition from full film lubrication down to boundary and dry contact conditions.
- Parametric analysis of lubrication transition can be performed.
- The tribofilm growth can be simulated on realistic timescales with different values of starting (conventional) λ ratios.
- The effect of different contact parameters on the tribofilm growth behaviour can be studied.
- The effect of tribofilm growth on the contact operating parameters can be performed.
- The model can be adapted to most experimental configurations and the most common configuration of a ball-on-disc has been presented.
- The plastic deformation can be simulated without actual asperity contact conditions. Thus allowing simulation of plastic yielding caused by fluid pressures as well.
- A detailed study of the relative contribution of plastic deformation, wear and tribofilm growth can be performed and their mutual effects studied.

- The simulations can be performed in time and the realtime evolution of not only the average parameters is possible but the evolution of the actual surface profiles is possible.
- The model is capable of producing 2-D and 3-D wear track profiles. The behaviour observed from the average wear depth profiles does not give complete information about the wear of the tribosystem. The wear track profiles give detailed information about the wear and its causes and correlations in the wear behaviour can be easily identified.

8.2 General conclusion and discussion

A robust solver was developed based upon the line by line TDMA algorithm and advanced concepts like the semi-system approach and the unified solution algorithm were implemented. The deformation convolution was solved using the highly optimized fftw library to speed up the calculation process. The numerical grid justification was given and the results from the model compared against the published simulation results. The model was used to simulate the transition of lubrication by starting with a higher speed and reducing the speed in steps. The central film thickness and contact area ratios were measured for every speed. The transition speeds for full film to mixed and mixed to boundary / dry conditions could be easily identified. The contact area and contact load ratios were simulated and linked to lubrication transition. The variation of these parameters with rolling speed presented a Stribeck type behaviour.

The plastoelastohydrodynamic lubrication model was validated against experimental results and the effect of geometry update due to wear and plastic deformation was simulated and the differences that this update procedure has on the lubricant film thickness and pressure profiles was discussed. The elastic perfectly plastic

deformation successfully produces the differences in pressure film thickness profiles. The film thickness profile is flattened in the middle of the contact while the film thickness constriction at the exit of the contact region becomes deeper due to plastic deformation and the depth of this constriction increases further with geometry update. This topic was not further explored as this was not the main topic of this thesis but is left for future exploration.

The tribofilm growth inside a mixed lubricated contact was simulated by scaling down the experimental geometries. The experimental time scales were simulated by matching the loading cycles that the individual ball and disc undergo in a real experiment. The mean tribofilm growth values obtained from the current model capture realistic experimental observations as evidenced by the match of tribofilm growth values from the model against the experimental tribofilm growth results. The tribofilm grows in a patchy fashion and small patches coalesce to form bigger patches as the tribofilm growth process continues. The model also captures the overshoot in the tribofilm mean values which has been observed experimentally as well. This overshoot is linked to the removal and coverage of the tribofilm and has been included in the tribofilm growth model within the overall model. The complete flowchart for simulating the tribofilm growth was given and the model was implemented in a quasi-static mode. The tribofilm removal is linked to the durability of the tribofilm. The tribochemical film growth model used in the current mixed lubrication modelling study was originally developed and used in a dry contact model. Thus, the predicted tribofilm mean thickness values from the current study are comparatively lower. But the model captures all the qualitative features like the overshoot and a mean limiting value of tribofilm thickness, very efficiently. The effect of SRR value on the tribofilm growth is also well reproduced.

The tribofilm growth and removal and the wear of the substrate along with the plastic deformation modify the lubrication behaviour. This was studied for the first time and the effect of tribofilm growth on the key parameters defining the lubrication performance was studied. First the combined effect of geometry update due to wear, plastic deformation and tribofilm growth on the central film thickness, lambda ratio, contact area ratio and contact load ratio was studied over time. Then simulations were performed to study the effect tribofilm growth on the contact performance. A comparison of the conventional and modified parameters was also performed and the weakness of the conventional definitions of the central film thickness and the lambda ratio was highlighted. The effect of tribofilm growth on the central film thickness, lambda ratio, roughness evolution contact area ratio, contact load ratio and the maximum local instantaneous pressure was presented. The growth of tribofilm roughens the contact. The contact area and contact load ratios also increase due to growth of tribofilm. This might seem detrimental in the beginning but the increase in roughness enables more lubricant entrapment and therefore the central film thickness also increases due to tribofilm growth and is expected to improve lubrication performance. Thus, a final plot of the film thickness ratio gives the complete picture. The tribofilm growth increases the lambda ratio and improves lubrication regime. The effect of central film thickness improvement is stronger compared to the detrimental effect of increase in roughness due to tribofilm growth. The antiwear action of ZDDP tribofilm is not only due to the reaction layer formation but the physical growth of tribofilm results in increase of lambda ratio and thus improves lubrication and reduces wear.

The wear of the tribosystem in the current work was modelled by modifying the Archard's wear equation. The wear in a tribochemically active system depends on the reaction layer formation. Thus, the wear model was implemented to consider the

effect of antiwear behaviour of ZDDP. The wear coefficient for the tribofilm was considered 10 times less than the wear of steel-steel contacts. The antiwear character can be successfully observed and predicted by the current model. The wear was found to affect tribofilm growth and vice versa. The more the growth of tribofilm, the less the wear and the more the wear the less the tribofilm growth. The wear modelled is the wear of the substrate in the presence of tribofilm and is referred to as mild wear. A comparison of the average wear depth results shows that the wear on the ball increases with increasing speed of the ball as the number of loading cycles increases with increasing speed of the ball. This trend was more clear when the 2-D and 3-D wear tracks were plotted. For the disc it was not possible to identify a correlation like this but it was found that the wear is generally greater for the negative SRR values than for the positive SRR values. For the positive SRR values, the disc is moving slower and the disc moves faster for negative SRR values. Thus, it can be inferred that the speed of the counterpart motion inside the contact is related its wear. Another important results that can be concluded from the wear results is that the complex interaction between the roughness, wear, plastic deformation and tribofilm growth necessitates further investigation into this wear behaviour and further work needs to be done.

8.3 Future work

The developed model provides a platform for further development. The difficulties associated with the experimental study of mixed lubrication demand that the models to describe mixed lubrication phenomenon are actively developed. Therefore, the model needs refinements and additions to ultimately achieve a lubrication solver that can be used directly in industries:

- The modelling of friction in the mixed lubrication condition. The mixed friction is the sum of solid contact friction, the lubricant shear and the reaction layer friction. These key concepts need to be modelled to simulate friction.
- The inclusion of the variable elastic modulus in defining the mechanical properties is required. The contact area ratio controls the friction characteristics and is directly related to the modulus.
- The interaction between the time scales in the Reynolds equation and the quasi-static time scale.
- A parametric study on the effect of various contact parameters on the contact area and contact load ratios.
- Models to include fatigue failure of the tribocontacts in this mixed lubrication conditions. The presence of ZDDP additive increases the surface fatigue phenomenon, called micropitting significantly.
- The inclusion of oxide layer through the oxide layer growth model. This can be done by describing the oxide layer as a competing Arrhenius type phenomenon and simulating the dynamic contact characteristics.
- The simulation of the effect of electric double layer during electro active chemical interactions at the interface.
- A proper temperature calculation procedure to simulate the entire temperature distribution inside the mixed lubricated contact should be implemented rather than fixing the temperatures.
- A proper temperature calculation procedure based upon the real time heat partition functions. This will give the dynamic heat transfer characteristics of the contact.

- The calculation of sub surface stresses to access the material failure from a more fundamental point of view.
- A complete analysis to capture the removal behaviour of the tribofilm. The removal of the tribofilm has been observed to occur preferentially at the edges of the wear track but to draw some conclusion, more work needs to be done.
- The current tribofilm growth model is not clearly including the effect of shear. To prove the idea of shear based growth of tribofilm, some simulations need to be done in the full film condition with thicker lubricants to create more friction.
- The integration of different tribofilm growth models to get a generalized tribofilm growth model that considers the growth of tribofilm due to all possible driving factors.

Bibliography

1. Reynolds, O., *On the Theory of Lubrication and Its Application to Mr. Beauchamp Tower's Experiments, Including an Experimental Determination of the Viscosity of Olive Oil*. Proceedings of the Royal Society of London, 1886. **40**(242-245): p. 191-203.
2. Almqvist, T., *Computational fluid dynamics in theoretical simulations of elastohydrodynamic lubrication*, 2004, Luleå tekniska universitet.
3. Ingole, S.P. and J. Valdes, *Tribo-chemistry and Tribo-corrosion*, in *Tribology for Scientists and Engineers*. 2013, Springer. p. 729-746.
4. Heinicke, G., *Tribochemistry Carl Hanser Verlag*. Munich, Germany, 1984.
5. Wood, R.J., et al., *Tribological design constraints of marine renewable energy systems*. Philosophical Transactions of the Royal Society A: Mathematical, Physical and Engineering Sciences, 2010. **368**(1929): p. 4807-4827.
6. Habeeb, J. and W. Stover, *The role of hydroperoxides in engine wear and the effect of zinc dialkyldithiophosphates*. ASLE transactions, 1986. **30**(4): p. 419-426.
7. Willermet, P., L. Mahoney, and C. Haas, *The effects of antioxidant reactions on the wear behavior of a zinc dialkyldithiophosphate*. ASLE TRANSACTIONS, 1979. **22**(4): p. 301-306.
8. Stachowiak, G. and A.W. Batchelor, *Engineering tribology*. 2013: Butterworth-Heinemann.
9. Kankar, P., S.C. Sharma, and S. Harsha, *Nonlinear vibration signature analysis of a high speed rotor bearing system due to race imperfection*. Journal of Computational and Nonlinear Dynamics, 2012. **7**(1): p. 011014.
10. Leighton, M., et al., *Surface specific asperity model for prediction of friction in boundary and mixed regimes of lubrication*. Meccanica, 2017. **52**(1-2): p. 21-33.
11. Hua, D., et al., *A Mixed Elastohydrodynamic Lubrication IVIodel With Asperity Contact*. 1999.
12. Chang, L., Y.-R. Jeng, and Q. Yu, *A unified mixed-lubrication model of rolling-sliding line contacts from elastohydrodynamic lubrication to boundary lubrication*. Proceedings of the Institution of Mechanical Engineers, Part J: Journal of Engineering Tribology, 2016. **230**(9): p. 1056-1070.
13. Heshmat, H., *Tribology of interface layers*. 2010: CRC Press/Taylor & Francis.
14. Ducu, D., R. Donahue, and J. Gandhi, *Design of capacitance probes for oil film thickness measurements between the piston ring and liner in internal combustion engines*. Journal of engineering for gas turbines and power, 2001. **123**(3): p. 633-643.
15. Glovnea, R., et al., *Electrical methods for the evaluation of lubrication in elastohydrodynamic contacts*. Tribology Online, 2012. **7**(1): p. 46-53.
16. Andrade, J.D., *X-ray photoelectron spectroscopy (XPS)*, in *Surface and interfacial aspects of biomedical polymers*. 1985, Springer. p. 105-195.

17. Zhu, D. and Q.J. Wang, *On the λ ratio range of mixed lubrication*. Proceedings of the Institution of Mechanical Engineers, Part J: Journal of Engineering Tribology, 2012. **226**(12): p. 1010-1022.
18. Dwyer-Joyce, R., T. Reddyhoff, and J. Zhu, *Ultrasonic measurement for film thickness and solid contact in elastohydrodynamic lubrication*. Journal of Tribology, 2011. **133**(3): p. 031501.
19. Benabdallah, H. and D. Aguilar, *Acoustic emission and its relationship with friction and wear for sliding contact*. Tribology Transactions, 2008. **51**(6): p. 738-747.
20. Zhu, D. and Q.J. Wang, *Elastohydrodynamic lubrication: a gateway to interfacial mechanics—review and prospect*. Journal of Tribology, 2011. **133**(4): p. 041001.
21. Landolt, D. and S. Mischler, *Tribocorrosion of passive metals and coatings*. 2011: Elsevier.
22. Andersson, J., et al., *Semi-deterministic chemo-mechanical model of boundary lubrication*. Faraday discussions, 2012. **156**(1): p. 343-360.
23. Ghanbarzadeh, A., *Mechano-chemical modelling of boundary lubrication*, 2016, University of Leeds.
24. Brizmer, V., et al., *The Influence of Tribolayer Formation on Tribological Performance of Rolling/Sliding Contacts*. Tribology Letters, 2017. **65**(2): p. 57.
25. Stachowiak, G.W., *Wear: materials, mechanisms and practice*. 2006: John Wiley & Sons.
26. Dowson, D., *Tribological principles in metal-on-metal hip joint design*. Proceedings of the Institution of Mechanical Engineers, Part H: Journal of Engineering in Medicine, 2006. **220**(2): p. 161-171.
27. Rodrigues, D. *Failure Mechanisms in Total-Joint and Dental Implants*. danieli.wikidot.com [Electronic] 2017; Biomaterials for Osseointegration and Novel Engineering (BONE lab)].
28. Fischer, T., *Tribochemistry*. Annual Review of Materials Science, 1988. **18**(1): p. 303-323.
29. Venner, C.H. and A.A. Lubrecht, *Multi-level methods in lubrication*. Vol. 37. 2000: Elsevier.
30. Roelands, C.J.A., *Correlational aspects of the viscosity-temperature-pressure relationship of lubricating oils*. 1966.
31. Dowson, D. and G. Higginson, *Elastohydrodynamic lubrication, the fundamentals of roller and gear lubrication*, 1966, Pergamon, Oxford.
32. Petrusevich, A.f.l., *Principal conclusions from contact-hydrodynamic theory of lubrication*. 1950: Associated Technical Services.
33. Lubrication, H., *An average flow model for determining effects of three-dimensional roughness on partial hydrodynamic lubrication*. 1978.
34. Patir, N., *Application of average flow model to lubrication between rough sliding surfaces*.
35. Christensen, H., *Stochastic models for hydrodynamic lubrication of rough surfaces*. Proceedings of the Institution of Mechanical Engineers, 1969. **184**(1): p. 1013-1026.
36. Christensen, H. and K. Tonder, *The hydrodynamic lubrication of rough bearing surfaces of finite width*. Journal of Lubrication Technology, 1971. **93**(3): p. 324-329.

37. Johnson, K., J. Greenwood, and S. Poon, *A simple theory of asperity contact in elastohydro-dynamic lubrication*. *Wear*, 1972. **19**(1): p. 91-108.
38. Greenwood, J. and J. Williamson. *Contact of nominally flat surfaces*. in *Proceedings of the Royal Society of London A: Mathematical, Physical and Engineering Sciences*. 1966. The Royal Society.
39. Tallian, T., et al., *Lubricant films in rolling contact of rough surfaces*. *ASLE TRANSACTIONS*, 1964. **7**(2): p. 109-126.
40. Valori, R., T. Tallian, and L. Sibley. *Elastohydrodynamic Film Effects on Load-Life Behavior of Rolling Contacts*. in *MECHANICAL ENGINEERING*. 1965. ASME-AMER SOC MECHANICAL ENG 345 E 47TH ST, NEW YORK, NY 10017.
41. Tallian, T., *On competing failure modes in rolling contact*. *ASLE TRANSACTIONS*, 1967. **10**(4): p. 418-439.
42. Tallian, T., *Pressure and traction rippling in elastohydrodynamic contact of rough surfaces*. *Journal of Lubrication Technology*, 1974. **96**(3): p. 398-406.
43. Liu, J., T. Tallian, and J. McCool, *Dependence of bearing fatigue life on film thickness to surface roughness ratio*. *ASLE TRANSACTIONS*, 1975. **18**(2): p. 144-152.
44. Tallian, T., Y. Chiu, and E. Van Amerongen, *Prediction of Traction and Microgeometry Effects on Rolling Contact Fatigue Life*. *Journal of Lubrication Technology*, 1978. **100**(2): p. 156-165.
45. Elrod, H.G., *Thin-film lubrication theory for Newtonian fluids with surfaces possessing striated roughness or grooving*. *ASME J. Lubr. Technol*, 1973. **95**(4): p. 484-489.
46. Rhow, S.K. and H.G. Elrod, *Effects on Bearing Load-Carrying Capacity of Two-Sided Striated Roughness*. *J. Lubric. Technol.(Trans. ASME, F)*, 1974. **96**(4): p. 554-560.
47. Elrod, H., *A general theory for laminar lubrication with Reynolds roughness*. *Journal of Lubrication Technology*, 1979. **101**(1): p. 8-14.
48. Berthe, D. and M. Godet, *Équation de l'écoulement laminaire entre deux parois rapprochées en mouvement relatif*. *CR Académie des Sciences, Paris*, 1971. **272**: p. 1010-1013.
49. Elrod, H.G., *A Review of Theories for the Fluid Dynamic Effects of Roughness on Laminar Lubricating Films*, 1977, DTIC Document.
50. Corporation, N., *Lubrication Regimes Explained*, in *Machinery Lubrication2017*, www.machinelubrication.com. p. 6.
51. Lee, K. and H. Cheng, *Effect of surface asperity on elastohydrodynamic lubrication*. 1973.
52. LUBRECHT, A., W. TEN NAPEL, and R. BOSMA, *The influence of longitudinal and transverse roughness on the elastohydrodynamic lubrication of circular contacts*. *Journal of tribology*, 1988. **110**(3): p. 421-426.
53. KWEH, C., H. EVANS, and R. SNIDLE, *Micro-elastohydrodynamic lubrication of an elliptical contact with transverse and three-dimensional sinusoidal roughness*. *Journal of tribology*, 1989. **111**(4): p. 577-584.
54. CHANG, L., C. CUSANO, and T. CONRY, *Effects of lubricant rheology and kinematic conditions on micro-elastohydrodynamic lubrication*. *Journal of tribology*, 1989. **111**(2): p. 344-351.

55. CHANG, L., M. WEBSTER, and A. JACKSON, *On the pressure rippling and roughness deformation in elastohydrodynamic lubrication of rough surfaces*. Journal of tribology, 1993. **115**(3): p. 439-444.
56. Venner, C.H., *Multilevel solution of the EHL line and point contact problems*. 1991: University of Twente.
57. Kweh, C., et al., *Simulation of elastohydrodynamic contacts between rough surfaces*. ASME Transactions Journal of Tribology, 1992. **114**: p. 412-419.
58. Patir, N. and H. Cheng. *Effect of surface roughness orientation on the central film thickness in EHD contacts*. in *Proc. 5th Leeds-Lyon Symp. on Tribol., London*. 1978.
59. Greenwood, J. and J. Tripp, *The contact of two nominally flat rough surfaces*. Proceedings of the institution of mechanical engineers, 1970. **185**(1): p. 625-633.
60. Zhu, D. and H. Cheng, *Effect of Surface Roughness on the Point Contact EHL*. Journal of Tribology, 1988. **110**(1): p. 32-37.
61. Zhu, D., H.S. Cheng, and B.J. Hamrock, *Effect of surface roughness on pressure spike and film constriction in elastohydrodynamically lubricated line contacts*. Tribology Transactions, 1990. **33**(2): p. 267-273.
62. GOGLIA, P., T. CONRY, and C. CUSANO, *The effects of surface irregularities on the elastohydrodynamic lubrication of sliding line contacts. I. Single irregularities. II. Wavy surfaces*. Journal of lubrication technology, 1984. **106**(1): p. 104-119.
63. Lubrecht, A., *The numerical solution of the elastohydrodynamically lubricated line-and point contact problem, using multigrid techniques*, 1987, University of Twente.
64. Xu, G. and F. Sadeghi, *Thermal EHL analysis of circular contacts with measured surface roughness*. TRANSACTIONS-AMERICAN SOCIETY OF MECHANICAL ENGINEERS JOURNAL OF TRIBOLOGY, 1996. **118**: p. 473-483.
65. Zhu, D. and X. Ai, *Point contact EHL based on optically measured three-dimensional rough surfaces*. TRANSACTIONS-AMERICAN SOCIETY OF MECHANICAL ENGINEERS JOURNAL OF TRIBOLOGY, 1997. **119**: p. 375-384.
66. Cheng, H.S., et al., *Mixed lubrication analyses by a macro-micro approach and a full-scale mixed EHL model*. 2004.
67. Dobrica, M.B., M. Fillon, and P. Maspeyrot, *Mixed elastohydrodynamic lubrication in a partial journal bearing—comparison between deterministic and stochastic models*. Journal of tribology, 2006. **128**(4): p. 778-788.
68. Akbarzadeh, S. and M. Khonsari, *On the prediction of running-in behavior in mixed-lubrication line contact*. Journal of Tribology, 2010. **132**(3): p. 032102.
69. Morales-Espejel, G.E., A. Wemekamp, and A. Félix-Quiñonez, *Micro-geometry effects on the sliding friction transition in elastohydrodynamic lubrication*. Proceedings of the Institution of Mechanical Engineers, Part J: Journal of Engineering Tribology, 2010. **224**(7): p. 621-637.
70. Chang, L., *A deterministic model for line-contact partial elastohydrodynamic lubrication*. Tribology international, 1995. **28**(2): p. 75-84.

71. Zhao, J., F. Sadeghi, and M.H. Hoeprich, *Analysis of EHL circular contact start up: part I—mixed contact model with pressure and film thickness results*. 2001.
72. Holmes, M., H.P. Evans, and R.W. Snidle, *Comparison of transient EHL calculations with start-up experiments*. Tribology Series, 2003. **41**: p. 79-89.
73. Zhao, J. and F. Sadeghi, *Analysis of EHL circular contact shut down*. TRANSACTIONS-AMERICAN SOCIETY OF MECHANICAL ENGINEERS JOURNAL OF TRIBOLOGY, 2003. **125**(1): p. 76-90.
74. Popovici, G., C. Venner, and P. Lugt, *Effects of load system dynamics on the film thickness in EHL contacts during start up*. TRANSACTIONS-AMERICAN SOCIETY OF MECHANICAL ENGINEERS JOURNAL OF TRIBOLOGY, 2004. **126**(2): p. 258-266.
75. Zhu, D. and Y.-Z. Hu, *The study of transition from elastohydrodynamic to mixed and boundary lubrication*. The advancing frontier of engineering tribology, Proceedings of the 1999 STLE/ASME HS Cheng Tribology Surveillance, 1999: p. 150-156.
76. Hu, Y.-Z. and D. Zhu, *A full numerical solution to the mixed lubrication in point contacts*. ASME J. Tribol, 2000. **122**(1): p. 1-9.
77. Ai, X., *Numerical analyses of elastohydrodynamically lubricated line and point contacts with rough surfaces by using semi-system and multigrid methods (volumes 1 and 2)*. 1993.
78. Holmes, M., H. Evans, and R. Snidle. *Analysis of mixed lubrication effects in simulated gear tooth contacts*. in *ASME/STLE 2004 International Joint Tribology Conference*. 2004. American Society of Mechanical Engineers.
79. Li, S. and A. Kahraman, *A mixed EHL model with asymmetric integrated control volume discretization*. Tribology International, 2009. **42**(8): p. 1163-1172.
80. Liu, Y., et al., *Effects of differential scheme and mesh density on EHL film thickness in point contacts*. Journal of Tribology, 2006. **128**(3): p. 641-653.
81. Liu, Y., et al., *Effects of differential scheme and viscosity model on rough-surface point-contact isothermal EHL*. Journal of Tribology, 2009. **131**(4): p. 044501.
82. Zhu, D., *On some aspects of numerical solutions of thin-film and mixed elastohydrodynamic lubrication*. Proceedings of the Institution of Mechanical Engineers, Part J: Journal of Engineering Tribology, 2007. **221**(5): p. 561-579.
83. Wang, W., et al., *Solution agreement between dry contacts and lubrication system at ultra-low speed*. Proceedings of the Institution of Mechanical Engineers, Part J: Journal of Engineering Tribology, 2010. **224**(10): p. 1049-1060.
84. Bec, S., et al. *Relationship between mechanical properties and structures of zinc dithiophosphate anti-wear films*. in *Proceedings of the Royal Society of London A: Mathematical, Physical and Engineering Sciences*. 1999. The Royal Society.
85. Spikes, H., *The history and mechanisms of ZDDP*. Tribology letters, 2004. **17**(3): p. 469-489.
86. Schwarz, U.D., *Tracking antiwear film formation*. Science, 2015. **348**(6230): p. 40-41.

87. Barnes, A.M., K.D. Bartle, and V.R. Thibon, *A review of zinc dialkyldithiophosphates (ZDDPS): characterisation and role in the lubricating oil*. Tribology International, 2001. **34**(6): p. 389-395.
88. Nicholls, M.A., et al., *Review of the lubrication of metallic surfaces by zinc dialkyl-dithiophosphates*. Tribology International, 2005. **38**(1): p. 15-39.
89. Dacre, B. and C. Bovington, *The adsorption and desorption of zinc diisopropyldithiophosphate on steel*. Asle Transactions, 1982. **25**(4): p. 546-554.
90. Thomas, B.C., *Wear modeling with sensitivity to lubricant chemistry*, 2007, Massachusetts Institute of Technology.
91. Rudnick, L.R., *Lubricant additives: chemistry and applications*. 2009: CRC press.
92. Fujita, H., R. Glovnea, and H. Spikes, *Study of zinc dialkyldithiophosphate antiwear film formation and removal processes, part I: experimental*. Tribology transactions, 2005. **48**(4): p. 558-566.
93. Fuller, M.S., et al., *The use of X-ray absorption spectroscopy for monitoring the thickness of antiwear films from ZDDP*. Tribology Letters, 2000. **8**(4): p. 187.
94. Yin, Z., et al., *Application of soft X-ray absorption spectroscopy in chemical characterization of antiwear films generated by ZDDP Part I: the effects of physical parameters*. Wear, 1997. **202**(2): p. 172-191.
95. Vengudusamy, B., et al., *Tribological properties of tribofilms formed from ZDDP in DLC/DLC and DLC/steel contacts*. Tribology International, 2011. **44**(2): p. 165-174.
96. Gosvami, N., et al., *Mechanisms of antiwear tribofilm growth revealed in situ by single-asperity sliding contacts*. Science, 2015. **348**(6230): p. 102-106.
97. Zhang, J. and H. Spikes, *On the mechanism of ZDDP antiwear film formation*. Tribology Letters, 2016. **63**(2): p. 1-15.
98. Mingwu, B., Z. Xushou, and Q. Shangkui, *Tribological properties of silicon nitride ceramics coated with molybdenum films under boundary lubrication*. Wear, 1993. **169**(2): p. 181-187.
99. Pasaribu, H. and P.M. Lugt, *The composition of reaction layers on rolling bearings lubricated with gear oils and its correlation with rolling bearing performance*. Tribology transactions, 2012. **55**(3): p. 351-356.
100. Minfray, C., et al., *Experimental and molecular dynamics simulations of tribochemical reactions with ZDDP: zinc phosphate-iron oxide reaction*. Tribology Transactions, 2008. **51**(5): p. 589-601.
101. Morina, A. and A. Neville, *Tribofilms: aspects of formation, stability and removal*. Journal of Physics D: Applied Physics, 2007. **40**(18): p. 5476.
102. Martin, J.M., *Antiwear mechanisms of zinc dithiophosphate: a chemical hardness approach*. Tribology letters, 1999. **6**(1): p. 1-8.
103. Aktary, M., M.T. McDermott, and G.A. McAlpine, *Morphology and nanomechanical properties of ZDDP antiwear films as a function of tribological contact time*. Tribology letters, 2002. **12**(3): p. 155-162.
104. Nehme, G., R. Mourhatch, and P.B. Aswath, *Effect of contact load and lubricant volume on the properties of tribofilms formed under boundary lubrication in a fully formulated oil under extreme load conditions*. Wear, 2010. **268**(9): p. 1129-1147.

105. Nicholls, M., et al., *Nanometer scale chemomechanical characterization of antiwear films*. Tribology Letters, 2004. **17**(2): p. 205-216.
106. Pereira, G., et al., *Chemical characterization and nanomechanical properties of antiwear films fabricated from ZDDP on a near hypereutectic Al-Si alloy*. Tribology Letters, 2005. **18**(4): p. 411-427.
107. Mourhatch, R. and P.B. Aswath, *Tribological behavior and nature of tribofilms generated from fluorinated ZDDP in comparison to ZDDP under extreme pressure conditions—Part II: morphology and nanoscale properties of tribofilms*. Tribology International, 2011. **44**(3): p. 201-210.
108. Mosey, N., et al., *Interpretation of experiments on ZDDP anti-wear films through pressure-induced cross-linking*. Tribology Letters, 2006. **24**(2): p. 105-114.
109. Demmou, K., et al., *Temperature effects on mechanical properties of zinc dithiophosphate tribofilms*. Tribology international, 2006. **39**(12): p. 1558-1563.
110. Martin, J.M., et al., *The two-layer structure of Zndtp tribofilms: Part I: AES, XPS and XANES analyses*. Tribology international, 2001. **34**(8): p. 523-530.
111. Crobu, M., et al., *Tribochemistry of bulk zinc metaphosphate glasses*. Tribology letters, 2010. **39**(2): p. 121-134.
112. Williams, J., *The behaviour of sliding contacts between non-conformal rough surfaces protected by 'smart' films*. Tribology Letters, 2004. **17**(4): p. 765-778.
113. Fujita, H. and H. Spikes, *The formation of zinc dithiophosphate antiwear films*. Proceedings of the Institution of Mechanical Engineers, Part J: Journal of Engineering Tribology, 2004. **218**(4): p. 265-278.
114. Suarez, A.N., *The behaviour of antiwear additives in lubricated rolling-sliding contacts*, 2011, Luleå tekniska universitet.
115. Naveira-Suarez, A., et al., *Evolution of ZDDP-derived reaction layer morphology with rubbing time*. Scanning, 2010. **32**(5): p. 294-303.
116. Gonsel, S., H. Spikes, and M. Aderin, *In-situ measurement of ZDDP films in concentrated contacts*. Tribology transactions, 1993. **36**(2): p. 276-282.
117. Zhang, Z., et al., *Tribofilms generated from ZDDP and DDP on steel surfaces: Part 1, growth, wear and morphology*. Tribology Letters, 2005. **19**(3): p. 211-220.
118. Bulgarevich, S., et al., *Population of transition states of triboactivated chemical processes*. Journal of Friction and Wear, 2010. **31**(4): p. 288-293.
119. Bulgarevich, S., et al., *Thermodynamic and kinetic analyses of probable chemical reactions in the tribocontact zone and the effect of heavy pressure on evolution of adsorption processes*. Journal of Friction and Wear, 2011. **32**(4): p. 301-309.
120. Ghanbarzadeh, A., et al., *Development of a new mechano-chemical model in boundary lubrication*. Tribology International, 2016. **93**: p. 573-582.
121. Eyring, H., *Viscosity, plasticity, and diffusion as examples of absolute reaction rates*. The Journal of chemical physics, 1936. **4**(4): p. 283-291.

122. Schallamach, A., *The velocity and temperature dependence of rubber friction*. Proceedings of the Physical Society. Section B, 1953. **66**(5): p. 386.
123. Zhurkov, S.N. *Kinetic concept of the strength of solids*. in *ICF1, Japan 1965*. 1965.
124. Bell, G.I., *Models for the specific adhesion of cells to cells*. Science, 1978. **200**(4342): p. 618-627.
125. Willermet, P., et al., *Mechanism of formation of antiwear films from zinc dialkyldithiophosphates*. Tribology International, 1995. **28**(3): p. 177-187.
126. LUTHER, H., B. E, and D. STAECK, *INVESTIGATION OF DECOMPOSITION OF DIALKYL DITHIOPHOSPHATES IN HYDROCARBONS*. ERDOL UND KOHLE ERDGAS PETROCHEMIE, 1969. **22**(9): p. 530-&.
127. Jensen, R., S. Korcek, and M. Rokosz, *Friction reducing and antioxidant capabilities of engine oil additive systems under oxidative conditions*. Lubrication Science, 1998. **10**(2): p. 99-120.
128. Jensen, R., S. Korcek, and M. Johnson, *Friction-reducing and antioxidant capabilities of engine oil additive systems under oxidative conditions. II. Understanding ligand exchange in a molybdenum dialkyldithiocarbamate/zinc dialkyldithiophosphate additive system in various base oils*. Lubrication science, 2001. **14**(1): p. 25-42.
129. Kennerly, G. and W. Patterson, *Kinetic studies of petroleum antioxidants*. Industrial & Engineering Chemistry, 1956. **48**(10): p. 1917-1924.
130. Burn, A., *The mechanism of the antioxidant action of zinc dialkyl dithiophosphates*. Tetrahedron, 1966. **22**(7): p. 2153-2161.
131. Howard, J., et al., *Metal complexes as antioxidants. I. The reaction of zinc dialkyldithiophosphates and related compounds with peroxy radicals*. Canadian Journal of Chemistry, 1973. **51**(10): p. 1543-1553.
132. Willermet, P., L. Mahoney, and C. Bishop, *Lubricant Degradation and Wear III. Antioxidant Reactions and Wear Behavior of a Zinc Dialkyldithiophosphate in a Fully Formulated Lubricant*. ASLE TRANSACTIONS, 1980. **23**(3): p. 225-231.
133. Coy, R. and R. Jones, *The thermal degradation and EP performance of zinc dialkyldithiophosphate additives in white oil*. ASLE transactions, 1981. **24**(1): p. 77-90.
134. Yamaguchi, E. and P. Ryason, *Inelastic electron tunneling spectra of lubricant oil additives on native aluminum oxide surfaces*. Tribology transactions, 1993. **36**(3): p. 367-374.
135. Fuller, M.L.S., et al., *Solution decomposition of zinc dialkyl dithiophosphate and its effect on antiwear and thermal film formation studied by X-ray absorption spectroscopy*. Tribology international, 1998. **31**(10): p. 627-644.
136. Bancroft, G., et al., *Mechanisms of tribochemical film formation: stability of tribo- and thermally-generated ZDDP films*. Tribology Letters, 1997. **3**(1): p. 47-51.
137. Fuller, M., et al., *Chemical characterization of tribochemical and thermal films generated from neutral and basic ZDDPs using X-ray absorption spectroscopy*. Tribology International, 1997. **30**(4): p. 305-315.

138. Taylor, L., A. Dratva, and H. Spikes, *Friction and wear behavior of zinc dialkyldithiophosphate additive*. Tribology transactions, 2000. **43**(3): p. 469-479.
139. Taylor, L. and H. Spikes, *Friction-enhancing properties of ZDDP antiwear additive: part I—friction and morphology of ZDDP reaction films*. Tribology transactions, 2003. **46**(3): p. 303-309.
140. Taylor, L.J. and H.A. Spikes, *Friction-enhancing properties of ZDDP antiwear additive: part II—influence of ZDDP reaction films on EHD lubrication*. Tribology transactions, 2003. **46**(3): p. 310-314.
141. Huang, P., *Numerical Calculation of Elastohydrodynamic Lubrication: Methods and Programs*. 2015: John Wiley & Sons.
142. Zargari, E.A., *Computational Analysis of Integral and Differential Formulations of the Elastohydrodynamic Lubrication Film Thickness Equation*, 2007, University of Leeds.
143. Dowson, D. and G.R. Higginson, *A Numerical Solution to the Elasto-Hydrodynamic Problem*. Journal of Mechanical Engineering Science, 1959. **1**(1): p. 6-15.
144. Houpert, L.G. and B.J. Hamrock, *Fast approach for calculating film thicknesses and pressures in elastohydrodynamically lubricated contacts at high loads*. Journal of Tribology, 1986. **108**(3): p. 411-419.
145. Oh, K. and S. Rohde, *Numerical solution of the point contact problem using the finite element method*. International Journal for Numerical Methods in Engineering, 1977. **11**(10): p. 1507-1518.
146. Hughes, T., C. Elcoate, and H. Evans, *Coupled solution of the elastohydrodynamic line contact problem using a differential deflection method*. Proceedings of the Institution of Mechanical Engineers, Part C: Journal of Mechanical Engineering Science, 2000. **214**(4): p. 585-598.
147. Holmes, M., et al., *Transient elastohydrodynamic point contact analysis using a new coupled differential deflection method part 1: theory and validation*. Proceedings of the Institution of Mechanical Engineers, Part J: Journal of Engineering Tribology, 2003. **217**(4): p. 289-304.
148. Lubrecht, A.A., *The numerical solution of the elastohydrodynamically lubricated line-and point contact problem, using multigrid techniques*, 1987, Universiteit Twente.
149. Pu, W., J. Wang, and D. Zhu, *Progressive mesh densification method for numerical solution of mixed elastohydrodynamic lubrication*. Journal of Tribology, 2016. **138**(2): p. 021502.
150. Versteeg, H.K. and W. Malalasekera, *An introduction to computational fluid dynamics: the finite volume method*. 2007: Pearson Education.
151. Johnson, K.L. and K.L. Johnson, *Contact mechanics*. 1987: Cambridge university press.
152. Liu, S., Q. Wang, and G. Liu, *A versatile method of discrete convolution and FFT (DC-FFT) for contact analyses*. Wear, 2000. **243**(1): p. 101-111.
153. Ju, Y. and T. Farris, *Spectral analysis of two-dimensional contact problems*. TRANSACTIONS-AMERICAN SOCIETY OF MECHANICAL ENGINEERS JOURNAL OF TRIBOLOGY, 1996. **118**: p. 320-328.
154. Brandt, A. and A. Lubrecht, *Multilevel matrix multiplication and fast solution of integral equations*. Journal of Computational Physics, 1990. **90**(2): p. 348-370.

155. Polonsky, I. and L. Keer, *Fast methods for solving rough contact problems: a comparative study*. ASME J. Tribol, 2000. **122**(1): p. 36-41.
156. Frigo, M. and S.G. Johnson, *The design and implementation of FFTW3*. Proceedings of the IEEE, 2005. **93**(2): p. 216-231.
157. Press, W.H., et al., *Numerical recipes in FORTRAN 77, vol. 1*. New York, NY: Press Syndicate of the University of Cambridge, 1992.
158. Press, W.H., et al., *Numerical recipes in Fortran 90*. Vol. 2. 1996: Cambridge university press Cambridge.
159. Morales-Espejel, G., et al., *A limiting solution for the dependence of film thickness on velocity in EHL contacts with very thin films*. Tribology transactions, 2005. **48**(3): p. 317-327.
160. Zhu, D., *A limiting solution for the dependence of film thickness on velocity in EHL contacts with very thin films-Discussion*, 2005, TAYLOR & FRANCIS INC 325 CHESTNUT ST, SUITE 800, PHILADELPHIA, PA 19106 USA.
161. Sahlin, F., et al., *A mixed lubrication model incorporating measured surface topography. Part 1: Theory of flow factors*. Proceedings of the Institution of Mechanical Engineers, Part J: Journal of Engineering Tribology, 2010. **224**(4): p. 335-351.
162. Ren, N., et al., *Plasto-elastohydrodynamic lubrication (PEHL) in point contacts*. Journal of tribology, 2010. **132**(3): p. 031501.
163. Ren, N., D. Zhu, and Q.J. Wang, *Three-Dimensional Plasto-Elastohydrodynamic Lubrication (PEHL) for Surfaces With Irregularities*. Journal of Tribology, 2011. **133**(3): p. 031502.
164. Sahlin, F., et al., *A mixed lubrication model incorporating measured surface topography. Part 2: Roughness treatment, model validation, and simulation*. Proceedings of the Institution of Mechanical Engineers, Part J: Journal of Engineering Tribology, 2010. **224**(4): p. 353-365.
165. Busby, J.T., M.C. Hash, and G.S. Was, *The relationship between hardness and yield stress in irradiated austenitic and ferritic steels*. Journal of Nuclear Materials, 2005. **336**(2-3): p. 267-278.
166. Pavlina, E. and C. Van Tyne, *Correlation of yield strength and tensile strength with hardness for steels*. Journal of Materials Engineering and Performance, 2008. **17**(6): p. 888-893.
167. Zhang, P., S. Li, and Z. Zhang, *General relationship between strength and hardness*. Materials Science and Engineering: A, 2011. **529**: p. 62-73.
168. Kennedy Jr, F.E., *Maximum and Average Flash Temperatures in Sliding Contacts*. Journal of tribology, 1994. **116**: p. 167.
169. John, S.T., Y. Song, and Z. Liu, *Effects of Temperature and Pressure on ZDDP*. Tribology Letters, 2007. **28**(1): p. 45-49.
170. Nakayama, K., *Triboemission of charged particles and resistivity of solids*. Tribology Letters, 1999. **6**(1): p. 37-40.
171. Kajdas, C.K., *Importance of the triboemission process for tribochemical reaction*. Tribology International, 2005. **38**(3): p. 337-353.
172. Kajdas, C., et al., *The relevance of negative ion mass spectroscopy to the interpretation of the reaction of metal dialkyldithiophosphates during lubricated rubbing*. ZFI Mitteilungen, 1986. **115**: p. 107-112.

173. Spikes, H. and W. Tysoe, *On the commonality between theoretical models for fluid and solid friction, wear and tribochemistry*. Tribology Letters, 2015. **59**(1): p. 21.
174. Tian, X. and B. Bhushan, *A numerical three-dimensional model for the contact of rough surfaces by variational principle*. Journal of Tribology, 1996. **118**(1): p. 33-42.
175. Ghanbarzadeh, A., et al., *A semi-deterministic wear model considering the effect of zinc dialkyl dithiophosphate tribofilm*. Tribology Letters, 2016. **61**(1): p. 12.
176. Akchurin, A. and R. Bosman, *A Deterministic Stress-Activated Model for Tribo-Film Growth and Wear Simulation*. Tribology Letters, 2017. **65**(2): p. 59.
177. Morales-Espejel, G.E. and V. Brizmer, *Micropitting modelling in rolling-sliding contacts: application to rolling bearings*. tribology transactions, 2011. **54**(4): p. 625-643.
178. Fujita, H. and H. Spikes, *Study of zinc dialkyldithiophosphate antiwear film formation and removal processes, part II: Kinetic model*. Tribology transactions, 2005. **48**(4): p. 567-575.
179. So, H. and Y. Lin, *The theory of antiwear for ZDDP at elevated temperature in boundary lubrication condition*. Wear, 1994. **177**(2): p. 105-115.
180. Kuzharov, A., et al., *Molecular mechanisms of self-organization at friction. Part VI. Analysis of thermodynamic features of tribochemical reactions*. Journal of Friction and Wear, 2007. **28**(2): p. 218-223.
181. Kennedy, F.E., *Frictional heating and contact temperatures*. Modern tribology handbook, 2001. **1**: p. 235-272.
182. Chang, L. and Y.-R. Jeng, *A mathematical model for the mixed lubrication of non-conformable contacts with asperity friction, plastic deformation, flash temperature, and tribo-chemistry*. Journal of Tribology, 2014. **136**(2): p. 022301.
183. Furustig, J., *Semi-deterministic numerical simulations of wear on various scales: From chemo-mechanical effects to the wear of components in orbital type hydraulic motors*, 2014.
184. Hu, Y. and K. Tonder, *Simulation of 3-D random rough surface by 2-D digital filter and Fourier analysis*. International Journal of Machine Tools and Manufacture, 1992. **32**(1-2): p. 83-90.
185. Parsaeian, P., *Effect of Water on the Interfacial Mechanisms of the Tribofilms Formed by Zinc Dialkyl Dithiophosphate: Experimental and Analytical Study*, 2017, University of Leeds.
186. Petrusevich, A.f.l., *Principal Conclusions from Contact-hydrodynamic Theory of Lubrication*. 1951: Associated Technical Services.
187. Wang, W., et al., *A comparative study of the methods for calculation of surface elastic deformation*. Proceedings of the Institution of Mechanical Engineers, Part J: Journal of Engineering Tribology, 2003. **217**(2): p. 145-154.
188. Wang, W.-Z., et al., *A mixed lubrication model with consideration of starvation and interasperity cavitations*. Proceedings of the Institution of Mechanical Engineers, Part J: Journal of Engineering Tribology, 2012. **226**(12): p. 1023-1038.
189. Jakobsson, B. and L. Floberg, *The finite journal bearing, considering vaporization*. 1957: Gumperts Förlag.

190. Elrod, H.G., *A cavitation algorithm*. ASME J. Lubr. Technol., 1981. **103**: p. 350.
191. Luan, B. and M.O. Robbins, *The breakdown of continuum models for mechanical contacts*. Nature, 2005. **435**(7044): p. 929-932.
192. Spikes, H., *The borderline of elastohydrodynamic and boundary lubrication*. Proceedings of the Institution of Mechanical Engineers, Part C: Journal of Mechanical Engineering Science, 2000. **214**(1): p. 23-37.
193. Luo, J., S. Wen, and P. Huang, *Thin film lubrication. Part I. Study on the transition between EHL and thin film lubrication using a relative optical interference intensity technique*. Wear, 1996. **194**(1-2): p. 107-115.
194. Martini, A., et al., *Molecular dynamics characterization of thin film viscosity for EHL simulation*. Tribology Letters, 2006. **21**(3): p. 217-225.
195. Zhu, P.-z., et al., *Molecular dynamics study on friction due to ploughing and adhesion in nanometric scratching process*. Tribology Letters, 2011. **41**(1): p. 41-46.
196. Dunaevsky, V., *A Proposed New Film Thickness-Roughness Ratio, Az, in Rolling Bearings: Notes on an Engineer's Experience with Surface Texture Parameters*, 2017, SAE Technical Paper.
197. Luo, J. and S. Liu, *The investigation of contact ratio in mixed lubrication*. Tribology international, 2006. **39**(5): p. 409-416.
198. Brizmer, V., H. Pasaribu, and G.E. Morales-Espejel, *Micropitting performance of oil additives in lubricated rolling contacts*. Tribology Transactions, 2013. **56**(5): p. 739-748.
199. Whitehouse, D.J. and J. Archard. *The properties of random surfaces of significance in their contact*. in *Proc. R. Soc. Lond. A*. 1970. The Royal Society.
200. Bowden, F.P. and D. Tabor, *The friction and lubrication of solids*. Vol. 1. 2001: Oxford university press.
201. Handbook, A., *Friction, lubrication and wear technology*. ASM International, 1992. **18**: p. 175-183.
202. Nilsson, R., *On wear in rolling/sliding contacts*, 2005, KTH.
203. Dwyer-Joyce, R., *Predicting the abrasive wear of ball bearings by lubricant debris*. Wear, 1999. **233**: p. 692-701.
204. Lancaster, J., *Material-specific wear mechanisms: relevance to wear modelling*. Wear, 1990. **141**(1): p. 159-183.
205. Meng, H. and K. Ludema, *Wear models and predictive equations: their form and content*. Wear, 1995. **181**: p. 443-457.
206. Meng, H.-C., *Wear modeling: evaluation and categorization of wear models*. 1994.
207. Sullivan, J., *Boundary lubrication and oxidational wear*. Journal of Physics D: Applied Physics, 1986. **19**(10): p. 1999.
208. Zhang, H., et al., *A micro-contact model for boundary lubrication with lubricant/surface physiochemistry*. Journal of tribology, 2003. **125**(1): p. 8-15.